THE UNIVERSITY *of* EDINBURGH

FUNCTIONAL DISSECTION OF A CORTICAL MICROCIRCUIT FOR SPATIAL COMPUTATION

HUGH PASTOLL

Doctor of Philosophy
Institute for Adaptive and Neural Computation
School of Informatics
University of Edinburgh
2013

ABSTRACT

In mammals, spatial learning and memory depend on neural processing carried out in the hippocampal formation. Interestingly, extracellular recordings from behaving animals have shown that cells in this region exhibit spatially modulated activity patterns, thus providing insights into the neural activity underlying spatial behaviour. One area within the hippocampal formation, layer II of the medial entorhinal cortex, houses cells that encode a grid-like map of space using a firing rate code. At the same time, oscillatory signals at distinct theta (4–12 Hz) and gamma (30–120 Hz) frequencies are also present in layer II, providing a substrate for a timing code. To understand how layer II of the medial entorhinal cortex produces these outputs I sought to characterise the electrical properties and functional computational architecture of its microcircuitry.

The functionality of any neural circuit depends on the electrical properties of its constituent cells. Because the grid cells in layer II are likely to be stellate cells, I used the perforated patch-clamp technique to accurately assess the intrinsic excitable properties of this cell type. Compared to whole-cell recordings, these recordings indicate that some intrinsic properties of stellate cells, such as spike clustering, which is revealed to be robust, are more likely to play a functional role in circuit computation. Conversely, other intrinsic properties, such as spontaneous membrane potential fluctuations, which are confirmed to be insufficiently stable to support reliable interference patterns, are revealed to be less likely than other, more robust electrical properties to play a direct role in circuit function.

The characteristic connectivity profiles of different cell types are also critical for circuit function. To investigate cell type-specific connectivity in layer II I used optogenetic stimulation in combination with *in vitro* electrophysiology to record synaptic activity in different cell types while selectively activating distinct subpopulations of cells with light. Using this method I found that connections between stellate cells are absent or very rare and that communication between stellate cells is instead mediated by strong feedback inhibition from fast-spiking interneurons.

Dissecting oscillatory activity in neural circuits may be important for establishing functionally relevant circuit architecture and dynamics but is difficult *in vivo*. I accomplished this *in vitro* by recapitulating the interacting theta and gamma rhythms that are observed *in vivo* with an optogenetic method. I found that locally driving a subset of neurons in the layer II microcircuit at theta frequency with a light stim-

ulus produced a nested field rhythm at gamma frequency that was also evident as rhythmic inhibition onto stellate cells. Critically, these interacting rhythms closely resembled those recorded from behaving animals. In addition, I found that this theta-nested gamma is sufficiently regular to act as a clock-like reference signal, indicating its potential role in implementing a timing code. To functionally dissect the circuit I performed multiple simultaneous whole-cell patch-clamp recordings during circuit activation. These recordings revealed how feedback interactions between stellate cells and fast-spiking interneurons underpin the theta-nested gamma rhythm.

Together, these results suggest that feedback inhibition in layer II acts as a common substrate for theta-nested gamma oscillations and possibly also grid firing fields, thereby providing a framework for understanding how computations are carried out in layer II of the medial entorhinal cortex.

ACKNOWLEDGEMENTS

I am particularly grateful to my supervisor, Dr Matt Nolan, whose encouragement, insights and support made this work possible. I am also grateful to my co-supervisor, Dr Mark van Rossum, for his help and input throughout my PhD.

Many thanks also to my colleagues Dr Melanie White, Helen Ramsden and Lukas Solanka for being such excellent collaborators and for their contributions to work presented in this thesis.

Finally, I would like to thank all my fellow students and friends in the DTC, not only for all their help and advice, but also for providing a congenial and intellectually stimulating environment that has contributed so much to my enjoyment of my time in Edinburgh.

DECLARATION

I declare that this thesis was composed by myself, that the work contained herein is my own except where explicitly stated otherwise in the text, and that this work has not been submitted for any other degree or professional qualification except as specified.

Edinburgh, 2013

Hugh Pastoll, May 3, 2013

CONTENTS

1 INTRODUCTION

1.1 THE MEC IS A CORTICAL CIRCUIT FOR SPATIAL NAVIGATION

To find food, shelter and mates animals must navigate through complex environments. To navigate successfully, animals must track and predict their own location relative to their environment, a process that requires integration of information about the geometry of the environment, landmarks and recent self-motion (Etienne and Jeffery, 2004; Jeffery, 2007). Despite the central importance of navigation for survival, the neural mechanisms that encode and integrate environmental and self motion information remain largely unclear.

Computation of self motion information may, however, provide a window onto the neural processes underlying spatial navigation. Self motion information is sufficient to enable mammals to track their location for substantial distances, independent of environmental cues (Mittelstaedt and Mittelstaedt, 1980; Etienne and Jeffery, 2004) by relying on integration of speed and directional heading information, a process known as path integration (Etienne and Jeffery, 2004; Jeffery, 2007). In the medial entorhinal cortex (MEC) of behaving animals, patterns of neural activity encode space (Hafting et al., 2005, 2008) in a manner consistent with the output of a system computing self motion by integration of speed and directional information (McNaughton et al., 2006; Jeffery, 2007; Navratilova et al., 2012).

Two distinct patterns of neural activity in the MEC, grid firing fields (Hafting et al., 2005) and theta phase precession (Hafting et al., 2008), encode space in different ways but in neither case is the underlying physiology well explained. However, because these different forms of activity must rely on common neural circuitry, elucidating the cellular basis of this activity will not only shed light on the neural mechanisms for spatial navigation by path integration, but will also provide insights into how cortical neural circuity can simultaneously support separate coding schemes.

1.1.1 *Neural activity in the hippocampal formation encodes space*

Cells that encode space were first found in the rat hippocampus, an area in the hippocampal formation region (O'Keefe and Dostrovsky, 1971). Extracellular recordings from the hippocampus revealed that 'place cells' in this area encode an animal's

position in space by increasing their spiking rate only when the animal occupies a distinct location in its environment (O'Keefe and Dostrovsky, 1971) and by firing action potentials at progressively earlier phases of the ongoing theta frequency field oscillation as the animals traverses a cell's 'place field' (O'Keefe and Recce, 1993). These hippocampal recordings provided an initial indication that the hippocampal formation, of which the entorhinal cortex is also part, is centrally involved in spatial processing.

Intact neural processing in many areas in the hippocampal formation is required for normal spatial behaviours. Consistent with the physiology of place cells, lesions of the hippocampus impair spatial abilities, (Kaada et al., 1961; Moser et al., 1993). However, lesions of upstream areas in the hippocampal formation also produce spatial behaviour deficits. Entorhinal cortex lesions impair spatial, but not contextual, learning and retention (Good and Honey, 1997; Steffenach et al., 2005) and lesions of the dorsal presubiculum (also known as the postsubiculum) adversely affect performance on uncued spatial tasks (Taube et al., 1992). Together, these results suggested that separate areas in the hippocampal formation work together to route processed spatial information to the hippocampus.

Consistent with an organisation of the hippocampal formation in which important spatial processing also occurs upstream of the hippocampus, cells in upstream areas also encode spatial information, but in other ways. Cells in the dorsal presubiculum and parasubiculum signal directional heading with firing rates that increase when an animal faces a particular direction but do not depend on the animal's location in the environment (Taube et al., 1990; Boccara et al., 2010). The firing rate of head direction cells correlates weakly with locomotor speed, suggesting one possible afferent route for speed information (Jeffery, 2007). Many cells in the entorhinal cortex are also spatially modulated (Fyhn et al., 2004; Krupic et al., 2012), with a substantial portion of these cells displaying remarkable periodic maps of space (Hafting et al., 2005).

The firing patterns of presubicular, parasubicular, entorhinal and hippocampal cells suggest that head direction information may be integrated with linear speed information (Jeffery, 2007) in the entorhinal cortex to produce orientation independent maps of space which then serve as an important input to the hippocampus. Understanding how integration of speed and directional information in the entorhinal cortex is achieved will be important for dissecting the neural mechanisms underlying path integration.

Grid firing fields in the MEC encode location with a rate code

Many spatially modulated cells in the MEC fire preferentially when an animal's position in space coincides with a vertex of an imaginary triangular grid imposed on its

environment (Hafting et al., 2005; Sargolini et al., 2006; Barry et al., 2007; Brun et al., 2008; Fyhn et al., 2008; Langston et al., 2010; Brandon et al., 2011; Koenig et al., 2011; Yartsev et al., 2011; Giocomo et al., 2011a; Krupic et al., 2012; Killian et al., 2012; Stensola et al., 2012). Because the position of an animal is coded by periodic changes in cells' firing rates as the animal moves through locations that are determined entirely by their coordinates in an abstract map anchored on the external environment, 'grid cells' provide an allocentric map of space (see figure 1.1).

Grid fields are present in rat pups as soon as they explore outside their nest (P16) but the periodicity and spatial coherence of the grid fields continues to increase until adulthood (P28+) (Langston et al., 2010), suggesting experience plays a role in shaping grid firing output. In adult animals grid field spacing can rescale with both resizing of the environment (Barry et al., 2007) and expand in response to novel environments (Barry et al., 2012), indicating that grid cells integrate environmental information with other inputs to renew features of the spatial maps (Barry et al., 2007; Stensola et al., 2012).

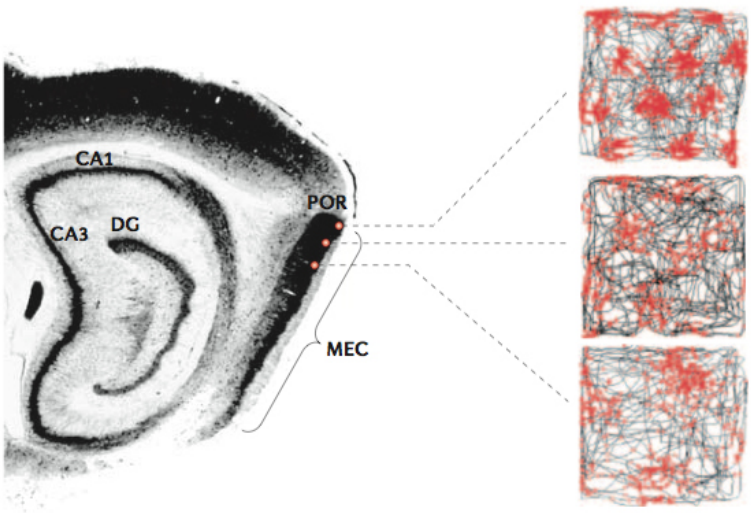

Figure 1.1: **Grid cells have periodic firing fields with grid spacing that varies with anatomical location. Left:** Sagittal section indicating location of recorded cells (red dots) in the MEC. **Right:**. Tracks of animal position in a square enclosure (grey lines) turn red when indicated cells fire an action potential. The resulting spiking tiles space with a periodic triangular pattern. *Figure from McNaughton et al. (2006).*

Grid cells may be common to all mammalian species. Single unit recordings have demonstrated the existence of grid cells in rats (Hafting et al., 2005), mice (Fyhn et al., 2008), bats (Yartsev et al., 2011), and monkeys (Killian et al., 2012) and BOLD signals from imaging studies in humans are consistent with secondary characteristics of grid cells observed in rats (Doeller et al., 2010). Together, these studies indicate that rate coding of space through grid firing fields may be a universal feature of mammalian spatial computation.

Grid cells multiplex rate and temporal codes

The output of many, but not all, grid cells is modulated by a prominent ongoing local field potential (LFP) oscillation in the theta (4 – 12 Hz) range (Hafting et al., 2005, 2008; Krupic et al., 2012; Stensola et al., 2012). Interestingly, in addition to encoding space with a firing rate code, grid cells in the superficial layers of the MEC also encode spatial information by the phase of their action potentials relative to the ongoing LFP theta frequency oscillation (Hafting et al., 2008). As an animal runs through a cell's grid firing field, the spikes occur at increasingly earlier phases of theta cycles (Hafting et al., 2008) meaning that the theta phase of spikes depends on the position of the animal in space. This theta phase precession of spatially modulated cells is similar to that observed in place cells in the hippocampus (O'Keefe and Recce, 1993), is robust at the single trial level and provides information that improves estimation of location from firing rate patterns (Reifenstein et al., 2012).

Because precise timing of action potentials relative to the theta oscillation is required for theta phase spatial encoding, grid cells are implementing a spike timing, or temporal, code that has substantially higher time resolution than would be required purely for generation of grid firing fields. Because this temporal code coexists with the firing rate code, the MEC multiplexes the two different codes, effectively providing separate channels for different forms of spatial information (Panzeri et al., 2010). The circuit mechanisms in the MEC that underly this dual coding scheme remain unclear.

Topographical organisation of grid cell output

Several features of grid cell output are topographically organised within the MEC. Both the spacing between the vertices of the grid cell map and the size of the grid firing fields varies with anatomical location along the dorsal-ventral axis of the MEC (Brun et al., 2008) (see Figure 1.1), indicating that grid cells encode space at different scales. Recent evidence indicates that instead of following a continuous gradient, grid spacing and size are clustered in distinct groups of values (Stensola et al., 2012). Similar discrete clustering of grid alignment, grid distortion and theta frequency modulation suggest that grid activity is produced by modular circuits in the MEC (Stensola et al., 2012). The modules appear to be functionally independent, but can overlap along the dorsal-ventral axis, indicating that anatomical location does not perfectly predict circuit participation (Stensola et al., 2012).

The topographical organisation of grid cell features provides insight into both hippocampal and entorhinal processing. Theoretical neural networks have shown that output of grid cells with different spatial scales can be combined to produce non-

or sparsely periodic place fields in downstream cells (McNaughton et al., 2006; Fiete et al., 2008) suggesting that topographically organised features of grid cells play a key role in place cell generation (McNaughton et al., 2006; Jeffery, 2007). The modular dorsal-ventral organisation of grid cell output also places important constraints on how the circuitry of the MEC produces grid fields and can provide insights into which properties of MEC circuitry are likely to contribute to grid cell output (Garden et al., 2008; O'Donnell and Nolan, 2011).

1.1.2 *Towards an understanding of the circuit for spatial computation*

Grid cells are unevenly distributed across the layers of the MEC. While grid cells are present in deeper layers of the MEC (Hafting et al., 2005; Sargolini et al., 2006) they are most prevalent in layer II of the MEC (Sargolini et al., 2006). Other layers of the MEC also contain head direction cells and conjunctive grid-by-head direction cells, (where firing depends both on location and heading) but these types of cells are not present in layer II (Sargolini et al., 2006). The relative homogeneity of spatial firing patterns in layer II of the MEC suggest that the results of processing of heterogenous ideothetic information encoded by the deeper layers of the MEC and other upstream areas is processed in layer II to produce stable allothetic spatial maps in layer II, which are then routed to the hippocampus (McNaughton et al., 2006). The microcircuitry of layer II therefore provides an important focus for investigating how the MEC produces grid firing fields. Furthermore, explaining how the microcircuitry of the MEC layer II enables the coexistence of grid cell rate coding with phase precession and interacting oscillatory rhythms that accompany spatial behaviours presents an important challenge.

Understanding how any neural microcircuit performs its computations requires knowledge of three things: (i) the nature of the synaptic inputs to the circuit, (ii) the characteristics of the components that comprise the circuit (the electrical properties of neurons) and (iii) the functional interactions between the different types of neurons in the circuit. To further our understanding of how the layer II microcircuit in the MEC performs its spatial computations it will be necessary to build on existing knowledge in all these areas.

1.2 CIRCUIT RHYTHMS AND SPATIAL COMPUTATION IN THE MEC

Cortical networks oscillations are a prominent feature of neural circuit output in behaving animals (Buzsaki and Draguhn, 2004). The frequency and amplitude of cortical oscillations depend on behavioural state (Vanderwolf, 1969; Buzsaki, 2002;

Buzsaki and Draguhn, 2004; Klausberger and Somogyi, 2008; Fries, 2009; Canolty and Knight, 2010; Buzsaki and Wang, 2012) and coupling of oscillatory activity across different frequency bands is associated with a range of cognitive states (Buzsaki and Draguhn, 2004; Canolty and Knight, 2010; Buzsaki and Wang, 2012) suggesting that oscillations with different properties are likely to be critical for different forms of neural function and that interactions between distinct rhythms play important roles in cognition.

Network oscillations have many features that could be important for a range of different neural functions. It is thought that network oscillations are likely to be critical for temporal codes (Buzsaki, 2002; Lisman, 2005; Buzsaki and Draguhn, 2004), as they provide a reference signal with phase that could provide accurate timestamps for precisely timed action potentials. Oscillations can also synchronise activity across separate cortical areas (Buzsaki, 2002; Buzsaki and Draguhn, 2004; Canolty and Knight, 2010), which may be critical for precisely timed communication and has been proposed to play important roles in memory (Fell and Axmacher, 2011). Because the excitability of cells can depend on network oscillation phase, control over the gain of communication between two areas, and therefore routing of information, could be achieved by either shifting the relative phase offset between phase-locked oscillations in different areas (Fries, 2009) or by entraining two areas to a common oscillation frequency (Colgin et al., 2009). In addition, high frequency oscillations may influence communication between areas by restricting the spiking of assemblies of neurons to narrow time windows that may be required for coincidence detection by cells in downstream areas (Buzsaki and Wang, 2012). They may also reduce noise and amplify circuit signals and artificial generation of fast rhythms enhances signal transmission *in vivo* (Sohal et al., 2009).

However, despite their importance for neural function, the cellular mechanisms responsible for oscillations are often poorly understood. In particular, the mechanisms that coordinate interactions between oscillations in different frequency bands are not known and the relationship between the network mechanisms that support oscillatory activity and those that govern generation of firing rate codes remains unclear. Elucidating the circuitry that underlies the generation and regulation of neural rhythms in the MEC will be important for understanding the computational contributions and limits of rhythms in this area, including, potentially, how space is encoded by phase precession in the superficial MEC.

1.2.1 *Theta-nested gamma oscillations in the MEC*

In rodent entorhinal cortex, prominent local field potential oscillations in the theta (4–12 Hz) and high gamma (60–120 Hz) bands accompany spatial behaviours (Mitchell and Ranck, 1980; Chrobak and Buzsaki, 1998; Colgin et al., 2009). Extensive characterisation of the properties of these rhythms and their interactions, coupled with an understanding of their cellular mechanisms, will provide important insights into how they contribute to spatial information processing in the MEC.

Theta frequency oscillations

In behaving rodents, an LFP rhythm of ~8 Hz is present in all layers of the MEC (Mitchell and Ranck, 1980; Alonso and García-Austt, 1987; Chrobak and Buzsaki, 1998; Mizuseki et al., 2009). Time-frequency analysis reveals that theta rhythm frequency and power are very stable across time in the superficial layers of anaesthetised rats (Quilichini et al., 2010) (albeit at the lower frequency of 4 Hz) suggesting that, in rodents, the ongoing theta signal may serve to act as a constant reference signal for a timing code. However, in behaving bats the LFP only exhibits intermittent periods of theta power, despite persistent grid cell activity (Yartsev et al., 2011). It is thus not clear whether an ongoing theta rhythm is required for spatial navigation in all mammals, but in rodents it appears to facilitate a temporal code that may act in parallel to rate coded grid firing fields and thereby enhance spatial navigation. However, the two codes may not be completely independent as pharmacological reduction of the theta rhythm is accompanied by a reduction of the spatial periodicity of grid cells (Koenig et al., 2011; Brandon et al., 2011).

Theta activity is phase locked across all layers of the MEC and may therefore act as a common reference signal across all layers. In rodents, the phase of the theta oscillation is synchronised across layers II–V with layer I phase being reversed (shifted by π radians) (Chrobak and Buzsaki, 1998; Mizuseki et al., 2009; Quilichini et al., 2010), producing a phase-locked theta rhythm in layer I that is offset by half a theta cycle from oscillations in the other layers. This shift is apparent in anaesthetised (Alonso and García-Austt, 1987; Quilichini et al., 2010) and behaving (Mitchell and Ranck, 1980; Mizuseki et al., 2009) animals, but it remains unclear whether this is due to phase shifted synaptic inputs arriving in layer I or whether it reflects a return current from source to the current sink of synaptic inputs to other layers. The computational significance of the shift is also not clear.

The MEC theta rhythm organises spike output in both rodents and bats (Fyhn et al., 2004; Mizuseki et al., 2009; Yartsev et al., 2011). Spikes from cells in the superficial layers of the MEC are modulated by theta rhythm phase (Fyhn et al., 2004; Hafting

et al., 2005; Mizuseki et al., 2009; Krupic et al., 2012; Stensola et al., 2012) and because cells in different layers (and different cell types within layers) preferentially spike at different phases of the theta rhythm (Mizuseki et al., 2009) it appears that action potential output is controlled in relation to the theta rhythm and is not just a direct consequence of depolarising synaptic inputs arriving at theta frequency. The theta rhythm therefore appears to regulate interactions between many components of the MEC circuitry.

Theta frequency oscillations provide a common reference for the coding of space throughout the hippocampal formation. Entorhinal theta is coupled to theta rhythms elsewhere in the hippocampal formation, including the hippocampus (Buzsaki, 2002; Mizuseki et al., 2009; Colgin et al., 2009) suggesting that entorhinal theta spike phase information could be utilised by the downstream computations in the hippocampus. Furthermore, both grid cells (Hafting et al., 2005, 2008; Reifenstein et al., 2012) and place cells (O'Keefe and Recce, 1993) encode spatial information by theta phase precession of action potentials as animals move through grid and place fields respectively, suggesting that phase precession may depend on mechanisms that coordinate activity between the entorhinal cortex and the hippocampus. Phase precession in layer II of the MEC remains following muscimol inactivation of the the dorsal hippocampus, suggesting that it can be generated by hippocampus-independent mechanisms (Hafting et al., 2008).

Gamma frequency oscillations

Gamma frequency (30–120 Hz) oscillations are also present in the MEC. In rodents they have a relatively high frequency of ~90 Hz (Chrobak and Buzsaki, 1998; Colgin et al., 2009), whereas in bats brief episodes of gamma activity span a much wider range of frequencies, from low (30–60 Hz) to high (60–120 Hz) gamma ranges (Yartsev et al., 2011). In rodents, gamma oscillations are modulated by the ongoing theta rhythm such that gamma oscillations emerge in the trough of each theta cycle and the frequency of gamma varies with theta frequency (Chrobak and Buzsaki, 1998). It is not clear how the phase relationship between theta and gamma amplitude is maintained, whether the amplitude of theta modulates the gamma frequency or if, in addition to the phase–amplitude coupling between theta and gamma, the theta-nested gamma exhibits clock like properties (i.e there is also phase-phase coupling between theta and gamma), as has been observed in the hippocampus (Belluscio et al., 2012).

Gamma activity is also synchronised across the MEC. Similar to the theta rhythm, in behaving rodents, the gamma LFP is phase-locked across all layers, with a phase reversal between layers I and II (Chrobak and Buzsaki, 1998). However, the ampli-

tude of the gamma LFP varies substantially across layers, being strongest in layers II and III, which provide a major input to the hippocampus, and is weakest in the deeper layers (Chrobak and Buzsaki, 1998). Because spikes from both putative principal neurons and interneurons are phase locked to the gamma LFP, with all spikes preferentially occurring at the trough of gamma oscillations (Chrobak and Buzsaki, 1998), MEC output from the superficial layers to the hippocampus is substantially coordinated by the gamma rhythm, with spikes occurring in narrow time windows, which may be essential for activating target cells in the hippocampus.

Computational roles of theta-nested gamma

The theta phase – gamma amplitude relationship (or cross frequency phase–amplitude coupling) in the MEC is thought to have important consequences for information coding in the hippocampal formation (Lisman, 2005; Buzsaki and Wang, 2012). First, nested gamma may serve to discretise the theta phase (Figure 1.2 A). If all spikes that correspond to an individual gamma 'bin' are assigned the same 'theta' phase, phase readout of spikes may be more robust to noise than if exact theta phase readout was required. Second, because separate distinct assemblies of MEC cells might fire on subsequent gamma cycles within each theta cycle (Figure 1.2 B), theta-nested gamma could provide a mechanism for organising ensemble output into distinct sequences that may play an important role in spatial memory (Lisman, 2005; Fell and Axmacher, 2011).

Phase–phase coupling between gamma rhythms in the MEC and other areas may also play an important role in spatial computations. Because cells are more excitable at the trough of the LFP gamma cycle, regulating the gamma phase relationship between two areas would change the gain of the communication between them (Fries, 2009). Theta-nested gamma phase synchronisation between the MEC and the CA1 field of the hippocampus is an example of how communication between two areas can depend on gamma phase synchronisation. The high frequency gamma in the MEC is synchronised with a fast gamma rhythm of similar frequency in the CA1 field of the hippocampus in a subset of theta cycles, suggesting that communication between the MEC and CA1 may be regulated on a theta cycle basis by controlled switching between different frequency gamma rhythms in CA1 (Colgin et al., 2009). It remains unclear how this temporary gamma phase synchronisation is achieved.

Phase–phase cross frequency coupling between the theta rhythm and the nested gamma rhythms may extend the computational repertoire of cortical circuits (Figure 1.2). In cross frequency phase–phase coupling the theta phase of sequential clock-like nested gamma oscillation cycles remains fixed across theta episodes (Fell and Axmacher, 2011; Buzsaki and Wang, 2012) and enables more temporally fine grained

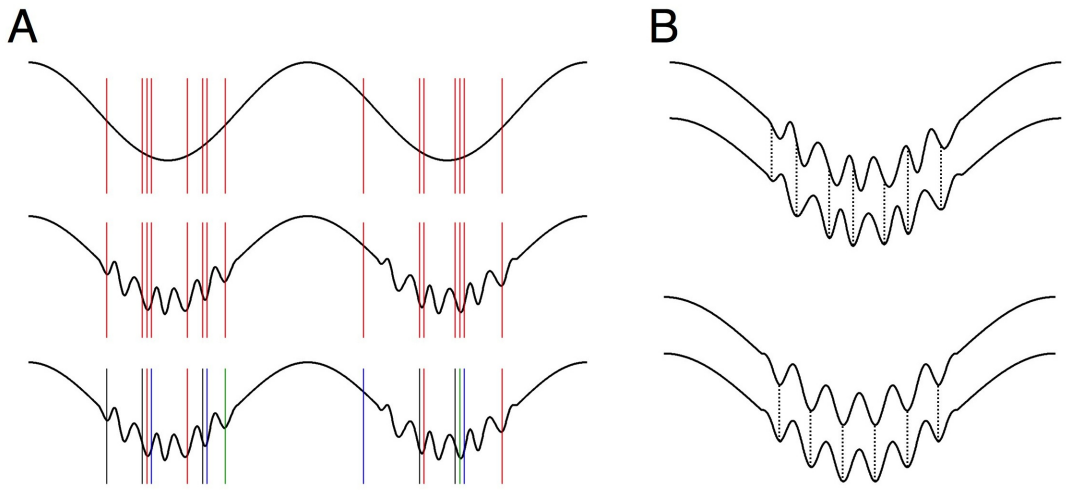

Figure 1.2: **Computational advantages of different types of coupling between theta and gamma rhythms. A** The theta phase of the LFP (black waveform) can be used as a reference for a spiking timing code. Each individual spike (red line) can be assigned an exact phase value based on the continuous phase of the LFP theta signal (upper). An additional gamma nested gamma oscillation in the trough of the theta oscillation (theta–gamma phase–amplitude coupling) provides a way to discretise theta phase (middle). In this arrangement multiple spikes that occur in the same gamma 'bin' are assigned the same discretised theta phase value. Distinct but overlapping ensembles neurons (different coloured spikes are from different cells) can contribute to groups of spikes occurring in consecutive gamma bins (bottom). **B** In cross frequency phase–amplitude coupling between theta and gamma oscillations the gamma phases are not necessarily aligned across consecutive theta cycles (upper). Gamma phases are aligned in the case of cross frequency phase–phase coupling or clock-like theta-nested gamma (bottom).

computations than simple phase–amplitude coupling. For example, sequences of information can be encoded with a higher temporal resolution (Fell and Axmacher, 2011). Furthemore, other cortical areas that are 'aware' of the phase of a given theta rhythm could predict the phase of the phase coupled gamma oscillations at a future point in time, potentially enabling temporal coordination of future spiking with future gamma phase. In addition, increasing cross-frequency phase–phase coupling between areas that are already synchronised to a common theta rhythm would increase gamma phase coupling between the areas as well (Fell and Axmacher, 2011). Evidence that gamma is regular within theta cycles in the MEC is consistent with cross frequency phase–phase coupling (Chrobak and Buzsaki, 1998), but it remains unknown whether circuits of the MEC are capable of maintaining phase-phase coupling between the theta and gamma rhythms or even whether clock-like theta-nested gamma is critical for spatial computation.

1.2.2 *Circuit mechanisms of entorhinal rhythms*

LFP signals arise from transmembrane current flow that creates voltage gradients between the recorded location and a ground reference (Lindén et al., 2011; Buzsaki et al., 2012). Synaptic currents typically underlie the majority of the LFP signal, but action potential and sub-threshold ionic current fluctuations can also play substantial roles (Buzsaki et al., 2012). For a given LFP recording location, transmembrane currents in local neurons contribute the majority of the LFP signal (Buzsaki, 2002; Buzsaki et al., 2012). However, while nearby cells always act as the *source* of a rhythmic LFP, they may not necessarily act as rhythm *generators*, as local rhythmic synaptic activity may be generated by rhythmic spiking in distal areas (Buzsaki, 2002).

The origin of the entorhinal theta rhythm

An understanding of how the entorhinal theta rhythm is generated could provide important insights into its computation role. However, the circuit mechanisms that generate it remain unclear. Two major candidate mechanisms have been proposed, each with different implications for entorhinal circuit function and grid cell generation.

One possibility is that theta oscillations are generated within the MEC by intrinsic electrophysiological mechanisms in layer II cells that are activated at depolarised membrane potentials (Alonso and Llinás, 1989) and which may be engaged by the depolarising effects of cholinergic input from the medial septum *in vivo* (Klink and Alonso, 1997b; Buzsaki, 2002). Principal cells in layer II exhibit spontaneous membrane potential activity in the theta range when depolarised close to action potential threshold by somatic current injection (Alonso and Llinás, 1989) and with perfusion of the muscarinic receptor agonist carbachol *in vitro* (Klink and Alonso, 1997b). It has been argued that these membrane potential fluctuations are the driving force behind the entorhinal theta rhythm (e.g. Giocomo et al., 2007; Yoshida et al., 2011).

However, these membrane potential fluctuations may not be sufficiently periodic or sustained to produce the rhythmic LFP oscillations observed *in vivo* (Dodson et al., 2011) and it is not clear whether known circuit mechanisms in the MEC would enable synchronisation across the network of theta frequency fluctuations generated in individual cells. Furthermore, it is not clear how this would account for theta oscillations present in other layers of the MEC, as principal cells in layer III do not display these properties (Dickson et al., 1997) and they have also not been reported in cells in deeper layers. Together, these considerations suggest that intrinsic membrane potential fluctuations may not be solely responsible for the theta LFP observed *in vivo*.

The main competing hypothesis is that the entorhinal theta rhythm is generated outside the MEC. In the medial septum, an area with projections to the MEC, cholinergic and GABAergic neurons fire non-adapting action potential bursts at theta frequency (Alonso et al., 1996; Serafin et al., 1996). Theta rhythms in the MEC are disrupted when the medial septum is lesioned (Mitchell et al., 1982; Jeffery et al., 1995; Koenig et al., 2011; Brandon et al., 2011), indicating that input from cells in the medial septum is required for generation of theta oscillations in the MEC. However, the loss of the MEC theta rhythm may reflect a lack of an afferent drive that may normally produce theta rhythms by activating mechanisms intrinsic to the MEC and so these experiments do not provide definitive evidence that the MEC theta rhythm is directly inherited from the medial septum. However, the entorhinal theta rhythm in awake animals is likely resistant to block of muscarinic receptors (Buzsaki, 2002), suggesting that depolarising cholinergic drive may not be necessary for theta generation in awake animals and that therefore theta frequency GABAergic input from the septum may play an important role.

Finally, pharmacological models of theta frequency activity have not provided much insight into the cellular mechanisms of theta oscillations. Perfusion of carbachol can elicit brief episodes of LFP theta activity that is synchronised across all layers of the MEC in some *in vitro* preparations (Dickson and Alonso, 1997; van der Linden et al., 1999; Dickson et al., 2000a), supporting an intrinsic, cholinergic dependent generation of LFP theta in the MEC. However, these theta-like episodes do not resemble the sustained theta activity observed in behaving rodents. They are also sensitive to atropine (Dickson and Alonso, 1997), which the hippocampal formation theta rhythm is not (Buzsaki, 2002), suggesting that this theta-like activity is not an appropriate model of MEC theta *in vivo*.

Pharmacological induction of gamma rhythms in the MEC

Mechanisms for generation of gamma rhythms are typically divided into two classes – those that rely on interactions within an interconnected network of inhibitory cells (I–I networks) and those that rely on interactions between reciprocally connected pools of inhibitory and excitatory cells (E–I networks) (Whittington et al., 2010; Buzsaki and Wang, 2012). In I–I gamma a general excitatory drive can induce rhythmic spiking in a network of mutually inhibiting cells. The rhythm arises because all cells in the network are only able to spike once they have recovered from the inhibition imposed by other cells in the population. Critically, in this configuration, the time constant of the inhibition controls the oscillation frequency and the depolarising synaptic input to inhibitory cells need not occur at the dominant network frequency (Whittington et al., 2010; Buzsaki and Wang, 2012). In contrast, E–I gamma develops when a group

of excitatory cells drive a group of inhibitory cells to fire, which in turn suppress the firing of the excitatory group for a fixed duration. Importantly, not all members of each group need to fire on every oscillation cycle, meaning that distinct subsets of cells can contribute to consecutive gamma oscillation cycles. In this type of gamma the time constant of excitation and inhibitory decay together determine the gamma frequency (Whittington et al., 2010; Buzsaki and Wang, 2012). In E–I networks with physiological levels of heterogeneity, gamma either develops rapidly or not at all, with its robustness depending on the total number of cells in the network (Börgers et al., 2012).

In vitro pharmacological models of gamma aim to reproduce *in vivo* gamma rhythms *in vitro*, permitting detailed dissection of the cellular circuitry involved in rhythm generation and potentially enabling identification of the underlying circuit mechanisms. Arterial perfusion and local injection of carbachol in guinea pig whole brain preparations (van der Linden et al., 1999; Dickson et al., 2000a) and application of kainate to brain slices (Cunningham et al., 2003, 2004, 2006; Middleton et al., 2008) both induce LFP oscillations in the low gamma frequency range (<45 Hz) in the MEC and have been proposed as models of the gamma activity observed *in vivo*.

Recordings during pharmacologically induced gamma activity provide insights into the circuit mechanisms that underlie it. Locally restricted application of carbachol at separate MEC locations produces LFP gamma rhythms that are not coherent, suggesting that gamma can be produced by local independent assemblies of cells in the superficial layers of the MEC (Dickson et al., 2000a). In one report of kainate gamma, EPSPs occur in interneurons at a frequency ~10 Hz below the network rhythm (Cunningham et al., 2003), suggesting that the excitation originates from cells that do not participate in the gamma rhythm and that an I–I mechanism therefore produces the gamma rhythm. Conversely, however, other data suggest that, consistent with an E–I mechanism, basket cell interneurons receive phasic excitation at the network gamma frequency during kainate gamma (Middleton et al., 2008), and therefore the actual circuit mechanism of kainate gamma remains unclear.

However, several considerations suggest these types of pharmacological gamma are not good models for *in vivo* gamma. First, the frequency of carbachol and kainate gamma is much lower (<45 Hz) than observed in rodents *in vivo* (~ 90 Hz) (Chrobak and Buzsaki, 1998; Colgin et al., 2009), suggesting that they are generated by different circuit mechanisms. Second, pharmacological gamma is not reliably theta modulated, and therefore provides little clue as to whether these types of gamma oscillation can develop and recede within individual theta cycles, as is observed *in vivo*, and do not yield any other mechanistic insights into the relationship between theta and gamma rhythms. The phase profiles of the gamma activity across MEC layers are

also inconsistent; whereas the phase of *in vivo* gamma reverses between layers I and II, the phase of carbachol gamma reverses *across* layer II (van der Linden et al., 1999; Dickson et al., 2000a) and kainate gamma phase reverses between layers II and III (Cunningham et al., 2003), again suggesting that the cellular mechanisms underlying each form of gamma may differ.

Directions for dissection of MEC rhythms

Despite the potential for pharmacologically induced LFP rhythms to provide insights into *in vivo* theta-nested gamma in the MEC, it appears that a mechanistic understanding of the theta and gamma rhythms and the relationship between them awaits either a more physiological way of inducing LFP oscillations *in vitro* or more direct *in vivo* data, which is challenging to obtain. It therefore remains important to establish whether *in vivo*-like theta-nested gamma rhythms can be generated locally, what the connection between theta and gamma rhythms is, and which cell types in different layers of the MEC contribute to rhythmic activity and how the circuitry underlying the LFP rhythms is configured.

1.3 THE ANATOMY AND FUNCTIONAL CONNECTIVITY OF LAYER II OF THE MEC

The microcircuitry of layer II plays a critical role in the system for spatial processing, influencing both rate and temporal coding of space, and contributes to oscillations that may be critical for temporal codes. A high proportion of cells (~50 %) in layer II have grid firing fields (Hafting et al., 2005; Sargolini et al., 2006) or are otherwise spatially modulated (Hafting et al., 2005; Krupic et al., 2012) and, unlike other layers of the MEC, this information appears to be encoded in a manner independent of ideothetic head direction information (Sargolini et al., 2006). Because many cells in layer II are a major source of input to the hippocampus, it is likely that this information is transmitted directly to the hippocampus and is therefore critical for the genesis of place fields and representation of spatial location.

Many influential ideas of layer II function are predicated on the presence of particular layer II microcircuit configurations. For example, recurrent excitation within layer II forms the basis of many important models of grid cell generation in layer II (Fuhs and Touretzky, 2006; Guanella et al., 2007; Navratilova et al., 2012) and has been proposed to underly genesis of epileptiform activity in this area (Kumar et al., 2007). In addition, interactions between excitatory stellate cells and fast spiking interneurons have been proposed to underly some forms of gamma frequency activity (Middleton et al., 2008). However, many of these ideas are based on assumptions for which the underlying evidence is not yet compelling.

1.3.1 *Anatomy of layer II*

The MEC is part of the entorhinal cortex, an allocortical (as opposed to neocortical) structure situated, in rodents, along the caudal extreme of the cerebrum (Braak and Braak, 1985; Amaral and Witter, 1989; Canto et al., 2008) (see Figure 1.3). The EC comprises the MEC and the lateral entorhinal cortex (LEC) (Witter et al., 1989), which are distinguished based on cytoarchitectonic (Witter et al., 1989; Canto et al., 2008; Canto and Witter, 2011) and extrinsic connectivity (Burwell and Amaral, 1998a; Burwell, 2000). Lesion studies indicate that the MEC and LEC also underpin distinct behavioural functions (Van Cauter et al., 2012).

Further subdivisions of the MEC into distinct dorsolateral, intermediate and ventromedial bands are sometimes made based on their projections to the hippocampus (Dolorfo and Amaral, 1998; Kerr et al., 2007; Canto et al., 2008). The dorsolateral band projects exclusively (Dolorfo and Amaral, 1998) to more septal areas of the hippocampus while the ventromedial band projects exclusively to the temporal areas of the hippocampus. However, because no cytoarchitectonic differences have been identified between the bands (Kerr et al., 2007), location within the MEC can be more accurately conveyed by providing a quantitative measurement of position along the dorsal-ventral axis rather than reporting band membership as this may not map onto any meaningful divisions (Figure 1.3 illustrates the dorsolateral-ventromedial axis largely coincides with the dorsal-ventral axis).

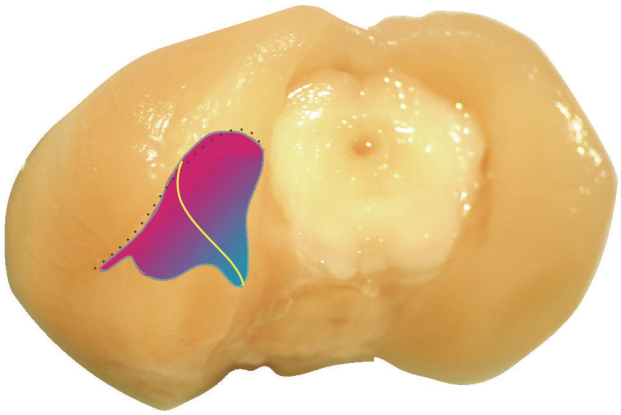

Figure 1.3: **Anatomical location of the LEC and MEC in rodent.** The LEC (lateral to yellow dividing line) and MEC (medial to yellow dividing line). More dorsal parts of the EC (magenta - dorsolateral band) are connected with more septal parts of the hippocampus and more ventral parts of the EC (cyan - ventromedial band) are connected with more temporal parts of the hippocampus. *Figure from Canto et al. (2008).*

Cytoarchitecture of layer II of the MEC

Stellate cells are the most numerous cell type in layer II, accounting for ~70% of all cells in the layer in mice and are relatively more abundant in the superficial part of the layer (Alonso and Klink, 1993; Klink and Alonso, 1997a; Gatome et al., 2010). They contribute the majority of the perforant path output to the dentate gyrus (DG) and CA3 fields of the hippocampus and therefore play a prominent role in entorhinal–hippocampal communication (Steward and Scoville, 1976; Schwartz and Coleman, 1981; Ruth et al., 1982; Köhler, 1986; Ruth et al., 1988; Insausti et al., 1997; Dolorfo and Amaral, 1998). Anatomically, stellate cells are characterised by a stellate dendritic architecture with multiple primary dendrites that arborize in layers I, II and III and axons that travel to the hippocampus in the sub-laminar direction but also have arborisations in layers I, II, III and V (Cajal, 1995; Alonso and Llinás, 1989; Klink and Alonso, 1993; Jones, 1994; Klink and Alonso, 1997a; Heinemann et al., 2000; Erchova et al., 2004; Burton et al., 2008; Garden et al., 2008). Stellate cells are excitatory and are immunopositive for glutamate (glutamate+) (Canto et al., 2008; Varga et al., 2010). In addition, many, if not all, stellate cells are reelin+ (Varga et al., 2010)

Another type of projection cell, pyramidal cells, account for ~15 % of cells and are more abundant in the deeper portion of layer II (Klink and Alonso, 1997a; Gatome et al., 2010). Pyramidal cells have a single large apical dendrite, which exits the soma in the superficial direction and arborises primarily in layer I, and basal dendrites that arborize in layers II and III (Klink and Alonso, 1997a; Canto et al., 2008; Canto and Witter, 2011). They are presumed glutamatergic (Canto et al., 2008), but it remains unclear where pyramidal cells project and direct synaptic responses from pyramidal to other connected cells have not been found. Pyramidal cells may correspond to calbindin positive (CALB+) cells, which project to contralateral MEC and avoid the hippocampus (Varga et al., 2010), but the relative proportion of CALB+ cells in layer II (similar to the reported proportion of reelin+ cells, which project to the dentate gyrus of the hippocampus) and their sometimes non-pyramidal morphologies suggests CALB+ and pyramidal cells may not be synonymous.

Pyramidal and stellate cells are further distinguished by their electrophysiological properties (Alonso and Klink, 1993). There is some suggestive electrophysiological evidence that these categories may map onto the reelin+ / CALB+ division of glutamatergic cells, and therefore have distinct axonal targets (Varga et al., 2010) but this has not been definitively demonstrated (cf Alonso and Klink, 1993; Varga et al., 2010).

A wide variety of interneurons with heterogenous morphology and immuno reactive signatures make up the remainder of the cells in layer II (Canto et al., 2008). Parvalbumin positive (PV+) cells with a horizontal chandelier morphology and cholecystokinin positive (CCK+) basket cells both have axon arbors primarily confined to

layer II, have dendrites in layers I and II are relatively abundant (Wouterlood et al., 1995; Canto et al., 2008; Varga et al., 2010). CCK+ basket cell interneurons innervate CALB+, but not reelin+, glutamatergic cells in layer II, suggesting that one type of inhibitory input is selective for pyramidal cells (Varga et al., 2010). Other identified types of GABAergic cells include two types of multipolar PV+ and distinct calretinin+ multipolar cells as well as CALB+ interneurons, all with dendrites confined to the superficial layers of the MEC (Canto et al., 2008; Gatome et al., 2010). Fast spiking GABAergic PV+ cells in superficial MEC, likely including cells in layer II, provide direct functional input to interneurons in CA1 (Melzer et al., 2012). Many interneurons with fast spiking characteristics have morphologies consistent with chandelier and basket cell subtypes (Jones and Bühl, 1993; Middleton et al., 2008). However, the electrophysiological characteristics of most interneuron types in layer II of the MEC have not been established.

In contrast to layer II, deeper layers in the MEC lack stellate cells, with the principle projection cells instead being pyramidal cells (Dickson et al., 1997; Canto et al., 2008; Canto and Witter, 2011) (for reviews of the anatomical properties of cells in deeper layers see Canto et al., 2008; Canto and Witter, 2011). Cells in layers III–VI send axonal projections to every layer superficial to the layer that contains their somata (Köhler, 1986; Canto et al., 2008) and although the apical dendrites of pyramidal cells in the deeper layers branch in the superficial layers, focal injections of anterograde tracer dye in the superficial MEC suggest that connections from superficial to deep layers may be relatively rare (Köhler, 1986). There are also at least three varieties of interneuron in layer III (Canto et al., 2008), including fast spiking goblet cells with axons and dendrites that arborize in layers II and III (Middleton et al., 2008). Layers IV–VI contain multipolar interneurons with axon arborisations that are confined to the deep layers (Canto et al., 2008; Canto and Witter, 2011). The most superficial layer, layer I, is only very sparsely populated by cell bodies and contains mainly horizontal fibre tracts and dendritic arborisations from cells with somata in deeper layers (Canto et al., 2008). These considerations suggest that principal cells in all layers may innervate cells in layer II of the MEC (Köhler, 1986). However, the abundant overlap of dendritic and axonal arborizations within layer II of cells with somata in layer II (Köhler, 1986; Canto et al., 2008; Garden et al., 2008), suggest that information transfer between cells in layer II is likely play a particularly prominent role in MEC function.

1.3.2 *Dissecting the layer II microcircuit*

Layer II receives synaptic inputs from diverse areas. To understand how these inputs are processed, the cellular targets and functional nature of the afferent inputs must be established.

Cortical inputs to the MEC

The MEC receives inputs from sensory and associational cortical areas, suggesting that sensory information is integrated directly with other contextual information in the superficial layers of the MEC (Burwell and Amaral, 1998a; Witter et al., 1989; Burwell, 2000; Kerr et al., 2007). Large, layer spanning injections of retrograde tracer in the MEC indicate that it receives substantial inputs from the piriform cortex (involved in olfaction) and visual associational areas that arise primarily in layer II of these structures (Burwell and Amaral, 1998a). Other notable cortical inputs arise from the frontal areas, retrosplenial cortex and posterior parietal cortex (Burwell and Amaral, 1998a; Kerr et al., 2007). Efferent connections back to these cortical areas are also present, but are typically substantially weaker (Kerr et al., 2007), suggesting that information flows largely from the cortex to the MEC.

Information about the strength, kinetics and plasticity of synaptic inputs to an area are important for developing a functional account of network computation. However, not only are functional nature of cortical afferents to layer II largely unknown but detailed anatomical information is also lacking, as previous studies used large retrograde injections which do not localise cortical inputs to a specific layer in the MEC. Furthermore, the identity cortical cells of origin and the layer II cellular targets of afferent inputs from these areas are poorly characterised, if at all (Burwell and Amaral, 1998a; Witter et al., 1989). How the cortex influences computation in layer II of the MEC therefore remains unclear.

Subcortical inputs to layer II strongly influence MEC function

The MEC receives inputs from diverse subcortical areas, many of which include a modulatory component. Retrograde tracer injections in the MEC have revealed labelled cells in the thalamic nuclei, (including the nucleus reuniens), the septal nuclei (including medial septum) and the amygdala (Segal, 1977; Mitchell et al., 1982; Kerr et al., 2007).

Input from the medial septum appears to be particularly important for MEC function (Chapman and Racine, 1997). Anterograde tracer injections into the medial septum produce labelled axons in layer II of the MEC, many labelled projecting cell bodies in the medial septum are positive for acetylcholine (Alonso and Köhler, 1984)

and medial septum lesions reduce acetylcholine staining in the MEC (Mitchell et al., 1982), suggesting a strong cholinergic input from the medial septum to layer II of the MEC. Many cells that project from the medial septum to the MEC also express GABA or glutamate, indicating that the medial septum can influence the MEC in different ways (Manns et al., 2001). Consistent with the anatomical evidence, electrical stimulation of the medial septum produces strong field potentials in layer II of the MEC (Chapman and Racine, 1997) although it is not clear from these experiments which cells types are recruited during stimulation or which cells in superficial MEC the septal inputs target.

Hippocampal formation inputs to layer II cells

The standard view of hippocampal formation circuitry is that information flows to the hippocampus from the superficial layers of the MEC, which in turn receive input from many other areas in the hippocampal formation (van Strien et al., 2009). The majority of hippocampal information is believed to be subsequently routed by the hippocampus back to the cortex via the deep layers of the MEC (van Strien et al., 2009). The MEC therefore exerts a profound influence over hippocampal processing, both gating its inputs and regulating its outputs to the cortex.

Inputs to the MEC from other areas in the hippocampal formation play an important role in determining the output of the MEC to the hippocampus. The functional characteristics these inputs to the MEC differ depending on the area of origin. Tracer evidence shows that projections originating from layers II–V of the postrhinal cortex have abundant axon collaterals in layer II of the MEC (Naber et al., 1997; Burwell and Amaral, 1998a,b). In contrast, input to the MEC from the perirhinal cortex is extremely sparse (Burwell and Amaral, 1998a,b). Electrical stimulation of the superficial presubiculum and parasubiculum reveals functional monosynaptic connections to stellate cells in layer II (Canto et al., 2012) (Figure 1.4), even though the presubicular axons only collateralise in layers I and III of the MEC (van Groen and Wyss, 1990b). Whole-cell recordings from stellate cells, in combination with glutamate uncaging data and the electrical stimulation, reveals that parasubicular stimulation produces large responses onto both stellate cells (Canto et al., 2012) and fast spiking interneurons (Jones and Bühl, 1993) whereas presubicular stimulation has only been shown to yield smaller positive responses in stellate cells (Canto et al., 2012) (see Figure 1.4). Because GABAergic axons comprise a substantial portion of the input from the dorsal presubiculum to the dorsal parts of the MEC (Van Haeften et al., 1997), inputs from this area may instead have a large inhibitory influence. Unfortunately, the significance of the different inputs to layer II of the MEC for spatial computation remains unclear.

Although a majority of the MEC input from the hippocampus targets the deep layers, a minority of the input is directly routed back to the superficial layers of the MEC from CA1 and the subiculum (van Strien et al., 2009). Tracer data show CA1 and subicular axon collaterals in the superficial layer of the MEC (van Groen and Wyss, 1990a; Tamamaki and Nojyo, 1995) and electrical stimulation of CA1 and the subiculum produces field EPSPs in MEC layer II (Craig and Commins, 2007). Electrical activation of the hippocampus produces initial IPSPs in principal cells in layer II that are followed by excitation (Gnatkovsky and de Curtis, 2006) (see Figure 1.4). While this may reflect feedforward inhibition local to layer II, optogenetic evidence indicates that GABAergic output from CA1 directly innervates layer II of the MEC, although this largely targets fast spiking (FS) interneurons in superficial layer II (Melzer et al., 2012) (Figure 1.4). Grid cell coherence depends on input from the hippocampus (Fyhn et al., 2004; Bonnevie et al., 2013), so both direct and indirect connections may play an important role in spatial processing, but the precise circuit mechanisms remain unclear.

Anatomical evidence suggests that all layers of the MEC provide a particularly strong input to layer II, but that connections in the other direction are weak (Köhler, 1986), suggesting that environmental and self motion information is generally routed towards layer II within the MEC. Electrical stimulation of the deep layers elicits large IPSPs in stellate cells with a fast EPSP component arising at higher stimulus intensities (Jones and Bühl, 1993), indicating that the influence of the deeper layers on layer II can be excitatory or inhibitory (Figure 1.4). Stimulation in the deep layers of the MEC and parasubiculum produces strong AMPA-dependent IPSPs along with fast and slow excitatory responses in stellate cells (Jones, 1994) and produces EPSPs in layer II fast spiking interneurons that are dominated by an NMDA dependent component and scale with stimulus intensity (Jones and Bühl, 1993). Inhibition onto interneurons, on the other hand, appears to be minimal (Jones and Bühl, 1993), suggesting that the inhibitory influence of the deeper layers on layer II is mediated by feedforward inhibition.

Integration of synaptic input in layer II stellate cells is frequency dependent. Electrical stimulation of the deep layers and the LEC produces EPSPs in stellate cells that sum preferentially with higher (>5 Hz) frequency stimulation (Gloveli et al., 1997) and stimulation of afferent fibres in layer I also produces EPSPs in stellate cells with frequency dependent summation, which depends on the intrinsic properties of the membrane (Garden et al., 2008) (Figure 1.4). Afferent excitation onto stellate cells therefore appears to be generally frequency dependent, suggesting that differential integration of high and low frequency information may be important for processing of spatial information.

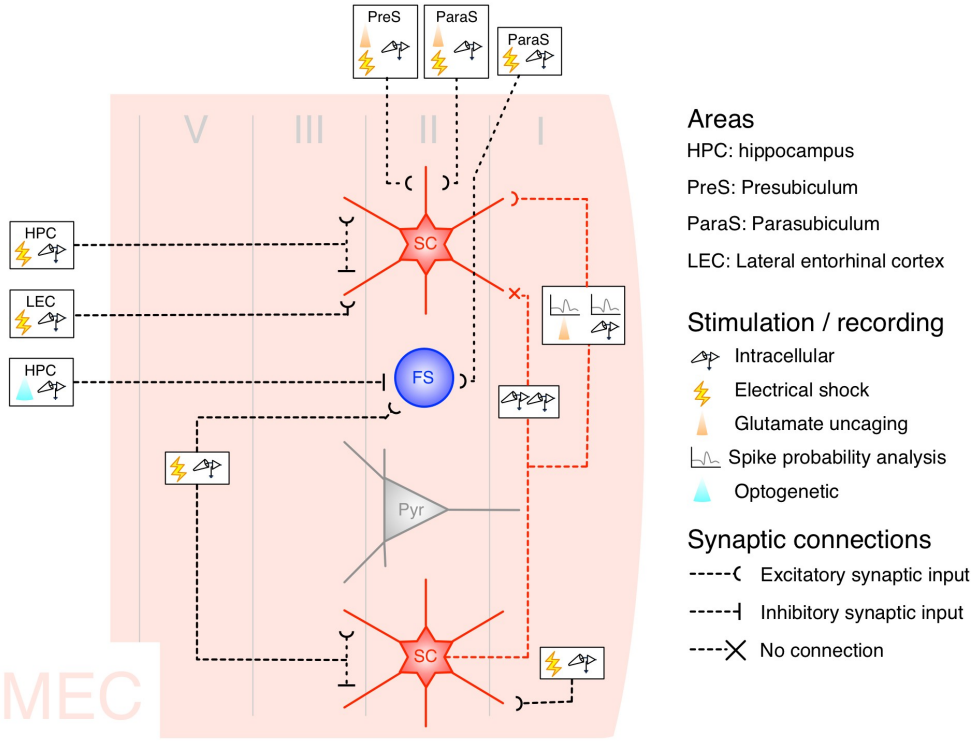

Figure 1.4: **Tested functional inputs to layer II cells from the hippocampal formation.** Schematic indicating known functional connections to stellate cells (SCs), fast spiking interneurons (FS) and pyramidal cells (Pyr) in layer II of the MEC. The layer specific arborisation of dendrites is accurate for SCs and pyramidal cells but because FS interneurons are likely to comprise a heterogenous population of different interneuron subtypes their dendritic arbors are not shown. The location of stimulation is indicated by the location of 'experiment boxes' in the MEC, unless between identified cell types (e.g. SCs), or by area label in the boxes outside of the MEC. Stimulation and associated recording methods are indicated in the left and right of the boxes. Except for paired recordings from SCs and optogenetic stimulation in the hippocampus, the cellular origin of stimulated synaptic inputs in unknown. The exact location on the dendritic arbor of indicated synaptic inputs is not necessarily accurate.

Connectivity within layer II

Because stellate cells comprise the majority of cells in layer II and provide a major input to the hippocampus, providing an account of their connections within layer II will be important for elucidating layer II microcircuit function and therefore for how the firing fields of grid cells are generated. However, many aspects of their connectivity within layer II remain unclear.

Electrical stimulation outside layer II (Jones, 1994) and analysis of spontaneous synaptic events in stellate cells (Jones and Woodhall, 2005) initially suggested that, relative to other layers in the MEC, stellate cells in layer II were dominated by inhibition and that therefore recurrent excitation between stellate cells might be low. Surprisingly, paired intracellular recordings failed to find any connections between >100 pairs of stellate cells (Dhillon and Jones, 2000) (Figure 1.4) suggesting that connections

between stellate cells are in fact absent or extremely sparse, an unexpected result in light of the substantial recurrent connectivity between principal cells in deeper layers of the MEC (Dhillon and Jones, 2000) and other cortical areas (Mason et al., 1991; Deuchars et al., 1994; Song et al., 2005). However, because paired *in vitro* recordings may suffer from cell selection bias and sectioning in certain planes may sever functional connections, this evidence is not conclusive. Nevertheless, consistent with this conclusion, a small number of simultaneous extracellular–intracellular recordings from putative excitatory - stellate cell pairs *in vivo* did not reveal any excitatory connections to electrophysiologically identified stellate cells (Quilichini et al., 2010).

However, studies using other techniques cast doubt on this conclusion. First, in two separate studies photo-uncaging of caged glutamate in layer II by laser stimulation revealed monosynaptic EPSCs in stellate cells (Kumar et al., 2007; Beed et al., 2010). Second, *in vivo* extracellular recordings from anaesthetised rats found pairs of putative excitatory of cells in which firing of one cell reliably increased the firing probability of the other at monosynaptic delays (Quilichini et al., 2010) (Figure 1.4). Together, these results have been interpreted as evidence for the existence of recurrent excitatory connections between stellate cells, an assumption of many models of grid cell generation (Fuhs and Touretzky, 2006; Guanella et al., 2007; Navratilova et al., 2012), yet none of these experiments provides direct evidence for this conclusion. Because neither method can definitively identity presynaptic cells, synaptically driven excitatory responses in stellate cells may therefore reflect activation of other cell types in the superficial MEC, possibly including pyramidal cells in layer II. On the other hand, paired recordings may be subject to bias in cell selection, potentially leading to a skewed sampling of the population which may miss connected cell pairs, especially in slice preparations where the density of connections will be reduced. The data therefore remain consistent with the absence of connections between stellate cells, but are not well established.

Very little is known about interneuron connectivity in layer II. CCK+ interneurons exclusively target CALB+ glutamatergic cells, which do not project to the hippocampus and may correspond to pyramidal cells, whereas PV+ interneurons target all glutamatergic cell types including reelin+ cells which form the basis of the perforant path and are very likely to be stellate cells (Varga et al., 2010). However, it remains unclear what electrophysiological phenotype distinguishes PV+ and CCK+ interneurons (Varga et al., 2010). Inhibitory IPSPs are present in stellate cells during pharmacologically induced gamma activity (Cunningham et al., 2003; Middleton et al., 2008), but because the pharmacological agonists are bath applied, the origin of this input is unclear although it may result from fast spiking interneurons in layer II as they are thought to be involved these rhythms (Middleton et al., 2008).

To advance our understanding of how the microcircuitry of layer II contributes to grid firing fields and oscillatory rhythms, functional connections between identified cell types in the layer require better characterisation. First, an unbiased method that enables extensive and selective testing of recurrent connectivity between stellate cells is needed and could be achieved by optogenetic techniques. Second, functional connections between stellate cells and electrophysiologically characterised interneurons in layer II should also be determined. Identification of connections between different interneuron types and pyramidal cells will eventually also be necessary to construct a more complete picture of the functional wiring of this important circuit.

1.4 INTRINSIC EXCITABLE PROPERTIES OF STELLATE CELLS[1]

Grid cells found in layer II are likely to be stellate cells - they are the principal excitatory cell type in the layer where grid cells are most frequently found (Alonso and Klink, 1993; Hafting et al., 2005; Sargolini et al., 2006) and have been shown to encode space in animals navigating along narrow tracks (Burgalossi et al., 2011) in a manner consistent with grid cell output in linear environments (Hafting et al., 2008; Brun et al., 2008; Mizuseki et al., 2009). If stellate cells play such a central role in representing space, their intrinsic excitable properties will be a major determinant of the functional capabilities of the underlying MEC circuitry. An accurate understanding of these excitable properties is therefore essential for assessing which kinds of computation the MEC is able to support. This will not only help to discriminate between the many existing models of MEC circuit function but could also suggest new avenues of research by providing novel insights into the cellular mechanisms that are available for spatial computation.

The intrinsic excitable properties of stellate cells initially drew attention because of their promise to account for the theta-frequency oscillations present in field recordings from mice engaged in exploratory spatial behaviours (Alonso and García-Austt, 1987; Dickson et al., 1995; White et al., 1998). Subsequent research has described a number of other salient intrinsic excitable properties, including many that appear suitable for subserving a range of different computational roles.

1 *The literature discussion in this section is adapted from*: Pastoll, H. et. al. 2012. Intrinsic electrophysiological properties of entorhinal cortex stellate cells and their contribution to grid firing fields. *Frontiers in Neural Circuits.* 6: 17.

1.4.1 *Ion channels determine the intrinsic electrical properties of stellate cells*

The intrinsic excitable properties of any neuron are determined by its distinctive complement of ion channels (Llinás, 1988). The complement of ion channels expressed by stellate cells has not been exhaustively established and changes during development with expression of many channels only appearing to stabilise in rats by ~P18 (Burton et al., 2008). Moreover, ion channel expression also varies systematically with position along the dorsal-ventral axis of the MEC (Giocomo and Hasselmo, 2008; Garden et al., 2008), and there is evidence to suggest that this change reflects a gradient in the number but not identity of channels (Garden et al., 2008). Despite these sources of variation, a core complement of ion channels mediate conductances that endow stellate cells with distinctive electrophysiological properties that are largely similar across species and shape their contribution to entorhinal circuit function. The ion channel species that play particularly important roles in the determination of the intrinsic electrical properties of stellate cells are outlined below.

Sodium conductances

Like most neurons, stellate cells have sodium channels with rapid activation and inactivation kinetics that activate at voltages above ~-50 mV, producing transient sodium currents (Na_T) that provide the depolarising drive during action potentials (White et al., 1993; Magistretti and Alonso, 1999) (Figure 1.5 C). Another type of sodium channel provides a persistent sodium conductance (Na_P) that has slow inactivation kinetics and activates at membrane potentials ~10-15 mV below Na_T (Alonso and Llinás, 1989; Magistretti et al., 1999) (Figure 1.5 C). These properties of Na_P enable it to play a major role in shaping the electrical response of the membrane at potentials near action potential threshold (peri-threshold potentials).

Potassium conductances

A delayed rectifier potassium conductance (K_{DR}) activates at potentials positive to ~-45 mV and contributes to repolarisation of the membrane potential during action potentials (Eder et al., 1991; Eder and Heinemann, 1996) (Figure 1.5 C). A distinct A-type potassium conductance (K_A) in stellate cells differs from K_{DR} in its strong inactivation, requiring hyperpolarisation of the membrane to potentials below -60 to remove the inactivation (Eder et al., 1991; Eder and Heinemann, 1996) (Figure 1.5 C). Both conductances influence the repolarisation of the action potential but the K_A conductance may contribute to the difference in the shape of action potentials in stellate cells when triggered from peri-threshold and resting potentials (cf. Figures

1.5 A and B). The molecular identity of channels mediating K_A and K_{DR} conductances in stellate cells is unknown.

Other voltage gated potassium channels have relatively minor conductances in stellate cells. There is evidence for a non-inactivating voltage gated potassium current that is suppressed by muscarinic agonists (Yoshida and Alonso, 2007) and some evidence for an inward rectifying potassium conductance active at hyperpolarised voltages and sensitive to Ba^{2+} block (Dickson et al., 2000b). In neither case do the effects of these conductances on stellate cell intrinsic properties appear to be pronounced.

Voltage independent Ba^{2+}-sensitive potassium channels contribute a substantial proportion of the leak conductance at resting membrane potentials (Garden et al., 2008) (Figure 1.5 C). Immunohistochemical and pharmacological evidence suggest these channels are two-pore TASK channels (Deng et al., 2007; Garden et al., 2008; Deng et al., 2009).

Calcium-dependent potassium conductances (K_{Ca}) in stellate cells are activated by Ca^{2+} influx through voltage gated calcium channels (Khawaja et al., 2007). There are two components, one fast and one slow, neither sensitive to apamin, but the slow component appears to be modulated by the cAMP pathway (Khawaja et al., 2007). These channels may therefore play an important role in the afterhyperpolarisation following action potentials.

Voltage dependent Calcium conductances

Two calcium conductances in stellate cells can be distinguished on the basis of their activation and inactivation voltage dependencies (Figure 1.5 C). High voltage activated calcium channels (Ca_{HVA}) activate at ~-50 mV whereas low voltage activated calcium channels (Ca_{LVA}) activate at ~-60 mV and inactivate at more hyperpolarised voltages relative to Ca_{HVA} channels (Bruehl and Wadman, 1999; Visan et al., 2002; Castelli and Magistretti, 2006). Depolarisation from peri-threshold potentials will therefore activate Ca_{HVA} but not Ca_{LVA} .

I_h conductance

A prominent hyperpolarisation-activated cation current (I_h) in present in stellate cells (Robinson and Siegelbaum, 2003) (Figure 1.5 C). It activates at voltages below ~-50 mV with a half maximal activation of -80 mV and has a reversal potential of ~ -20 mV (Dickson et al., 2000b; Nolan et al., 2007). The activation is best fit with the sum of two exponentials with a fast time constant of ~80 ms and a slow time constant of ~400 ms (Dickson et al., 2000b; Nolan et al., 2007). I_h is mediated by hyperpolarisation-activated cyclic nucleotide gated (HCN) channels of which four different types (HCN1–4) have been identified (Robinson and Siegelbaum, 2003). HCN1

appears to be responsible for the fast component of the I_h conductance and contributes the majority of the conductance in stellate cells (Nolan et al., 2007).

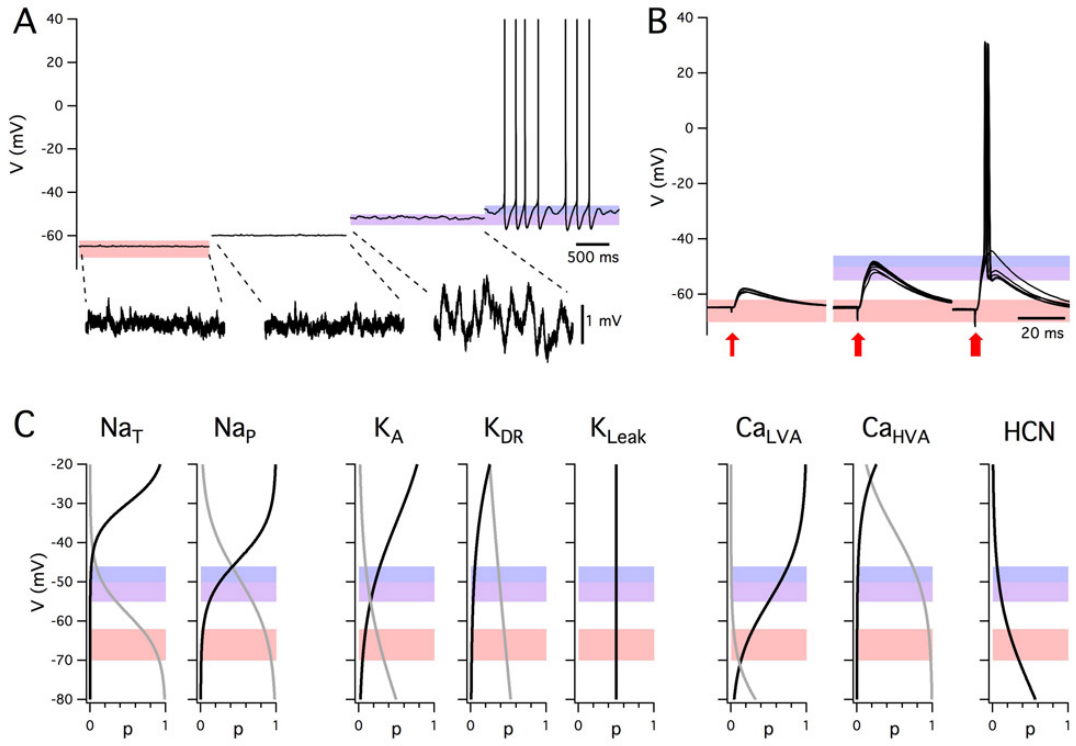

Figure 1.5: **Summary of intrinsic electrophysiological properties of stellate cells from layer II of the medial entorhinal cortex. (A)** Example of membrane potential activity at rest and during injection of constant current. Shading indicates the range of typical resting membrane potentials (orange), peri-threshold potentials (purple), and threshold for initiation of action potential firing (blue). Sub-threshold activity is shown on an expanded voltage-scale below. **(B)** Examples of excitatory post-synaptic potentials evoked by stimuli of increasing amplitude (left to right). Each block shows five consecutive responses to stimuli of identical intensity. Data in **(A)** and **(B)** are obtained with whole-cell patch-clamp recordings from the same stellate cell in the presence of picrotoxin (50 μM) and CGP55845 (1μM) to block inhibitory synaptic transmission. **(C)** Voltage dependence of stellate cell conductances. Boltzmann fits for activation (black) and inactivation (gray). From left: Na_T activation ($V_{1/2}$ = -29.9 mV,k = 3.9 mV), inactivation ($V_{1/2}$ = -58.2 mV, k = -5 mV) Magistretti et al. (1999); Na_P activation ($V_{1/2}$ = -44.4 mV, k = 5.2 mV), inactivation ($V_{1/2}$ = -48.8 mV, k = -10 mV) Magistretti et al. (1999); K_A : activation ($V_{1/2}$ = -34.7 mV, k = 12 mV), inactivation ($V_{1/2}$= -80.3 mV, k = -12 mV) where $V_{1/2}$ parameters were calculated from Eder and Heinemann (1996); K_{DR} : activation ($V_{1/2}$ = -34.8 mV, k = 11 mV), inactivation ($V_{1/2}$ = -74.3 mV, k = -15 mV) where $V_{1/2}$ is given in Eder and Heinemann (1996) and the slopes were estimated from (Eder and Heinemann, 1996); K_{Leak} (conductance is constant); Ca_{LVA} : activation ($V_{1/2}$ = -45 mV, k = 8 mV), estimated from threshold and peak amplitude data in Bruehl and Wadman (1999), inactivation ($V_{1/2}$ = -89 mV, k = -6.9 mV) (Bruehl and Wadman, 1999); Ca_{HVA} activation ($V_{1/2}$ = -11.1 mV, k = 8.4 mV) (Castelli and Magistretti, 2006), inactivation ($V_{1/2}$ = -37 mV, k = -8.7 mV) (Bruehl and Wadman, 1999); HCN activation ($V_{1/2}$ = -83.1 mV, k = -8.1 mV) (Nolan et al., 2007). *Helen Ramsden derived the traces in panel* ***(C)*** *from the literature and Dr. Matthew F Nolan made the figure.*

1.4.2 *Intrinsic excitable properties depend on membrane potential*

Because the conductances of most ion channels expressed by stellate cells are voltage dependent, the membrane's electrical properties will depend on the level of depolarisation of the cell. These properties can thus differ considerably across the physiological range of potentials (Figure 1.5). For example, ion channels that open at depolarised potentials influence action potential initiation and repolarisation, but may not contribute to the resting membrane conductance (e.g. Na_T and Ca_{HVA}, Figure 1.5 A–C).

Active ion channels can also play distinctive roles within a narrow range of membrane potentials. For example, ion channels that are open at membrane potentials below that required for the initiation of action potentials contribute to intrinsic electrical activity that is independent of synaptic input (Figure 1.5 A, B) and also regulate integration of synaptic responses as the membrane moves towards action potential threshold (Figure 1.5 B, C).

Because the intrinsic excitable properties depend on the membrane potential, the key intrinsic properties of stellate cells associated with resting, peri-threshold and supra-threshold potentials may play distinct roles in circuit function and so are best considered separately.

Excitable properties of the membrane at resting potential

In the absence of significant synaptic input stellate cells have a stable resting potential. The excitable properties of the membrane at a cell's resting potential determine its response to synaptic inputs arriving in baseline condition and thus have a major influence on the depolarisation and action potential output in response to afferent activity.

At physiological temperatures in brain slices from mature (>30 day) rodents the resting membrane potential of a stellate cell is typically in the range of -60 mV to -70 mV (Alonso and Llinás, 1989; Alonso and Klink, 1993; Jones, 1994; Erchova et al., 2004; Nolan et al., 2007; Garden et al., 2008; Boehlen et al., 2010) and cells do not fire spontaneous action potentials. In anaesthetised adult rats the resting potential is approximately -70mV (Quilichini et al., 2010).

Input resistance describes the magnitude of the membrane potential deflection in response to current inputs and is a measure of excitability. At rest, input resistance is low in stellate cells, typically lying between 20 and 80 MΩ. The membrane time constant is a measure of how quickly the membrane potential reacts to current inputs and depends on the membrane capacitance and resistance. In stellate cells it lies is in the range 5–15 ms (Alonso and Llinás, 1989; Alonso and Klink, 1993; Jones, 1994;

Erchova et al., 2004; Nolan et al., 2007; Garden et al., 2008; Boehlen et al., 2010). These properties appear similar in rats and mice (cf. Nolan et al., 2007; Garden et al., 2008; Boehlen et al., 2010), change during development (Burton et al., 2008) and are substantially different when measured at room temperature (Dickson et al., 2000b). A large part of the within-study variation in input resistance and time constant can be explained by differences in neuronal location along the dorsal-ventral axis of the MEC (Garden et al., 2008; Boehlen et al., 2010) (see Section 1.4.3 below).

A further source of variation between studies is the recording method used to investigate stellate cell properties. After accounting for a neuron's position, it appears that sharp electrode recordings produce membrane potentials that are typically more negative, input resistance that is lower and membrane time constants that are shorter compared to data from whole-cell recordings (Boehlen et al., 2010). Therefore, as in hippocampal neurons (Spruston and Johnston, 1992), sharp electrode recordings may underestimate input resistance and the membrane time constant of stellate cells. On the other hand, whole-cell recordings may modify the resting membrane potential and input resistance of stellate cells as dialysis of the cell contents is likely to perturb the normal intracellular environment, so obtaining accurate results may require the use of perforated patch-clamp methods, which minimise the disruptive effect of recording on cellular processes.

The conductances that are open at rest determine the membrane's excitable properties at this potential. The ionic basis for the stellate cell resting potential involves a balance between a depolarising drive from the I_h current and a hyperpolarising drive from a leak potassium current. The I_h depolarises the resting membrane potential by approximately 10 mV (Dickson et al., 2000b; Haas et al., 2007; Nolan et al., 2007). The leak potassium channels that are open at rest in stellate cells may account for the majority of the remaining resting membrane conductance (Deng et al., 2007; Garden et al., 2008). The interaction of these two conductances may thus be sufficient to produce the properties of the membrane at rest.

Small perturbations of the membrane potential of a stellate cell are opposed after a short delay, leading to a characteristic 'sag' response (Alonso and Llinás, 1989; Alonso and Klink, 1993; Klink and Alonso, 1993, 1997a; Jones, 1994; van der Linden and Lopes da Silva, 1998; Dickson et al., 2000b; Nolan et al., 2007). The sag response is due to a change in the depolarising inward current provided by I_h (Dickson et al., 2000b; Nolan et al., 2007). During responses to negative current steps the membrane potential hyperpolarises and I_h slowly activates, thus causing a return depolarisation. Conversely, when the membrane potential depolarises I_h slowly deactivates, causing the membrane potential to then hyperpolarise. I_h block by Cs^+ or ZD7288 abolishes the sag (Klink and Alonso, 1993; Jones, 1994; Dickson et al., 2000b; Haas et al., 2007;

Nolan et al., 2007), while deletion of HCN1 reduces the amplitude and slows the kinetics of the sag (Nolan et al., 2007; Giocomo and Hasselmo, 2009).

Around resting potential stellate cells also exhibit resonant properties. These are typically investigated by observing the membrane response to sinusoidally modulated current inputs spanning a range of frequencies. Membrane potential responses are largest to inputs that fluctuate at frequencies in the theta range (4–12 Hz) (Haas, 2002; Erchova et al., 2004; Schreiber et al., 2004). This theta-frequency resonance distinguishes stellate cells from other nearby neurons (Erchova et al., 2004). At lower frequencies the membrane potential response also has a small phase advance relative to the injected current, whereas at higher frequencies the membrane potential lags behind the injected current (Erchova et al., 2004; Nolan et al., 2007; Heys et al., 2010).

Resonant properties also appear to be sensitive to recording method. Two properties are often used to describe resonance: the frequency of the resonance peak (F) and the relative amplitude of the peak (Q) (Hutcheon et al., 1996). Previous studies indicate that F is greater for sharp-electrode (Erchova et al., 2004; Boehlen et al., 2010) compared to whole-cell recordings (Nolan et al., 2007; Boehlen et al., 2010; Heys et al., 2010). Q also appears to be greater in sharp electrode recordings than whole-cell recordings at resting potentials (Boehlen et al., 2010), suggesting that recording method affects the magnitude of the resonance which in turn could influence the interpretation of the potential role of resonance in circuit function. Moreover, although Q increases with depolarisation from hyperpolarised to depolarised potentials when measured with sharp electrode recordings (Boehlen et al., 2010), whole-cell patch-clamp recordings exhibit an opposite dependence (Nolan et al., 2007; Boehlen et al., 2010), leaving the true effect of depolarisation on the resonant properties of stellate cells unclear.

At resting membrane potentials the attenuation of low frequency signals that is essential for resonance in stellate cells requires HCN1 channels (Nolan et al., 2007). Deletion of HCN1 or pharmacological block of I_h abolishes resonance by increasing the amplitude of responses to current inputs with frequencies less than 4 Hz (Haas et al., 2007; Nolan et al., 2007) and also abolished the phase advance (Nolan et al., 2007). Thus, resonance at resting membrane potentials can be explained by I_h opposing slow changes in the membrane potential (Hutcheon and Yarom, 2000; Nolan et al., 2007; Dudman and Nolan, 2009; Dodson et al., 2011). Roles for other ion channels in resonance are less clear. In other cell types persistent sodium currents and M-type potassium currents underly resonance at more depolarised voltages and block of I_h has little effect (Hu et al., 2002). In stellate cells the M-current blocker XE991 reduces the frequency and amplitude of the resonance peak at more depolarised voltages, but not at resting membrane potentials, suggesting an involvement of I_M at depolarised

potentials, but the frequency shift is on average less than 1 Hz and the reduction in amplitude appears quite small (Heys et al., 2010). Moreover, application of ZD7288 abolishes resonance at depolarised potentials (Boehlen et al., 2013), indicating that I_h plays a central role in resonance across a range of potentials in stellate cells.

Theta-frequency resonance could selectively amplify the response of stellate cells to inputs arriving at theta frequency, allowing those inputs to have the greatest influence on stellate cell activity. However, the actual relationship between theta-frequency resonance and stellate cell responses to more physiological inputs is not fully understood, but theta-frequency resonance is observed when stellate cells are probed with non-periodic frozen-noise inputs (Schreiber et al., 2004).

Stellate cells at peri-threshold potential

When the membrane potential of a stellate cell is depolarised from rest to close to the threshold for action potential firing it becomes unstable, appearing to oscillate with frequency in the theta range (4–12 Hz) (Alonso and Llinás, 1989; Alonso and Klink, 1993; Dickson et al., 2000c; Erchova et al., 2004; Nolan et al., 2007; Dodson et al., 2011; Yoshida et al., 2011). This is of considerable interest, first because it suggests a cellular correlate of the network theta rhythm recorded from the MEC and other hippocampal regions *in vivo* (Dickson et al., 2000c; Stewart et al., 1992; Mizuseki et al., 2009) and second because it has been argued that theta-frequency oscillations may be a substrate for encoding of spatial information by grid cells (Burgess et al., 2007; Giocomo et al., 2007).

The mechanism responsible for peri-threshold theta-frequency activity has been subject to debate. One class of ionic mechanism proposes that theta-frequency activity is generated by a periodic oscillator. This follows from the consideration that adding an amplifying conductance such as Na_P to a resonator can lead to the generation of oscillations (Hutcheon and Yarom, 2000). Consistent with this idea, models of stellate cells that include Na_P and I_h can produce periodic membrane potential oscillations at peri-threshold potentials (Dickson et al., 2000c; Fransén et al., 2004). An important test of this oscillator model is whether the theta activity is periodic. In this case power spectra of the activity will have a single spectral peak that will have a stable frequency in consecutive analysis windows (Hajimiri and Lee, 1998; Dodson et al., 2011). However, theta-frequency activity from whole-cell recordings (Nolan et al., 2007; Dodson et al., 2011) does not match this prediction. Instead, the theta activity during sub-threshold sweeps has a frequency that changes apparently unpredictably (Dodson et al., 2011). These observations are evidence against some models of grid cell firing fields that I discuss below. While these properties could perhaps be explained by variation in the period of an oscillator (Zilli et al., 2009),

the variation would be so high that this would amount to an oscillatory system with dynamics that are essentially swamped by noise.

A second class of ionic mechanism that can account for peri-threshold theta frequency activity is based on evidence that stochastic gating of membrane ion channels can cause the membrane potential to fluctuate at theta frequencies (White et al., 1998). Direct support for this mechanism comes from experiments in which theta-frequency activity is abolished by pharmacologically blocking Na_P. When a dynamic clamp is then used to reintroduce a purely deterministic version of Na_P, theta frequency fluctuations remain absent (Dorval and White, 2005). In contrast, reintroduction of stochastic Na_P channels restores theta-frequency activity (Dorval and White, 2005). Consistent with this mechanism, detailed models of stellate cells, in which all ion channels gate stochastically, reproduce spectral properties of theta-frequency activity (Dudman and Nolan, 2009; Dodson et al., 2011).

Peri-threshold theta-frequency activity is consistently recorded from stellate cells with both sharp electrode and whole-cell techniques. However, the frequency of membrane potential activity during whole-cell recordings (Giocomo et al., 2007; Nolan et al., 2007; Giocomo and Hasselmo, 2009; Boehlen et al., 2010; Dodson et al., 2011) appears to be lower than during sharp electrode recordings (Alonso and Llinás, 1989; Klink and Alonso, 1993; White et al., 1998; Erchova et al., 2004; Boehlen et al., 2010). This discrepancy suggests that one or both of the recording methods interfere with the generation of theta-frequency activity. It is thus unclear whether theta-frequency activity would exhibit increased regularity in the absence of disruptions induced by these recording methods.

Stellate cells at supra-threshold potentials

Stellate cells generate action potentials when their membrane potential is depolarised above approximately -50 mV (Alonso and Klink, 1993; Jones, 1994). When action potentials are initiated during injection of constant positive current they are followed immediately by an after-polarisation with several components. First, there is a shallow and rapid afterhyperpolarisation (AHP), which is followed by a brief after-depolarization (ADP). Finally, at typical physiological spiking rates ($<\sim$20 Hz) (Sargolini et al., 2006), there is a slower AHP which maintains the membrane potential below its peri-threshold value (Alonso and Klink, 1993). These properties are seen with whole-cell and sharp electrode recordings, but their relative prominence may differ (Boehlen et al., 2010).

Initiation of the action potential is blocked by TTX (Alonso and Llinás, 1989), but not by riluzole (Dorval and White, 2005), indicating that it requires Na_T, but not Na_P. Ca^{2+}-dependent activation of K_{Ca} is important for the later stages of repolarisation

and for the AHP (Klink and Alonso, 1993; Khawaja et al., 2007). The recovery of the membrane potential to rest following the peak of the AHP is accelerated by activation of I_h mediated by HCN1 channels (Nolan et al., 2007). The initial rapid component of the AHP and the ADP are not fully understood; they are difficult to account for in current biophysical models of stellate cells (Fransén et al., 2004; Dudman and Nolan, 2009) and may play important roles in generation of grid cell firing fields (Navratilova et al., 2012).

When action potentials are triggered by brief synaptic input, the waveform of the afterpolarisation differs (Figure 1.5 B), but while this difference may be important for physiological activation of stellate cells it has so far received very little attention.

Compared with other neuron types in the MEC, stellate cells generate distinctive clustered patterns of action potentials during maintained supra-threshold depolarisation (Alonso and Klink, 1993; Klink and Alonso, 1993; Nolan et al., 2007; Engel et al., 2008; Fernandez and White, 2008) (Figure 1.5 A). During whole-cell recordings, spikes within a cluster have similar inter-spike intervals that are independent of the overall firing frequency and that are often in the high theta range (about 8–12 Hz) (Nolan et al., 2007; Fernandez and White, 2008). Clustered patterns of spikes are most robust when the overall spike frequency is less than 5 Hz, with the inter-cluster interval sometimes being a second or longer (Nolan et al., 2007). At higher overall spike frequencies clustered patterns of spikes are no longer detectable. Spike trains show very little frequency adaptation at firing rates below the typical physiological maximum (~20 Hz) (Alonso and Klink, 1993; Sargolini et al., 2006). Importantly, while clustered patterns of action potential firing have peaks in their power spectra in the theta-frequency range, the underlying mechanism is distinct from that of sub-threshold theta-frequency resonance (Nolan et al., 2007; Fernandez and White, 2008).

Ion channels that determine the amplitude and duration of the AHP appear to be critical for determining the pattern of spiking activity generated by stellate cells (Fransén et al., 2004; Nolan et al., 2007; Fernandez and White, 2008; Dudman and Nolan, 2009). Deletion of HCN1 or block of I_h greatly reduces spike clustering (Nolan et al., 2007). This can be explained by a model in which action potentials are triggered by stochastic fluctuations in membrane potential (Dudman and Nolan, 2009). In this model HCN channels engaged during the AHP provide a depolarising drive that transiently increases the probability that membrane potential noise will trigger an action potential (Dudman and Nolan, 2009). Alternatively, termination of spike clusters could be achieved through incremental elevation of intracellular Ca^{2+} following each action potential (Fransén et al., 2004). However, with this mechanism it is difficult to explain the probabilistic properties of clustered spike firing that are accounted for by

stochastic models (Dudman and Nolan, 2009). A model based on inductor-dependent resonance can also reproduce statistics of clustered spiking trains (Engel et al., 2008) but this model appears inconsistent with experiments showing that the dominant frequency of spike train power spectral densities can be manipulated independently from that of peri-threshold membrane potential activity (Fernandez and White, 2008).

Synaptic integration

For excitatory glutamatergic synaptic input, stimulation at theta frequency produces little or no temporal summation of the response. However, different forms of input may be processed differently to glutamatergic input and theta modulated GABAergic or cholinergic synpatic input (for example from the medial septum) remain to be investigated. On the other hand, glutamatergic stimulation at gamma frequencies (40–80 Hz) causes strong temporal summation (Gloveli et al., 1997; Garden et al., 2008; Canto et al., 2012). This frequency dependence may reflect the fact that glutamatergic synaptic currents are very short compared with the membrane time constant (Garden et al., 2008) and so fast synaptic inputs will have very different temporal structure to the continuous sinusoidal inputs that are typically used to investigate resonant properties. Pharmacological manipulation of input resistance changes the time window for synaptic integration, suggesting that I_h and K_{leak} conductances may regulate coincidence detection in stellate cells (Garden et al., 2008).

1.4.3 *Dorsal-ventral organisation of intrinsic electrical properties*

The functional output of the MEC is topographically organised along the dorsal-ventral axis (Hafting et al., 2005; Brun et al., 2008; Stensola et al., 2012), suggesting that intrinsic properties with dorsal-ventral organisation are likely play a key a role in generating the functional output. Identifying the intrinsic properties with dorsal-ventral organisation may shed light on not only on which intrinsic properties are critical for circuit function but also on the mechanisms that are used by the MEC to generate its output. Intrinsic properties that are reported to vary as a function of dorsal-ventral location are therefore discussed below.

Gradients in resting properties

Stellate cells at dorsal locations have lower input resistance and faster membrane time constants than those at ventral locations (Garden et al., 2008; Boehlen et al., 2010). This organisation can be accounted for by dorsal-ventral gradients in the density of both leak potassium channels and HCN channels that mediate I_h (Garden et al., 2008).

Thus, in dorsal neurons a greater density of leak potassium and HCN conductances lowers the input resistance and membrane time constant compared with more ventral neurons. Consistent with a dorsal-ventral gradient in I_h, dorsal neurons have greater sag than ventral neurons (Garden et al., 2008).

Stellate cells exhibit a gradient in their frequency selectivity, with dorsal cells having a resting resonance peak at higher frequencies than cells from more ventral locations (Giocomo et al., 2007; Boehlen et al., 2010). Differences in the density of currents through HCN channels could account for this organisation of resonance frequencies, as greater I_h amplitude in dorsal cells will more effectively oppose slow changes in membrane potential, thus causing greater attenuation of low frequency inputs (Nolan et al., 2007; Heys et al., 2010). While not found in mature neurons (Garden et al., 2008), differences in the kinetics of I_h could in principle also account for the dorsal-ventral organisation of membrane resonance (Giocomo and Hasselmo, 2008), but this would not explain the dorsal-ventral organisation of input resistance (Garden et al., 2008). The gradient in the amplitude of resonance at resting potentials may depend on recording method, as Q values differ between dorsal ventral locations with whole-cell patch-clamp recordings but not with sharp electrode recordings (Boehlen et al., 2010).

Gradients in peri-threshold properties

Just as for the resonant response to injected current, the properties of peri-threshold theta-frequency activity also follow a dorsal-ventral gradient (Giocomo et al., 2007; Giocomo and Hasselmo, 2008, 2009; Dodson et al., 2011; Yoshida et al., 2011). The ionic basis for the dorsal-ventral organisation of theta frequency activity appears to involve differences in I_h. Knockout of the HCN1 subunit flattens the frequency gradient of the fluctuations (Giocomo and Hasselmo, 2009), although following pharmacological block of I_h a gradient nevertheless remains (Dodson et al., 2011). If the theta-frequency activity was periodic then these differences could be explained by models in which ion channels gate deterministically and the kinetics of I_h vary with location (Yoshida et al., 2011). However, as discussed above, models of this kind do not appear to account for the stochastic nature of theta-frequency activity. In contrast, both the variability and the frequency of the largest amplitude activity are accounted for by models in which all ion channels gate stochastically and in which the density of HCN and leak potassium channels follows a dorsal-ventral organisation (Dodson et al., 2011). It is therefore possible that the dorsal-ventral organisation of intrinsic theta-frequency activity is a secondary consequence of control of the resting integrative properties of stellate cells by these ion channels.

Gradients in supra-threshold properties

Dorsal-ventral gradients in patterns of action potential output have not previously been investigated. Nevertheless, the dorsal-ventral gradient in I_h density (Garden et al., 2008) could be expected to support spike pattern gradients through the influence of I_h on the AHP (Nolan et al., 2007; Dudman and Nolan, 2009), which does show a gradient in its duration (Boehlen et al., 2010). Because activation of HCN channels accelerates repolarisation following the peak of the action potential AHP (Nolan et al., 2007; Dudman and Nolan, 2009), the greater density of HCN channels in dorsal cells could reduce the duration of the AHP and, therefore, increase the intra-cluster spike frequency.

In addition, the threshold-current required to initiate action potential firing follows a dorsal-ventral organisation (Garden et al., 2008; Boehlen et al., 2010). The organisation of the threshold-current is at least in part explained by the lower input resistance of dorsal compared to more ventral neurons, resulting from their higher density of leak potassium and HCN channels (Garden et al., 2008).

Synaptic integration gradient

The waveforms of evoked and spontaneous excitatory synaptic potentials recorded from stellate cells follow a dorsal-ventral organisation that is also explained by the density of currents through HCN and leak potassium channels. For neurons located more dorsally, EPSPs are shorter than for neurons located more ventrally (Garden et al., 2008). One consequence is that gamma frequency inputs to stellate cells at ventral locations sum more effectively relative to cells at more dorsal locations (Garden et al., 2008). Another is that dorsal cells have narrower time windows for detection of coincident synaptic activity than ventral cells and may, therefore, be better at temporal discrimination (Garden et al., 2008). Importantly, either leak potassium channels or HCN channels alone can support the gradient in integrative properties, although block of either channel increases the duration of EPSPs (Garden et al., 2008). Simulations suggest that gradients in the amplitude of the currents that organise synaptic integration are sufficient to also account for the dorsal-ventral organisation of peri-threshold theta-frequency activity (Dodson et al., 2011).

1.4.4 *From ion channels to grid firing fields*

The electrophysiological investigations of stellate cells described above provide a foundation to begin addressing questions about cellular mechanisms for spatial computations carried out within the MEC. For example, what is the relationship between

computational properties evaluated with *in vitro* experiments and generation of grid firing fields? What are the roles in generation of grid firing fields of particular ion channels expressed by stellate cells? Does modulation of the intrinsic electrophysiological properties of stellate cells play roles in firing during spatial behaviours? Answering these and related questions will require integration of cellular data with predictive models for computation carried out during spatial behaviours, and testing of these models using recordings from behaving animals and specific manipulation of cellular properties of stellate cells.

Ion channel manipulation in behaving animals

A more direct method for revealing what roles intrinsic electrical properties play in spatial behaviours is to manipulate them in behaving animals. A promising way to do this is through genetic deletion of ion channels. HCN1 forebrain knockout mice (Nolan et al., 2004) do not express HCN1 in entorhinal cortex and the expression of other ion channels does not appear to adapt in order to compensate for resulting changes in electrophysiological properties (Nolan et al., 2007). In these animals, grid cells still exist (Giocomo et al., 2011a), as do place cells in the hippocampus (Hussaini et al., 2011). These observations provide strong evidence against models for neuronal representation of space that require functions attributed to HCN1, including models based on interference between intrinsic oscillations. In addition, the theta rhythm in the hippocampus is stronger in the HCN1 knockout animals (Nolan et al., 2004) and since entorhinal theta is likely to be a determinant of hippocampal theta (Stewart et al., 1992), it is unlikely that HCN channels in the entorhinal cortex are pacemakers of entorhinal theta-frequency activity.

Nevertheless, it appears that HCN1 does have a regulatory effect on spatial computations: the grid cells observed in the HCN1 knockout mice are larger and more stable than in control animals, the spacing between grid fields is increased, and the frequency of the theta oscillations uniformly lowered, yet the dorsal-ventral organisation of grid fields is maintained, so that on average firing fields at all locations are larger and further apart in HCN1 knockout compared to control mice (Giocomo et al., 2011a). Despite these changes, these mice surprisingly display enhanced hippocampus-dependent learning and memory (Nolan et al., 2004).

Why does HCN1 deletion have these effects? One possibility is that increased grid-field size and spacing reflect an increased time-window for synaptic integration or summation of synaptic responses in stellate cells (Garden et al., 2008). What mechanisms maintain the dorsal-ventral organisation of grid field properties in the absence of HCN1? A possibility is that control of synaptic integration by the dorsal-ventral organisation of leak potassium channels is sufficient to coordinate these properties

of grid fields (Garden et al., 2008) although gradients in other conductances could potentially also contribute. What aspects of HCN1 channel function are critical to the computational roles of the channel? On the one hand, these roles may reflect control of sub-threshold resonant or oscillatory dynamics of stellate cells through voltage-dependent gating of HCN1 (Nolan et al., 2007; Giocomo et al., 2011a). On the other hand, the pattern of spike output from stellate cells may be independent of sub-threshold resonant properties (Fernandez and White, 2008), and instead the key function of HCN1 may be simply through its contribution to the resting membrane potential and conductance (Nolan et al., 2007). Further experimental investigation will be required to address these and other questions about the relationship between HCN1 channels, leak potassium channels and grid firing fields.

1.5 MODELS OF MEC CIRCUIT FUNCTION

Two major activity patterns in the MEC of behaving animals are grid firing fields and theta-nested gamma oscillations. Integration of speed and directional information is thought to be central to the function of layer II and many different computational models of the circuit mechanisms responsible for producing grid firing fields from speed and directional inputs have been proposed (see Giocomo et al., 2011b; Zilli, 2012, for reviews).

However, the lack of detailed knowledge about the circuitry of layer II means that either models are not well constrained by existing evidence or remain abstract. Despite these restrictions, by suggesting testable hypotheses and highlighting areas of conflict, computational models play an important role in the pursuit for understanding of the mechanisms for spatial computation in the MEC.

Different grid firing field models depend on distinct circuit mechanisms

Two general classes of abstract model have been proposed to account for generation of grid firing fields (Burgess and O'Keefe, 2011; Giocomo et al., 2011b). In one, grid fields are produced by interference between oscillations or periodic synaptic inputs with frequency sensitive to an animal's velocity (Burgess et al., 2007; Giocomo et al., 2007; Blair et al., 2008; Burgess, 2008; Hasselmo, 2008). In the second, grid fields result from bumps in an attractor network that are shifted by velocity inputs (Fuhs and Touretzky, 2006; McNaughton et al., 2006; Guanella et al., 2007; Burak and Fiete, 2009; Navratilova et al., 2012).

Models that compute location through oscillatory interference rely on stable oscillations that are sensitive to velocity. Initial versions of these models proposed that theta-frequency activity of stellate cells reflected one or more oscillations of this kind

(Burgess et al., 2007; Giocomo et al., 2007). However, several cellular properties argue against this mechanism. First, while theta-frequency activity can be interpreted as the output of a periodic oscillator (Dickson et al., 2000c; Fransén et al., 2004), the data *in vitro* from whole-cell recordings suggests it is more likely to reflect filtered stochastic noise (White et al., 1998; Nolan et al., 2007; Dodson et al., 2011). This is a substantial problem as filtered noise signals are not periodic and computation by oscillatory interference mechanisms is extremely sensitive to noise (Burak and Fiete, 2009). Second, models that require independent oscillations occurring in different dendrites appear to be impossible to implement given known cable properties of dendrites (Remme et al., 2010). Third, intrinsic theta-frequency activity is abolished by synaptic conductances that mimic activity that might occur *in vivo* (Fernandez and White, 2008).

Alternative implementations of oscillatory interference models assume that neurons that act as velocity-sensitive oscillators are located upstream of grid cells (Blair et al., 2008; Burgess, 2008; Hasselmo, 2008). Recent evidence suggests that firing of 'theta cells' in the anterior thalamus, hippocampus and medial septum may perform this function (Welday et al., 2011). In these cells theta-frequency bursts of action potentials are modulated by both movement speed and movement direction. However, it is unknown whether these cells synapse with stellate cells and how the intrinsic properties of stellate cells might influence responses to these inputs. One possibility for example, is that dorsal-ventral gradients in theta-frequency resonance or synaptic integration could contribute to decoding of inputs from velocity sensitive oscillators.

In models of grid cell firing that rely on network attractor states the influence of stellate cell integrative properties has received less direct attention. While these models are typically implemented using abstract neurons, in all cases tuning of neuronal gain is necessary for the network to produce attractor states (Fuhs and Touretzky, 2006; McNaughton et al., 2006; Burak and Fiete, 2009; Navratilova et al., 2012). Therefore models of this kind can also be used to make predictions for how intrinsic properties of stellate cells might influence grid firing fields. A recent attractor model predicts possible roles for the AHP and ADP, along with synaptic NMDA conductances, in grid cell firing, periodicity, and phase precession (Navratilova et al., 2012). This model assumes dorsal-ventral tuning of NMDA kinetics, but observations of dorsal-ventral organisation of synaptic integration (Garden et al., 2008) would likely also predict experimentally observed dorsal-ventral spacing of grid firing fields using models of this kind (Navratilova et al., 2012). Dorsal-ventral gradients in the AHP waveform are also consistent with this model (Boehlen et al., 2010).

One concern for attractor models is that their output is sensitive to the specifics of their connection weights between their constituent cell types, but these are not well constrained by experimental data. Some models rely on recurrent excitation between

stellate cells to generate activity bumps (Fuhs and Touretzky, 2006; Guanella et al., 2007; Navratilova et al., 2012) but there is only indirect evidence to support this (Kumar et al., 2007; Beed et al., 2010) and some direct evidence against it (Dhillon and Jones, 2000). Another influential version demonstrates that purely inhibitory interactions between cells can produce grid fields (Burak and Fiete, 2009) but does not provide an account of how stellate cells, which are most likely to be grid cells but are excitatory, participate in network function or produce grid firing fields. Experiments that elucidate the spatial profile and functional connectivity between different cells types in the MEC will therefore distinguish between present attractor models and inform future proposals for circuit mechanisms responsible for the development of grid firing field output.

A common circuitry for theta-nested gamma and grid firing fields?

In addition to producing grid firing fields, circuitry in the superficial layers of the MEC also supports theta-nested gamma rhythms (Chrobak and Buzsaki, 1998). Establishing the relationship between synaptic dynamics in different cell types and LFP during spatial behaviours or *in vitro* recapitulation of *in vivo* rhythms will help define the circuitry that is involved in generating the theta-nested gamma rhythm. An important outstanding question will be whether different non-overlapping subsets of circuit elements support rhythm generation and grid firing fields or instead whether a common circuitry enables both theta-nested gamma oscillations and grid firing fields, thereby permitting multiplexing of rate and temporal coding in the MEC.

1.6 DISCUSSION

Layer II of the MEC is in many ways an ideal circuit for investigating how neural computations are performed in associational cortical areas. The behavioural correlates, firing patterns and oscillatory LFP output of layer II are particularly well characterised for an associational cortical area and, together with considerable knowledge of firing patterns of cells in upstream areas, this knowledge provides an excellent platform for investigating how afferent activity is integrated and transformed into output by local circuitry.

However, despite the helpful constraints provided by the output of layer II and its afferent areas, many of the circuit mechanisms involved in the transformation of the afferent activity to grid firing fields and theta-nested gamma oscillations remain poorly understood. The cellular origin and functional dynamics of many synaptic inputs remain unknown and greater detail about the amplitude, kinetics and frequency

dependence of identified synaptic inputs to layer II will be important for developing a deeper understanding of layer II circuit function.

How do the intrinsic electrical properties of cells in layer II contribute to circuit output? The difficulty of selectively manipulating ion channel expression in layer II cells *in vivo* means that directly observing the effect of altering intrinsic properties of cells on behaviour remains a challenge. Instead, indirect clues to the behavioural relevance of intrinsic properties remain important – intrinsic properties that are anatomically organised in a manner that reflects the discretised, modular gradient in grid cells are particularly likely to be important for spatial behaviours. However, despite extensive investigations of many intrinsic properties of stellate cells, it remains to be determined how properties that follow a dorsal-ventral gradient, including theta frequency resonance and peri-threshold fluctuations, input resistance, AHP durations and spike patterns might interact with other circuit properties to enable the characteristic outputs of layer II. Finally, a thorough understanding of the contributions of intrinsic properties is hampered by a lack of agreement between results obtained with different recording methods. In Chapter 3 I examine the intrinsic electrical properties of stellate cells with perforated and whole-cell patch-clamp methods to evaluate their possible contributions to layer II function.

The nature of the connections between and amongst different cell types within layer II determine its functionality. Elucidating these connections will be critical for distinguishing between different models of layer II function, but no connection pattern have been definitively established. Of particular interest is whether recurrent excitatory connections between stellate cells play an important role in layer II function, but despite receiving much experimental attention a consensus has not been reached. In Chapter 4 I address these issues by using a combination of targeted optogenetic stimulation and pharmacological manipulation to dissect many aspects of the layer II microcircuit.

Finally, an understanding of the computationally relevant properties of theta-nested gamma oscillations and the roles that different cell types in layer II play in generating them has been frustrated by an inability to recapitulate interacting oscillations in physiologically plausible conditions *in vitro*. In Chapter 5 I employ rhythmic optogenetic activation of the layer II microcircuit *in vitro* to induce theta-nested gamma oscillations that closely resemble those observed in rodents *in vivo*. This enables interrogation of the cellular mechanisms responsible for these interacting rhythms and permits further investigation of the functional properties and limits of the nested LFP oscillations.

2

MATERIALS AND METHODS

2.1 INTRODUCTION[1]

To investigate the properties of mouse medial entorhinal cortex microcircuitry, including intrinsic excitable properties of cells, synaptic connectivity and functional circuit computations, as well as the dorsal-ventral organisation of these properties, I prepared acute parasagittal brain slices from mice. I activated cells in layer II of the MEC using optogenetic and electrophysiological methods and made whole-cell, perforated patch-clamp and field recordings from layer II.

The materials and methods discussed in this chapter form the basis of the experiments that are described throughout this thesis. Chapter-specific methods are included in the relevant chapters.

In all animal experiments I complied with the United Kingdom Animals (Scientific Procedures) Act 1986.

2.2 MATERIALS

To maintain tissue before and during preparation of brain slices I kept tissue immersed in cutting artificial cerebrospinal fluid (cutting ACSF) (see Table 2.1 for ingredients list and suppliers).

To cut slices I used either a Vibratome 3000 sectioning system (The Vibratome Co., St. Louis) or a Leica VT 1200 vibratome (Leica Microsystems GmbH, Wetzlar).

After slicing and during recording slices were maintained in standard ACSF (see Table 2.1). During recordings slices were perfused with ACSF using a gravity-fed perfusion system driven by a Watson-Marlow 323 perfusion pump (Watson-Marlow Pumps Group, Falmouth) and extracted from the bath via a waste chamber using a DYMAX-5 air pump (Charles Austen pumps Ltd., Byfleet).

To block synaptic transmission I perfused slices with synaptic receptor antagonists (see Table 2.2).

1 *Work discussed in sections 2.2, 2.3 and 2.6 is adapted from, or appears in:* Pastoll, H. et. al. 2012. Preparation of Parasagittal Slices for the Investigation of Dorsal-ventral Organization of the Rodent Medial Entorhinal Cortex. *Journal of Visualized Experiments*. e3802.

	Cutting ACSF (mM)	**Standard ACSF** (mM)	**Internal solution** (mM)	**CAS number**	**Supplier catalogue code**
NaCl	86	124		7647-14-5	Sigma S9888
NaH_2PO_4	1.2	1.2		13472-35-0	Sigma 71505
KCl	2.5	2.5	10	7447-40-7	Sigma P3911
$NaHCO_3$	25	25		144-55-8	Fischer S/4240
Glucose	25	20		50-99-7	Sigma G5767
Sucrose	75			57-50-1	Sigma S5016
$CaCl_2$	0.5	2		10043-52-4	VWR 190464K
$MgCl_2$	7	1	2	7786-30-3	Sigma 63020
K Gluconate			130	299-27-4	Sigma G4500
HEPES			10	7365-45-9	Sigma H3375
EGTA			0.1	67-42-5	Sigma E4378
Na_2ATP			2	34369-07-8	Sigma A7699
Na_2GTP			0.3	36051-31-7	Sigma G8877
Na PhosphoCreatine			10	19333-65-4	Sigma P7936
Biocytin (optional)			2.7	576-19-2	Sigma B4261

Table 2.1: **Composition of recording solutions.**

For visualising slices and cells I used an upright Olympus BX51 WI microscope (Olympus UK Ltd., Southend-on-Sea) fitted with Nomarski differential interference contrast imaging (DIC). Images were acquired with an infrared-capable mono 12-bit CCD camera (Q-Imaging, Surrey) controlled by Q-capture software (Q-Imaging, Surrey).

For whole-cell and perforated patch recordings I used a Multiclamp 700B amplifier (Molecular Devices, Sunnyvale) connected to an Instrutech ITC-18 digitiser (HEKA Electronics, Lambrecht) and controlled by Axograph X software (Axograph Scientific, Sydney). To record local field potentials I used an Axopatch 200B amplifier (Molecular Devices, Sunnyvale).

I patched cells and obtained field recordings using borosilicate glass pipettes with a 1.5 mm external diameter and a 0.86 mm internal diameter (Harvard Apparatus Ltd, Kent) pulled on a Sutter P97 electrode puller (Sutter Instruments, Novato).

To provide 470 nm illumination I used an LEDC5 700 mA light emitting diode (LED) (Thorlabs) driven by an LEDD1 driver (Thorlabs) using a TPS001 power supply (Thorlabs). The LED was attached to the epifluorescence port of the microscope and the light beam directed through a 40X objective using a mirror located in the filter

housing. To measure the power of the light in the focal plane of the 40X objective I used a Lasercheck power meter (Coherent Inc., Santa Clara)

	Concentration (μM)	**Target receptor**	**CAS number**	**Supplier catalogue code**
NBQX	5	AMPA	118876-58-7	Abcam ab120046
D-AP5	50	NMDA	79055-68-8	Abcam ab120003
Picrotoxin	50	$GABA_A$	124-87-8	Abcam ab120315
CGP55845	1	$GABA_B$	149184-22-5	Abcam ab120337

Table 2.2: **Receptor antagonists.**

2.3 METHODS FOR PREPARING PARASAGITTAL BRAIN SLICES FROM MICE

Parasagittal slices containing MEC layer II from mice permit easy investigation of the dorsal-ventral organisation of MEC microcircuitry properties. To prepare parasagittal slices I relied on procedures described in Nolan et al. (2007), Garden et al. (2008) and Dodson et al. (2011). I used adult male mice (5-9 weeks), with exact age range depending on experiment.

Dissecting out the cerebral hemispheres

To avoid the effects of anaesthetic on neuronal properties I used cervical dislocation without anaesthetic to euthanise mice. Immediately after euthanasia I carefully removed the brain and placed it in cold (4–8 °C) cutting artificial cerebrospinal fluid (ACSF) (see Table 2.1 for composition) bubbled to saturation with carbogen (95% O_2, 5% CO_2). The cutting ACSF had low Na^+ to reduce excitability, elevated Mg^{2+} to sustain NMDA receptor block and high sucrose to provide an energy source.

After three minutes I removed the brain from the cutting ACSF using a spatula and gently placed it in an upright position (dorsal side facing upwards) onto filter paper moistened with the cutting ACSF (Figure 2.1 A). To facilitate accurate mounting of the hemispheres, I used a razor or scalpel to remove as much of the cerebellum as possible without impacting the MEC (located at the caudal extreme of the cerebrum) and removed the rostral third of the cerebrum by sectioning in the coronal plane (Figure 2.1 B). I then hemisected the brain, taking care that the section was exactly along the vertical plane of the midline (Figure 2.1 C). After hemisection, I returned the hemispheres to the bubbled cutting ACSF for one and a half minutes.

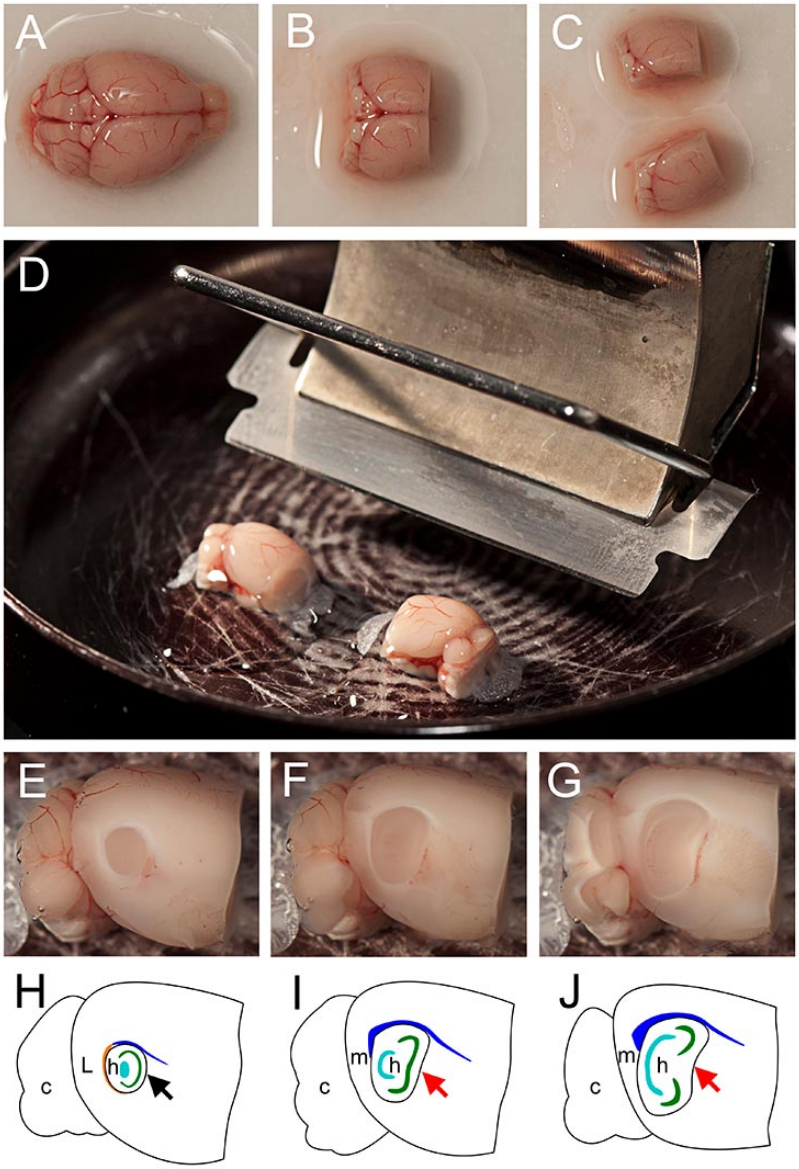

Figure 2.1: **Preparation of parasagittal slices. A** Whole brain resting with dorsal side facing upwards on filter paper moistened with cutting ACSF. **B** Brain after removal of cerebellum and rostral third of frontal cortex. **C** Hemisected brain ready for mounting. **D** mounted hemispheres on glue strip parallel to cutting edge of vibratome blade prior to submersion in cutting ACSF and slicing. **E** Appearance of section containing LEC during the slicing procedure after the removal of lateral tissue and not yet sufficiently medial for a standard parasagittal MEC slice. **F** Appearance of 'lateral' part of the MEC after removing a further 400 µm of tissue (the surface is 400 µm medial to that shown in (**F**)). **G** Appearance of 'medial' part of the MEC after a 400 µm parasagittal slice has been cut. **H-I** Schematics of (**E-F**) respectively indicating anatomical landmarks, c: cerebellum, L: lateral entorhinal cortex (LEC), m: Medial Entorhinal Cortex (MEC), h: hippocampus, orange: external capsule, blue: corpus callosum, cyan: dentate gyrus, green: CA3 and CA1. The appearance of rostral boundary of the hippocampus in slices that contain LEC is convex (relative to the hippocampus) (black arrow in (**H**)) whereas in slices that contain only MEC, the boundary can be linear (red arrow in (**I**)) or concave (red arrow in (**J**)). The approximate shapes of coloured anatomical landmarks were obtained from the annotations in the Allen Brain Atlas (http://mouse.brain-map.org/atlas/ARA/Sagittal/browser.html).

Mounting the hemispheres on a vibratome

I used a vibratome to cut brain sections. Before mounting the cerebral hemispheres, I ensured that the cutting edge of the vibratome blade was angled at 20 degrees from horizontal (Figure 2.1 D). On the mounting surface of the vibratome I aligned a shallow strip of superglue parallel to the vibratome blade, approximately the width of an hemisphere and long enough to accommodate the two hemispheres end-to-end. Taking care to minimize physical impact, I removed each hemisphere from the cutting ACSF with a spatula and positioned it so that its medial surface rested on the spatula and its dorsal extent faced towards the microtome blade. I gently slid each hemisphere onto the strip of superglue, ensuring that the medial surface of each hemisphere was parallel to the microtome base. For best results I ensured that the dorsal surface of each hemisphere was parallel to and faced the vibratome blade (Figure 2.1 D).

Maintaining the preparation during slicing

Following mounting I immediately submerged the hemispheres in cold cutting ACSF (4 – 8 °C) and maintained the temperature and carbogen saturation throughout the slicing procedure. On the Intracell vibratome model, direct cooling and bubbling of the solution in the cutting chamber was not practical, so I periodically replenished the cutting ACSF solution in the chamber with fresh chilled and bubbled solution.

Cutting sections

Using the vibratome, I removed cortex from both hemispheres in the sagittal plane until I identified the lateral most extent of the MEC (typically ~1 mm down from the lateral surface) (Figure 2.1 F). Between cuts I lifted the vibratome blade up by 200 µm to avoid dragging the blade back over and damaging the exposed tissue. I simultaneously cut 400 µm parasagittal sections from both hemispheres until the medial extremity of the MEC was reached (when the hemispheres are lined up as shown in Figure 2.1 D they will both be cut at the same time). The lateral extremity of the MEC can be identified by the absence of the thick white band around the ventro-caudal curve of the hippocampus (the external capsule), the non-convex shape of its rostral boundary and the angular dorso-caudal 'corner'. Figure 2.1 E illustrates the circular appearance of the hippocampus in the parasagittal plane lateral to the MEC. Figures 2.1 F-G illustrate how sections within the MEC appear at different lateral-medial positions when slicing. Note the progressively more bean-shaped appearance of the hippocampus at more medial positions. Each hemisphere typically yields two or three 400 µm thick slices containing the MEC.

Separation of superficial and deep layers

In experiments that required separation of layer II from deeper layers, immediately after a slice had been cut I placed it onto filter paper saturated with cutting ACSF. I then used a scalpel to make an incision between layers II and III from the approximate dorsal border parallel to the rostral edge of the slice. This left a strip along the dorsal edge of the slice intact to facilitate storage and manipulation, but the severed all connections within the MEC between layers II and III.

Incubating slices

After each cut I immediately placed the slices in carbogen-saturated standard ACSF (see Table 2.1 for composition) maintained in a water bath at 35°C. I allowed slices to incubate at 35°C for approximately 15 minutes in the ACSF after slicing was complete. Thereafter, I removed the slice holder from the water bath and continued bubbling with carbogen at room temperature for at least 45 minutes.

2.4 RECORDING METHODS

2.4.1 *Identification of targeted cell types*

I used a low magnification (4X) objective to identify an approximate recording region within the MEC layer II (Figure 2.2 A-B), and then switched to a high magnification (40X) objective to identify viable cells within this region (Figure 2.2 C-D). As a typical example, I visually identified putative layer II stellate cells by their polygonal or ovoid shape and multiple primary dendrites with similar diameter, and absence of a single large diameter apical dendrite (Klink and Alonso, 1997a; van Groen, 2001; Garden et al., 2008). They are reliably identified on the edge of the layer I/II border, where they are abundant and often appear in small groups (Garden et al., 2008; Burgalossi et al., 2011) (Figure 2.2 C-D). Other cell types are also visually identifiable. For example, layer II fast spiking interneurons have large somata and layer II pyramidal cells have a prominent single apical dendrite that exits in the superficial direction.

At this point I performed whole-cell or perforated patch-clamp recordings from targeted cells (see below). During recordings I verified the identity of each neuron by testing for characteristic cell-type specific electrophysiological properties.

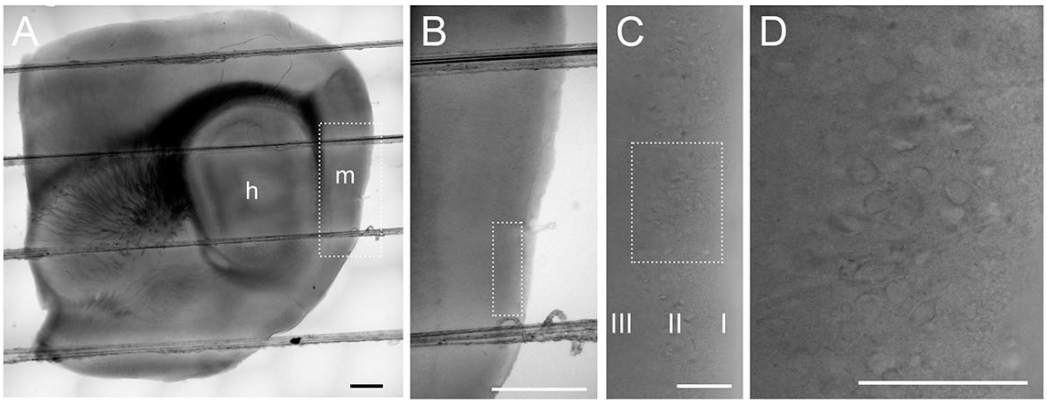

Figure 2.2: **Identifying MEC layer II cells under DIC illumination**. **A** Example composite image of a parasagittal brain slice at low magnification (4X). Separate images have been aligned and blended in Adobe Photoshop CS5 to remove distracting edges and vignetting. Important landmark areas h: hippocampus, m: MEC. **B** Crop from an individual low magnification (4X) image that contains layer II of the MEC, visible as the darker vertical band near the right hand edge. **C** MEC layer II at high magnification (40X) with DIC illumination. The image is an aligned and blended composite of several images. The dense central band of cells is Layer II. **D** Single high magnification DIC image showing a group of healthy putative stellate cells and interneurons in layer II. As shown here, stellate cells often occur in groups on the border of layer I/II. Pyramidal cells tend to be found closer to the Layer II/III border. The dotted outlines in (**A-C**) indicate the extent of (**B-D**) respectively. Scale bars: in (**A**) and (**B**) 500 µm, in (**C**) and (**D**) 100 µm.

2.4.2 *Whole-cell and perforated patch-clamp recordings*

To record membrane potential and membrane current from cells I used the patch-clamp technique (Neher and Sakmann, 1976; Neher et al., 1978). Depending on the experiment, I either recorded in whole-cell configuration (Hamill et al., 1981) or used perforated patch-clamp (Horn and Marty, 1988).

Recordings were obtained at ~35.5°C. Patch pipettes had tip resistances in the 3–7 MΩ range. To permit the reversible $Ag + Cl^- \rightleftharpoons AgCl + e^-$ reaction I chlorided silver electrodes by maintaining a +9 V potential at the silver electrode while it was submersed in a 9% NaCl solution. All membrane seals were >1 GΩ (typically >2 GΩ) as calculated from the current response to -10 mV steps in voltage clamp. Pipettes were filled with an internal solution designed to mimic the chemical composition of the cytoplasm (see Table 2.1). For whole-cell recordings, after a stable seal had formed I ruptured the cell membrane with negative pressure to enter whole-cell configuration and achieve electrical access to the interior of the cell (Hamill et al., 1981).

For perforated patch recordings I used a pore-forming antibiotic to provide electrical access to the cell. To do this I front-filled electrodes with standard intracellular solution (see Table 2.1) and then back-filled with intracellular solution also containing the antibiotic amphotericin B (final concentration 0.075–0.15 mg/ml) dissolved in

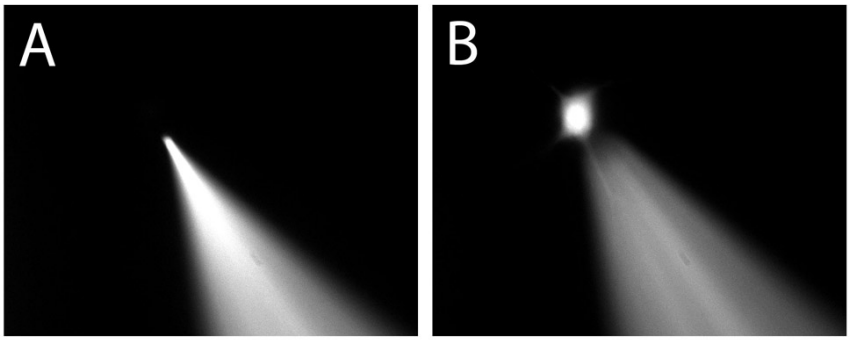

Figure 2.3: **Perforated patch recordings exclude fluorescent dye from the cell. A** Alexa 488 fluorescence in the recording pipette >40 min after seal formation. Note the absence of fluorescence from the recorded cell body (not visible). **B** Two minutes subsequent to deliberate break-in to whole-cell configuration in the recorded cell shown in **(A)**. The somatic region of the recorded cell rapidly becomes visible after break-in. The absence of fluorescence from recorded cell thus indicates that accidental break-in to whole-cell configuration has not occurred. The focal plane is slightly different along the z-axis between the two images.

DMSO (final concentration 3–6 µl/ml) (Akaike and Harata, 1994). To avoid antibiotic diffusion into the ACSF and onto the slice I patched cells as rapidly as possible after filling the electrodes. Typically the access resistance had decreased sufficiently to begin data acquisition by ~20–40 min after seal formation. I ensured that break-in had not occurred during the recording by including the fluorescent dye Alexa 488 (Invitrogen) in the pipette. Because Alexa 488 is excluded from the cell with perforated patches but is admitted in whole-cell configuration, the absence of fluorescence from the cell during recording indicates that accidental break-in to whole-cell configuration has not occurred (See Figure 2.3).

I did not correct for the liquid junction potential of +12.9 mV between the ACSF and intracellular solution (bath relative to the pipette). I measured the liquid juction potential using a 3 M KCl salt bridge following the procedure described in Neher (1992). If the pipette solution and cytoplasm have different ionic molarities, the reduced mobility of larger ionic species across the perforated membrane could result in an extra junction potential (Neher, 1992). Nevertheless, in my recording conditions I have no reason to believe this was a complicating factor that could undermine comparisons between results obtained with whole-cell and perforated patch recording techniques. The lack of a significant difference in the spike threshold voltage measured using the two techniques provides support for this interpretation (see Table 3.3).

To record membrane potential I recorded in current clamp mode. I used pipette capacitance neutralisation so that the amplifier instead of the recorded cell provided the majority of the current to charge stray capacitance, thereby minimising electrode

filtering. I applied bridge balance correction to eliminate voltage drop error resulting from current flow across the electrode resistance (for more detail see Sherman-Gold and Maertz, 2008). I made an initial estimate of the pipette capacitance using the Multiclamp 700B inbuilt routine and did fine corrections manually. I periodically estimated the access resistance by changing the bridge balance correction magnitude until the instantaneous component of the voltage response to -50 pA steps was eliminated. For whole-cell current clamp recordings access resistances were 10–30 MΩ and for perforated patch recordings final access resistances were 24–85 MΩ.

To record membrane currents I recorded in voltage clamp mode with series resistance compensation applied ($\geqslant$ 70% prediction and correction) to reduce command potential errors (Armstrong and Gilly, 1992). To allow the 700B amplifier to accurately specify an adjusted command potential (necessary in order for cells to experience membrane voltages similar to the command voltage profile) estimates of the membrane capacitance and access resistance must be provided during each recording. Because the current required to charge the membrane capacitance can saturate the 500 MΩ feedback resistor on the 700B amplifier headstage it can instead be delivered by a dedicated capacitor. Since current injected over the capacitor is 'invisible' to the user, switching to injecting current over this capacitor provides a method for estimating membrane capacitance: when all the membrane capacitive current has been transferred, no slow capacitance transient is visible in the current response to steps in the holding potential. I first adjusted the (faster) pipette capacitance compensation manually during the procedure until sharp transients were minimised. The access resistance determines the time constant of the capacitive charging so I estimated this and the membrane capacitance magnitude by changing their estimates on the amplifier until the slow capacitive transient was removed. For whole-cell recordings in voltage clamp access resistances were always <25 MΩ (typically <20 MΩ) and were always low enough to avoid escaped spikes.

Online low pass filtering was effected by a two-pole Bessel filter in the 700B amplifier and data sampled with at least double the filtering frequency cutoff. For membrane potential recordings, the low pass cutoff was 10 kHz with either 20 or 20.513 kHz sampling rates (the latter rate imposed by the digitiser for recordings on more than 2 channels). For membrane current recordings the low pass cutoff was 5 kHz with sampling at 10 or 20.513 kHz.

2.4.3 *Field recordings*

When recording extracellular local field potentials I recorded in current clamp mode. The gain was set to 500 and data was filtered online at 1 kHz and sampled at >2

kHz (typically at the same frequency as the accompanying intracellular recordings). I used pipettes with resistance of 5–10 MΩ when filled with ACSF.

2.5 OPTOGENETIC STIMULATION METHODS

2.5.1 *Activating cells with light*

When investigating microcircuit function it is an advantage to be able to maximise spatial and temporal control of the electrical activity of genetically defined subgroups of cells (Luo et al., 2008). Optogenetic methods make such investigations possible in mammals through cell-type specific transgenic expression of microbial opsins that permit fine temporal control of cells' membrane potentials (Gradinaru et al., 2007; Zhang et al., 2010; Yizhar et al., 2011; Fenno et al., 2011).

To investigate medial entorhinal cortex circuit function I used mice homozygous for the microbial opsin channelrhodopsin-2 (ChR2) (Arenkiel et al., 2007). The mice (stock number 007612) were obtained from the Jackson Laboratory (http://jaxmice.jax.org/). In these mice the channelrhodopsin-2 transgene is under the control of the Thy1-promoter and fused to a yellow fluorescent reporter protein (YFP) (Arenkiel et al., 2007). Because the Thy1-ChR2-YFP DNA construct is inserted randomly in the genome, different founder lines have different expression patterns. I used founder line 18, which has layer-specific Thy1-ChR2-YFP expression in many areas including entorhinal cortex, hippocampus, thalamus and neocortex (Arenkiel et al., 2007). I discuss MEC layer and cell-type specific expression patterns in Chapter 4.

The microbial opsin channelrhodopsin-2

Channelrhopsin-2 is cation-permeable light-gated membrane channel protein derived from the green alga *Chlamydomonas reinhardii* (Nagel et al., 2003). Because the reversal potential of the channel in Ringer's solution (ACSF) at physiological pH (~7.5) is ~-20 mV, illuminating mammalian cells that express the channelrhodopsin-2 transgene with blue light drives their membrane potential towards action potential threshold, thus providing control over their electrical activity (Nagel et al., 2003; Boyden et al., 2005). It is maximally activated by ~460 nm (blue) light and the photocurrent decays very slowly (time constant $>$ 5 seconds) beyond ~100 ms after onset of constant illumination, providing an effectively steady-state photocurrent (Nagel et al., 2003; Arenkiel et al., 2007; Bamann et al., 2008; Ernst et al., 2008).

Stimulation hardware configuration

I delivered light to the slice using an LED connected to the epifluorescence port of the microscope. Light was redirected onto the slice through the 40X objective using a mirror in the light path. The driving current (up to a maximum of 700 mA) determines the irradiance output (brightness) of the LED and is under the control of a command voltage (range 0–5 V). To enable illumination with varying intensity I connected the voltage command input to an analog out port on the ITC-18 digitiser that I controlled using custom protocols in Axograph X.

In all experiments illumination was done with the field iris diaphragm at its minimum aperture. This delivered an approximately 90 µm spot of light onto the surface of the slice (Figure 2.4 A).

2.5.2 *Calibration of irradiance*

To induce ramped and sinusoidal photocurrents in cells I needed to modulate the irradiance of the LED. In order to determine the voltage command profile to the LED I first had to establish the relationship between the command voltage and the irradiance measured in the focal plane of the 40X objective.

Measuring irradiance

I measured the total power of 470 nm light at the focal plane of the 40X objective with the LaserCheck power meter. Because irradiance is defined as power per area, I measured the power and divided this measurement by the estimated approximate cross-sectional area of the light beam in the focal plane of the 40X objective to obtain irradiance in mW/mm^2 (see Figure 2.4).

Writing protocols for controlling irradiance intensity

To derive voltage commands to deliver a desired irradiance profile over time I first fitted voltage as a function of irradiance from my irradiance data using MATLAB's lsqcurvefit algorithm.

$$V_{cmd} = f(Light_{irrad})$$

I generated irradiance profiles in MATLAB as a function of time with a pre-specified sampling rate

$$Light_{irrad} = g(t)$$

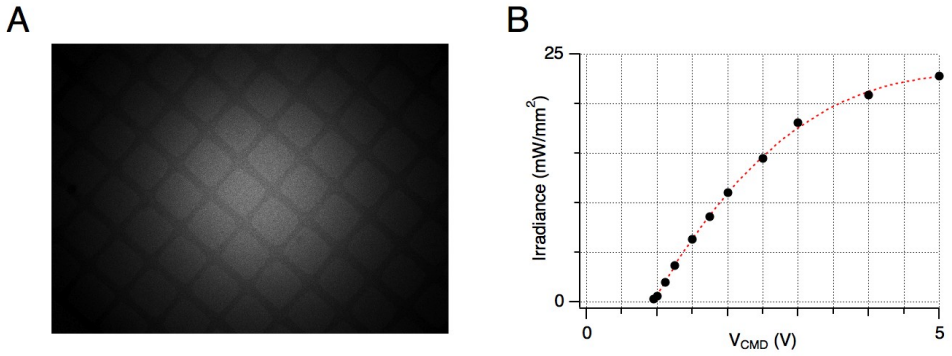

Figure 2.4: **LED voltage – irradiance relationship**. **A** Light beam with diameter of ~90 µm superimposed on 25 µm grid. Contrast is increased to clearly show the extent of the light and grid pattern. **B** Black markers are irradiance estimates for the light made using the LaserCheck powermeter at different voltage inputs to the LED. Dotted red line is a polynomial fit.

The final voltage command then becomes

$$V_{cmd} = f(g(t))$$

I exported the time and V_{cmd} vectors as text files and then converted them in Axograph to protocols. The command voltages and corresponding irradiance profiles for light stimuli used during experiments are shown in Figure 2.5.

2.6 METHODS FOR MEASURING CELL LOCATION ALONG THE DORSAL-VENTRAL MEC AXIS

2.6.1 *Imaging the location of interest and the surrounding slice*

Being able to accurately determine the position of cells along the dorsal-ventral axis is important for investigating dorsal-ventral gradients in circuit properties. To measure the position of a recorded neuron along the dorsal-ventral axis I first used a low magnification objective to image the MEC region of the slice and surrounding areas. Depending on the constraints of the recording configuration I either (i) marked the location of interest by including the recording electrode in an image (Figure 2.6 A) or (ii) pinpointed the recording location by stepping down the field iris diaphragm to leave a bright circle around the location of interest in a duplicate image, which I then superimposed on the initial image of the recording location and its surroundings (Figure 2.6 B). Up to 3 separate low magnification (4X) images were sometimes required to cover the area from a ventral recording location to the dorsal border of the MEC. I then stitched these images together using the Align Layers algorithm in Adobe

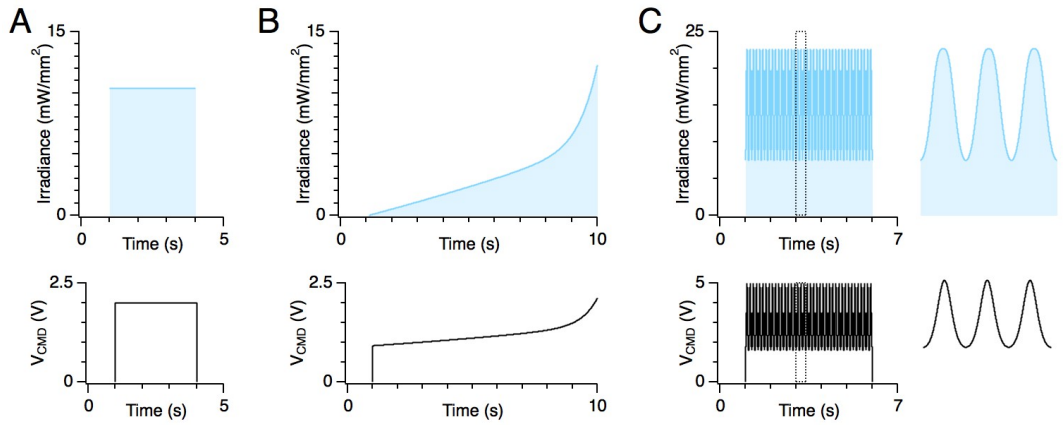

Figure 2.5: **Irradiance protocols**. **A** Constant 3 second light stimulus of ~10 mW/mm^2 (upper) and corresponding voltage command (lower). **B** Ramped light protocol with an irradiance maximum of ~12 mW/mm^2 and accompanying voltage command (lower). Note the V_{CMD} offset of about 0.9 V. **C** Sinusoidal optical stimulus (upper left) and corresponding voltage command (lower left). Horizontal expansions of the portions of the irradiance protocol and voltage command indicated by dotted lines (right panels). Note how the voltage commands depart from a sinusoid to produce a sinusoidal irradiance profile. Also note different scale of the ordinate axes to **(A)** and **(B)**.

Photoshop CS5 to provide an image that distance measurements could be taken from (Figure 2.6).

2.6.2 *Establishing the dorsal border of the MEC*

The dorsal border of the MEC provides a convenient landmark from which to measure dorsal-ventral position whereas the ventral border of the MEC is not as well defined. Figure 2.7 illustrates how the MEC cellular landmarks defined in Nissl stained slices at different medial-lateral positions appear under DIC illumination. These landmarks can be used to determine the dorsal border of the MEC.

Figure 2.7 A shows the circular hippocampus (Figure 2.7 (i)) and lack of a parasubicular protrusion into layer I (Figure 2.7 (iv)) associated with parasagittal slices containing Lateral Entorhinal Cortex (LEC). Figure 2.7 B-C show typical slices that contain the MEC. The dorsal part of the prominent dark dorsal Entorhinal/Parasubicular boundary region in the DIC illuminated slices contains an area of the parasubiculum. The parasubiculum area is clearly revealed by Nissl staining in the corresponding images in column (iii). The dorsal border of the MEC (black arrows in 2.7 B and 2.7 C column (iv)) is ventral to the group of parasubicular cells that protrudes far out into layer I (red arrows in 2.7 B and 2.7 C column (iv)). Comparison of Figures 2.7 B and 2.7 C columns (ii) and (iii) shows that the dorsal border of the MEC in the

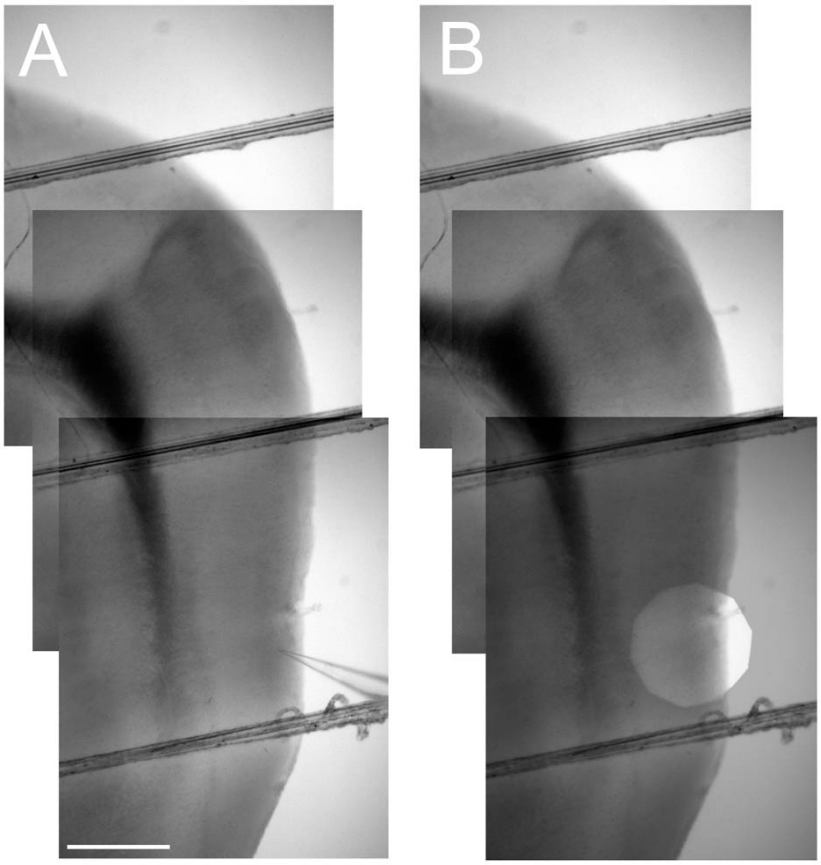

Figure 2.6: **Measuring the dorsal-ventral position of locations of interest**. **A** Aligned low magnification (4X) images that include the entire dorsal-ventral extent of the MEC between the location of interest (marked by the tip of a recording electrode) and the dark dorsal entorhinal boundary region (used to establish the dorsal border of the MEC - see Figure 2.7). **B** As in (**A**) but including a superimposed image with a stopped down field iris diaphragm (overlaid with reduced opacity) instead of a recording electrode to mark the location of interest.

Nissl sections corresponds to a location that is ventral to the dorsal edge of the dark Entorhinal/Parasubicular boundary region in the DIC slice (black arrows).

The location of the border can be estimated from DIC images and comparison to reference images (see also van Groen (2001)). Future validation of the dorsal MEC border with molecular markers will improve the accuracy of this estimate. Stained reference sections, and sections that are processed for morphological identification of labeled neurons, may be subject to considerable shrinkage so comparison of absolute distances relative to landmarks in DIC and reference sections therefore first requires measurement and correction for shrinkage (see e.g. (Garden et al., 2008)).

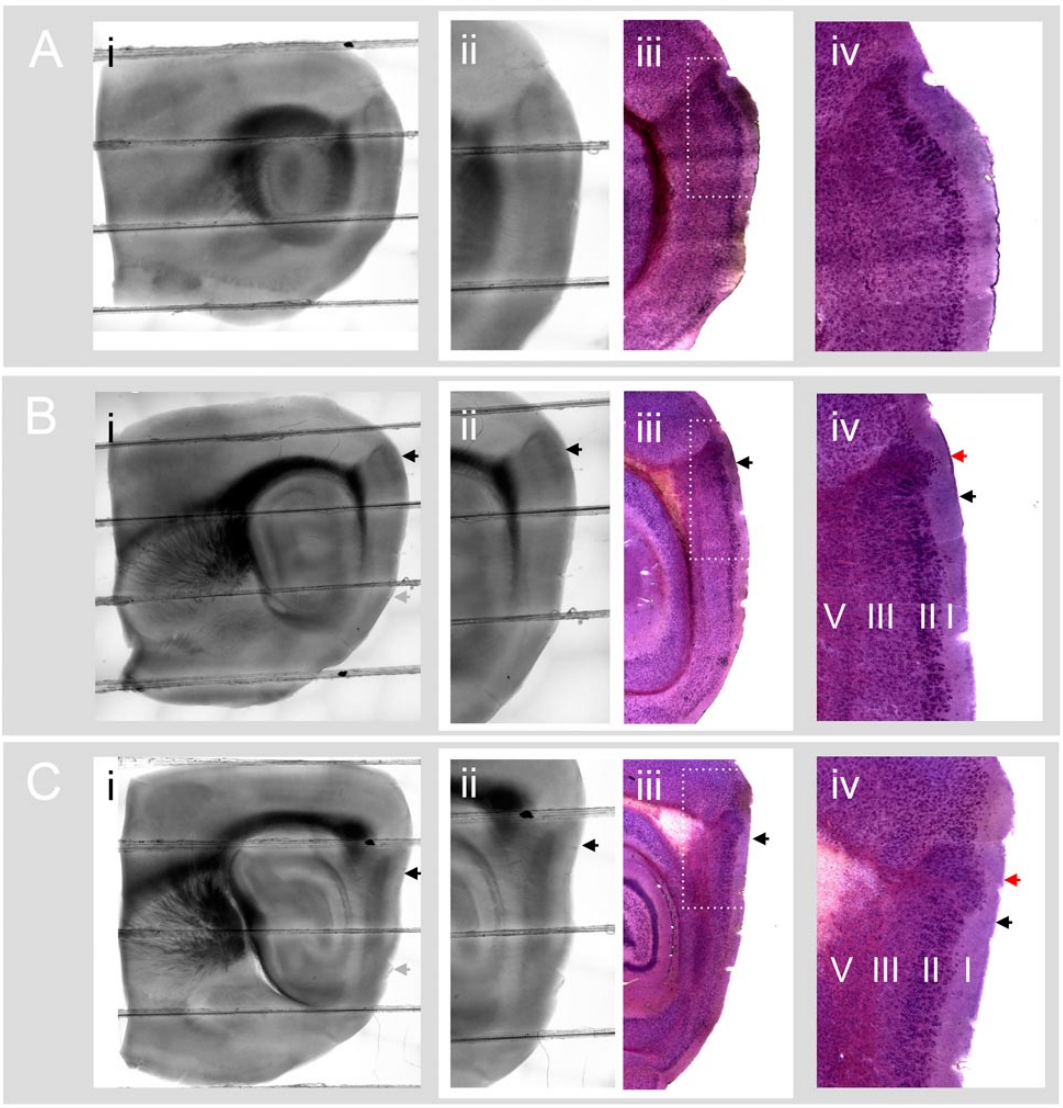

Figure 2.7: **Estimating the dorsal border of the MEC from DIC images of parasagittal slices**. **A-C** Parasagittal sections (lateral to medial) from the Entorhinal Cortex. DIC and Nissl sections are from different mice. **A-C** column (i): Parasagittal slices (400 μm thick) (aligned and blended composites of low magnification (4x) images). **A-C** (ii): Close up of the entorhinal cortex under DIC illumination showing the characteristic darker region with an inverted 'U' shape that indicates the boundary region between dorsal MEC and Parasubiculum in the top area of each image (partially obscured in **(C)** (ii) by the slice anchor chord) . **A-C** column (iii) Nissl stained slices (40 μm thick) from a different mouse aligned with images in **A-C** (ii). The darker, dense layer of cells is layer II. Comparing columns (ii) and (iii) shows how the Nissl stained cells appear in DIC images. **A-C** column (iv): Detail of Nissl stained slices. **B** and **C** column (iv) include cells from the parasubiculum (dorsal part of the dark Entorhinal/Parasubicular boundary region in the DIC images) and cells from dorsal MEC. In (**B**) (iv) and (**C**) (iv) the large dorsal patch of parasubicular cells that extends deep into layer I is easily visible (red arrows). The ventral edge of these patches corresponds to the dorsal border of the MEC (black arrows). In (**A**) (iv) the parasubicular patch is absent, indicating that the slice is too lateral for a standard parasagittal MEC slice preparation. In all panels, black arrows indicate the dorsal border of MEC. Grey arrows indicate the approximate ventral border of the MEC. *Nissl stained images provided by Dr. Melanie White.*

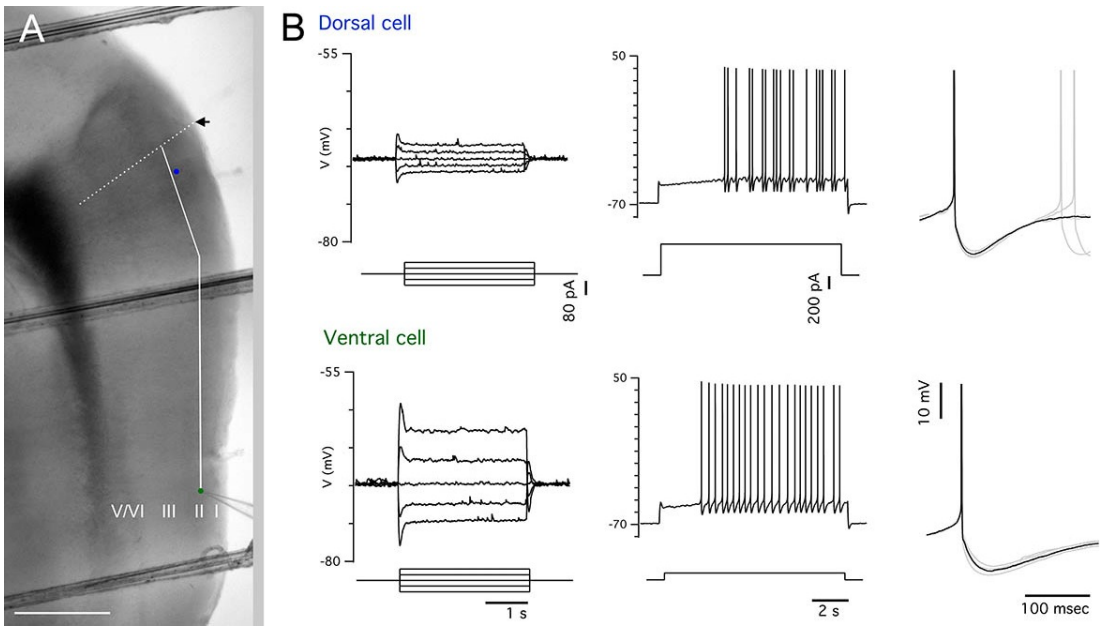

Figure 2.8: **Representative distance measurement and recording results**. **A** Blended and cropped portion of the image in Figure 2.6 A. The positions of a dorsal cell and a ventral cell are indicated by blue and green filled circles respectively. The black arrow marks the estimated dorsal border of the MEC and is extended into the deep layers by the white dotted line. The solid white line is a guide showing the contour path along which the pixel measurement of distance from the dorsal border of the MEC to the ventrally located cell was taken. Scale bar: 500 μm. **B** Whole-cell patch-clamp recordings from the dorsal (upper panel) and ventral (lower panel) cells indicated in (**A**) showing characteristic stellate cell electrophysiological properties which vary between dorsal and ventral locations. Left panels: sub-threshold responses (upper traces) to a series of small current steps (lower) used to calculate input resistance. Central panels: spiking responses (upper traces) to a large positive current step (lower). Right panels: Three superimposed example spikes from traces in the middle panels showing spike details.

2.6.3 *Calibration and measurement of distances*

To facilitate easy measurement of distance in images I used the same low magnification (4X) objective to image a 250×250 μm reference grid to establish a pixel:distance conversion ratio. I used Adobe Photoshop CS5 to measure the pixel distance from the dorsal border of the MEC to the location of interest along the contour of the MEC and converted the pixel distance to distance in μm (Figure 2.8 A).

Figure 2.8 A shows an example low magnification composite image of a parasagittal slice after recording, with the locations of two recorded neurons and measurement guides superimposed. Recordings from the marked dorsal and ventral stellate cells are shown in Figure 2.8 B. These recordings help to establish the identity of the cells and illustrate how electrical properties of MEC layer II stellate cells can differ at dorsal and ventral locations.

2.7 ANALYSIS AND STATISTICS

I performed analysis using both standard functions and custom written scripts in MATLAB (The MathWorks, Natick, MA, USA) and IGORpro (Wavemetrics, Lake Oswego, OR, USA). For statistics I used either R (www.r-project.org), Excel (Microsoft, Redmond, WA, USA) or IGORpro. In statistical analyses, n denotes the number of patched cells, unless data points are specified as paired recordings. The number of mice, N, is not reported for individual experiments, but was always $\geqslant 2$ and typically $\geqslant 3$. The average number of recorded cells per mouse was 3.3.

Means are reported as $\pm$SEM. I used the adjusted R-squared measure as the coefficient of determination for linear models. Adjusted R-squared (R^2) compensates for the tendency of the standard R-squared statistic to increase with the number of explanatory variables in the model and is derived from the standard R-squared (R_s^2) as follows:

$$R^2 = R_s^2 - (1 - R_s^2)\left(\frac{p}{n-p-1}\right)$$

where p is the number of explanatory variables in the model. Unlike R_s^2, R^2 can therefore assume negative values.

3

A COMPARISON OF THE INTRINSIC PROPERTIES OF STELLATE CELLS USING PERFORATED AND WHOLE-CELL PATCH-CLAMP METHODS

Work discussed in this chapter is adapted from, or appears in: Pastoll, H. et. al. 2012. Intrinsic electrophysiological properties of entorhinal cortex stellate cells and their contribution to grid firing fields. *Frontiers in Neural Circuits.* 6: 17.

3.1 INTRODUCTION

Stellate cells account of the majority of cells in the MEC (Alonso and Klink, 1993; Gatome et al., 2010) and are the main excitatory output of the MEC to the dentate gyrus (DG) and CA3 fields of the hippocampus (Steward and Scoville, 1976; Schwartz and Coleman, 1981; Ruth et al., 1982; Köhler, 1986; Ruth et al., 1988; Insausti et al., 1997; Dolorfo and Amaral, 1998). Input to the hippocampus from the perforant path is important for spatial behaviours (Good and Honey, 1997; Steffenach et al., 2005), suggesting that stellate cells play an important role in spatial processing in the hippocampal formation. Stellate cells are known to be spatially modulated, with firing patterns on tracks that is consistent with grid cell firing patterns in linear environments (Burgalossi et al., 2011; Schmidt-Hieber and Häusser, 2013).

Since stellate cells are a critical component of the medial entorhinal cortex (MEC) microcircuitry (Cajal, 1995; Steward and Scoville, 1976; Alonso and Llinás, 1989; Burgalossi et al., 2011), spatial computations performed by the MEC must engage their intrinsic excitable properties. The intrinsic excitable properties of stellate cells will thus constrain the possible functional repertoire of the MEC layer II microcircuit, and an understanding of their intrinsic properties will thus provide valuable insights into the computational strategies employed by the MEC.

3.2 MEASUREMENTS OF INTRINSIC PROPERTIES DIFFER DEPENDING ON RECORDING METHOD

Experiments investigating stellate cell intrinsic properties have used either sharp electrode (e.g. Alonso and Llinás, 1989; Alonso and Klink, 1993; Haas, 2002; Erchova et al., 2004; Schreiber et al., 2004; Boehlen et al., 2010) or whole-cell (e.g. Nolan et al., 2007;

Giocomo et al., 2007; Garden et al., 2008; Boehlen et al., 2010; Heys et al., 2010) recordings. However, both these recording methods impact normal cellular function and so may yield data that do not accurately reflect the intrinsic properties of undisturbed cells. The different recording methods also impact cells in different ways, evidenced by the existence of conflicting data. For example, sharp electrode recordings typically lead to lower estimates of the resting membrane potential and input resistance (Boehlen et al., 2010) and higher estimations of the peak resonant frequencies (c.f Erchova et al., 2004; Nolan et al., 2007). Why do the different recording methods produce these, and potentially other, dissimilar results and how can these disagreements be addressed in order to obtain accurate measurements of the intrinsic excitable properties of stellate cells?

Sharp electrode recordings introduce a somatic shunt

In sharp electrode recordings the cell is penetrated with a high resistance electrode. Because the membrane is punctured its resistance decreases – current can leak across the membrane more easily (Spruston and Johnston, 1992; Staley et al., 1992). This leak comprises a non-specific electrode leak current and another mediated by an sustained potassium conductance (Staley et al., 1992). This leak creates a somatic shunt as current input that leaks out across the artifactual conductances will not be available to charge the membrane capacitance, so given current inputs will create smaller voltage deflections.

In other cell types, direct comparisons between whole-cell patch-clamp and sharp electrode recordings show that ionic flux from the extracellular medium across the ruptured membrane can lead to altered resting potentials, lower input resistance and decreases in the membrane time constant (Staley et al., 1992; Li et al., 2004). Furthermore, recording artefacts such as large and variable tip potentials and the apparent (but not actual) hyperpolarisation of resting membrane potentials can also be a problem (Li et al., 2004).

In addition, damage to the membrane inflicted by the electrode entry into the cell will likely lead to Ca^{2+}-dependent intracellular repair mechanisms which engage a number of intracellular signalling pathways (McNeil and Steinhardt, 2003). This may disrupt processes that are important for maintaining intrinsic excitable properties.

Whole-cell recordings can lead to washout of intrinsic properties

To obtain whole-cell patch-clamp recordings the cell membrane is ruptured to provide electrical access to the cell (Hamill et al., 1981). Since even large molecules can diffuse freely between the cytoplasm and the pipette solution, loss of cell contents critical for maintenance of normal cellular processes can occur, disrupting normal

cell function (Spruston and Johnston, 1992; Akaike and Harata, 1994). Processes that are known to suffer gradual washout (rundown) during whole-cell recordings include second-messenger signalling, Ca^{2+} buffering and channel activities (Akaike and Harata, 1994). Washout of intrinsic properties in other cell types has been shown to depend on the dominant ion in the internal solution, indicating that intrinsic properties can be sensitive to the exact composition of the dialysing solution (Kaczorowski et al., 2007).

In stellate cells the disruption of [Ca^{2+}]-dependent processes is a particular concern. For example, since stellate cells express Ca^{2+}-dependent potassium channels (Khawaja et al., 2007), their electrical activity depends on the intracellular Ca^{2+} concentration, which is itself regulated by voltage-dependent Ca^{2+} channels (Bruehl and Wadman, 1999). Because calcium can diffuse freely between the cytoplasm and the pipette, whole-cell patch-clamp recordings could attenuate this dependency and thereby remove an important aspect of the cells' normal electrical response. Other intracellular processes in stellate cells may also be subject to rundown, but have not been reported.

In addition, the damage to the membrane that is necessary to achieve whole-cell configuration will also likely initiate Ca^{2+}-dependent intracellular repair mechanisms (McNeil and Steinhardt, 2003).

Perforated patch recordings are minimally disruptive

One way to avoid the problems associated with whole-cell and sharp electrode recording methods is to use the perforated patch-clamp method. This technique minimises the disruptive effects of recording on cellular processes and so produces data that are free from somatic shunt and washout artefacts.

As with whole-cell patch-clamp, perforated patch-clamp permits gigaohm seals to form between the membrane and the glass pipette, reducing noise and maintaining the integrity of the membrane (Horn and Marty, 1988; Akaike and Harata, 1994). However, in perforated patch recordings, antibiotics that permeabilise the membrane are included in the pipette solution (Horn and Marty, 1988; Akaike and Harata, 1994). The antibiotics form stable pores in the membrane that permit electrical access to the interior of the cell (Horn and Marty, 1988; Akaike and Harata, 1994) while avoiding dialysis of the intracellular contents as the pores formed by the antibiotic only allow monovalent ions (e.g. Na^{+}, K^{+}) to pass. Larger ions such as Ca^{2+}, Mg^{2+} and $SO_4{}^{2-}$ cannot traverse the membrane and so the normal intracellular concentrations of these ions are maintained (Akaike and Harata, 1994).

Because the pores formed by the antibiotics are small (Akaike and Harata, 1994) and because the Ca^{2+}-dependent repair response to membrane damage depends

on the degree of the damage (McNeil and Steinhardt, 2003), it is likely that any effect the repair response has on intrinsic excitable properties during perforated patch recordings is much lower than during sharp electrode and whole-cell recordings.

Different pore-forming antibiotics including nystatin, amphotericin B and gramicidin have been used successfully for perforated patch-clamp recording. Amphotericin B has the advantage that the pores it forms are resilient and so permit long (>60 min) recordings (Akaike and Harata, 1994).

Because of the benefits afforded by perforated patch recording technique I decided to use this method to establish accurate characterisations of the intrinsic excitable properties of stellate cells. I reasoned that by potentially resolving inconsistencies and revealing novel properties, perforated patch data would help to evaluate the accuracy of data obtained using the other recording techniques. It could thus also serve as a test for establishing the suitability of the other recording techniques for investigating the various intrinsic electrical phenomena exhibited by stellate cells.

3.3 INTRINSIC EXCITABLE PROPERTIES OF STELLATE CELLS

I systematically investigated the intrinsic excitable properties of stellate cells discussed in Section 1.4 of Chapter 1 using the perforated patch-clamp method. To directly compare intrinsic excitable properties recorded with whole-cell and perforated patch-clamp techniques I recorded separately from populations of stellate cells using both methods under the same conditions.

To reduce noise resulting from synaptic inputs I blocked excitatory glutamate AMPA and NMDA receptors with NBQX (5 μM) and D-AP5 (50 μM) and inhibitory $GABA_A$ and $GABA_B$ receptors with Picrotoxin (50 μM) and CGP55845 (1 μM) respectively throughout recordings. To ensure that the results were not biased by variation in electrophysiological properties arising from variation in the the dorsal-ventral location of the recorded cells I ensured that cells in both recording conditions were evenly sampled from across the dorsal-ventral extent of layer II and controlled for the dorsal-ventral position of the recorded cells by using Analysis of Covariance (ANCOVA) for statistical analyses (see Zar, 1998; Crawley, 2005, for details of ANCOVA).

3.3.1 *Membrane properties at rest*

To investigate the basic electrophysiological properties of the membrane around resting potential I injected a series of small current steps in current clamp and recorded the membrane response (see Figure 3.1 A,C). From these traces I calculated the rest-

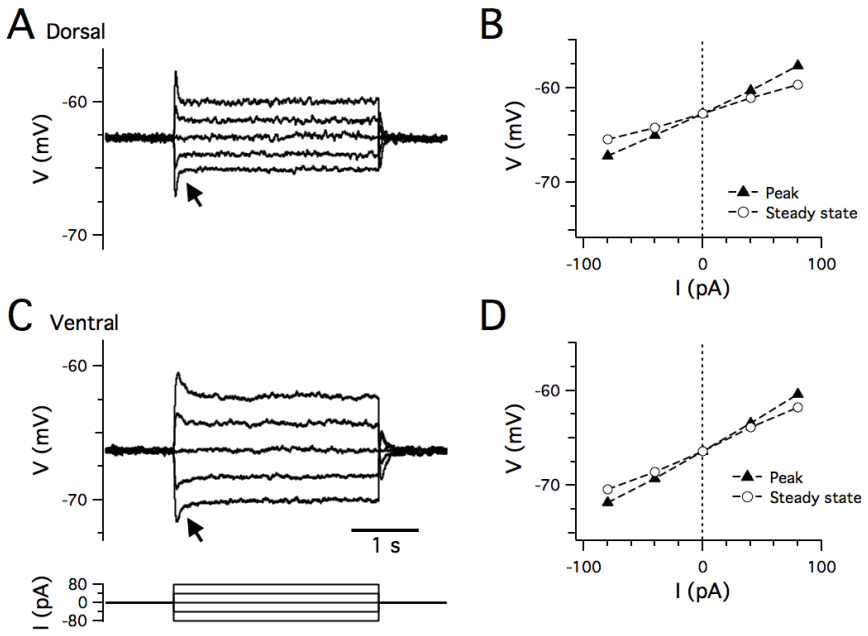

Figure 3.1: **Resting membrane properties**. **A,C** Examples of perforated patch-clamp recordings of membrane potential responses to current steps **(C, lower)** recorded from dorsal **(A)** and ventral **(C)** stellate cells. Arrows indicate the membrane potential 'sag'. **B,D** Peak (closed triangles) and steady-state (open circles) membrane potential responses plotted as a function of current step amplitude for data from dorsal **(B)** and ventral **(D)** stellate cells in **(A,C)**.

ing membrane potential, input resistance, membrane time constant and the sag coefficient.

The resting membrane potential

I estimated resting membrane potential by taking the mean value of the resting trace (the trace in each series with no current injection). I found that for perforated patch recordings the mean resting potential was ~3 mV more depolarised than for whole-cell recordings ($p = 0.047$; Table 3.1).

Input resistance

Figure 3.1 B,D displays the steady state (mean of each trace for 2 s before the offset of the current step) and peak (value of most extreme deflection) membrane potential deflections during current steps plotted against the injected current. The input resistance is defined as the magnitude of the voltage change divided by the amplitude of the current input, and so can be read off as the slope of the graph. Within cells, the input resistance does not change much across the range of membrane potentials reached during the small current steps.

	Perforated patch (n = 11)	**Whole-cell** (n = 14)	**p**	**Test**
Resting V_m (mV)	-64.2 ± 0.7	-67.1 ± 0.8	0.047	ANCOVA
Input resistance (+ve) (MΩ)	55.5 ± 9.6	34.9 ± 3.5	0.0002	ANCOVA
Input resistance (-ve) (MΩ)	53.8 ± 9.4	32.5 ± 3.0	0.0004	ANCOVA
Membrane time constant (ms)	11.2 ± 0.9	12.7 ± 0.9	0.64	ANCOVA
Sag coefficient	0.66 ± 0.02	0.58 ± 0.01	0.0005	ANCOVA
Location (μm)	1096 ± 192	1114 ± 206	0.92	t-test

Table 3.1: **Sub-threshold membrane properties.**

I calculated input resistance values from the mean steady-state membrane voltage deflection in response to both positive and negative current input steps. I found that perforated patch recordings revealed input resistances ~60% higher than those recorded with whole-cell patch-clamp (IR (+ve) p = 0.0002, IR (-ve) p = 0.0004; Table 3.1).

Membrane time constant

I estimated the membrane time constant, τ_m, by fitting a single exponential function to the segment of each voltage trace following the current injection step (Nolan et al., 2007). To do this I wrote a script in MATLAB that extracted the segment of each trace from the current onset to the peak of the voltage deflection. The duration of each extracted segment thus depended on the delay to the voltage deflection maximum. The script then used lsqcurvefit function to estimate the value of the parameters V_{offset}, $V_{amplitude}$ and τ_m that minimised the value of the expression

$$V_{offset} + (V_{amplitude} \times e^{\frac{-t}{\tau_m}}).$$

The script enabled visual confirmation of all fits by superimposing the fit onto the extracted segment of trace (see Figure 3.2). Because the time constant of the relaxation from the maximum to steady-state voltage is much slower than τ_m, and because the single exponential function typically fit the entire extracted trace segment very well, it is likely that there was minimal contamination of the estimated τ_m by the sag.

I calculated the mean τ_m value for each cell by finding the mean of estimated τ_m fits for all individual traces in response to different current steps (Table 3.1). The membrane time constant did not significantly differ between recording methods (p = 0.64) (Table 3.1).

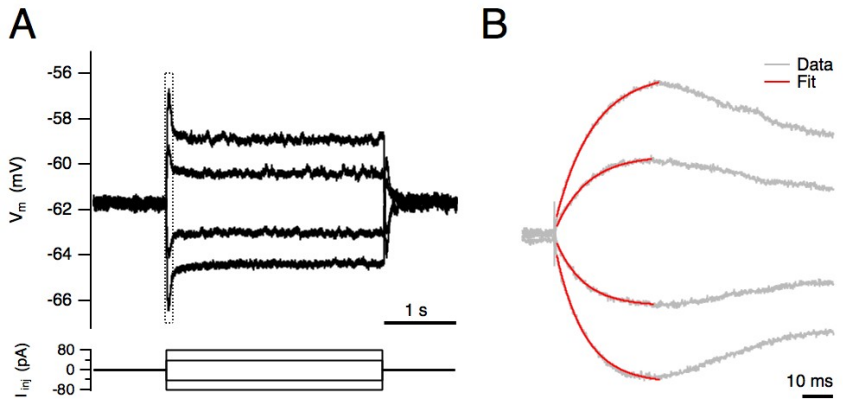

Figure 3.2: **Time constant estimation**. **A** Example voltages traces (upper) in response to sub-threshold current steps (lower). **B** Expansion of the voltage traces (from dotted box in (**A**)) (grey), and superimposed single exponential fits (red) to the rising phase of the voltage response to the current inputs. The fits fit the data well and provide an estimation of the membrane time constant.

Sag coefficient

The Sag coefficient measures the ratio of the magnitude of the steady-state to maximal voltage deflections (a lower coefficient indicates a greater sag) (Nolan et al., 2004, 2007) (see Table 3.1 and Figure 3.1). Perforated patch recordings exhibited a small (~13%) but significant decrease in sag magnitude relative to whole-cell recordings (Table 3.1). Because the sag reflects activation (in the hyperpolarising direction) or inactivation (in the depolarising direction) of I_h, and I_h opens at hyperpolarised voltages, the reduction in sag may be accounted for by the difference in resting membrane potential between the two recording methods.

Theta-frequency resonance

To compare the resonant properties of stellate cells in different recording conditions I injected a constant amplitude sinusoidal current waveform with frequency linearly increasing from 1–20 Hz (grey trace, Figure 3.3) (Erchova et al., 2004; Nolan et al., 2007). I analysed the responses from cells at rest (Figure 3.3 A,D black trace) and when depolarised with a holding current to peri-threshold potentials (Figure 3.3 A,D red trace). I considered the peri-threshold potential to be the highest mean membrane potential that did not result in spiking during the sinusoidal current injection. I found this to be approximately -55 to -50 mV. To determine the appropriate holding current I found the minimal holding current that elicited spikes during sinusoidal stimulus and decreased it by 10 pA.

To calculate the resonant frequency impedance peak, F_{Z-max}, I found the maximum of the impedance spectrum (the real part of the ratio of the voltage and input current amplitude spectra) (Erchova et al., 2004; Nolan et al., 2007). Because cell membranes act as low-pass filters which attenuate high frequency inputs, in non-resonant cells F_{Z-max} is close to 0 (Erchova et al., 2004). However, in stellate cells, with perforated patch recordings, I found that F_{Z-max} lies in the theta-frequency range (Figure 3.3). It has similar values when measured with whole-cell recordings at both resting potential ($p = 0.84$) and when depolarised to peri-threshold potential ($p = 0.56$) (see Table 3.2 and also Giocomo et al. (2007); Nolan et al. (2007); Boehlen et al. (2010); Heys et al. (2010)).

To quantify the magnitude of the resonance, Q, I used the ratio between the impedance value at F_{Z-max} and the impedance value at 1 Hz (higher Q values reflect a larger resonance peak) (Erchova et al., 2004; Nolan et al., 2007). At resting potentials I found that Q does not differ significantly between the two methods ($p = 0.1$; Table 3.2). However, with perforated patch-clamp recordings Q is significantly smaller at peri-threshold compared to resting membrane potentials ($p = 0.03$; Table 3.2). In these whole-cell recordings Q is similar when measured at resting potential (-65 mV) and peri-threshold potentials (-50 to -55 mV) ($p = 0.4$; Table 3.2). However, previous results indicate that Q is reduced on depolarisation from -70 to -60 mV in whole-cell recordings (Nolan et al., 2007). This apparent discrepancy may be explained by resonance at peri-threshold potentials resulting from a different mechanism to that observed at resting potentials.

To obtain the lag between the input current and recorded voltage I calculated their relative phase (the imaginary part of the ratio of the Fourier transforms of the membrane voltage and input current waveform) (Nolan et al., 2007). Positive phase values (downward in Figure 3.3 C,F) reflect a phase advance of the voltage response relative to the injected current. The phase advance observed at low (< 5Hz) frequencies and lag at higher frequencies observed with perforated-patch recordings is consistent with whole-cell data (Nolan et al., 2007).

These recordings indicate that resonant properties of stellate cells are largely similar for perforated-patch and whole-cell recordings, suggesting that whole-cell recordings may be more suitable than sharp-electrode recording methods for assessing resonant properties of stellate cells, as sharp-electrode recordings often conflict with whole-cell data (e.g. Boehlen et al., 2010). However, there is one discrepancy between the whole-cell and perforated-patch recording methods. The significantly smaller magnitude of resonance at peri-threshold potentials compared to resting potentials that is not observed with whole-cell recordings may indicate washout of a conductance that dampens resonance at peri-threshold potentials and suggests that reso-

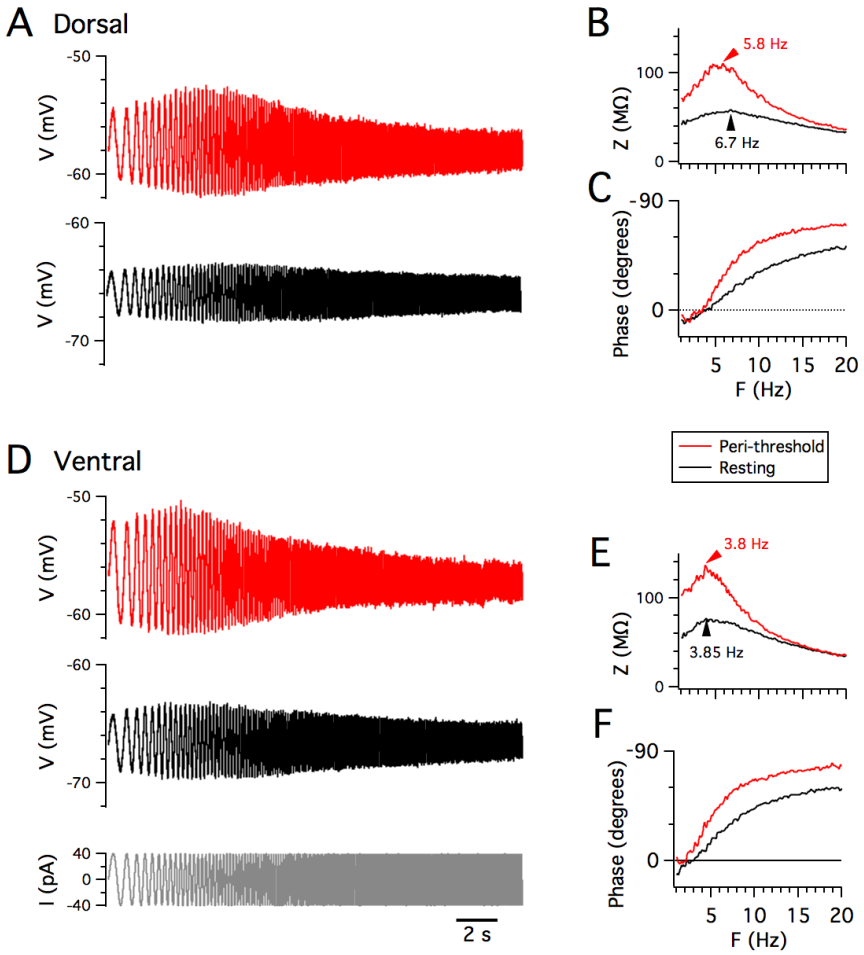

Figure 3.3: **Membrane potential resonance. A,D** Examples of perforated patch-clamp recordings of membrane potential responses from resting potential (black) and from depolarized membrane potential (red) to ZAP current waveforms (grey) **(D, lower)**, from dorsal **(A)** and ventral **(D)** stellate cells. **B,E** Membrane impedance plotted as a function of frequency. **C,F** Membrane phase plotted as a function of frequency. **(B,C)** and **(E,F)** are calculated from data in **(A)** and **(D)**, respectively.

nance at resting and peri-threshold potentials may rely on different ionic mechanisms.

3.3.2 *Peri-threshold spontaneous activity*

To investigate spontaneous peri-threshold activity I injected 20 s current steps to depolarise cells to close to spiking threshold (Dodson et al., 2011). I used a current step ~10 pA lower than the minimum magnitude for eliciting spikes. To avoid onset artefacts and to allow the membrane potential to reach steady state I examined the final 15 s of each 20 s trace for theta-frequency activity.

	Perforated patch (n = 5)	**Whole-cell** (n = 14)	**p**	**Test**
Q (resting)	2.0 ± 0.2	1.7 ± 0.1	0.1	ANCOVA
Q (peri-threshold)	1.6 ± 0.1	1.8 ± 0.1	0.3	ANCOVA
F_{Z-max} (Hz) (resting)	5.9 ± 1.0	6.1 ± 0.5	0.84	ANCOVA
F_{Z-max} (Hz) (peri-threshold)	4.7 ± 0.9	4.4 ± 0.4	0.56	ANCOVA
	Resting	**Peri-threshold**	**p**	**Test**
Q (perforated patch)	2.0 ± 0.2	1.6 ± 0.1	0.03	Paired t-test
Q (whole-cell)	1.7 ± 0.1	1.8 ± 0.1	0.4	Paired t-test
F_{Z-max} (Hz) (perforated patch)	5.9 ± 1.0	4.7 ± 0.9	0.02	Paired t-test
F_{Z-max} (Hz) (whole-cell)	6.1 ± 0.5	4.4 ± 0.4	2.8e-6	Paired t-test

Table 3.2: **Resonant properties.**

In theory, theta-frequency membrane potential activity could be due to different mechanisms, including true oscillatory processes, filtered noise or random walk dynamics (Figure 3.4). Power spectra and autocorrelograms, which have been used by previous studies to investigate theta-frequency activity (Alonso and Llinás, 1989; Giocomo et al., 2007; Nolan et al., 2007; Boehlen et al., 2010) may not reliably distinguish between these mechanisms. Indeed, synthetic data generated by random processes, such as high variance gaussian noise with lowpass filtering and random walks with decay, can produce power spectra with prominent peaks and regular autocorrelations, potentially giving the misleading impression that these data are generated by genuine oscillatory processes (see Figure 3.4 D,E second and third columns). Because cell membranes act as low pass filters and have history dependence, signals produced by random processes in real cells may appear oscillatory if analysed with these techniques. This could be a particular problem if 'ideal' trace segments are selected as representative of a particular neuron, especially if the criterion for selection is that they appear to reveal an oscillatory signal.

Lomb analysis distinguishes random and periodic processes

To overcome the uncertainties associated with using Fourier power spectra and autocorrelograms to identify oscillatory processes I used Lomb least-squares analysis, which provides a measure of the statistical significance of peaks in a power spectrum (Lomb, 1976; Horne and Baliunas, 1986; Zechmeister and Kürster, 2009). The significance of each frequency component is estimated by comparing its power in the Lomb periodogram against the exponential distribution that frequency powers would follow if the signal were pure Gaussian noise. This permits comparison of all the statistically significant frequency components in a given trace segment with

others in a series of consecutive trace segments to test whether significant frequency components remain similar. If consecutive segments have dissimilar significant frequency components this indicates that the underlying signal is not stable (and thus unlikely to be periodic), even if significant frequency components exist within each trace segment.

Lomb processing is computationally expensive so to reduce the number of data points I bandpass filtered traces from 0.5 – 50 Hz and resampled at 100 Hz. To do the Lomb analysis I wrote a script using an implementation in MATLAB of the algorithm described in Press et al. (1992) with the oversampling parameter set to 4 and and the highest frequency set to the Nyquist rate (100 Hz).

The output of an oscillator depends on amplitude noise ($\alpha(t)$), phase noise ($\phi(t)$) and additive noise. The expression for a noisy output signal (where additive noise is sampled from a Gaussian distribution) can thus be given as:

$$s_{output} = \alpha(t) \cdot \cos(t + \phi(t)) + \mathcal{N}(\mu, \sigma^2)$$

When applied to 10 consecutive 3 s synthetic trace segments, Lomb analysis clearly distinguishes data generated by periodic processes, even in the presence of high magnitude additive noise or phase noise, from data generated by purely random processes (Figure 3.4 rightmost column). The periodic processes (Figure 3.4 B,C) produce narrow ranges of significant frequencies in each trace segment with a most significant frequency that is stable across consecutive segments. On the other hand, the random processes (Figure 3.4 D,E) produce a wide range of significant frequencies, with a most-significant frequency that varies substantially across trace segments.

Peri-threshold theta-frequency activity

I found that with perforated patch-clamp recordings that all stellate cells generated substantial voltage fluctuations (~2 mV amplitude) at membrane potentials close to spike threshold (Figure 3.5 A,E,F,J).

To directly compare this data to previous findings (Alonso and Llinás, 1989; Giocomo et al., 2007; Nolan et al., 2007; Boehlen et al., 2010) I needed to initially use similar analysis methods. I therefore first used standard Fourier decomposition to generate spectrograms of the peri-threshold activity with MATLAB. Using spectrograms with short (1 s) Hanning windows (32768 points, 90% overlap) reveals that the membrane activity is characterised by non-stationary brief epochs of power at theta frequencies (Figures 3.5 B,G). The use of long windows (6.5 s, 131072 points, 95% overlap) for spectrograms, as in some previous studies (e.g. Yoshida et al., 2011), may

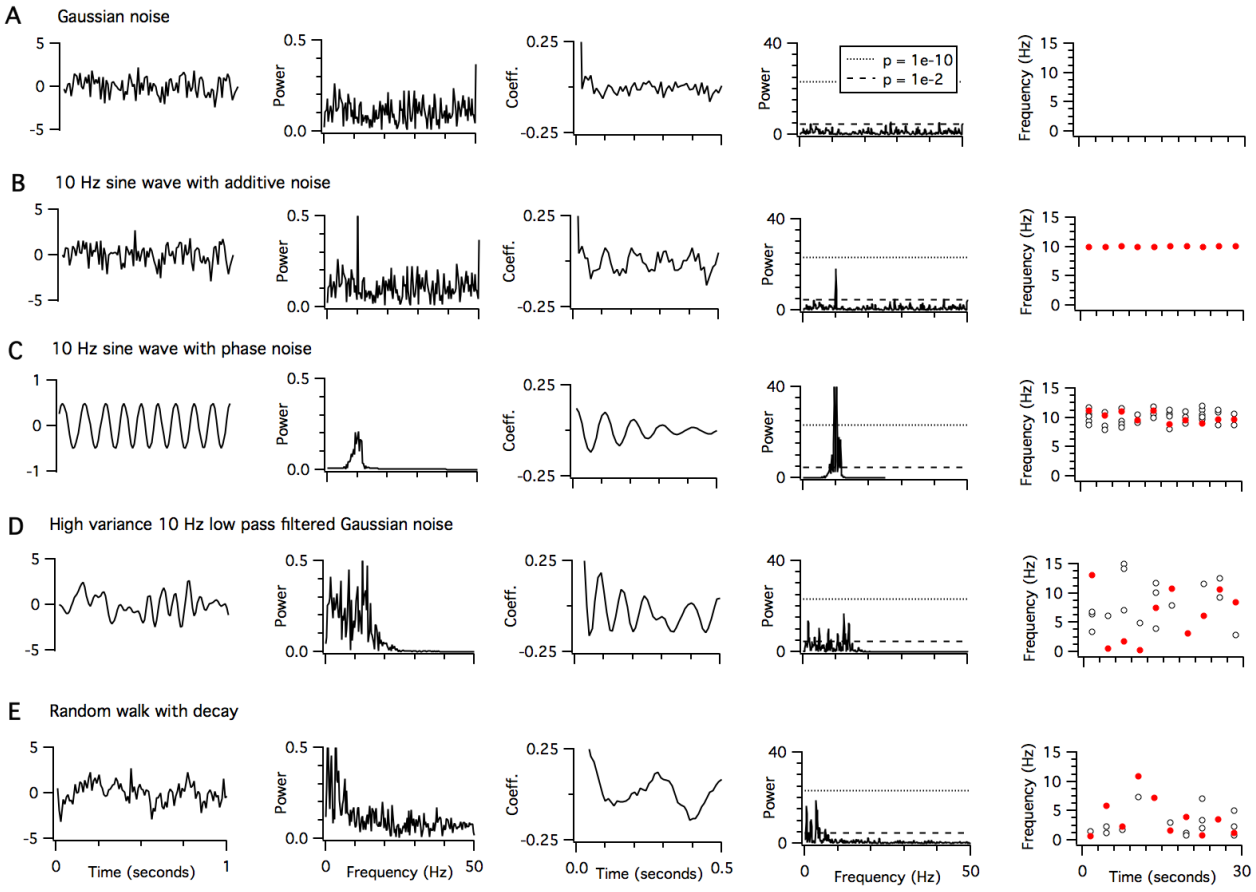

Figure 3.4: **Comparison of methods for analysis of oscillatory activity. A–E** Examples of analysis of signals in the presence of different types of noise. **A** Unit variance pure Gaussian noise (no rhythmic component). **B** A 10 Hz sine wave with added unit variance Gaussian noise. **C** A 10 Hz sine wave with amplitude 0.5 units containing phase noise with maximum period shift of ± 0.5 units. **D** High (2 unit) variance Gaussian noise filtered with a cut off of 10 Hz. **E** A random walk generated by incremental addition of low (1 unit) variance Gaussian noise with a 25 ms decay time constant. The first column shows 1 s of example data, the second to fourth columns shows the power spectral density, the autocorrelation function and the Lomb spectra generated from 3 s waveforms generated by each process, while the fifth column plots the frequency of the largest amplitude significant peak in the Lomb spectra (red filled circles) and the frequencies of all other significant peaks (open circles) for 10 consecutive simulation epochs each of duration 3 s.

cause this transient activity to appear sustained (cf Figures 3.5 B–C, G–H). This could give the impression that the activity is generated by a stable periodic process.

However, when consecutive segments of activity are analysed with Lomb periodograms, the instability is manifest as variability in the frequency of the most significant activity peak and as multiple peaks in each segment (Figure 3.5 D,I). This variability is clear from representative data (Figures 3.5 E,J). Variability in the frequency of activity is also apparent during periods between action potential clusters (Figure 3.5K). Considering only the most significant peak in each of five epochs of

duration 3s, the mean frequency is 3.6 ± 0.5 Hz (n = 11), while the range of significant frequencies across all five epochs is 3.2 ± 0.55 Hz (n = 11).

Together, this data and analysis indicates that the spontaneous peri-threshold activity is not rhythmic. This contrasts with earlier reports that used sharp electrode and whole-cell recordings and relied on autocorrelation and Fourier decomposition methods for analysis (Alonso and Llinás, 1989; Klink and Alonso, 1993; Dickson et al., 2000b; Giocomo et al., 2007; Boehlen et al., 2010). Instead, I find using Lomb analysis that the spontaneous activity is in fact characterised by multiple overlapping significant frequency components, with no single dominant frequency. In addition, each frequency component is transient, indicating that the membrane potential is characterised by rapidly changing combinations of frequencies.

3.3.3 *Supra-threshold activity*

Are the characteristic features of stellate cell action potentials and their after-polarisations seen with whole-cell and sharp electrode recordings (Alonso and Llinás, 1989; Klink and Alonso, 1993; Nolan et al., 2007) also maintained during perforated patch recordings? To answer this I directly compared spike characteristics measured during perforated patch and whole-cell recordings.

The action potential and its after-polarisation

The rheobase current is the minimally sufficient injected current required to elicit action potentials. Consistent with the difference in input resistance between the different recording methods I found the rheobase current was significantly smaller with perforated patch recordings (Table 3.3). To ensure that, on average, cells in the different conditions spiked at similar rates I applied 20 s current steps with magnitude such that cells fired action potentials in the 1–3 Hz range (Figure 3.6). I wrote a MATLAB script that analysed the resulting spike trains by identifying individual action potentials and measuring their properties of interest.

I found that the properties of the spike parts of action potentials were very similar across different recording conditions. There were no significant differences between spike maxima, spike width or spike thresholds (Table 3.3). In contrast, I found that the AHPs were significantly shorter in perforated patch recordings ($p = 0.03$), even though their voltage minima did not differ significantly ($p = 0.08$; Table 3.3).

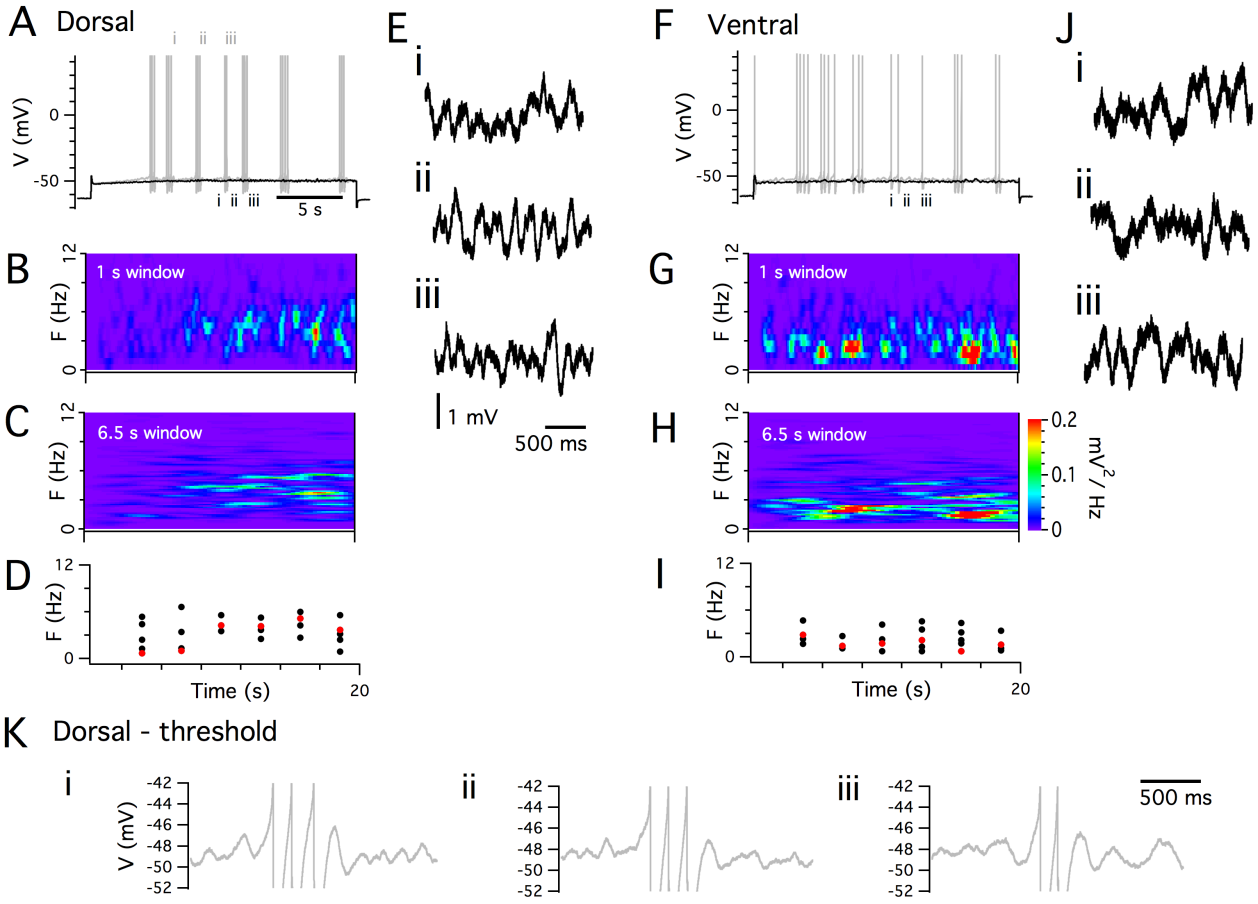

Figure 3.5: **Peri-threshold theta-frequency activity. A,F** Examples of perforated patch-clamp recordings of peri-threshold (black) and threshold (grey) membrane potential responses to current steps. **B,G** Spectograms from peri-threshold responses in **(A,F)**, calculated with 1 s windows. **C,H** Spectrograms from the same traces calculated using 6.5 s windows. **D,I** Frequency of the most significant component (red) and all other significant frequencies (black) of peri-threshold membrane potential activity in **(A,F)**. Frequencies are obtained from Lomb periodograms of contiguous 3 s segments of data. **E,J** Examples of consecutive 2 s segments of data from peri-threshold activity in **(A,F)**. **K** Examples of 1.5 s segments of membrane potential activity triggered by final spikes of three consecutive clusters of action potentials in **(A)**. Note the different frequency of the theta activity following each spike cluster.

Patterns of spiking output

Changes in the duration of the AHP predict changes in the patterns of spike output. The association between changes in the duration of the AHP and the spiking patterns has been shown in HCN1 knockout animals, and during pharmacological block of I_h (Nolan et al., 2007), and has been described in modelling studies (Dudman and Nolan, 2009).

At low (<~5 Hz) overall spike frequencies stellate cells tend to spike in clusters (Alonso and Klink, 1993; Klink and Alonso, 1993; Nolan et al., 2007; Engel et al.,

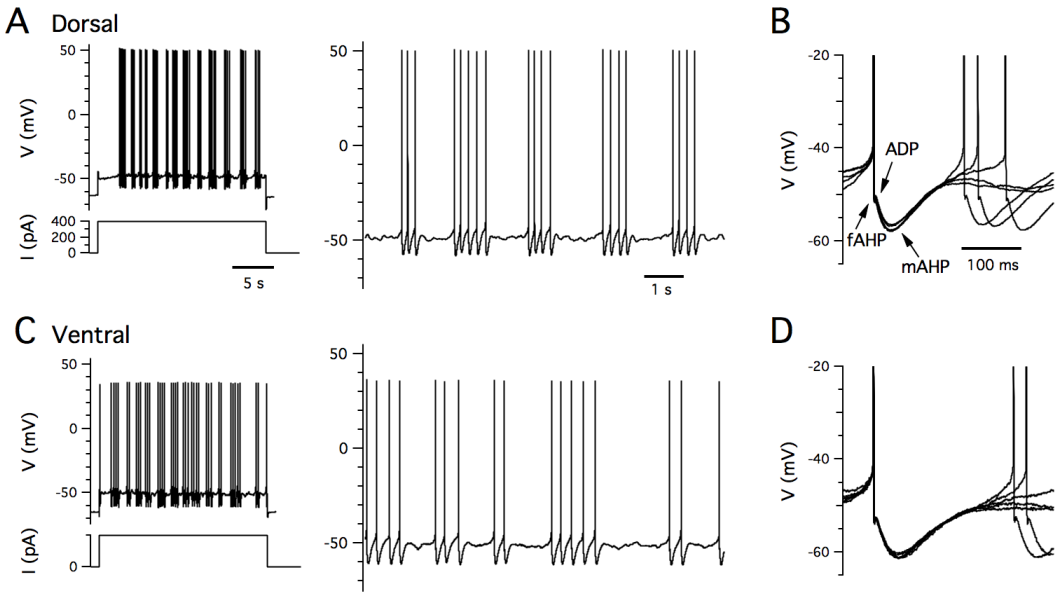

Figure 3.6: **Clustered firing patterns. A,C** Examples of perforated patch-clamp recordings of supra-threshold membrane potential responses (upper left) to positive current steps (lower left) from dorsal **(A)** and ventral **(C)** stellate cells. Action potentials on an expanded time base are shown to the right. **B,D** Examples of five consecutive action potential after-polarisations captured from traces in **(A,C)**. Arrows indicate components of the after-polarisation.

2008; Fernandez and White, 2008). This clustering is also evident in perforated patch recordings (Figure 3.6). To analyse spike clustering I applied the criteria employed by Nolan et al. (2007) and considered a series of spikes a cluster only if the time elapsed between the first (last) spike in the series and a previous (following) spike was >300 ms and the delay between every pair of consecutive spikes in the series was <200 ms. Consistent with a reduced AHP duration I found that the frequency of spikes within clusters was ~50% higher in perforated patch recordings compared to whole-cell recordings ($p = 0.004$), despite a similar number of spikes per cluster in the different recording conditions ($p = 0.1$; Table 3.3). The perforated patch recordings also revealed that clustering in stellate cells is exceptionally robust (Figure 3.6 A,C and Table 3.3). I quantified the robustness of clustering, P_C, as the probability that any given spike occurs within a cluster (Nolan et al., 2007). In perforated patch recordings ~85% of spikes occurred within clusters (P_C = ~0.85) compared to only ~26% in whole-cell recordings (P_C = ~0.26), a greater than 3-fold increase ($p = 1.1e\text{-}5$; Table 3.3).

The robust spike clustering, the higher frequency of spikes in clusters and the shorter AHP revealed by the perforated patch recordings provides new information about a set of mechanisms that may play a functional role in MEC layer II microcircuit computations.

	Perforated patch (n = 11)	**Whole-cell** (n = 13)	**p**	**Test**
Overall spiking frequency (Hz)	2.1 ± 0.1	2.3 ± 0.1	0.17	ANCOVA
Rheobase (pA)	182 ± 19	246 ± 22	0.005	ANCOVA
Spike max (mV)	41.9 ± 1.7	45.8 ± 1.0	0.06	ANCOVA
Spike width at half-height (ms)	0.59 ± 0.02	0.6 ± 0.01	0.65	ANCOVA
Spike threshold (mV)	-44.7 ± 1.5	-42.5 ± 0.7	0.16	ANCOVA
AHP minimum (mV)	-60.9 ± 0.7	-59.2 ± 0.6	0.08	ANCOVA
AHP width at half-height (ms)	64.3 ± 3.9	74.9 ± 4.1	0.03	ANCOVA
Intra-cluster spike frequency (Hz)	11.8 ± 1.3	7.8 ± 0.3	0.004	ANCOVA
Spikes per cluster	2.6 ± 0.1	3.8 ± 0.7	0.1	ANCOVA
Proportion of spikes in clusters (P_C)	0.85 ± 0.06	0.26 ± 0.01	1.1e-5	ANCOVA

Table 3.3: **Action potential properties.**

3.3.4 *Rundown of conductances in whole-cell configuration*

The perforated patch data described above suggest that during whole-cell recordings there may be washout of a conductance that is not necessary for clustered firing patterns, but that increases their probability of occurrence.

I took advantage of the relatively large differences between whole-cell and perforated patch-clamp methods in the AHP duration and P_C to estimate the time course of changes that takes place during intracellular dialysis associated with whole-cell recording from stellate cells (Figure 3.7). To do this I measured the AHP half-duration and P_C at intervals of 2, 5, 10, 20 and 30 min after break-in to whole-cell configuration (n = 12). I also compared these values to those obtained during perforated patch-clamp recordings (n = 11). I found that even within 2 min of break-in to whole-cell configuration – the shortest interval within which I could reliably estimate the threshold current to trigger spike firing – P_C differed significantly from that measured with perforated patch-clamp recording (p = 0.003, ANCOVA; Figure 3.7 E). P_C continued to change throughout the duration of the 30 min whole-cell recording (2 min vs 30 min, p = 0.004, paired t-test). There was no significant difference between the AHP half-duration in perforated patch experiments and 2 min into the whole-cell recordings (p = 0.7, ANCOVA). However, the AHP duration subsequently lengthened (2 min vs 30 min, p = 8e-4, paired t-test; Figure 3.7). In contrast to the change in P_C, the AHP duration appeared to reach a steady state before the end of the 30 minute recordings (Figure 3.7 F).

The different timecourses of the P_C and AHP washouts suggests that at least two different intracellular mechanisms are affected during whole-cell recordings. It also

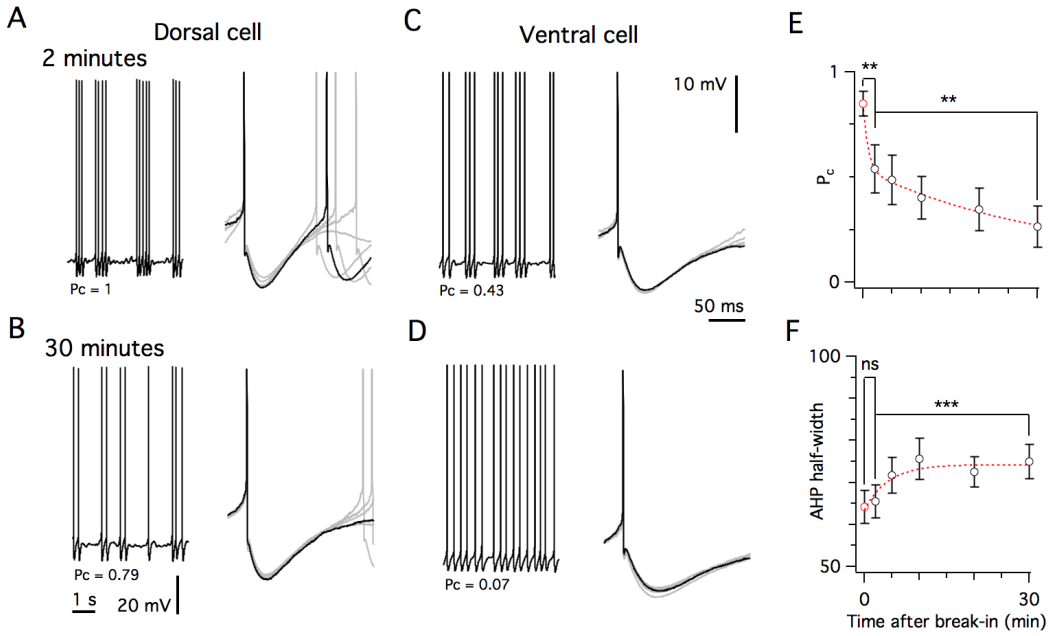

Figure 3.7: **Washout of spiking properties during whole-cell recording. A,C** Spiking pattern (left) and after-hyperpolarization (right) in a dorsal **(A)** and ventral **(C)** stellate cell approximately 2 min after break in. **B,D** Spiking pattern and after-hyperpolarisation from the same cells as in **(A,C)**, 30 min after break-in. **E** Decrease of the probability of spikes occurring in a cluster (Pc) over time after break-in. **F** Increase in the after-hyperpolarisation width at half-height over time. In **(E,F)** the red data point at time zero is from the perforated patch data. ANCOVA was used for comparisons between data obtained using different recording methods and Student's paired t-test to test differences within cells at different time points.

suggests that the AHP duration is not the only determinant of P_C and that a separate conductance, which may be independently regulated, also contributes to spike clustering.

3.4 DORSAL-VENTRAL ORGANISATION OF MEMBRANE PROPERTIES

Much of the variation in the intrinsic properties of stellate cells recorded using whole-cell and sharp electrode techniques is explained by the position of the recorded cell along the dorsal-ventral axis of the MEC (Giocomo et al., 2007; Garden et al., 2008; Boehlen et al., 2010). To test whether these gradients in intrinsic properties are maintained with perforated patch recordings I re-analysed the data described above, using linear regression to investigate the relationship between the location of recorded cells and their intrinsic excitable properties. Cell recording locations were evenly distributed along almost the entire extent of the dorsal-ventral axis in both recording conditions and the mean location was not significantly different ($p = 0.92$, Figure 3.1, ranges: perforated-patch, 50–2110 µm; whole-cell, 80–2150 µm).

3.4.1 *Resting membrane properties*

Passive properties

In sharp electrode and whole-cell recordings stellate cells at dorsal locations have lower input resistance and faster membrane time constants than those at ventral locations (Garden et al., 2008; Boehlen et al., 2010). Consistent with these data, in perforated patch-clamp experiments I also found significant dorsal-ventral organisation of the input-resistance (R^2 = 0.53, p = 0.007) and membrane time constant (R^2 = 0.76, p = 0.0003), but not the resting membrane potential (R^2 = 0.11, p = 0.17) (Figures 3.8 A–C).

Frequency selectivity

As discussed in Chapter 1, previous recordings have demonstrated that dorsal cells exhibit resonance peaks at higher frequencies than cells in ventral locations (Giocomo et al., 2007; Boehlen et al., 2010). The perforated patch-clamp data are consistent with these results, as is the new whole-cell data, both of which show a clear gradient in the resonant frequency peak, F_{Z-max}, along the dorsal-ventral axis. This is true at rest and at peri-threshold potentials (Figures 3.8 E).

In my whole-cell data (Figure 3.8 D) as well as in previous sharp electrode and whole-cell recordings (Boehlen et al., 2010), the resonance magnitude, Q, appears to be somewhat larger at more dorsal locations. This trend is evident at resting and at more depolarised potentials although the effect is very small and only occasionally significant (Boehlen et al., 2010). The perforated patch data, however, does not reveal a gradient at either membrane potential, suggesting that any resonance magnitude gradient is not robust (resting: R^2 = -0.27, p = 0.73; peri-threshold: R^2 = 0.05, p = 0.35) (Figure 3.8 D).

3.4.2 *Peri-threshold theta-frequency activity*

To quantify the dorsal-ventral organisation of peri-threshold theta-frequency activity in perforated patch recordings I again used Lomb analysis to extract the significant frequency components from the peri-threshold activity. I determined the most significant frequency component from the entire final 15 s of the peri-threshold section of each recording and compared this to the average of the most significant frequencies obtained from each of 5 separate consecutive 3 s segments comprising the 15 s section of the trace (Figure 3.9 A,B (left panel)). The different analysis procedures produced different estimations of the most significant frequency, which is expected if the theta-

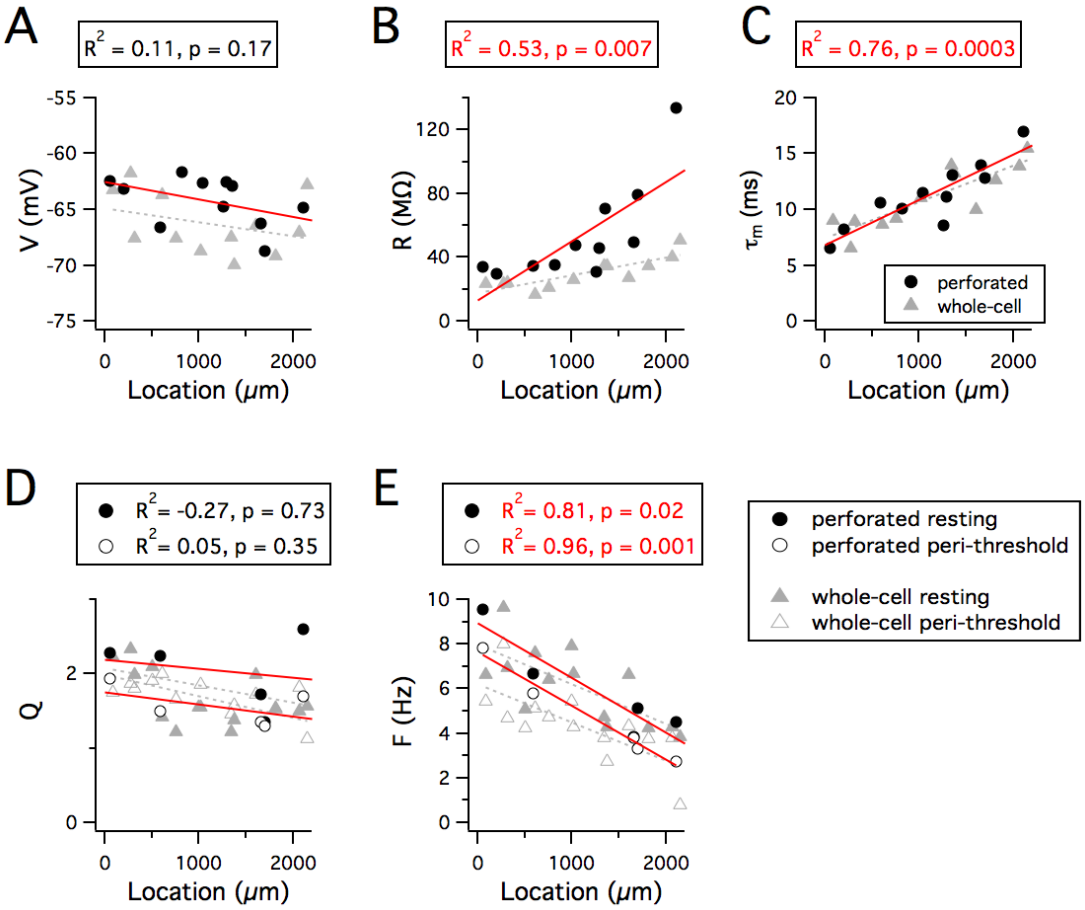

Figure 3.8: **Dorsal-ventral organisation of resting and resonant membrane properties. A–E** Resting membrane potential **(A)**, input resistance **(B)**, membrane time constant **(C)**, resonance amplitude **(D)** and resonant frequency **(E)** are plotted as a function of the location of the recorded stellate cell. Red lines indicate fits to the perforated patch-clamp data. Grey dashed lines indicate fits to the whole-cell data. Adjusted R^2 value and significance of the fit for the perforated patch-clamp data are stated above each plot. The R^2 and significance values for fits of the whole-cell data are as follows: V, R^2 = 0.04, p = 0.24; R, R^2 = 0.59, p = 0.0009; τ_m, R^2 = 0.64, p = 0.0003; Q_{rest}, R^2 = 0.22, p = 0.052; Q_{peri}, R^2 = 0.006, p = 0.32; F_{rest}, R^2 = 0.46, p = 0.005; F_{peri}, R^2 = 0.5, p = 0.003. Location refers to distance from the dorsal border of the MEC.

frequency activity exhibits unstable transient power in the theta band. However, the most significant frequencies followed dorsal-ventral gradients, with higher frequencies at more dorsal locations, in both the 15 s section (R^2 = 0.64, p = 0.002; Figure 3.9 A) and the 5 × 3 s trace segments (R^2 = 0.3, p = 0.046; Figure 3.9 B (left panel)). The range of the most significant peaks obtained from the 5 × 3 s segments was greater dorsally, indicating that cells at more dorsal locations can produce peri-threshold activity that spans a wider range of frequencies (R^2 = 0.37, p = 0.03, Figure 3.9 B (right panel)).

Measuring all significant frequency components from the 5 × 3 s segments shows that the average number of significant frequencies displayed by each cell in each 3 s segment does not vary with location along the dorsal-ventral axis (R^2 = -0.018, p = 0.39; Figure 3.9 C). Similar to the gradient in the most significant frequency, the mean of all significant frequencies across all segments from each cell also follows a dorsal-ventral gradient (R^2 = 0.68, p = 0.001) and there is a non-significant dorsal-ventral trend in the range of significant frequencies present in the 3 s segments (R^2 = 0.17, p = 0.11).

These data are consistent with the idea that peri-threshold activity reflects stochastic membrane potential fluctuations and suggests that the greater range of frequencies present in dorsal cells are due to a relatively increased presence of high-frequency components. Moreover, these data and analysis indicate that multiple significant frequency components are simultaneously present in peri-threshold activity throughout the dorsal-ventral extent of the MEC.

3.4.3 *Patterns of action potential output*

Spike clustering

I found that stellate cells exhibit a dorsal-ventral gradient in their pattern of action potential firing (Figure 3.10 A–B). This organisation of stellate cell firing patterns has not previously been described. With perforated patch-clamp recordings I found that, although spike clustering remains high in stellate neurons along the full dorsal-ventral extent of the MEC (Figure 3.10 A), the frequency with which spikes occur within clusters follows a gradient (Figure 3.10 B).

In contrast, I found that in whole-cell recordings spike clustering appears to be reduced in more ventral cells, leading to the emergence of a gradient in P_C (Figure 3.10 A). The dependence of P_C on location found with whole-cell recordings is consistent with a strong correlation between the AHP and clustering found using in whole-cell recordings from HCN1 knockout animals and pharmacological block of I_h (Nolan

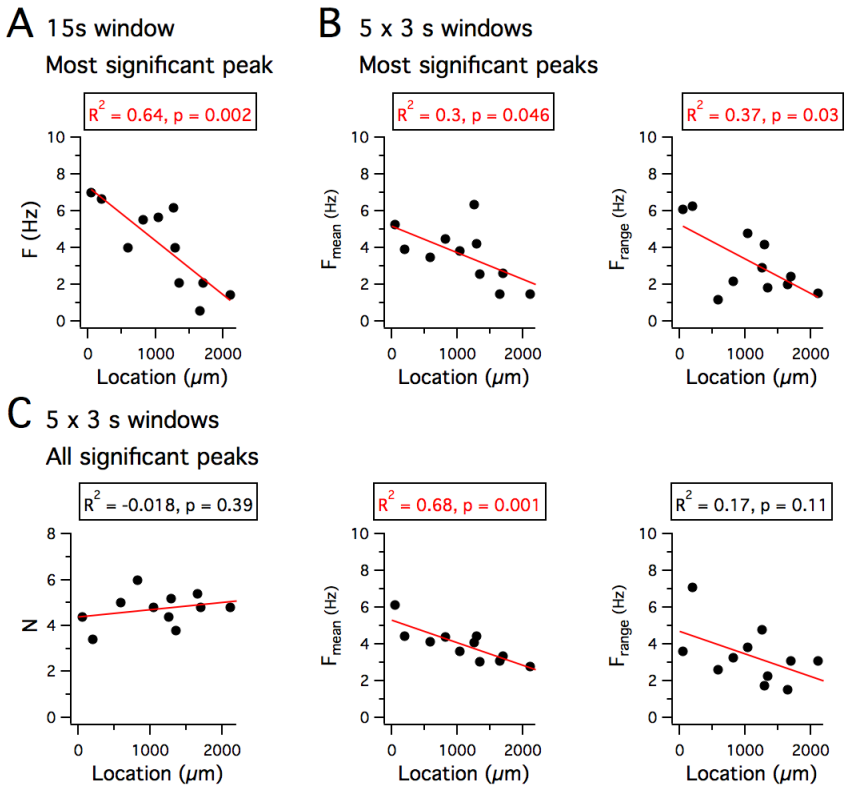

Figure 3.9: **Dorsal-ventral organisation of theta-frequency activity. A** The frequency of the most significant peak in a Lomb periodogram of 15 s of peri-threshold membrane potential activity is plotted as a function of the location of the recorded neuron. **B** The mean frequency (left) and the range of frequencies (right) of the most significant peak of Lomb periodograms, obtained from five consecutive 3 s duration segments of peri-threshold activity, is plotted as a function of the location of the recorded neuron. **C** The number of significant peaks (left), the mean frequency (middle) of all significant peaks, and the range of frequencies of all significant peaks (right), obtained from five consecutive 3 s duration segments of peri-threshold activity, plotted as a function of the location of the recorded neuron. Data analysed were from 5 s to 20 s after the onset of the largest amplitude current step that did not trigger action potential firing. Adjusted R^2 value and significance of the fit for the perforated patch-clamp data are stated above each plot. Location refers to distance from the dorsal border of the MEC.

et al., 2007) and when the AHP is reduced using dynamic clamp (Fernandez and White, 2008). In neither recording condition was the number of spikes per cluster dependent on location (Figure 3.10 C).

The absence of the spike clustering gradient from perforated-patch recordings suggests wash-out during whole-cell recordings of a factor that promotes clustered patterns of activity in ventral cells. One possible explanation is that rundown during whole-cell recordings causes a shift in the voltage dependence of HCN channels that reduces their influence on the AHP.

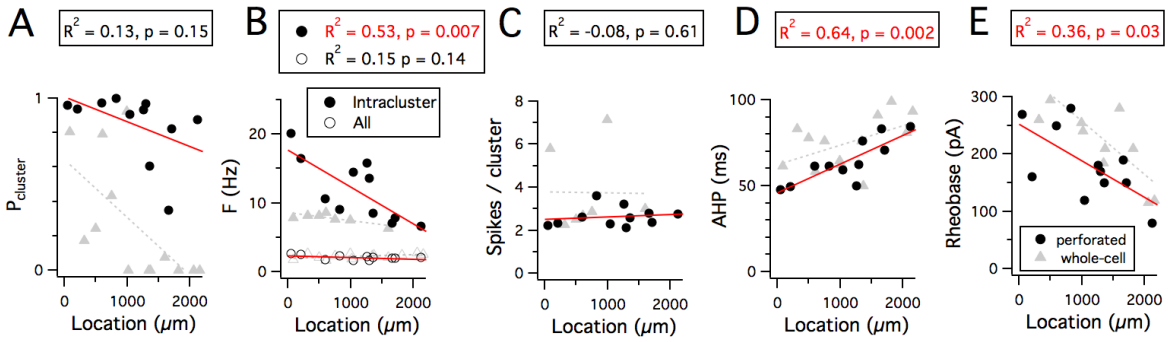

Figure 3.10: **Dorsal-ventral organisation of firing properties. A** Probability that a spike is part of a cluster. **B** Frequency of spikes throughout the 15 s duration analysis window (open symbols) or within a cluster (closed symbols). **C** Number of spikes per cluster. **D** Duration of the action potential after-hyperpolarisation. **E** Rheobase. All data are plotted as a function of the location of the recorded neuron. Data analysed were from 5 s to 20 s after the onset of the current steps that triggered action potential firing at frequencies in the range 1–3 Hz. Adjusted R^2 value and significance of the fit for the perforated patch-clamp data are stated above each plot. The R^2 and significance values for fits of the whole-cell data are as follows: $P_{cluster}$, R^2 = 0.35, p = 0.02; $F_{intracluster}$, R^2 = 0.56, p = 0.03; F_{all}, R^2 = 0.19, p = 0.08; Spikes/cluster, R^2 = 0.38, p = 0.08; AHP, R^2 = 0.19, p = 0.08; Rheobase, R^2 = 0.61, p = 0.0009. Location refers to distance from the dorsal border of the MEC. Perforated patch data are black circles, whole-cell data are grey triangles.

AHP gradient

Because the AHP mediates spike clustering (Nolan et al., 2007; Fernandez and White, 2008) differences in spike-clustering frequency should be accompanied by changes in the AHP. This is supported by whole-cell recordings which show that the AHP duration is shortest in more dorsal cells and increases for cells at progressively more ventral locations (Boehlen et al., 2010). In line with this finding, I also found a gradient in the AHP duration with perforated patch recordings (Figure 3.10 D).

Rheobase gradient

The threshold-current required to initiate action potential firing (rheobase) also follows a dorsal-ventral organisation (Garden et al., 2008; Boehlen et al., 2010). This organisation is maintained in perforated patch-clamp and whole-cell recordings (Figure 3.10 E). The organisation of the threshold-current is at least in part explained by the lower input resistance of dorsal compared to more ventral neurons, resulting from their higher density of leak potassium and HCN channels (Garden et al., 2008).

3.5 DISCUSSION

3.5.1 *Evaluating stellate cell intrinsic properties in light of perforated patch data*

Accurate characterisation of the intrinsic properties of stellate cells is important for understanding their contribution to circuit function. Previous data may not be reliable due to the uncertainties associated with data obtained using sharp electrode and whole-cell patch-clamp recording methods. I discuss here how the new perforated patch-clamp data supports earlier characterisations of some of the intrinsic excitable properties of stellate cells and resolves some inconsistencies between data obtained with the different recording methods and yields novel insights.

Key results confirmed by perforated patch recording

Many of the perforated patch recordings described above reinforce data obtained with sharp electrode and whole-cell recordings. In these cases, we can be confident that the phenomena under examination are real and not an artefact of the recording method.

The presence of dorsal-ventral gradients in input resistance and membrane time constant, and the absence of a resting membrane potential gradient, are evident in perforated patch, whole-cell (Giocomo et al., 2007; Garden et al., 2008; Boehlen et al., 2010) and sharp electrode (Boehlen et al., 2010) experiments. These data can are explained by dorsal-ventral gradients in the density of HCN1 channels that mediate the I_h current and potassium leak channels (Garden et al., 2008).

Frequency selectivity was similar in perforated patch and whole-cell recordings, with neither the resonant frequency nor resonance strength affected by recording method. Both F_{Z-max} and Q values are consistent with previous whole-cell recordings (Nolan et al., 2007). In contrast, while sharp electrode recordings produce Q values consistent with whole-cell and perforated patch data, they appear to over-estimate F_{Z-max} (Haas, 2002; Schreiber et al., 2004; Erchova et al., 2004; Boehlen et al., 2010). Nevertheless, perforated patch, whole-cell (Giocomo et al., 2007; Boehlen et al., 2010) and sharp electrode recordings (Boehlen et al., 2010) all reveal robust dorsal-ventral differences in F_{Z-max}. The frequency–phase relation appears similar in all recording methods (Erchova et al., 2004; Nolan et al., 2007).

The perforated patch recordings also reveal spontaneous peri-threshold theta-frequency membrane potential activity that qualitatively resembles activity reported in whole-cell (Dickson et al., 2000b; Giocomo et al., 2007; Nolan et al., 2007; Boehlen et al., 2010; Dodson et al., 2011; Yoshida et al., 2011) and sharp electrode (Alonso and Llinás, 1989; Alonso and Klink, 1993; Erchova et al., 2004; Boehlen et al., 2010) studies, although as

before, the sharp electrode studies report higher frequency fluctuations (Alonso and Llinás, 1989; Erchova et al., 2004; Boehlen et al., 2010). Importantly, Lomb analysis reveals that perforated patch activity is not more rhythmic than data obtained with whole-cell recordings (Dodson et al., 2011). As with the whole-cell recordings, the theta-frequency activity is not driven by a true oscillatory process, despite the apparently sustained peaks in the theta-frequency range in long-windowed spectrograms (e.g. Yoshida et al., 2011). Not only does Lomb analysis clearly show that separate trace segments typically contain multiple significant frequencies but it also shows that these frequency components (including the most significant frequency peaks) shift between consecutive trace segments. This indicates that the peri-threshold theta-frequency activity is not a stable oscillation.

Combined with the observation that theta-frequency activity of the type exhibited by perforated patch recordings can be explained by the filtering of stochastic membrane currents (Dodson et al., 2011), the absence of stable spectral peaks argues against mechanisms of theta-frequency activity generation that rely on interaction of deterministic conductances (e.g. Dickson et al., 2000b; Fransén et al., 2004). The ability of artificial stochastic, but not deterministic, Na_P currents (reintroduced using dynamic clamp) to rescue peri-threshold activity (Dorval and White, 2005) also supports this view. In addition, removing I_h does not necessarily abolish peri-threshold activity (Haas et al., 2007; Nolan et al., 2007). The disappearance of peri-threshold activity during pharmacological block of I_h with ZD7288 (Dickson et al., 2000b) can be explained by the non-specific effects of ZD7288 (including an effect as a Na^+ channel antagonist (Wu et al., 2012)). Therefore, instead of playing a deterministic role in generating peri-threshold activity, I_h may regulate peri-threshold frequency components by either preferentially filtering out more low frequency components in cells with large I_h conductances (Nolan et al., 2007) or possibly by differentially restricting the membrane potentials that can be reached before spiking is initiated.

Despite the absence of a true oscillatory signal, the frequency characteristics of the perforated patch peri-threshold activity do have a dorsal-ventral organisation. Similar to a previous Lomb analysis of whole-cell recordings (Dodson et al., 2011), the most significant frequency, the mean of all significant frequencies and the range of significant frequencies are all higher at more dorsal locations. This is consistent with the dorsal-ventral gradient in I_h removing low frequency components in more dorsal cell. When 'characteristic' frequencies are calculated by selecting autocorrelations with the largest peaks, the 'frequency' of peri-threshold activity also follows a dorsal-ventral gradient (Giocomo et al., 2007; Giocomo and Hasselmo, 2008, 2009; Dodson et al., 2011; Yoshida et al., 2011). Sharp-electrode recordings also exhibit a dorsal-ventral

frequency gradient (Boehlen et al., 2010). All recording methods therefore show a dorsal-ventral frequency gradient.

Finally, the shape of the action potential spike appears similar between whole-cell and perforated patch recordings, suggesting that any conductances affected by washout are not involved with spike generation and fast repolarisation. Similar to previous whole-cell recordings the duration of the spike AHP follows a dorsal-ventral gradient.

Novel insights from perforated patch recordings

The perforated patch data also differ in important respects from the data obtained using sharp electrode and whole-cell recording methods. Relative to these other recording techniques, perforated patch recordings reveal that stellate cells are more excitable, have resonance strength that does not vary across dorsal-ventral axis of the MEC, have a substantially shorter AHP and exhibit dramatically increased spike clustering. In addition, the perforated patch data also demonstrate a novel gradient in intra-cluster spike clustering frequency. These observations thus provide important new insights into properties of intrinsic excitable properties of stellate cells that may have implications for MEC circuit function.

1. Stellate cells have a significantly higher resting membrane potential in perforated patch recordings relative to the accompanying and previous whole-cell recordings (Nolan et al., 2007). The direction of this difference is opposite to that between whole-cell and sharp recordings in rat (Boehlen et al., 2010) where whole-cell recordings were more depolarised. This means it is likely that both whole-cell and, to an even larger degree, sharp electrode recordings overestimate the degree of voltage deflection required to induce spiking from rest and so may underestimate the excitability of stellate cells.

2. Perforated patch recordings also reveal that stellate cells have a higher input resistance than suggested by the accompanying and previous whole-cell data (Nolan et al., 2007). Since input resistance is significantly higher in whole-cell relative to sharp electrode recordings (Boehlen et al., 2010) this also suggests that stellate cells are more excitable than previously described, as they would require less current input to attain a given voltage deflection.

3. Where the existence of a dorsal-ventral resonance strength gradient has been suggested by whole-cell and sharp electrode data (cf. the new whole-cell data and Boehlen et al. (2010)) the effect is small and the relationship is not significant at both depolarised and resting potentials. In contrast, the perforated patch data do not reveal a resonance strength gradient at either membrane potential, suggesting that even if

a gradient does exist it is unlikely to play an important role in MEC microcircuit function.

4. A major difference between the recording methods is that the duration of the AHP is substantially shorter in perforated patch recordings. The reduction of the AHP duration translates into a higher frequency of spiking within spike clusters, even when overall spiking rates are maintained. Given the similar number of spikes per cluster in the different recording conditions, spike clusters thus appear to be more temporally compact than suggested by whole-cell recordings. The shorter AHP in perforated patch recordings also coincides with much more reliable spike clustering. The probability that any given spike is part of a cluster is much higher (~85%) in perforated patch recordings than in the new and previous whole-cell data (~26–40%) (Nolan et al., 2007).

5. Consistent with the dorsal-ventral gradient in AHP half-duration, the perforated patch recordings reveal a novel gradient in intra-cluster spike frequency. Because I_h promotes repolarisation of the AHP and thereby decreases the duration of the AHP (Nolan et al., 2007; Dudman and Nolan, 2009), the gradient in I_h (Garden et al., 2008) predicts this intra-cluster spike frequency gradient.

6. Despite the I_h and AHP gradient, in perforated patch recordings action potential clustering, P_C, remains robust (P_C = ~0.85) along the entire extent of the MEC. This suggests that the depolarising drive that I_h exerts during and directly after the AHP, which increases the probability of a spike following the AHP and thereby promotes clustered spiking (Nolan et al., 2007; Dudman and Nolan, 2009), is necessary but not always sufficient for robustly clustered spiking.

7. In whole-cell recordings P_C appears to follow a dorsal-ventral gradient. Interestingly, clustering can remain high (P_C > ~0.8) in dorsal cells. This suggests that more ventral cells could either be (i) more prone to the effects of washout of a conductance that promotes clustering or (ii) that because ventral cells have a lower I_h density they are more reliant for high clustering on the presence of a different conductance that is subject to washout.

The time course of rundown of conductances during whole-cell recordings

Spike clustering robustness fades within 2 min of achieving whole-cell configuration and continues to fall throughout the 30 min recordings. This decrease in clustering is accompanied by an increase in the AHP duration. However, the change in the AHP is initiated only after break-in to whole-cell configuration. These observations suggest that clustering could depend on two separate AHP-related conductances with different rates of rundown. The time course of washout of intrinsic excitable properties has been investigated in other cells types (Robinson and Cameron, 2000; Kaczorowski

et al., 2007). When washout does occur, gradual rundown of passive and AHP properties also continues throughout >30 min recordings (Robinson and Cameron, 2000; Kaczorowski et al., 2007).

These results suggest that signalling pathways sensitive to washout during whole-cell recording regulate the firing properties of stellate cells. They also highlight the importance of carefully timing data acquisition during whole-cell recordings – the same properties recorded early and late during a recording session may appear very different, artificially increasing variance and potentially leading to contradictory data sets.

3.5.2 *Implications for MEC microcircuit function*

The intrinsic excitable properties of MEC layer II stellate cells constrain and enable the functional repertoire of the MEC microcircuitry. What impact might the intrinsic properties that are investigated here with perforated patch recordings have on our understanding of how spatial representations are implemented by this microcircuitry?

The perforated patch recordings provide a revised estimate of the input-output function of stellate cells though improved estimates of their resting potential and input resistance. These revised estimates could be important for characterising how readily synaptic inputs integrate to initiate action potential firing (Garden et al., 2008). Because the exact functional connectivity is particularly important in attractor models of MEC circuit function, accurate characterisation of the excitability of stellate cells, including the synaptic integrative properties, will be important for constraining biophysically realistic implementations of this class of model.

Sub-threshold resonance is intact in perforated patch recordings, suggesting that stellate cells are able to selectively amplify theta-frequency inputs *in vivo*, possibly including the modulatory cholinergic (Mitchell et al., 1982) and inhibitory GABAergic (Manns et al., 2001) inputs from the medial septum. In addition, the dorsal-ventral gradient in the resonant frequency, but not the resonance strength, indicates that frequency selectivity works equally well across the entire dorsal-ventral extent of the MEC. The dorsal-ventral gradient in frequency selectivity is suggestive of a role in setting up the grid spacing gradient, but no concrete proposals for a mechanism have been put forward.

Lomb analysis of the perforated patch recordings confirms the transient and stochastic nature of peri-threshold theta-frequency activity (Dodson et al., 2011). Because no single frequency component of the peri-threshold activity is sustained over more than a few seconds, and the peri-threshold activity typically comprises multiple significant frequencies, computational mechanisms that depend on reliable interactions between

stable 'pure' frequencies are untenable. The oscillatory interference mechanism that underpins some models of grid firing fields (e.g. Burgess et al., 2007; Hasselmo, 2008) is one such mechanism - it relies on either (i) precise interactions between the phases of multiple independent slightly out-of-phase oscillations within a single cell to either directly generate interference patterns that form the basis of spiking output (Burgess et al., 2007) or (ii) persistent firing in cells locked to independent single oscillatory frequencies which produce regular synaptic trains in post-synaptic cells that sum to produce spikes when synaptic input from the pre-synaptic cells is in-phase (Hasselmo, 2008). Because there are typically multiple frequencies present in the peri-threshold activity and each individual frequency is maintained only for very short periods, interaction between such signals will fail to produce the reliable interference patterns required by models of this type.

Intrinsic excitable properties of cells are typically investigated *in vitro* in the presence of synaptic blockers to reduce or eliminate synaptic noise. These are very different conditions to those pertaining *in vivo* where cells are subject to synaptic bombardment and neuromodulatory influence (Destexhe et al., 2003). Therefore, one important test for the relevance of intrinsic excitable properties of stellate cells to circuit function is whether they are sustained and effective under *in vivo* conditions. Some properties, like theta-frequency membrane potential activity, can be robust to noisy current inputs, but do not appear to be robust in some high conductance conditions (Fernandez and White, 2008) and recent *in vivo* whole-cell recordings have revealed an absence of theta-frequency activity in stellate cells depolarised with current injection to peri-threshold potentials in resting mice (Schmidt-Hieber and Häusser, 2013). Others, like sub-threshold resonance, can change during cholinergic neuromodulation (Heys et al., 2010) but are also relatively unaffected by noise (Schreiber et al., 2004).

The very robust spike clustering revealed by perforated patch recordings is more suggestive of a functional *in vivo* role than the weak clustering observed during whole-cell recordings (Nolan et al., 2007) as the clustering is more likely to be sustained in noisy conditions. It is not yet clear, however, what the functional role of spike clustering could be. One possibility is that clustering, if sufficiently robust in *in vivo* conditions, maintains the spiking of a cell over a few hundred milliseconds after a spike is initially triggered, for example after entry to a grid field. The dorsal-ventral intra-cluster spike frequency gradient observed with perforated patch recordings may thus contribute the dorsal-ventral organisation of spatially modulated output in MEC, but it is not clear how this would be effected.

Unfortunately, it is not yet known what the conductance and membrane potential variance characteristics of stellate cells *in vivo* are. Studies in other cortical areas

have shown that background activity in the cortex can either be abundant (Destexhe et al., 2003) or sparse (Waters, 2006) and the effects of neuromodulation in the MEC of behaving animals are not well understood. Knowledge of the membrane potential trajectory and conductance changes in stellate cells in behaving animals will therefore contribute greatly to understanding which intrinsic excitable properties can realistically contribute to circuit function and thus shed light on what mechanisms are available to the MEC circuitry for implementing spatial computations.

4

AN OPTOGENETIC INVESTIGATION OF THE FUNCTIONAL ARCHITECTURE OF MEC LAYER II

The majority of work presented in this chapter, with the exception of the data and analyses in shown in Figures 4.8, 4.9 and 4.10 is adapted from or appears in: Pastoll et al. 2013. Feedback inhibition enables theta-nested gamma oscillations and grid firing fields. *Neuron*. 77, 141–154.

4.1 INTRODUCTION

How a neural microcircuit transforms its synaptic input into functionally useful output depends not only on the intrinsic properties of the different types of cells that make up the circuit, but also on the connections between them (Silberberg et al., 2005). Understanding how the MEC layer II produces its characteristic grid firing fields therefore requires understanding the nature of interactions between and within the distinct populations of cells that comprise the layer II microcircuit (Witter and Moser, 2006).

Despite the substantial recent interest in the MEC and the abundance of models addressing the computations it is hypothesised to implement, surprisingly little is known about its functional architecture. Elucidating this architecture is necessary both for constraining models of MEC layer II function and for suggesting new computational capabilities and experiments to investigate them, and is thus of critical importance for the development of our knowledge of spatial computation.

4.1.1 *Classification and identification of cell types in the MEC*

To functionally dissect a neural microcircuit, it is necessary to identify the different cells classes that it comprises, each of which may make distinct contributions to processing. Establishing an exhaustive catalogue of cells organised by morphology, molecular expression profile and physiology is a major task and may not be complete even for the most well studied circuits.

A number of glutamatergic and GABAergic cell types have been identified in layer II of the MEC using anatomical techniques (Canto et al., 2008). Neuron types that are distinguished by anatomical features are expected to have gene expression differences

and typically exhibit important electrophysiological differences. However, anatomical methods do not provide essential functional information and may not always distinguish anatomically similar but physiologically distinct cell types. These are important limitations as the role that a specific type of neuron plays in microcircuit processing is determined by its physiology and its physiological effect on other cells in the network. Electrophysiological data is therefore key for identifying cells types in the MEC and for understanding their functional role in circuit computations.

Many cells types in layer II of the MEC remain electrophysiologically poorly characterised. Two important exceptions are the principal projection stellate cells (Alonso and Llinás, 1989) and pyramidal cells (Alonso and Klink, 1993) which have received much attention and have electrophysiological properties that are relatively well understood. However, the electrical properties of interneurons in layer II have received very little attention. Fast spiking 'basket' interneurons with somata in layer II (Jones and Bühl, 1993) have been identified, but the because the anatomy of cells with a fast spiking phenotype has not been systematically investigated, it is possible that the ability to maintain sustained rapid firing (Jones and Bühl, 1993; Cunningham et al., 2003; Middleton et al., 2008) could be common to heterogenous interneuron populations within layer II that may not share other electrophysiological properties. Furthermore, interneurons with other distinct morphologies and molecular expression patterns with somata in layer II have not been physiologically characterised (at least to my knowledge), and therefore the electrical properties and identity of many important components of the layer II microcircuitry remain completely unknown.

4.1.2 *Functional connectivity between physiologically identified cell types*

Mapping the functional connections between different cell types is critical for understanding circuit function. Activating synaptic pathways with electrical stimulation has enabled investigation of the functional connectivity of afferent projection neurons from other areas to the MEC as well as interlaminar connectivity within the MEC (e.g. Jones, 1994; Gloveli et al., 1997) but because field electrical stimulation indiscriminately activates all cell types local to the stimulation location, this technique cannot be used to investigate connectivity within the local layer II microcircuit. For a long time paired intracellular recordings between electrophysiologically identified cells have therefore been the only reliable method for establishing local connectivity within layers. Recently, however, the advent of techniques that permit selective activation of genetically defined populations of cells (Luo et al., 2008) has promised to rapidly accelerate the mapping of neural connectivity, but these techniques have yet to be employed to investigate the connectivity of layer II microcircuitry.

Evidence for connections between excitatory cells in layer II

The possibility of robust recurrent excitation between stellate cells in layer II has received much attention, initially because of the potential for the superficial layers of the MEC to trigger and propagate epileptiform activity to the hippocampus (Stanton et al., 1987) and more recently because direct recurrent excitation between excitatory cells in layer II has been hypothesised to play a critical role in the generation of grid firing fields (Fuhs and Touretzky, 2006; Guanella et al., 2007; Navratilova et al., 2012). The ubiquity of recurrent excitation between principal cells in other cortical circuits (Chapeton et al., 2012) has lent credence to this idea.

However, the evidence for recurrent excitation between principal cells in layer II of the MEC remains inconclusive. Recurrent excitation between principal cells in other areas is reliably revealed with paired *in vitro* intracellular recordings, for example in neocortex (Mason et al., 1991; Deuchars et al., 1994; Song et al., 2005), the hippocampus (Miles and Wong, 1986) and in deeper layers of the MEC (Dhillon and Jones, 2000). However an *in vitro* study using paired intracellular sharp electrode recordings between electrophysiologically identified stellate cells (Dhillon and Jones, 2000) did not find any evidence of connected stellate cells, suggesting that layer II of the MEC may be an important exception to this trend. Nevertheless, because it is possible that slicing in a particular plane may artificially reduce the number of connections in the slice, and because visually guided intracellular recordings may lead to biased sampling of this small pool of connections, these data do not completely rule out the possibility that recurrent connections do exist between stellate cells.

Another complication is that other indirect data appears to support the existence of recurrent excitatory connectivity in layer II. First, independent studies using photo-uncaging of glutamate (Kumar et al., 2007; Beed et al., 2010) in layer II reported excitatory responses onto stellate cells and second, *in vivo* unit recordings revealed peaks at short latencies in the firing probability cross-correlations between simultaneously recorded putative excitatory cells, indicating the presence of mono-synaptic excitatory connections (Quilichini et al., 2010). However, because neither the identity of the photo-activated neurons during the photo-uncaging experiments nor the exact identities of the *in vivo* putative excitatory cells were definitively established, these data do not provide conclusive evidence that connections exist between stellate cells and may instead reflect connections originating from other cell types, including but not limited to pyramidal cells in layer II.

Therefore, despite the striking failure to find connected pairs of stellate cells with paired intracellular recordings, because of potential slice preparation shortcomings and biased cell sampling, hints of recurrent stellate connections by indirect techniques, and the prevalence of connections between excitatory cells in other cortical

areas, it remains unclear whether stellate cells do indeed form functional connections with each other. Definitively addressing this issue is therefore an important first step in dissecting the layer II microcircuit.

Connections between excitatory and inhibitory cells

Very little is known about the origin of inhibitory synapses onto stellate cells. Electrical stimulation of deeper layers in the MEC and parahippocampal regions elicits strong GABA mediated IPSPs onto stellate cells (Jones, 1994; Gloveli et al., 1997; Heinemann et al., 2000). However, the identity of the interneurons providing this inhibition is not clear and the IPSP responses are heterogenous, suggesting that they may arise from distinct types of interneurons, possibly with somata in different layers, further complicating interpretation of this data.

Very few studies have investigated excitation onto interneurons in layer II. Jones (1994) described heterogenous EPSPs onto fast spiking interneurons arising from electrical stimulation, but it is unclear if there is any contribution from excitatory cells in layer II. Middleton et al. (2008) recorded EPSPs during bath application of kainate, but again, the exact origin of these inputs is unclear. Other interneurons types have not been investigated.

The functional architecture of layer II thus remains largely unknown. Because of its importance for spatial processing in the MEC, application of experimental methods that permit rapid and reliable dissection of the microcircuitry in layer II could make a substantial contribution to our understanding of MEC function.

4.2 METHODS

To investigate connectivity between and within different cell populations in layer II, whilst avoiding the shortcomings associated with paired intracellular recordings and other indirect methods, I used an optogenetic strategy. Targeting transgenic light sensitive ion channels (Nagel et al., 2003) to genetically defined cell types permits selective light-driven activation of distinct cell types within a local microcircuit (Luo et al., 2008) and this enables investigation of the functional effects of activation of known cell types on recorded cells local to the stimulation site and therefore enables rapid and reliable dissection of neural microcircuits in transgenic mouse lines.

Thy1::ChR2-YFP mice express ChR2 in MEC layer II cells

To interrogate the layer II MEC microcircuitry I used a transgenic Thy1::ChR2-YFP mouse line (Arenkiel et al., 2007; Wang et al., 2007). To produce this mouse line

regulatory elements from the mouse Thy1.2 gene were fused with cDNA encoding a ChR2-YFP fusion protein to produce a Thy1-ChR2-YFP construct. Copies of this construct were then inserted into the genome by pronuclear injection (Wang et al., 2007). These mice thus express ChR2 under the control of a Thy1 promoter and the resulting ChR2 expression pattern can be visualised using fluorescence imaging.

The exact pattern of ChR2 expression depends on the locations of integration of Thy-ChR2-YFP constructs into the genome due to the influence of nearby regulatory sites. Because the locations of integration of the transgene constructs into the genome is not controlled during transgenesis, multiple founder mice lines exist (Arenkiel et al., 2007; Wang et al., 2007). I used founder line 18, which is backcrossed onto a C57-BL/6 background (Wang et al., 2007) and is available as from The Jackson Laboratory. Because expression of Thy1 is developmentally regulated (Morris, 1985) I only used adult (7-9 week) mice for experiments.

Adult Thy1::ChR2-YFP line 18 mice (hereafter ChR2-positive mice) express ChR2 in diverse cortical areas including the MEC (Figure 4.1 A). Because ChR2 is not expressed in all cell types, cortical ChR2 expression is often limited to distinct cortical layers. In the MEC ChR2 is expressed in cells with somata in layer II, but not layer I or layer III (Figure 4.1 B, C). This expression pattern is convenient because it enables light-induced activation of cells in layer II while avoiding any off-target effects from undesired activation of cells with somata in adjacent layers.

Targeted illumination of layer II cells

To locally activate a population of layer II cells I used a collimated 470 nm blue LED with user-controllable light intensity as a light source. I restricted the collimated light beam to approximately 90 µm by setting the field iris diaphragm to its minimum aperture. This narrow beam was then directed by a mirror in the filter housing onto the slice through a 40X objective (see Chapter 2 for further details). The light beam approximately covered the rostro-caudal width of layer II (Figure 4.1 C). Due to light scattering, nearby surrounding neuropil also received illumination. Because of the lack of ChR2 expression in layers I and III, this setup was therefore capable of activating cells in layer II while avoiding activation of cells in layers I and III (no ChR2 expression) and layer V (too far away). I was thus able to investigate the synaptic effects of activating only cells with somata in layer II of the MEC.

Electrophysiological identification of ChR2-positive cell types in layer II

To functionally dissect layer II microcircuitry I needed to determine the origin of light induced synaptic input onto recorded cells. I therefore needed to identify the cell types in layer II that were activated by the light stimulus. To determine which

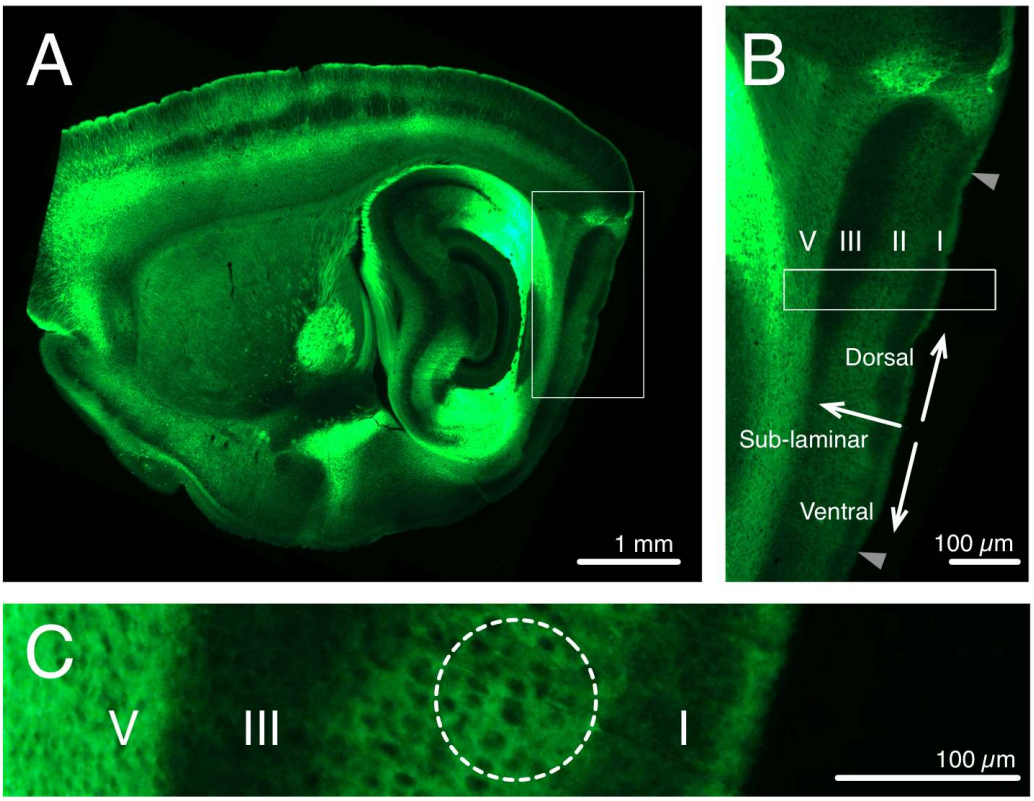

Figure 4.1: **Thy1::ChR2 expression. A** Sagittal section from an adult Thy1-ChR2-YFP line 18 mouse. YFP fluorescence indicates areas of ChR2 expression. **B** Close up of MEC (from the rectangular area in **(A)**). Grey arrowheads indicate dorsal and approximate ventral borders of the MEC. Roman numerals indicate layers. Layer IV is not marked as it contains very few cell bodies. **C** Detail from **(B)** showing layer specific expression of ChR2 in the MEC. In contrast to layer II, layers I and III do not contain YFP positive somata. The dotted circle indicates the approximate size of the stimulating light beam. Stellate cells are activated in a region of tissue substantially larger than the light beam cross-section. The rectangles in **(A)** and **(B)** indicate the external borders of **(B)** and **(C)** respectively.

cells types express ChR2 I made whole-cell patch-clamp recordings from cells and identified their cell type based on intrinsic electrophysiological properties and then tested their response to illumination with 470 nm light.

I patched cells guided by DIC illumination instead of by YFP fluorescence. The entire fusion ChR2-YFP protein is transported to the membrane (including dendrites) so the neuropil in layer II is saturated with the YFP fluophore and this prevents visualisation of somatic morphology (see Figure 4.1) with fluorescent imaging. In addition, DIC guided patching reduces bias against cell selection based on ChR2 expression.

In mice, layer II of the MEC comprises ~70% stellate cells and ~15% pyramidal cells with the remainder made up of fast spiking interneurons and other interneuron types (Gatome et al., 2010). I identified stellate cells by non-adapting spike trains with

clustered firing patterns (Figure 4.2 A) upon depolarisation with DC current injection, a prominent sag in response to sub-threshold current steps and a resting potential in the -60 – -70 mV range (Figure 4.2 D) and their characteristic spike and after-hyperpolarisation shapes (Figure 4.2 E) (Alonso and Llinás, 1989; Alonso and Klink, 1993). I identified fast-spiking (FS) interneurons by their ability to sustain rapid (>100 Hz) spike trains (Figure 4.2 B), absence or near absence of sag, low input resistance and hyperpolarised resting potential (Figure 4.2 F) and narrow action potentials with a short very hyperpolarised AHP (Figure 4.2 G) (Jones and Bühl, 1993; Middleton et al., 2008). Pyramidal cells exhibit non-clustered spike trains (Figure 4.2 C), low levels of sag and high input resistances relative to stellate cells (Figure 4.2 H) as well as characteristic spike shapes with a a prominent fAHP and a shallow AHP (Figure 4.2 I) (Alonso and Klink, 1993).

All recorded stellate cells (n = 235) responded robustly to illumination (Figure 4.2 J shows an example response to a light stimulus with a ramped intensity) as did all FS interneurons (n = 41) (Figure 4.2 K). Pyramidal cells did not respond to illumination (n = 11). Pyramidal were also not synaptically driven to fire during illumination - their membrane potential instead underwent a minor hyperpolarisation, suggesting a net inhibitory light-evoked synaptic influence (Figure 4.2 L). The majority of the very few cells in layer II that I was unable to conclusively identify based on electrophysiological criteria also did not respond directly to light.

A large majority of the stellate and FS interneuron depolarising response to light was mediated by the ChR2 photocurrent (also see Chapter 5) and cells were still driven to spike in the presence of excitatory synaptic blockers NBQX and AP5. To isolate the photocurrent I recorded in voltage clamp in the presence of NBQX and AP5 to block excitatory synaptic transmission and Picrotoxin and CGP55845 to block inhibitory transmission. Both stellate and FS interneurons exhibited robust photocurrents that scaled with the light intensity (Figure 4.2 M, N) whereas pyramidal cells did not (Figure 4.2 O).

4.3 RESULTS

4.3.1 *Stellate cells innervate fast spiking interneurons but not other stellate cells*

What synaptic inputs do cells experience during optogenetic activation of the layer II microcircuitry? To investigate the synaptic responses in stellate cells and fast spiking interneurons produced by optogenetic activation of a population of stellate cells, I first recorded synaptic currents in stellate cells and fast spiking interneurons in

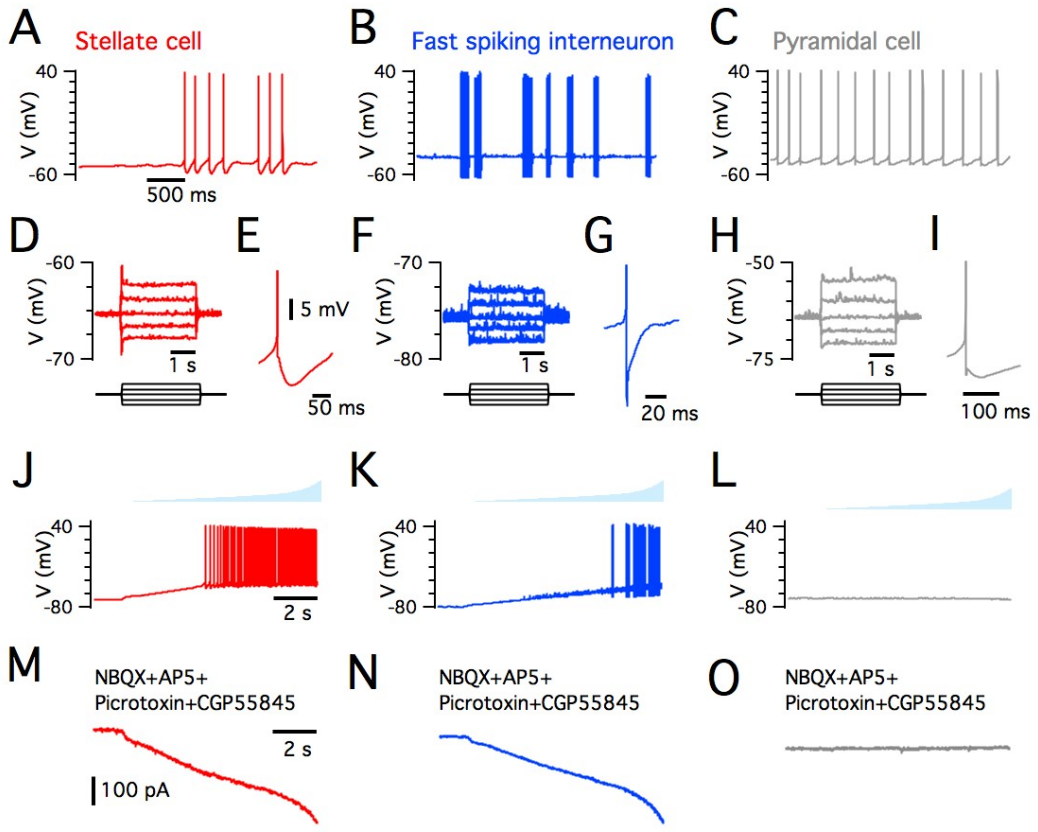

Figure 4.2: **Cell type specific expression of ChR2 in layer II. A–I** Identification of cell type by intrinsic electrophysiological properties. **A–C** Characteristic firing properties of different cell types in response to steady state depolarising injected current. Stellate cells exhibit clustered spiking at low firing rates. **(A)**. FS interneurons can sustain rapid (>100 Hz) firing (here shown in groups of action potentials) **(B)**. Pyramidal cells do not exhibit clustered spiking at low firing rates **(C)**. **D,F,H**. Characteristic IV properties for each cell type. Plots show voltage trace series (upper) in response to sub-threshold current steps from -80 to +80 pA in 40 pA increments (lower). Stellate cells display prominent sag responses, have ~20–80 MΩ input resistance and have a resting potential between -60 and -70 mV **(D)**. FS interneurons have no substantial sag, low input resistance and have hyperpolarised resting potentials (typically between -70 and -80 mV) **(F)**. Pyramidal cells have minor, slower sag, high input resistance and resting potentials between -60 and ~-65 mV **(H)**. **E, G, I** Characteristic spike shape for each cell type. Stellate cells have deep, slow AHPs **(E)**. FS interneurons have narrow spikes, with short, very deep AHPs **(G)** Pyramidal cells have shallow slow AHPs with a prominent fast AHP **(I)**. **J–O** Cell type specific response to illumination with 470 nm blue light. **J–L** Voltage response of cells to illumination with light intensity ramps up to ~15 mW/mm^2 in control conditions. Stellate cells **(J)** and FS interneurons **(K)** are activated by the light and fire action potentials. Pyramidal cells are not activated by the light and are not synaptically driven to fire **(L)**. **M–O** Photocurrents revealed in voltage clamp in the presence of Glutamate and GABA antagonists (holding potential -70 mV). Stellate cells **(M)** and FS interneurons **(N)** have large inward photocurrents with magnitudes that track the light intensity. Pyramidal cells have no photocurrent **(O)**.

control conditions and during subsequent block of synaptic inhibition to remove the influence of light-driven activation of GABAergic interneurons.

Stellate cells spike robustly during light ramps

I used a ramped light stimulus to drive stellate cells to spike. To quantify the effect of the illumination intensity on stellate cell firing rate I wrote a MATLAB script to calculate firing rate in a series of 500 ms windows with 100 ms offsets between the centres of each window. In control conditions stellate cells (n = 61) typically started spiking midway through the ramp stimulus and fired at an average of ~12 Hz at the peak irradiance (~12 mW/mm^2) of the light ramp (Figure 4.3 A, C). The ramped light stimulus therefore ensured that stellate cells would be sufficiently activated to provide reliable input to connected cells in the network.

To investigate how spike output during the ramped light stimulus depended on inhibitory synaptic transmission I blocked inhibitory GABAergic synaptic transmission with Picrotoxin and CGP55845 (Figure 4.3 B). Comparing the firing rates of stellate cells recorded before and after block of synaptic inhibition (n = 8) shows that although stellate cell spike output increased towards the end of the ramp by ~3 Hz when inhibition was blocked (Figure 4.3 D), repeated measures ANOVA with factors for light intensity (5 levels) and pharmacological condition (2 levels) revealed no significant difference between the spiking profiles in the different pharmacological conditions. Light intensity significantly influenced stellate cell spike rates ($p = 0.009$) but pharmacological condition did not ($p = 0.63$) and there was no interaction between the factors ($p = 0.51$) indicating that spike output remained largely similar in control and inhibition blocked conditions for the duration of the stimulus (Figure 4.3 B, D). Stellate cells were thus driven to spike robustly during the ramped stimulus before and after block of inhibition.

Stellate cells are dominated by inhibition and fast spiking interneurons by excitation

To observe the light-driven synaptic inputs to stellate cells and fast spiking interneurons I recorded in voltage clamp with a holding potential of -50 mV to reveal excitatory and inhibitory synaptic currents. I maintained a holding potential of -50 mV (between the reversal potential of glutamate (~0 mV) and $GABA_A$ (~-65 mV)) to ensure sufficient driving force to reveal inward excitatory synaptic currents and also, at least in the soma and the soma-proximal region of the dendritic tree where the space clamp is adequate, outward inhibitory synaptic currents (Williams and Mitchell, 2008)).

Stellate cells (n = 58) in control condition received abundant inhibitory synaptic inputs, with frequency and magnitude that scaled with the light intensity (Figure 4.3 E) whereas excitatory input appeared to be extremely minimal. In striking contrast,

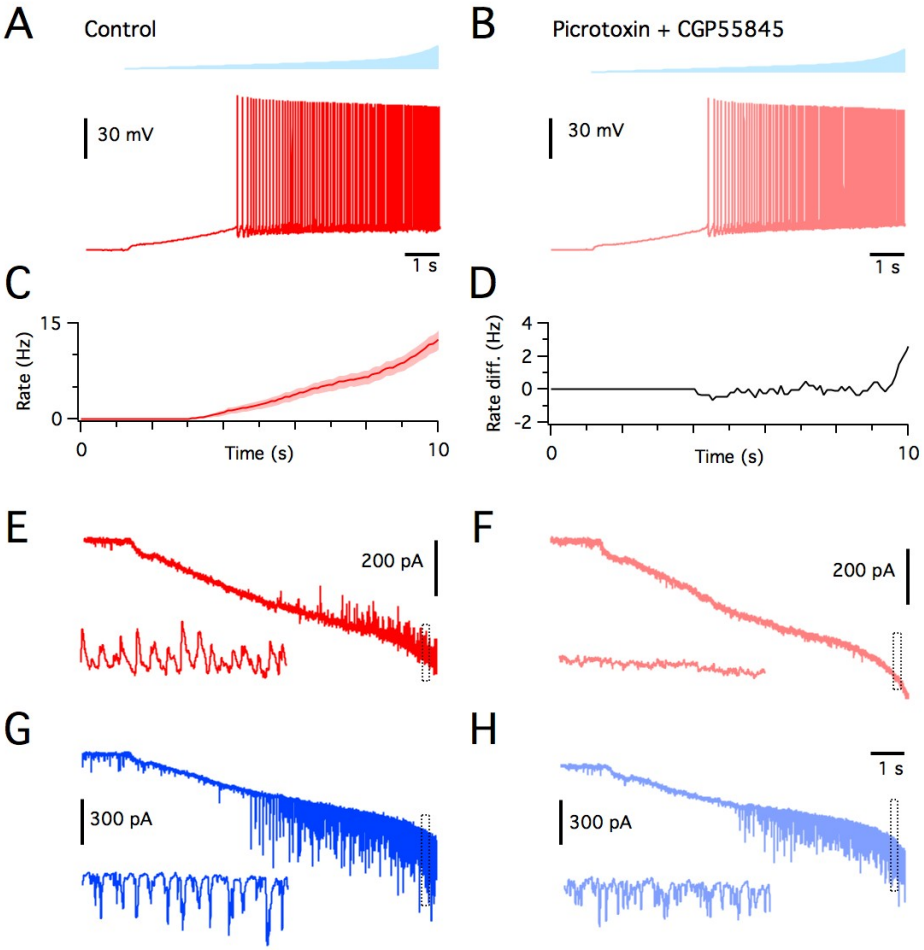

Figure 4.3: **Inhibition dominates synaptic inputs to stellate cells during optogenetic activation of layer II. A–D** Light ramps induce spiking in stellate cells. Example stellate cell response to light intensity ramp in control conditions **(A)** and during block of inhibition with $GABA_A$ and $GABA_B$ receptor antagonists Picrotoxin and CGP55845 respectively **(B)**. **C** Average stellate cell firing rate during light ramps (n = 61). **D** The difference in average firing rates increases at high light intensities after block of inhibition (n = 8). **E–H** Example voltage clamp recordings (holding potential -50 mV) from a stellate cell and interneuron pair before and after block of inhibition. Insets are expansions of the areas inside the dotted outlines in each trace. Outward (upward) inhibitory synaptic currents are evident in stellate cells in control conditions **(E)** but not during block of inhibition **(F)** where synaptic activity is dramatically reduced. FS interneurons exhibit large inward synaptic currents both before **(G)** and after **(H)** block of inhibition, indicating that excitation is still intact in the slice.

recordings from FS interneurons (n = 16) revealed an abundance of inward synaptic currents, with onset that coincided with the onset of stellate cell spiking (Figure 4.3 G). To examine excitatory transmission onto cells in the absence of interference from GABAergic inhibitory input I blocked inhibitory synaptic transmission in a subset of recordings by bath applying Picrotoxin and CGP55845. Block of inhibition dramatically reduced synaptic activity in SCs (Figure 4.3 F; same cell as in (E)), whereas synaptic activity in fast spiking interneurons remained robust, with large inward excitatory currents still being present (Figure 4.3 H; same cell as in (G)). These observations indicate that, in contrast to fast spiking interneurons, inhibition is the primary input to stellate cells during ramped light stimuli, despite other stellate cells being driven to spike at high rates. While stellate cells therefore provide strong and abundant inputs to fast spiking interneurons, their direct influence on other stellate cells appeared to be very limited.

Connections between stellate cells are rare or absent

To investigate whether functional excitatory connections exist at all between stellate cells I applied the ramped light stimulus while recording from stellate cells during block of inhibition and during block of both inhibitory and excitatory synaptic transmission (Figure 4.4). I reasoned that any glutamatergic excitation revealed by block of inhibition would be abolished by application of excitatory glutamatergic synaptic blockers and that therefore any difference in synaptic excitation between the two pharmacological conditions would be attributable to glutamatergic transmission. The critical test for the presence of functional excitatory connections between stellate cells is whether observed synaptic excitation depends on an *interaction* between irradiance level and pharmacological condition. If the level of synaptic excitation in a recorded cell increases with light level during the inhibition-only block condition, but not during block of both inhibition and excitation, an interaction would be evident as excitation onto stellate cells would depend on light level (and hence stellate spiking rates) in one pharmacological condition, but not the other. On the other hand, a uniform decrease in excitation throughout the duration of the light ramp after block of ionotropic glutamate receptors would not necessarily be evidence for light-driven excitatory synaptic activity. This is because stellate cells experience background excitatory synaptic inputs (Jones and Woodhall, 2005; Garden et al., 2008) (that could arise from excitatory connections originating in other areas) so a uniform decrease in excitation may be due to eliminating these spontaneous excitatory synaptic events with glutamatergic blockers. Similarly, an equal increase in excitation with irradiance level in both pharmacological conditions would also not count as evidence for light-dependent glutamatergic synaptic connections because the ramped light inten-

sity may produce non-specific synaptic effects (i.e. effects arising from initiation of non-glutamatergic synaptic transmission).

For stellate cells (n = 11), neither recordings made during the inhibition-only block condition nor during block of both excitation and inhibition revealed light-dependent inward synaptic currents (Figure 4.4 A). In comparison, recordings from FS interneurons (n = 3) showed a dramatic light-dependent increase in excitatory synaptic activity in the inhibition-only block condition, with initial major inward synaptic currents occurring in the window when stellate cells first begin to spike, but not during block of both inhibition and excitation, revealing an interaction between the light level and pharmacological condition (Figure 4.4 B). These observations suggested that stellate cells innervate FS interneurons during light ramps, but do not innervate other stellate cells.

To more carefully assess the effects of excitatory transmission onto recorded cells during ramped light protocols I computed the root mean square (RMS) power of membrane currents evoked by the light ramp stimulus. Synaptic inputs will increase the variance of the membrane current and so will manifest as an increase in RMS power. I wrote a MATLAB script that high pass filtered membrane current above 2 Hz to remove slow variance associated with the photocurrent and then calculated the RMS power for a series of 500 ms windows spanning the duration of the light ramp stimulus and with centres separated by 100 ms. I found that in stellate cells the average RMS power was very similar in both pharmacological conditions throughout the duration of the light ramp (Figure 4.4 C and inset) indicating that, consistent with previous observations (Jones and Woodhall, 2005; Garden et al., 2008) background glutamatergic excitation onto stellate cells is minor. The lack of a substantial increase in RMS power during the ramped light in either pharmacological condition suggests that the effects of illumination on non-specific synaptic transmission is also very small. Most importantly however, no interaction between irradiance level and pharmacological condition is apparent.

Synaptic depression cannot account for the lack of light-driven excitation onto stellate cells in the inhibition-only block condition. Because the recordings made in the inhibition-only block condition were the first occasion stellate cells had received illumination during the experiment, any initially functional connections that were subject to depression would be evident as a transient increase in RMS power during the window when stellate cells typically begin to spike (Figure 4.4 C and inset). This is not the case, indicating that synaptic depression is not responsible for the absence of observed connections between stellate cells.

In contrast, the average RMS power in FS interneurons rapidly increased with light intensity during the inhibition-only block condition, beginning in the time window

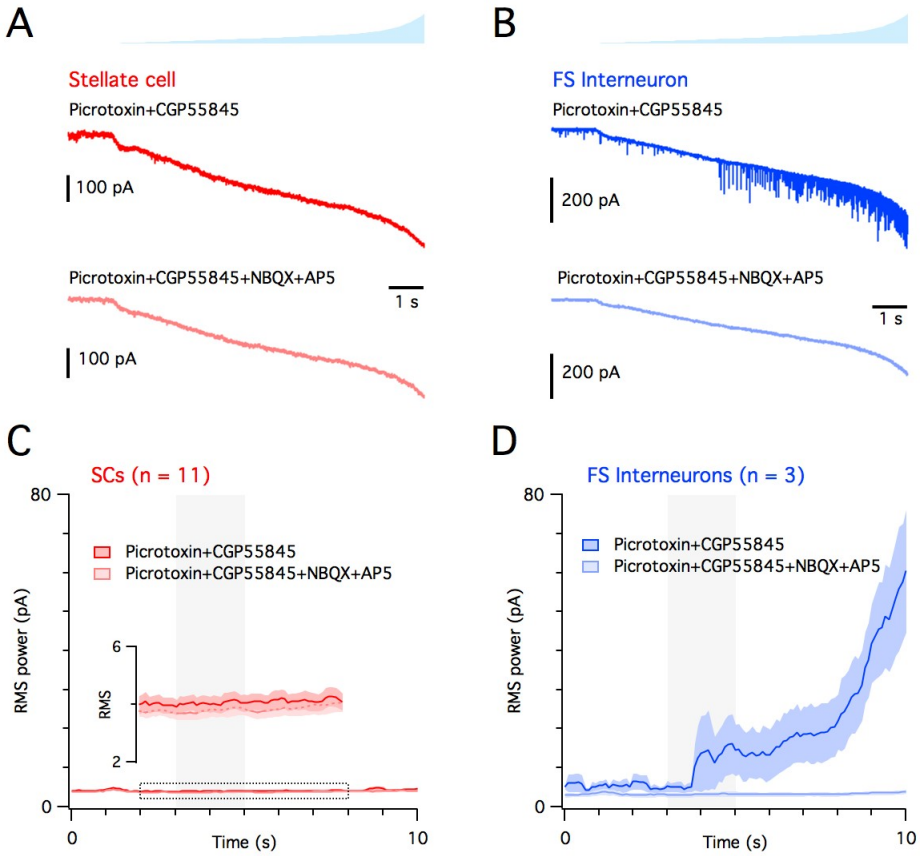

Figure 4.4: **No effects of synaptic connections between stellate cells are detectable. A–B** Voltage clamp recordings (holding potential -70 mV) from a stellate cell and an FS interneuron in response to a light intensity ramp (upper) during perfusion of GABA receptor antagonists CGP55845 and Picrotoxin to block inhibition (middle) and subsequently during additional block of excitation with glutamate antagonists NBQX and AP5 (lower). **A** Example traces from a stellate cell pre and post-block of excitation. The lack of difference between the pharmacological conditions implies an absence of light-driven excitation onto stellate cells in the inhibition block-only condition. **B** Example traces from a simultaneously recorded nearby FS interneuron showing the large difference in excitatory synaptic transmission resulting from pharmacological block of inhibition. The presence of excitation in the inhibition block-only condition indicates that excitatory transmission is intact in the slice. **C–D** Mean and SEM (shaded areas) of the root mean square (RMS) power of membrane currents in the different pharmacological conditions. Grey bands indicate the time window that stellate cells typically start spiking in response to the light ramp. **C** RMS power during stellate cell recordings (n = 11). There is no temporary increase in RMS during the time window that stellate cells typically start spiking. Inset is vertical expansion of the plot area delineated by the dotted line. **D** RMS power in interneurons (n = 3). Note the initial jump in RMS in the inhibition block-only condition when stellate cells begin to fire and subsequent increase in RMS throughout the remainder of the light ramp. Grey reference bands indicate approximate start of light induced spiking in stellate cells.

when stellate cells begin to spike, but was reduced and unaffected by light level during block of inhibition and excitation. Together, these observations support the conclusion that optogenetic activation of stellate cells produces excitation in FS interneurons but not other stellate cells.

To quantitatively test the effects of light level and pharmacological condition on RMS power in stellate cells (n = 11) I recalculated RMS for 5 non-overlapping consecutive 2 s windows in each trace. I then performed a repeated measures two factor ANOVA with pharmacology (2 levels) and irradiance (5 levels) as the two factors. This test revealed a small but significant main effect of block of excitation ($p = 0.03$), indicating a small change in RMS most likely due to block of spontaneous background glutamatergic synaptic activity (Figure 4.4 C (inset) shows the very small RMS difference between the pharmalogical conditions). However, the ANOVA did not reveal any significant main effect of light level ($p = 0.48$), indicating that afferent synaptic activity was independent of irradiance (and stellate spiking). Most importantly, no interaction between pharmacology and irradiance was evident ($p = 0.29$), indicating that light-dependent spiking induced in stellate cells had no detectable direct synaptic influence on other stellate cells in these recordings.

4.3.2 *Quantifying the probability of stellate–stellate connections*

Failure to observe light-dependent excitatory synaptic input to stellate cells does not necessarily mean that stellate cells do not connect to each other at all, as there is the possibility that connected pairs may not have been sampled during experiments. However, estimating the number of possible connections that are tested during these experiments provides a means to establish an upper limit on the probability of connections between of stellate cells. Estimating the number of tested pairs during each experiment requires knowledge of the number of stellate cells that are induced to fire action potentials during the ramped light stimulus. Together with knowledge of the stellate cell density in layer II, establishing how stellate cell spiking output depends on cells' distance from the centre of the illumination permits calculation of the number of activated stellate cells during the light stimulus and therefore provides a way to calculate an upper limit on stellate–stellate connection probability.

Spatial profile of stellate cell spiking response to illumination

How does spike output depend on distance from the centre of the illumination? Although cells directly under the ~90 μm diameter light beam are likely to be activated to a similar degree, cells with somata >45 μm away from the centre of the light may become sufficiently depolarised to spike due to portions of their dendritic tree being

activated and because light scattering may spread the illumination across a larger area. To determine the spatial extent of light-driven stellate cell activation I again recorded from stellate cells while systematically changing the position of the light source to observe how spike rates depended on the distance from recorded cells to the centre of the light beam.

To establish the relationship between stellate cell spike rate and illumination distance I recorded action potential output from stellate cells (n = 13) in the presence of inhibitory and excitatory synaptic blockers during application of an 8 second constant light step of ~10 mW/mm^2. To avoid the temporary initial high spike rate during the brief large depolarisation resulting from the sudden onset of the light I excluded the first 500 ms after the onset of the light step from average rate calculations (see Figure 4.5 A). I applied illumination at different light distances away from the recorded cell in dorsal, ventral and sub-laminar directions (Figure 4.5 A, B). To do this I moved the light beam away in fixed distance increments from a central position overhead the recorded cell using the manual stage adjustment controls. Because the movable stage could only travel along orthogonal axes, for these experiments I carefully oriented slices before recording so that the dorsal-ventral axis of the MEC was aligned with one of the stage movement axes.

I found that spike rate averages were greatest (~8 Hz) during the ~10 mW/mm^2 illumination when cells were directly under the centre of the light beam. The spike rate gradually decreased to ~1 Hz as light distance increased up to 100 μm (Figure 4.5 B). Although cells remained substantially depolarised at 150 μm away from the centre of the light (Figure 4.5 A), beyond 100 μm they were not sufficiently depolarised by the light to fire action potentials (Figure 4.5 A, B). This indicates that stellate cells are activated within a 100 μm distance of the light stimulus.

Estimate of number of activated cells

To obtain a lower bound on the number of stellate cells that are driven to spike during the light ramp stimulus I estimated the number of stellate cells that are activated during the light step stimulus. Based on the spatial profile of spiking during the light step protocol I estimated that cells were activated in a region of tissue with dorsal-ventral extent 200 μm, rostro-caudal extent 100 μm (approximate width of layer II) (Figure 4.5 C pink rectangle) and depth of of 100 μm, providing an activated tissue volume of 0.002 mm^3.

This is likely to be a substantial underestimate of the activated volume because (i) the final irradiance during the light ramps is 12 mW/mm^2 (compared to 10 mW/mm^2 for the light steps), so cells are likely to be activated further than 100 μm away from the centre of the light stimulus, (ii) cells are likely to be activated sub-

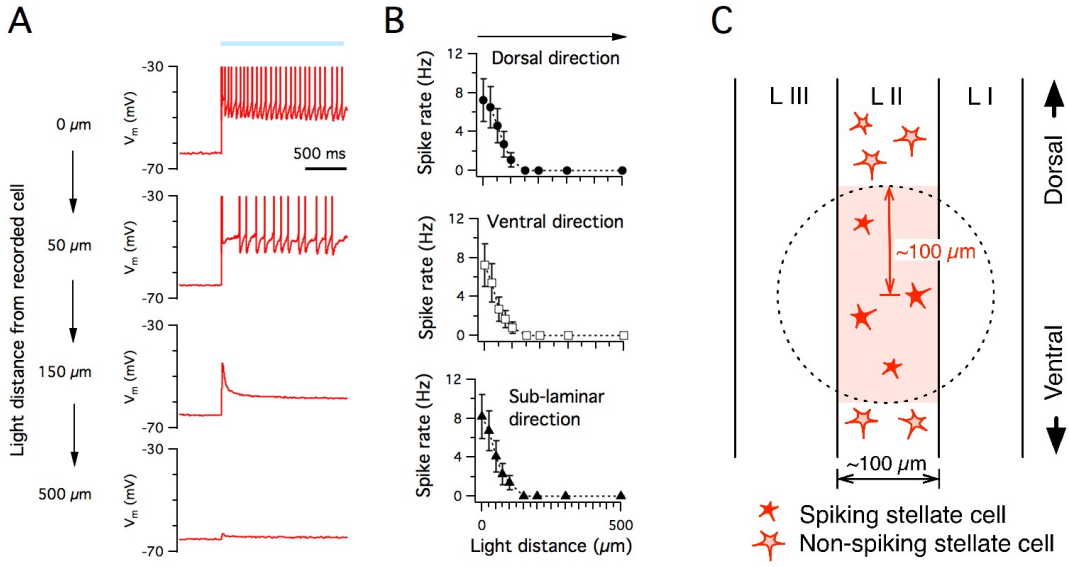

Figure 4.5: **Spatial profile of stellate cell activation. A** Example voltage traces from a stellate cell with the centre of the light positioned overhead (0 μm) and at 50, 150 and 500 μm away in the dorsal direction. The illumination had constant intensity, with an irradiance of ~10 mW/mm^2. **B** Relationships between stellate cell spike rate averages of stellate and light centre distance. Plots are for light moved in the dorsal direction (upper), ventral direction (middle) and in the sub-laminar direction (lower). Red trace in the upper panel corresponds to the example from **(A)**. **C** Schematic for calculation of region of tissue containing activated stellate cells. The dotted circle indicates the 100 μm radius of light activated cell spiking established in **(B)**. The pink rectangle indicates the area of layer II used for the calculation of activated tissue volume.

stantially deeper than 100 μm because the power of 470 nm light is still at 50% 100 μm below the surface of illuminated neural tissue (Aravanis et al., 2007) and (iii) I patched cells deep ($\geqslant$ 80 μm) below the slice surface, so more superficial cells would be more activated than the recordings discussed above would suggest.

How many stellate cells are there in this activated volume? There are approximately 17800 stellate cells in layer II of mouse MEC (74% stellate of a 24000 total (Gatome et al., 2010)). The approximate total volume of layer II is ~0.16 mm^3 (~2000 μm dorsal–ventral axis × ~100 μm superficial–deep axis × ~800 μm medial–lateral axis). The density of stellate cells is thus ~111000 / mm^3, which can be conservatively rounded down to ~200 cells in every 0.002 mm^3. Considering the 11 experiments that directly tested for light-induced EPSCs (see Figure 4.4) yields a total of ~2200 tested connections, which can again conservatively be rounded down to N = 2000 tested connections during which no connected pairs were detected.

Calculation of connection probability upper bound

Given this estimate of the total number of tested connections, it is possible to calculate the upper bound on overall connection probability, p_{max}, for some confidence interval, C, by application of the expression[1]

$$p_{max} = 1 - \sqrt[N+1]{1 - C}$$

where N is the number of tested connections connections (see Appendix 1 for derivation). Therefore, with N = 2000 and with 95% confidence (C = 0.95), the connection probability, p, is $< 1.5 \times 10^{-3}$ (or less than $\frac{1}{5}$th of 1 %). This is in stark contrast with estimates from the cortex and other areas in the hippocampal formation where connections probabilities between principal cells are on the order of 5 – 10 % (Dhillon and Jones, 2000; Song et al., 2005). This suggests that the strikingly low connectivity is likely to have special relevance for the computations implemented by layer II of the MEC.

4.3.3 *Feedback inhibition mediates stellate cell interactions*

Although stellate cells may not communicate directly with each other through excitatory synapses, it remains possible that they influence each other through indirect inhibitory connections. The strong inhibition observed in layer II of the MEC (Jones, 1994; Gloveli et al., 1997) could underlie indirect stellate cell interactions, but the cellular origin of this inhibition is unclear, and instead of providing a substrate for

1 See Appendix A for derivation

feedback inhibition between stellate cells it may primarily support feedforward inhibition (Finch et al., 1988).

4.3.4 *Excitation-driven inhibition onto stellate cells*

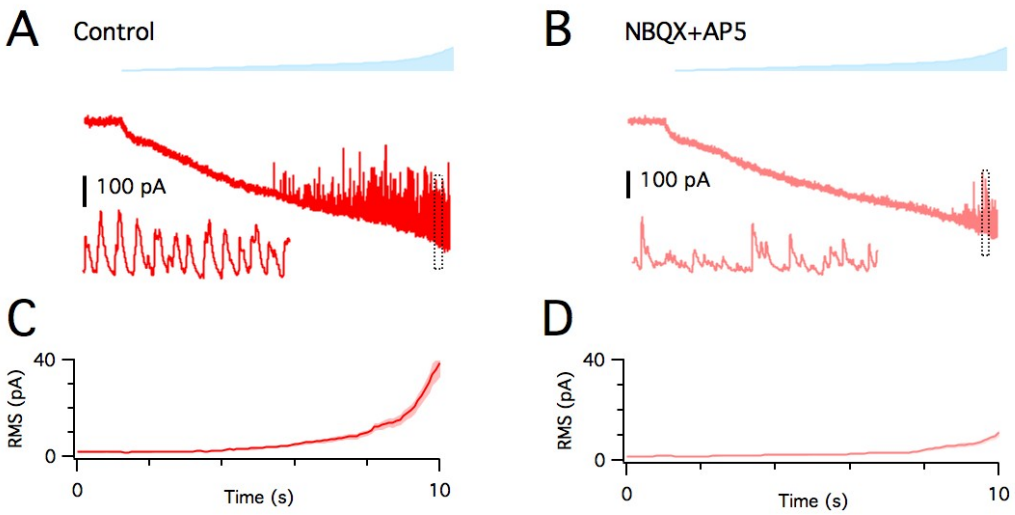

Figure 4.6: **Stellate cells communicate indirectly via inhibitory connections. A–D** Light ramps drive inhibition onto stellate cells in control conditions and during block of excitation with glutamate receptor antagonists NBQX and AP5. **A** Light ramp (upper) and example current trace from stellate cell (lower) and expansion of area enclosed by the dotted rectangle (inset). **B** Light ramp (upper) and trace from the same cell as in **(A)** after perfusion of NBQX and AP5. **C,D** Average RMS power of stellate cell membrane currents over time before and after block of excitation (n = 23), indicating that intact excitatory input from stellate cells in layer II increases inhibition onto stellate cells.

How does excitatory synaptic input from stellate cells onto interneurons influence inhibition onto other stellate cells? To test whether excitation of stellate cells drives inhibition onto other stellate cells I recorded from stellate cells in control conditions and during block of synaptic excitation with NBQX and AP5 to isolate the excitation-driven component of inhibition. I performed patch-clamp recordings from stellate cells (n = 23) in voltage clamp mode with a holding potential of -50 mV to reveal inhibitory synaptic input. I found that although inhibition was still present with excitatory synaptic transmission blocked (presumably due to direct photoactivation of ChR2 expressing FS interneurons) there was marked decrease in afferent inhibition onto stellate cells during block of excitation (Figure 4.6 A,B). To quantify the effect of blocking synaptic excitation on inhibitory synaptic input to stellate cells I calculated the RMS power of the membrane current in 500 ms windows with window centres separated by 100 ms as previously described. This analysis reveals a much larger increase in RMS power with ramped light during control conditions than with

synaptic excitation blocked (Figure 4.6 C,D). To test the reduction in inhibition I re-calculated RMS power for 5 non-overlapping consecutive 2 second windows in each trace. I then, as before, performed a multi-factor ANOVA with irradiance (5 levels) and pharmacological condition (2 levels) as the 2 factors. Both the main effects of the pharmacological manipulation ($p = 0.002$) and light level ($p = 8.5\times10^{-11}$) had significant effects, but most importantly the ANOVA revealed a significant ($p = 0.001$) interaction between irradiance level and pharmacological condition, consistent with a strong effect of stellate cell spiking on the membrane currents in other stellate cells.

4.3.5 *Paired recordings support feedback inhibition and substantiate an absence of recurrent excitation*

To directly test for connections between stellate cells in the parasagittal slice preparation and to investigate the functional connections between stellate cells and FS interneurons, I additionally tested for connected cell pairs by performing simultaneous recordings from stellate cells and stellate-FS interneuron pairs. To test for functional connections between cell pairs I induced spiking separately in each recorded cells by direct current injection. In each cell I induced >20 action potentials. I then used the Detect Events algorithm in Axograph (in the amplitude threshold crossing detection mode) to ascertain the time of each evoked action potential. I captured action potentials from the spiking cell as well as a segment of membrane potential trace from the other simultaneously recorded cell extending 10 ms before and 100 ms after each action potential. Averaging these captured membrane trace segments reduces noise and mitigates the effects of action potential transmission failure and so reliably reveals even very small PSPs if a connection exists (Figure 4.7 A–B). To ensure that I detected inhibitory connections, if I did not initially observe a PSP while inducing an FS interneuron to spike I injected a holding current in the non-spiking cell to depolarise its membrane potential away from the chloride reversal potential (~-70 mV) thereby providing an adequate driving force to GABAergic conductances.

These paired recordings revealed that connections from stellate cells to FS interneurons (Figure 4.7 A) and from FS interneurons to stellate cells (Figure 4.7 B) were common but did not reveal any connections between stellate cells (Figure 4.7 C,D). Connections between stellate cells and FS interneurons were detectable in both directions $> \frac{1}{3}$ of the time (Figure 4.7 C, D) and ~23 % of stellate-interneuron cell pairs had reciprocal connections. These data are thus consistent with results obtained with optogenetic investigations, providing further evidence that stellate-stellate connectivity is absent or extremely rare. In addition, they suggest that connections between stellate cells and local FS interneurons are very dense, and that feedback inhibition between

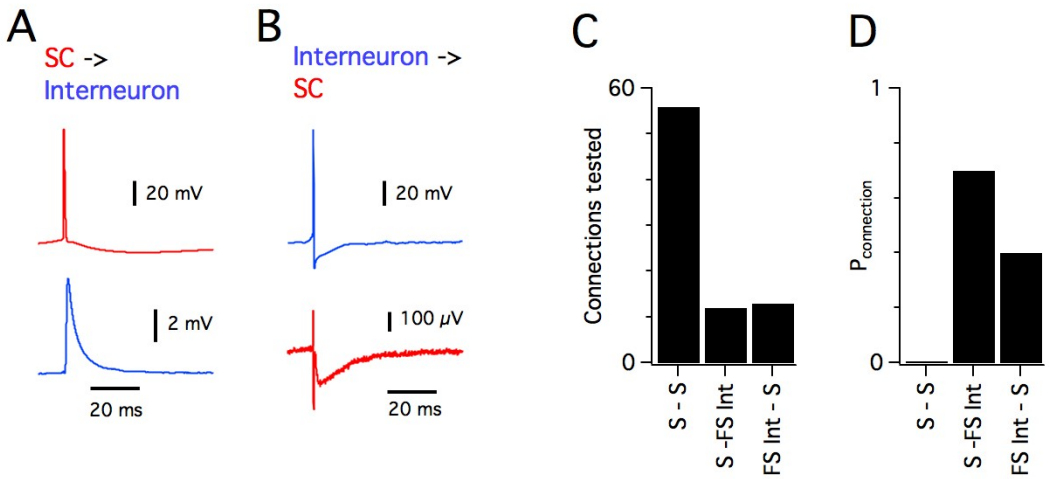

Figure 4.7: **Paired recordings reveal functional connections between FS interneuron - stellate pairs but not between stellate cells. A** Example connected SC-FS interneuron pair. Action potentials in the stellate cell evoked by current injection (upper) evoke EPSPs in the FS interneuron (lower). **B** Example FS interneuron-SC connected pair. Interneuron action potentials (upper) evoke IPSPs in stellate cells. Displayed PSPs in **(A)** and **(B)** are averages from across >20 trials. **C** Number of connections tested between different cell types. **D** Proportion of a tested connections exhibiting a detectable connection.

stellate cells and FS interneurons may therefore be the main mode of communication between stellate cells in layer II of the MEC.

4.3.6 *The dorsal-ventral organisation of inhibition*

Is there a dorsal-ventral organisation of feedback inhibition in layer II of the MEC? If feedback inhibition is the primary means of communication between stellate cells, one might suppose that a dorsal-ventral gradient of inhibition onto stellate cells from interneurons in layer II the MEC could contribute to the dorsal-ventral gradient in grid field spacing observed in behaving animals.

It is possible that inhibition to stellate cells from ChR2 expressing FS interneurons follows a dorsal-ventral gradient. It is also possible that inhibition resulting from stellate cell activation (excitation-driven inhibition) follows a gradient independent of the strength of 'direct' inhibition. To investigate these possibilities I recorded the magnitude of inhibition onto stellate cells at locations spanning the entire dorsal-ventral extent of the MEC both in control conditions and during block of excitatory synaptic transmission. Because both stellate cells and interneurons are directly activated by light, inhibition measured during control conditions reflects the aggregate effects of inhibition due to direct light activation of interneurons as well as excitation-driven

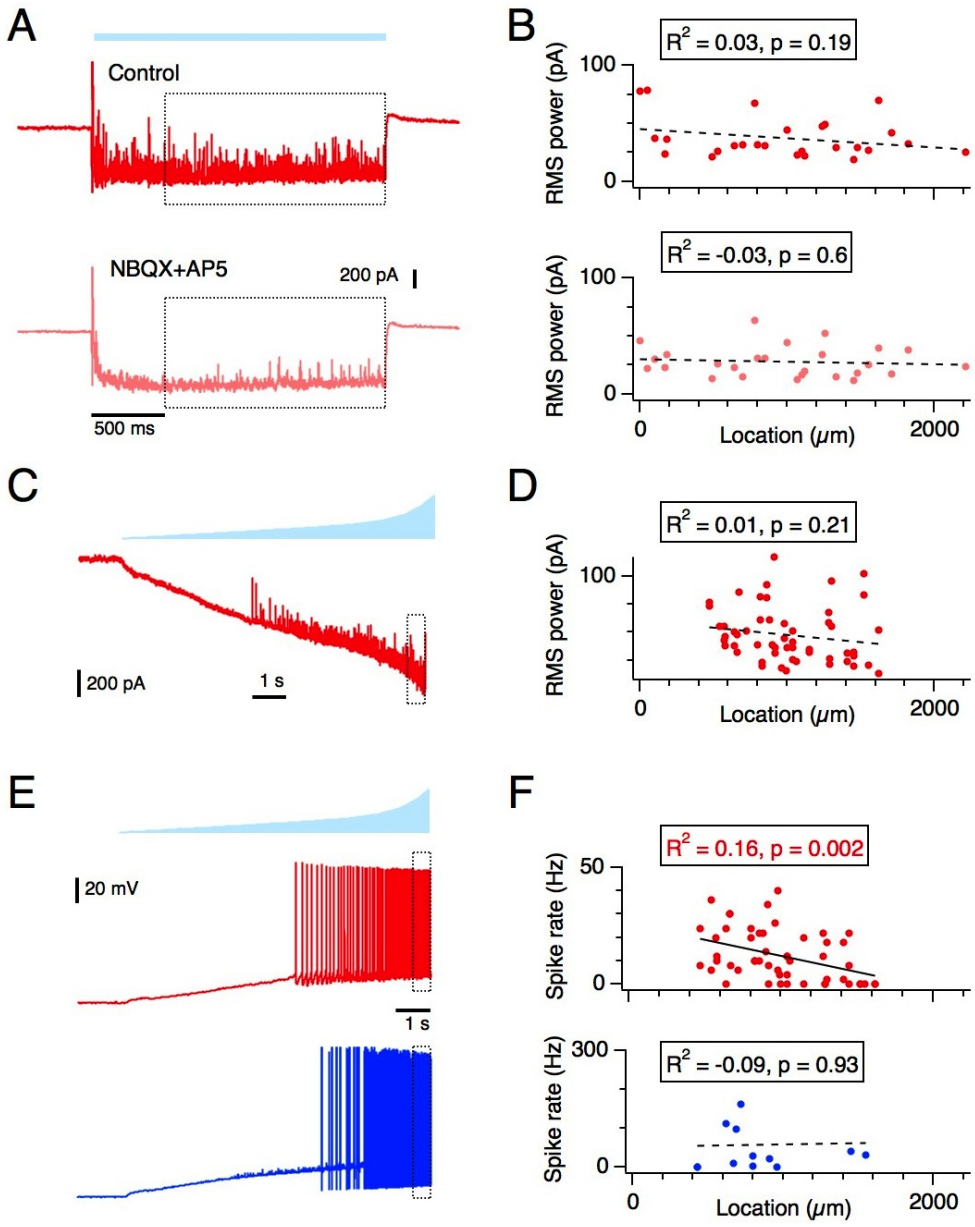

Figure 4.8: **Inhibition from FS interneurons onto stellate cells does not follow a dorsal-ventral gradient. A** Constant 10 mW/mm^2 light stimulus (upper), example traces from a cell in control conditions (middle) and during block of excitation with NBQX and AP5 (lower). The dotted rectangles indicate the region of traces used for calculating RMS power. **B** RMS power for all cells plotted as a function of location along the dorsal-ventral axis in control conditions (upper) or during block of excitation (lower). **C** Ramped light stimulus up to 12 mW/mm^2 (upper) and example trace from an SC (lower) showing outward synaptic currents during the light ramp. The dotted area indicates the RMS power measurement area. **D** Plot of RMS power against location on the dorsal-ventral axis for recordings during ramped light stimuli. **E** Ramped light stimulus (upper) and example membrane voltage responses from a stellate cell (middle, red trace) and an FS interneuron (lower, blue trace). The dotted area indicates the portion of the traces used to measure firing rate. **F** Plots of spike rate as a function of location for SCs (upper) and FS interneurons (lower).

inhibition, whereas inhibition measured during block of excitation with NBQX and AP5 reflects only direct light-activation of FS interneurons. The difference in inhibition in each cell between control and excitation blocked conditions should reveal the net excitation-driven inhibition.

To measure aggregate inhibition I recorded IPSCs in voltage clamp at a holding potential of -50 mV from stellate cells (n = 26) during 3 repetitions of a constant light steps (10 mW/mm^2) delivered directly overhead the recorded cells (Figure 4.8 A). To avoid light onset effects I analysed only the final 1.5 seconds from each 2 second light step (for a total analysis period of 4.5 seconds per cell). I favoured quantifying the magnitude of inhibition by calculating the average RMS power of membrane currents over using IPSC rate or charge transfer as measures of inhibition because an IPSC rate measure cannot discriminate between smaller and larger, possibly compound, events occurring at the same rate and charge transfer requires a baseline current from which to calculate total charge transfer, but I found that even after block of both excitation and inhibition with NBQX, AP5, Picrotoxin and CGP55845, photocurrents resulting from ChR2 activation were not sufficiently stable across long periods of time to act as a reliable baseline. Because of the (at most) extremely sparse connectivity between stellate cells, and the rarity of spontaneous background excitation, EPSCs during these recordings are rare or absent so variance in the membrane current and hence RMS power can be ascribed to inhibitory synaptic currents. I found that RMS power in stellate cells in layer II did not vary with location along the dorsal-ventral axis of the MEC either in control conditions (n = 27, p = 0.19) or during block of excitation (n = 26, p = 0.6) (Figure 4.10 B). Furthermore, the difference in RMS values for cells recorded in both conditions did also not follow a dorsal-ventral gradient (n = 26, R^2 = 0.02, p = 0.24, data not shown). These data suggest that neither form of inhibition follows a dorsal-ventral gradient.

To test the generality of these conclusions to other stimulation protocols I recalculated membrane current RMS power from stellate cells during the final 500 ms of ramped light stimuli (Figure 4.8 C). As with the light step data, I found no relationship between RMS power and dorsal-ventral location in control conditions (n = 53, p = 0.21) (Figure 4.8 D). There is thus no evidence that aggregate inhibition onto stellate cells follows a dorsal-ventral gradient.

One possible complicating factor is the existence of a gradient in spike rates. If, for example, RMS power in stellate cells were constant along the dorsal-ventral axis yet interneuron spiking followed a steep gradient, this would suggest that the actual influence of individual inhibitory cells did follow a gradient. Similarly, if stellate cells spike rates followed a steep gradient during control conditions and FS interneuron spike rates followed an opposite dorsal-ventral gradient during block of excitation,

then the opposing gradients in 'intrinsic' inhibition and excitation-driven inhibition could cancel each other out.

To test for dorsal-ventral gradients in spike rate I recorded the average spike rate in stellate cells and FS interneurons during the final 500 ms window of traces obtained during ramped light stimuli (Figure 4.8 E) and plotted them against cell location. While FS interneuron spike rates did not depend on dorsal-ventral location ($n = 13$, $p = 0.93$) (Figure 4.8 F (lower)), stellate cell spike rates did follow a shallow gradient ($n = 52$, $p = 0.002$) (Figure 4.8 F (upper)). One interpretation of this result is that the constant dorsal-ventral FS interneuron spike rate may result from a combination of a dorsal-ventral gradient in stellate cell spiking (possibly due to a small dorsal-ventral gradient in ChR2 expression) providing extra drive to more dorsal FS interneurons, offsetting a relative lack of 'intrinsic' dorsal inhibition. However, given the absence of sufficient data to assess a dorsal-ventral gradient of interneuron spike rates during block of excitation and the very shallow and noisy gradient in stellate spiking rates, it remains possible that the absence of a gradient in the RMS power in stellate cells reflect the lack of a dorsal-ventral gradient in FS interneuron mediated inhibition in layer II of the MEC.

4.3.7 *The spatial profile of inhibitory influence*

Models of grid cell output based on attractor dynamics require functional connection strength between cells in the network to be modulated by the distance (in network space) between the cells (Fuhs and Touretzky, 2006; McNaughton et al., 2006; Guanella et al., 2007; Burak and Fiete, 2009). Of particular interest, these models predict that circuitry for generating grid cells should exhibit surround inhibition or excitation, with at least one type of cell maximally innervating other cells at intermediate network distances and minimally innervating nearby or far away cells. If this network schema also exists in physical space, one would expect that the degree of synaptic influence between cells would depend on the distance between them, with inhibition or excitation peaking at intermediate distances. To investigate whether surround inhibition or excitation exist in layer II of the MEC and to potentially distinguish between these different schemas I asked how inhibition onto stellate cells depends on the distance between recorded stellate cells and groups of activated stellate and FS interneuron cells.

Different connectivity schemas predict different spatial profiles of inhibition onto stellate cells. Figure 4.9 illustrates the predicted spatial profile of experimentally recorded inhibition for three different connectivity schemas. The three different schemas that are considered are (i) local inhibition and local excitation (not predicted by grid

cell attractor models) (Figure 4.9 A–D), (ii) local inhibition and surround excitation (Figures 4.9 E–H) and, (iii) surround inhibition with local excitation (Figures 4.9 I–L). The connection profile schematic for (i) in Figure 4.9 A illustrates how both excitation and inhibition are maximal between nearby cells and decay with increasing distance between cells. In contrast, Figures 4.9 E depicts the connectivity schema for (ii), with local inhibition and surround excitation that is low between nearby cells and initially increases to a peak with increasing distance but then falls as the distances between cells increases even further. Figure 4.9 I depicts the connection schema for (iii), with local excitation and surround inhibition. Figures 4.9 B, F, J illustrate how the connectivity profiles in Figures 4.9 A, E, I translate into the spatial dependence of distinct components of inhibition. 'Direct' inhibition simply follows the spatial dependence of the inhibition connectivity schema profile, whereas 'indirect' or 'excitation-driven' inhibition follows a broader spatial profile (the 'indirect' inhibition spatial profiles are obtained by convolving the inhibition and excitation schema spatial profiles, and the resulting spatial 'smearing' of the indirect inhibition reflects the fact that excitatory cells can have an impact at greater distances than inhibitory cells, as they may innervate inhibitory cells that are closer to the location of the reference cell). The different inhibition profiles make different predictions for inhibition in different pharmacological conditions. Figures 4.9 C, G, H depict qualitative experimental predictions for distance dependent inhibition for the different connectivity schemas in two pharmacological conditions. First, in control conditions, total inhibition in recorded cells will reflect the aggregate of direct and excitation-driven inhibition (sum of the direct and indirect inhibition profiles in Figures 4.9 B, F, J). Second, during block of synaptic excitation, the excitation-driven component of inhibition will be removed, with only the directly activated inhibition component remaining. The difference between aggregate inhibition and direct inhibition revealed during block of excitation also depends on connectivity schema. Figures 4.9 D, H, L illustrate the qualitative distance dependent profiles of the difference between inhibition in control conditions and during block of excitation. Together, these three different connectivity schemas therefore make distinct testable predictions for inhibition profiles which can be evaluated against experimental data.

To record the magnitude of inhibition onto stellate cells and activate cell populations at different distances I again adopted an optogenetic approach. I recorded membrane currents in stellate cells in voltage clamp at -50 mV to reveal inhibition and activated groups of cells with a 10 mW/mm^2 beam of light with a diameter of ~90 μm which activated stellate cells and FS interneurons in a region with a 200 μm diameter (dotted circle depicted in Figure 4.10 A (see also Figure 4.5)). I moved the light beam moved between an overhead position and distances up to 500 um away

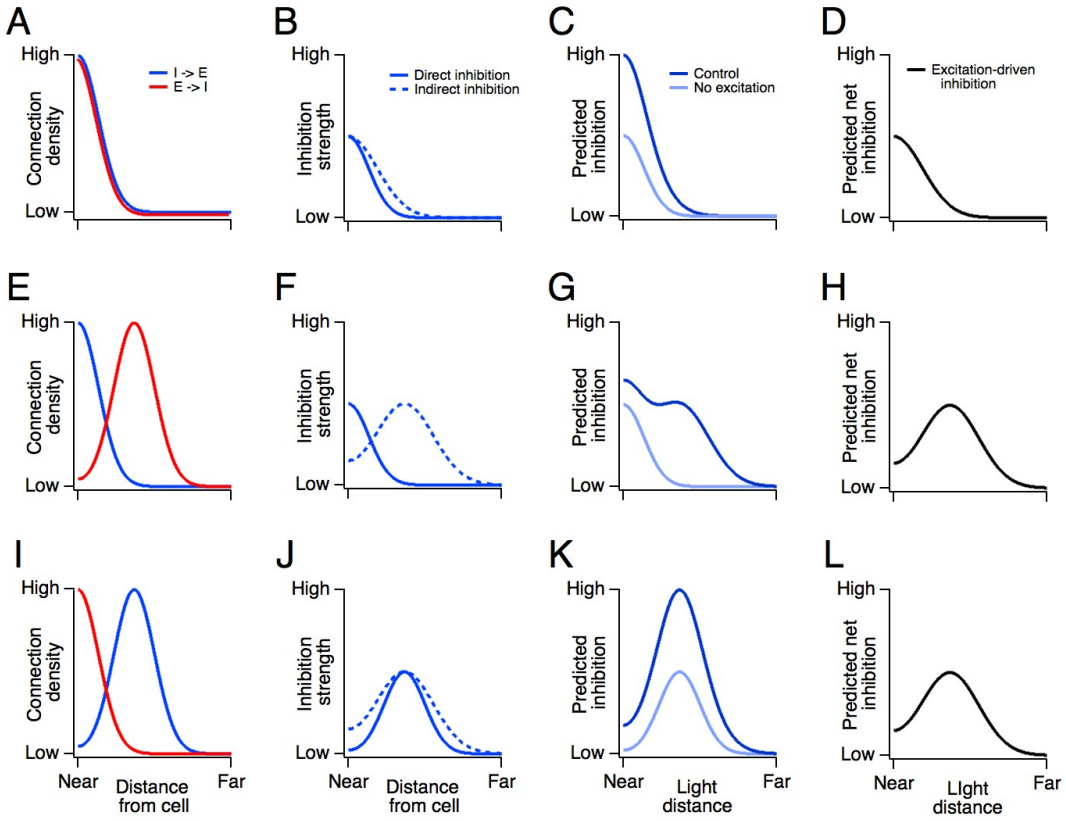

Figure 4.9: **Different feedback inhibition connectivity schemas and their qualitative distance-dependent experimental predictions. A–D** Connection schema with local inhibition and excitation and its experimental predictions. **A** Both maximal inhibition (blue line) and excitation (red line) is onto nearby cells and decays with distance. **B** Distance dependence of direct inhibition (solid blue line) and indirect excitation-driven inhibition (dashed blue line) associated with the organisation of connectivity depicted in **(A)**. **C** Qualitative experimental predictions for the spatial dependence of aggregated inhibition in control conditions (dark blue line) and directly activated inhibition during block of excitation (light blue line) arising from the inhibitory profiles in **(B)**. **D** The excitation-driven component of inhibition is the difference between aggregate inhibition and direct inhibition shown in **(C)**. **E–F** Connection schema with local inhibition and surround excitation and its experimental predictions. **E** Inhibition onto excitatory cells (blue line) has a local peak whereas excitation onto inhibitory cells (red line) has a centre surround organisation. **F** Spatial profiles of direct (solid blue line) and indirect (dashed blue line) inhibition associated with the connection in schema depicted in **(E)**. **G** Experimental predictions for the spatial profiles of aggregate inhibition (dark blue line) and direct inhibition (light blue line) arising from the inhibitory spatial profiles depicted in **(F)**. **H** The spatial profile of the excitation-driven component of inhibition. **I–L** as for **(E–H)** but for a circuit organisation with local excitation onto interneurons and centre surround inhibition onto excitatory cells.

in dorsal and ventral directions along the dorsal-ventral axis and recorded in both control conditions and during block of synaptic excitation with NBQX and AP5 to reveal the effects of excitation-dependent inhibition at different distances (Figure 4.10 B). To quantify the magnitude of inhibition I used RMS power, as direct excitation onto stellate cells is unlikely to contribute significantly to membrane current variance

in this preparation (see Figures 4.3 and 4.4). This method allowed me to investigate the distance dependent effects on inhibition in stellate cells during activation of a group of cells at different distances away from the recorded cell.

Using this method I found that both aggregate inhibition and indirect inhibition from directly light-activated interneurons monotonically decreased with light distance from the recorded cell, reaching a lower asymptote at a distance of ~500 μm in both dorsal (n = 15) and ventral (n = 16) directions (Figure 4.10 B,C,E,H). Importantly, EPSCs onto stellate cells were not apparent at any light distance, suggesting that the lack of recurrent excitation between stellate cells is not only restricted to nearby cells, but extends at least 500 μm away along the dorsal-ventral axis of the MEC (Figure 4.10 B). The magnitude of directly light-activated inhibition initially decreased more rapidly with light distance than aggregate inhibition (Figure 4.10 B,C,E,H) and because the difference in inhibition between the two pharmacological conditions reflects the direct effect of excitation-driven inhibition, the rapid decrease of direct light-activated inhibition means that the magnitude of the indirect excitation-driven inhibition peaked at a light distance approximately ~100 μm away from recorded cells along the dorsal-ventral axis (Figure 4.10 D,F,I). Alternatively, when expressed as a proportion of total inhibition, excitation-driven inhibition peaks at distance of ~200 μm in the dorsal direction (Figure 4.10 G) and at ~100 μm in the ventral direction (Figure 4.10 J).

These results suggest that the local circuitry in layer II of the MEC is characterised by local inhibition and surround excitation. First, the data are inconsistent with a connectivity schema with both local inhibition and excitation (Figure 4.9 A). In particular, the spatial profile of excitation-driven inhibition (the difference between aggregate inhibition and directly light-driven inhibition) has a peak at a location distal to recorded cells' position (Figures 4.10 D, F, I), a result qualitatively different to the prediction made by the purely local connectivity schema (Figure 4.9 D). Second, the data are also inconsistent with a connectivity schema where excitation is local but inhibition follows a centre surround organisation (Figure 4.9 I). In this case, the prediction for the profile of directly light-driven inhibition is different to that obtained during pharmacological block of excitation, which has a peak local to recorded cells (Figures 4.10 C, E, H). In contrast, the surround inhibition connection schema prediction is qualitatively different, with a peak distal to the recorded cells (Figure 4.9 K). Other connectivity schemas not depicted in Figure 4.9 are also inconsistent with the data. Schemas with uniform inhibitory connectivity would not produce a peaked inhibition profile and schemas with both surround inhibition and excitation would produce a direct inhibition profile with a peak distal to recorded cells, but this is not observed. These results are therefore only consistent with a connectivity schema

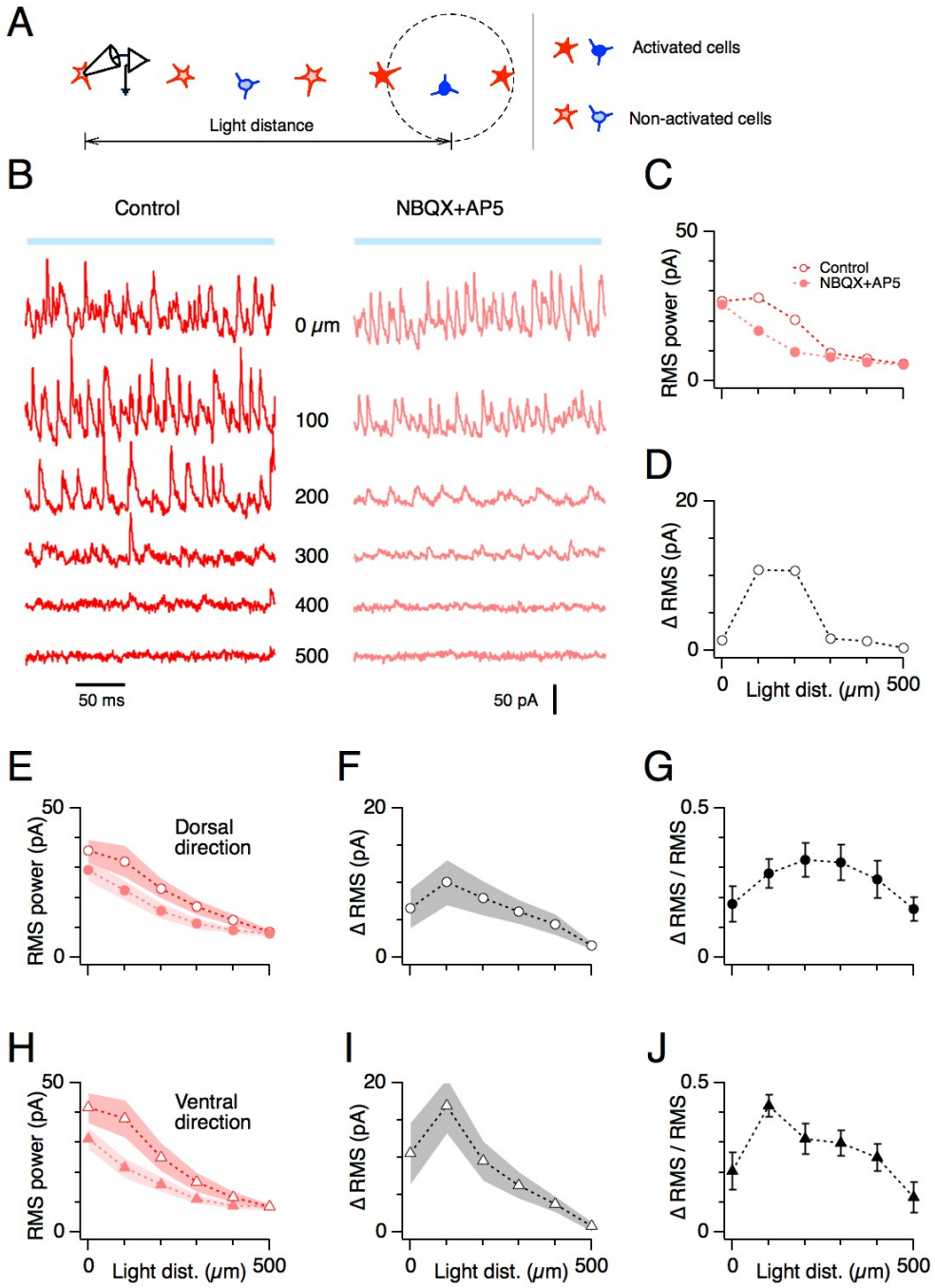

Figure 4.10: **Spatial profile of inhibition onto stellate cells. A** Schematic of the experimental setup. The recorded cell is indicated on the left, the dotted line indicates the region of tissue containing cells driven to spike directly by the constant 10 mW/mm^2 light stimulus and the illumination distance is indicated by the bi-directional arrow. **B** Current traces (recorded in voltage clamp with a holding potential of -50 mV) at increasing illumination distances from the recorded cell (increasing from overhead at the top to 500 µm in the dorsal direction at the bottom) in control conditions (left panel) and after block of excitation with NBQX and AP5 (right panel). **C** RMS power as a function of illumination distance for example shown in **(B)**. **D** Net excitation-dependent RMS power calculated by subtracting the RMS power with excitation blocked from the RMS power in control conditions in **(C)**. **E** Average population RMS power in control and excitation block conditions at different illumination distances in the dorsal direction. **F** Average population net excitation-dependent RMS power for illumination distances in the dorsal direction. **G** Net excitation-dependent RMS power as a proportion of total control RMS power for illumination distances in the dorsal direction. **H–J** As for **(E–G)** but for illumination distances in the ventral direction.

comprising surround excitation and local inhibition, suggesting that such a circuit organisation is present in layer II of the MEC.

4.4 DISCUSSION

The results presented in this chapter reveal that the microcircuitry of layer II of the MEC has properties that are notably distinct from neocortical and hippocampal microcircuits and which are likely to be critical for producing the characteristic grid firing field output. I discuss these findings and their implications for grid cell output below.

4.4.1 *The microcircuitry of the MEC is dominated by feedback inhibition*

Stellate-stellate connections are rare or absent

In the hippocampus (Miles and Wong, 1986), deeper layers of the MEC (Dhillon and Jones, 2000) and neocortical circuits (Mason et al., 1991; Deuchars et al., 1994), excitatory cells are innervated by a substantial proportion of nearby excitatory cells of the same type. Direct synaptic communication between excitatory cells in these circuits are thought to underly a wide range behavioural capabilities (Silberberg et al., 2005). In contrast, the results discussed above reveal that, surprisingly, the MEC performs its spatial computations without direct interactions between the vast majority, if not all, of the principal excitatory output cells in layer II. The evidence for lack of recurrent excitation between stellate cells in the MEC is strong - both the optogenetic and paired recording experiments described above are consistent with an absence of functional connections between stellate cells. Both these findings are also consistent with a previous study that failed to find connections between stellate cells with paired sharp electrode recordings (Dhillon and Jones, 2000) and also with another study subsequent to the publication of this work which also failed to find connections between stellate cells in mature adult rats using both extensive paired whole-cell recordings (>240 pairs) and targeted optogenetic stimulation of stellate cells (Couey et al., 2013). Taken together, these results suggest that excitatory connections between putative stellate cell pairs observed with indirect techniques (Kumar et al., 2007; Beed et al., 2010; Quilichini et al., 2010) are due to innervation of stellate cells by other excitatory cell types, possibly including pyramidal cells that constitute a small proportion of the cells in layer II of the MEC (Gatome et al., 2010). Therefore, unusually for a cortical area, the layer II microcircuit architecture appears to be organised with no or extremely sparse connections between the principal projection cells.

A lack of recurrent excitation is consistent with observations that both background and electrically evoked synaptic excitation in layer II is weak relative to the deeper layers (Jones, 1994; Dhillon and Jones, 2000; Jones and Woodhall, 2005). It is also consistent with the finding that inhibition is the dominant synaptic response onto cells in layer II during electrical stimulation of brain areas outside the MEC, especially at lower stimulation frequencies (Finch et al., 1988; Jones, 1994; Gloveli et al., 1997) and confirms that layer II is unlikely to be the source of spontaneous epileptiform activity *in vivo* (Dhillon and Jones, 2000).

Feedback inhibition mediates interactions between stellate cells

In contrast to the paucity of excitation, inhibition onto stellate cells in layer II appears to be extremely robust. The optogenetic experiments and paired whole-cell recordings described above show that connections from FS interneurons to stellate cells are common and have a substantial effect on stellate cell output. In fact, these experiments are likely to underestimate inhibition as connections may be severed during slicing and not all local FS interneurons were driven to spike during optogenetic stimulation, particularly during pharmacological block of excitation. Moreover, other interneuron types may also make a substantial contribution to overall inhibition.

Other physiological evidence is consistent with robust inhibition in layer II of the MEC. Background inhibition in layer II is high, and much higher than in layer V (Jones and Woodhall, 2005), and electrical stimulation outside of the MEC evokes strong inhibitory responses in layer II cells (Finch et al., 1988; Jones, 1994; Gloveli et al., 1997). Therefore, while inhibition in the MEC may not be as dense as the all-to-all local inhibitory connectivity observed in some neocortical areas with two-photon stimulation (Fino and Yuste, 2011), taken together, the evidence nevertheless indicates that stellate cells are embedded in a densely interconnected inhibitory network.

Excitation from stellate cells onto FS interneurons is also robust with high ($> 70\%$) local connection probabilities. These strong connections have large effects on interneuron output which, as the optogenetic experiments in Figure 4.6 show, in turn influence the membrane responses of other stellate cells in the network. In the absence of direct excitatory connections between stellate cells, this robust feedback inhibition enables communication between stellate cells via indirect inhibitory connections.

Because this feedback inhibition is likely to be critical for generation of grid firing fields, it is interesting to note that the dorsal-ventral spacing gradient evident in grid firing fields does not appear to be reflected by a gradient in inhibition onto stellate cells. Although the lack of a gradient in inhibition onto stellate cells may conceal opposing gradients in FS interneuron mediated and excitation-driven inhibition, the absence of an inhibition gradient onto stellate cells suggests that, despite the impor-

tance of inhibition from FS interneurons, an independent mechanism controls grid field spacing. What mechanism this might be remains unclear, but it is possible that it could involve interactions between cells in layer II and cells in deeper layers, depend on a gradient in intrinsic properties of cells in layer II, perhaps, for example, a gradient in how the inhibitory synaptic transmission is integrated along the dorsal-ventral axis, or depend on gradients in cellular properties in cell types that are not activated during the optogenetic experiments discussed here (O'Donnell and Nolan, 2011).

Local spatial organisation of excitation and inhibition

The magnitude of inhibition from FS interneurons to stellate cells and excitation to interneurons is modulated by physical distance in the network with local inhibition and surround excitation. Direct optogenetic activation of FS interneurons indicates that inhibition from FS interneurons to stellate cells is strongest between local cells, with direct inhibition decaying almost to baseline at distances of only ~300 μm in many cases, despite a wide area (100 μm radius) of activated tissue. In contrast, indirect excitation-driven inhibition extends further, with a peak at 100 μm. This spatial profile is consistent with a surround excitation organisation of the local circuitry, but not with purely local excitation onto FS interneurons.

Further experiments will be required to refine and substantiate the presence of a surround excitation connectivity schema in layer II of the MEC. First, the surround excitation connectivity schema remains to be tested by directly investigating the distance dependent profile of direct excitation onto interneurons. Second, detailed anatomical evidence revealing the spatial extent of stellate and FS interneuron axon arbours may also place restrictions on the exact spatial configuration of the network. Unfortunately, it is not yet clear how existing anatomical data, such as the local grouping of stellate cells into 'patches' (identified by cytochrome oxidase staining) or the mapping of dendritic arborisations to these patches (Burgalossi et al., 2011) could provide insights into the local organisation of feedback inhibition. Third, these experimental results may underestimate the spatial extent of excitation-driven inhibition. Despite the apparent restriction of excitation-dependent inhibitory influence to inter-cell distances shorter than 500 μm (see Figure 4.10 B), because FS interneurons distal to the light source are unlikely to be driven to spike purely by the synaptic input elicited light stimulation of other cells, the inhibitory effects that may result from activation of distal stellate cells may not be detectable in these experimental conditions. Therefore, further experiments will be important to more fully elucidate the local connectivity patterns in layer II.

Because long distance indirect communication between stellate cells separated by more than 500 μm cannot be ruled out, these experiments neither support nor oppose the influential 'lamellar' hypothesis (Andersen et al., 1971) – the idea that information flow in the hippocampal formation propagates from entorhinal cortex through the hippocampus exclusively along narrow *lamellae* (sectional planes) perpendicular to both the dorsal-ventral axis of the MEC and to the septo-temporal axis of the hippocampus (Andersen et al., 1971; Amaral and Witter, 1989). Nevertheless, it does appear that direct connections from FS interneurons to stellate cells are restricted to < 500 μm (and probably less, due to the spatial spread of direct FS interneuron activation by light), as IPSCs were not observed at light distances of 500 μm or greater (see Figure 4.10 B), so it may be possible that monosynaptic connections from FS interneurons to stellate cells are restricted to narrow lamellae along the dorsal-ventral axis of the MEC.

4.4.2 *Computational consequences of feedback inhibition*

A circuit architecture with absent or extremely sparse recurrent excitation between principal cells and locally organised 'surround excitation' places important constraints on our understanding of how layer II of the MEC implements spatial computations. Because grid cells are likely stellate cells, this architecture notably precludes models of grid firing fields that rely on recurrent excitation between grid cells.

Most published models of grid firing fields that utilise attractor dynamics rely on recurrent excitation (Fuhs and Touretzky, 2006; Guanella et al., 2007; Navratilova et al., 2012) and so are inconsistent with experimental findings (Dhillon and Jones, 2000; Pastoll et al., 2013; Couey et al., 2013). However, attractor mechanisms that either depend exclusively on recurrent inhibition (Burak and Fiete, 2009; Couey et al., 2013) or feedback inhibition (Pastoll et al., 2013) are consistent with a lack of recurrent excitation and predict a centre-surround organisation of the grid cell network (Burak and Fiete, 2009; Pastoll et al., 2013). However, of these models, only Pastoll et al. (2013) consider a network organisation with surround excitation and local inhibition, whereas other attractor models that do not rely on recurrent excitation instead propose networks with surround inhibition, but this assumption may be inconsistent with the optogenetic evidence for the spatial organisation of the local layer II microcircuit discussed in this chapter.

Models that rely on oscillatory interference mechanisms (Burgess et al., 2007; Burgess, 2008; Hasselmo, 2008; Zilli and Hasselmo, 2010) may actually benefit from a lack of recurrent excitation between grid cells as this may avoid contamination between cells tuned to different spatial frequencies or different theta oscillation phases. However,

circuits that are hypothesised to provide oscillatory signals may require robust recurrent excitation to overcome the effects of noise (Zilli and Hasselmo, 2010) and therefore any such circuits cannot rely on connections between stellate cells in layer II. Nevertheless, previously discussed considerations argue against this class of model.

Other network properties are also constrained by the layer II architecture revealed by experiments in this chapter. For example, the lack of recurrent excitation limits the locus of plasticity in the network that may be required for changes to grid firing field output, such as when switching between stripe and grid patterns (Krupic et al., 2012), during novelty-induced expansion of grid fields (Barry et al., 2007, 2012) or during modular re-alignment of grid fields (Fyhn et al., 2007; Monaco and Abbott, 2011). Robust feedback inhibition and the lack of recurrent excitation also have implications for the generation within layer II of oscillatory signals that are likely to play an important role in spatial computation (Chrobak and Buzsaki, 1998; Lisman, 2005; Colgin et al., 2009; Reifenstein et al., 2012). In the next chapter I explore what role feedback inhibition plays in generating interacting oscillatory signals that could play a central role in theta-phase precession in layer II (Hafting et al., 2008) and temporal coding schemes more generally.

4.4.3 *Conclusion*

The data and analyses presented in this chapter indicate a circuit architecture in layer II with absent or extremely sparse excitatory connections between principal projection cells and robust locally organised feedback inhibition between these cells and FS interneurons. In addition it appears that the feedback inhibition is locally organised such that FS interneurons preferentially innervate local stellate cells which in turn provide centre surround excitation, preferentially innervating interneurons at intermediate network distances. This connectivity schema is distinct from circuits in the deep layers of the MEC and other cortical areas and must play an important role in generating the characteristic grid firing field functional output of layer II.

5

FEEDBACK INHIBITION ENABLES CLOCK-LIKE THETA-NESTED GAMMA OSCILLATIONS

All work presented in this chapter, with the exception of the data and analyses in Figure 5.13, is adapted from or appears in: Pastoll et al. 2013. Feedback inhibition enables theta-nested gamma oscillations and grid firing fields. *Neuron*. 77, 141–154.

5.1 INTRODUCTION

Neurons can encode information through both the rate and the precise timing of their action potential output (Buzsaki and Draguhn, 2004; Fries, 2009). Activity in networks of cortical neurons oscillates with frequency and amplitude that depends on behavioral state, and these oscillations are believed to be critical for temporal codes that rely on precise spike timing (Buzsaki and Draguhn, 2004; Lisman, 2005; Colgin et al., 2009; Fries, 2009; Canolty and Knight, 2010; Buzsaki and Wang, 2012). In the MEC, oscillatory signals recorded from animals engaged in spatial behaviours are thought to support temporal codes that may play an important role in spatial navigation (Mitchell and Ranck, 1980; Chrobak and Buzsaki, 1998; Hafting et al., 2008). Identifying the cellular mechanisms in the MEC that support these oscillations will shed light on how the circuitry of the MEC enables temporal coding of spatial information.

5.1.1 *Theta-nested gamma as a temporal coding scheme in the MEC*

To enable temporal codes neural systems must encode and transmit information about the exact timing of action potentials. One way to accomplish this is to encode precise times of action potentials by their phase relative to an ongoing oscillatory reference signal. This technique for encoding exact spike times requires only a single frequency oscillation to provide a phase reference signal, but such a minimal system may not be practical as such 'continuous' or exact temporal encoding of spike phase may be unreliable in noisy neural systems. To address this, the reference signal could be discretised into phase 'bins' by superimposing a second, higher frequency oscillation onto the reference oscillation. If spikes that occur within the same high frequency cycle were considered to have the same phase value in terms of the reference

frequency oscillation, this system would provide a readout of reference phase that is relatively robust to noise, as small variations in the phase of spikes relative to the reference frequency cycle would not influence their discretised encoded phase value.

Cross frequency coupling of separate oscillatory signals may support discretised phase encoding of precise action potential timing. Cross frequency coupling of oscillations appears to be a general feature of of cognitive states (Buzsaki and Draguhn, 2004; Canolty and Knight, 2010; Buzsaki and Wang, 2012) and is evident in the neocortex (Canolty et al., 2006), hippocampus (Bragin et al., 1995) and entorhinal cortex (Chrobak and Buzsaki, 1998). Cross frequency coupling can manifest in different ways - for example phase-phase coupling occurs when the phase of each cycle of the high frequency rhythm is locked to different but invariant phases of the slower rhythm, producing a clock-like signal relative the phase of the slower rhythm that can act as a substrate for range of computational strategies (Lisman, 2005; Canolty and Knight, 2010). In contrast, cross frequency phase-amplitude coupling occurs when the amplitude of a faster rhythm is modulated by the phase of a slower rhythm. In this scenario, for example, the high amplitude high frequency activity can be 'nested' in the trough of each low frequency cycle. In this case, if the high frequency oscillation lies in the gamma range (40–120 Hz) and the low frequency signal lies in the theta band (4–12 Hz), the phase-amplitude relation between slow and fast rhythms could be described as theta-nested gamma. Both phase-amplitude coupling and phase-phase coupling may co-exist - for example theta-nested gamma may itself have clock-like properties (see Figure 1.2 B (lower)) which may yet further broaden the repertoire of strategies available for temporal coding.

Oscillatory signals suitable for implementing discretised temporal codes are present in the MEC. In rodents engaged in spatial behaviours a prominent theta rhythm is present in all layers of the MEC (Mitchell and Ranck, 1980; Chrobak and Buzsaki, 1998; Mizuseki et al., 2009; Quilichini et al., 2010). Grid cells in layer II encode space by the phase of their spikes relative to the ongoing theta rhythm (Fyhn et al., 2004; Hafting et al., 2005, 2008; Reifenstein et al., 2012) indicating that the theta signal may act as a slow reference signal for spatial computations based on temporal codes. In addition, oscillations in the high gamma frequency range (~60–120 Hz) are nested within the troughs of the theta LFP signal (Chrobak and Buzsaki, 1998; Colgin et al., 2009), producing a theta-nested gamma signal. Although the gamma oscillations are regular (Chrobak and Buzsaki, 1998), it remains unclear whether the gamma oscillation phase is coupled to the phase of the theta rhythm and hence whether a clock-like reference signal is present in the MEC.

5.1.2 *The relationship between theta and gamma rhythms*

Despite the potentially important role of theta-nested gamma for temporal coding of space, the mechanistic relationship between the theta and gamma rhythms in the MEC is unknown. Establishing the mechanistic relationship between the theta and gamma rhythms in the MEC would therefore shed light on their possible functional interactions, which would have important consequences for theories of temporal coding of spatial information in the MEC. An important question to ask about the mechanistic relationship between the rhythms is whether activation of the layer II circuitry at theta frequency is sufficient to elicit a simultaneous nested gamma rhythm from the same circuit, but this possibility has not been investigated. Because the theta rhythm in the MEC may be imposed onto the layer II circuitry by afferent inputs from theta cells in the medial septum or internally generated in layer II in response to depolarising inputs, I reasoned that recapitulating theta frequency activity in the MEC using an optogenetic method would shed light on the circuit dynamics that are present during theta frequency oscillations in behaving animals.

5.2 METHODS

Optogenetic methods have previously been used to elicit cortical rhythms. Short light pulses (Cardin et al., 2009; Sohal et al., 2009) and sinusoidally modulated light stimuli (Akam et al., 2012) delivered at gamma frequency can directly evoke or entrain gamma activity in neocortex and hippocampus. In addition, steady state (Börgers et al., 2012) and slowly ramped light stimuli (Adesnik and Scanziani, 2010; Akam et al., 2012) can also elicit gamma frequency oscillations through tonic depolarisation of circuits. However, optogenetic activation of circuits using a light stimulus with irradiance sinusoidally modulated at theta frequency has to my knowledge not been previously investigated. Whether optogenetic activation of the MEC layer II circuitry is able to elicit gamma rhythms and whether any gamma rhythms that do develop are able to do so during the brief individual cycles of an imposed theta rhythm therefore remain to be established.

To implement a theta drive to layer II of the MEC I used the Thy1-ChR2-YFP mouse described in Chapters 2 and 4. In this mouse stellate cells and FS interneurons, but not pyramidal cells, express ChR2 in layer II. This enables direct, graded activation of stellate cells and FS interneurons with modulated 470 nm light. As described in Chapter 2 I delivered a narrow (~90 μm) beam of light onto layer II of sagittal slices of the MEC by using an LED directed through the epifluorescence port of the microscope. To activate the layer II microcircuit at theta frequency I used a light stim-

ulation protocol with irradiance sinusoidally modulated at theta frequency (8 Hz). I used sinusoidal modulation in preference to a series of light pulses to avoid sharp onsets and excessive circuit synchronisation resulting from large photocurrents that are generated during rapid irradiance changes. I designed a voltage command to the LED (see Chapter 2, Section 2.5.2) to produce a light stimulus comprising a constant component (8 mW/mm^2) and a sinusoidally modulated component (14 mW/mm^2 trough to peak). The irradiance of the stimulus thus peaked at 22 mW/mm^2 on every theta cycle (the maximum LED irradiance) and decayed to 8 mW/mm^2 at each theta trough (see Figure 5.1 A). This irradiance profile ensured the layer II network was constantly activated for the duration of the stimulus (5 seconds), but was more or less strongly driven depending on the phase of the theta stimulus. Because cells express varying amounts of ChR2, and the peak irradiance during the sinusoidal stimulus was higher than the peak irradiance of the light ramp used to activate cells in Chapter 4, the sinusoidal stimulus is likely to recruit more cells and to activate cells more strongly (Börgers et al., 2012).

5.3 RESULTS

5.3.1 *Theta frequency stimulation generates nested gamma activity*

I found that theta frequency optical stimulation caused local field potential (LFP) oscillations nested within each theta cycle (Figure 5.1 A–C). Filtering the LFP in gamma (50 – 120 Hz) and theta (4 - 12 Hz) bands revealed a theta frequency component directly induced by the light stimulus and a gamma frequency component arising from circuit activation during theta stimulation (Figure 5.1 A). These results demonstrate that optogenetic theta frequency activation of stellate cells and FS interneurons in the layer II microcircuit produces an LFP signal that resembles LFP activity recorded in behaving animals (Chrobak and Buzsaki, 1998) (see Figure 5.2 for comparison).

To further examine the theta modulation of the nested LFP activity and to more accurately determine its frequency I performed time-frequency analysis on traces that were high pass filtered with a low cutoff of 30 Hz to remove the directly light driven theta frequency components (Figure 5.1 B–D). For this analysis I generated scalograms using Morlet wavelets (with the K parameter set to 6). I used this in preference to Fourier methods, as wavelet techniques can provide better resolution of high frequencies in short time windows. For automated analysis I wrote MATLAB scripts that incorporated wavelet functions provided by C. Torrence and G. Compo, which are available at http://atoc.colorado.edu/research/wavelets/. The wavelet analysis clearly shows that the nested LFP activity is restricted to a narrow range of frequen-

cies in the high gamma band, is very similar across theta cycles and coincides well with the trough of the theta cycle, disappearing on the peak of the theta cycle (Figure 5.1 B (upper)). The consistency of the frequency and theta phase of the nested LFP across all recordings is illustrated by the average of the theta-cycle averaged scalograms for all data (Figure 5.1 C). The frequency with peak power (the pseudofrequency corresponding to the peak power from theta cycle averaged scalograms from each cell) revealed that the nested activity had frequency 86.1 ± 2.4 Hz (range 62.4 – 100.8 Hz, n = 13).

These results show that the frequency and theta phase modulation of the optically induced nested LFP activity is similar to the frequency and theta phase of nested gamma activity recorded in the MEC of behaving animals (Chrobak and Buzsaki, 1998; Colgin et al., 2009). Notably, the frequency is much higher than the frequency of pharmacologically induced gamma oscillations, which also lack the prominent theta phase modulation observed *in vivo* (van der Linden et al., 1999; Dickson et al., 2000a; Cunningham et al., 2003; Middleton et al., 2008). Optically induced theta-nested gamma therefore appears to be an excellent model for theta-nested gamma observed *in vivo*.

5.3.2 *The same process mediates field and synaptic intracellular gamma*

Optogenetic recapitulation of circuit rhythms in slice preparations greatly facilitates dissection of the underlying circuitry. To begin to investigate the synaptic mechanisms mediating the nested gamma activity, I recorded membrane currents from SCs in voltage clamp with a holding potential of -50 mV to enable detection of excitatory and proximal inhibitory synaptic currents. I observed outward going nested synaptic currents occurring at the phase of theta corresponding to the peak light intensity and to the trough of the LFP theta. Wavelet analysis revealed an average frequency with peak power of 82.7 ± 2.1 Hz (range 64.2 – 100.8, n = 21) (Figure 5.1 A (lower)), a value very similar to the LFP activity and suggesting that both the LFP signal and nested gamma synaptic current reflect the same process.

To further investigate the relationship between the LFP and intracellular synaptic currents I quantified the relationship between their frequencies and relative timing. To ensure that these analyses were restricted to circuits that were strongly activated, I only analysed data where the maximum field power exceeded 350 pA^2. To investigate the relative timing of the LFP and synaptic activity, I performed cross-correlation analysis on simultaneously recorded LFP and intracellular signals. I found that the timing of the nested synaptic currents was similar to the theta-nested epochs of LFP gamma activity (peak correlation = 0.81 ± 0.02 n = 21) (Figure 5.1 E) with lags dis-

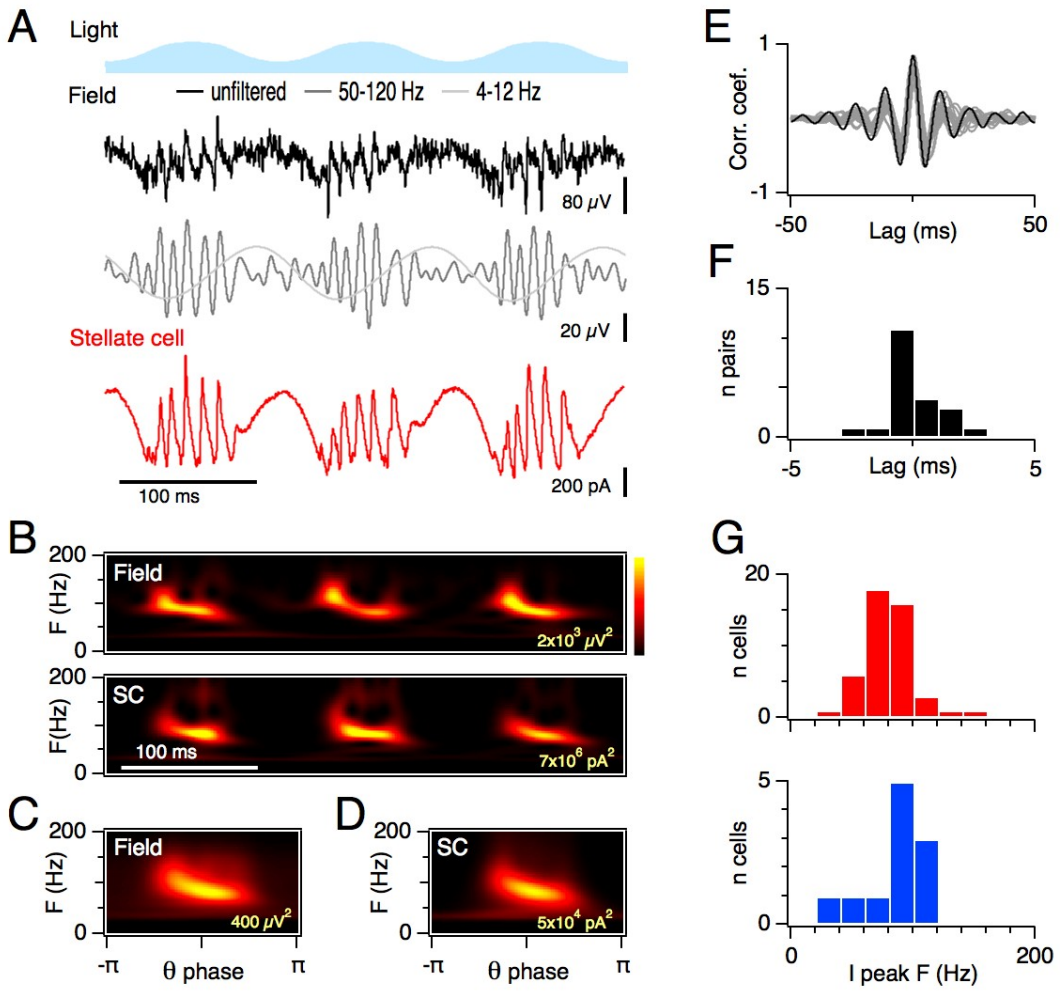

Figure 5.1: **Theta frequency stimulation drives nested gamma oscillations A** Example of extracellular field activity and membrane current recorded from a SC during theta modulated (8 Hz) optical stimulation of layer II of the MEC, illustrating gamma oscillations nested within each theta cycle. The field recording is also shown bandpass filtered to separate theta and gamma activity. **B** Scalograms of field (upper) and synaptic (lower) activity corresponding to data in **(A)**, plotting power for each frequency as a function of time. In all figures the power corresponding to the maximum of the color scale is indicated in the lower right of each plot. **C** Mean scalograms from all recordings of field (n = 27) as a function of phase of theta stimulation. **D** Mean scalograms from all recordings of SC synaptic activity (n = 44) as a function of phase of theta stimulation. **E** Cross-correlations between field potential and SC membrane currents (peak correlation = 0.81 ± 0.02, lag 0.12 ± 0.2 ms, n = 21). Example from **(A-B)** is in black, all other experiments are in grey. **F** Histogram of lag between field and SC synaptic activity calculated from **(E)**. **G** Histograms of the frequency of the peak in the scalogram of membrane currents during theta frequency stimulation of layer II recorded from stellate cells (upper) and from FS interneurons (lower).

tributed tightly around 0 ms (lag 0.12 ± 0.2 ms, n = 21) (Figure 5.1 F). To quantify the relationship between the frequencies I asked whether the frequency with maximum power for synaptic and simultaneously recorded field gamma activity was correlated. I found that the two signals were indeed highly correlated with a high coefficient of

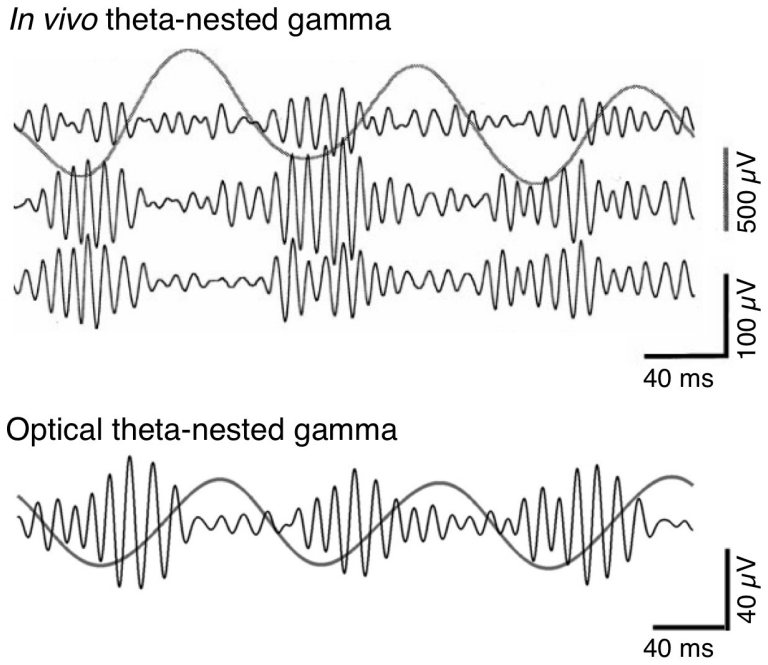

Figure 5.2: **Comparison of *in vivo* and optical *in vitro* theta-nested gamma.** Example LFPs recorded from three sites across layers II - III on a silicon probe from a behaving rat and filtered in the gamma band (black traces), with the MEC theta LFP (grey) superimposed (upper). LFP traces filtered in the theta and gamma bands during optically induced *in vitro* theta-nested gamma (lower) (same traces as in Figure 5.1 A). Top figure panel adapted from Chrobak and Buzsaki. (1998). Gamma oscillations in the entorhinal cortex of the freely behaving rat. *The Journal of Neuroscience*, 78(5):388–398.

determination (slope = 0.94, R^2 = 0.9, p = 4.2×10^{-11}, n = 21). Together, these data indicate that the LFP signal and intracellular synaptic gamma reflect the same circuit process.

Theta nested gamma frequency synaptic currents were also present in FS interneurons, but were inward going. The distributions of the frequency with peak power for all recorded cells were very similar for SCs and FS interneurons and were tightly distributed around their mean values (Figure 5.1 G), indicating that both SCs and FS interneurons participate in the same process.

5.3.3 *Spike firing during nested gamma oscillations resembles action potential output* in vivo

How do different neuron types contribute to the nested gamma activity? The outward-going nested synaptic currents recorded from SCs suggested that nested gamma oscillations involve inhibitory synaptic input to SCs (Figure 5.1 A). I therefore recorded the membrane potential of SCs and nearby FS interneurons during theta stimulation to investigate the temporal relationship between action potential generation in the different cell types and the theta-nested gamma activity (Figure 5.3 A). I found that SCs fired on average 1.5 $\pm$ 0.2 action potentials per theta epoch (n = 55), whereas interneurons fired 13.4 $\pm$ 3.1 spikes per epoch (n = 11), indicating that both these cell types were active during theta-nested gamma.

During optical stimulation the timing of action potential firing by both neuron types was theta modulated (44/48 SCs and 11/11 FS interneurons $P < 0.05$ vs a uniform distribution, Kuiper test). Within each theta cycle the phase of action potential firing by SCs and FS interneurons coincided with the theta phase of nested gamma oscillations (Figure 5.3 A–C), indicating that FS interneuron firing could provide a source of gamma frequency inhibition onto SCs and that SCs could provide gamma frequency synaptic excitation onto FS interneurons. The range of theta phases during which FS interneurons and SCs fired action potentials was similar (mean theta phase of first spike: SC -1.24 rads (from peak), n = 48; FS interneuron -1.72 rads, n = 11, p = 0.79, Non-Parametric Second Order Analysis of angles [NSOA]; mean theta phase of last spike (single spike theta episodes were ignored): SC 0.96 rads, n = 37; FS interneuron 1.12 rads, n = 11, p = 0.37, NSOA), indicating that both cell types are active during the same phase of the theta rhythm. However, I found that the distribution of SC and FS interneuron action potential times differed, with SC action potentials following a bimodal distribution with respect to the theta phase, whereas action potentials fired by interneurons followed a broad unimodal distribution (p = 6×10^{-4}, NSOA)(Figure 5.3 B–C). The frequency and relative timing of action potentials fired

by SCs and FS interneurons (including the bi-modal SC firing distribution) evident during optical theta stimulation is similar to that recorded from neurons in layer II of the MEC during theta activity in behaving animals (Chrobak and Buzsaki, 1998; Hafting et al., 2008; Mizuseki et al., 2009), further indicating that optically generated theta-nested gamma is functionally similar to the theta-nested gamma observed *in vivo*.

Interestingly, despite the prominent gamma oscillations, neither type of cell fired rhythmically at gamma frequencies. During optical stimulation FS interneurons fired at a wide range of rates whereas SCs never fired at the gamma oscillation frequency (Figure 5.3 D–E). Rhythmic firing by FS interneurons at gamma frequency would also be evident as peaks in the theta phase firing distribution, but this was not observed (Figure 5.3 A–C). This suggests that instead of gamma arising from rhythmic patterns of firing by individual cells, the oscillations arise from network interactions between SCs and FS interneurons and that spikes from different subsets of cells contribute to the generation of subsequent gamma cycles (Lisman, 2005).

5.3.4 *Theta-nested gamma is clock-like*

Because gamma oscillations that occur at invariant phases of successive theta cycles would be useful for temporal coding (Lisman, 2005) I asked whether phases of gamma cycles reliably occurred at similar phases of the theta stimulus. Surprisingly, despite the timing and number of spikes fired by stellate or inhibitory neurons differing between theta cycles, in some cells the gamma cycles aligned extremely well across all theta cycles (Figure 5.4 A–B), indicating that the layer II circuitry is able to generate gamma activity with a clock-like structure.

To evaluate how clock-like the gamma oscillations were I quantified the accuracy of the alignment of gamma cycles across theta cycles in each recorded cell. To restrict the analysis of clock-like properties of nested gamma to strongly activated circuits I considered only recordings where the root mean square (RMS) power of the average gamma activity during the theta cycle was > 5 times the average RMS power of baseline (defined as the first and last eighth of every theta cycle) activity. To quantify the variance in the time delay between consecutive gamma cycles a time for a reference gamma cycle must be established. To determine the time of the initial gamma cycle in each theta cycle for each cell I bandpass filtered traces between 60 and 100 Hz and found the median time of the first peak in every theta cycle that exceeded 3 standard deviations of the pre-illumination baseline. I then employed a Hilbert transform to ascertain zero-phase points on the trace and designated the zero-phase point in each theta cycle closest to the median time as the initial gamma cycle peak. In each theta

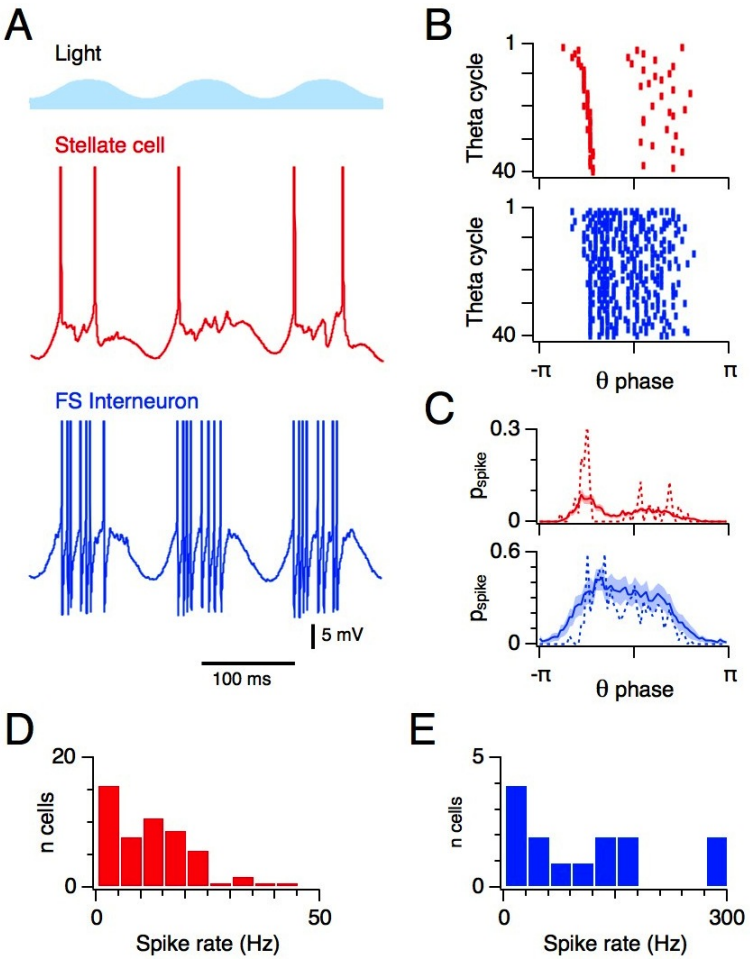

Figure 5.3: **Theta modulation of spiking during theta-nested gamma oscillations**. **A** Examples of action potentials fired by a SC and a FS interneuron recorded simultaneously during 8 Hz light stimulation, illustrating that both neuron types fire action potentials on the phase of the theta cycle at which nested gamma oscillations are observed. **B** Rasters of spikes fired by neurons in **(A)** for 40 consecutive theta cycles. **C** Probability of SC and FS interneuron action potentials for 2 ms windows with respect to the phase of theta stimulation. Solid lines are the population means (± SEM), dashed lines are the examples from **(A)**. **D** Histogram of the mean spike rate of stellate cells during theta frequency stimulation. **E** As for **(D)** except data is for fast spiking interneurons.

cycle, every subsequent zero-phase point corresponded to new gamma cycle. This analysis produced indexed gamma cycles as depicted in Figure 5.4 A–D. I then quantified the reliability of gamma oscillations in two ways. First, I compared the time of each indexed gamma peak during a single theta epoch with the average time of all gamma peaks with that index across all theta epochs. In many cells each indexed gamma peak fell within a 5 ms window of the average time on the majority of theta cycles (Figure 5.4 C). Second, I calculated the average offset of each indexed gamma from the average time gamma peaks with that index. I found that even on the fifth gamma peak of each theta cycle, the difference between the time of each gamma peak and the time of the corresponding average peak could be < 3 ms, compared with the gamma period of > 10 ms (Figure 5.4 D). Thus, for both measures, some, but not all, SCs demonstrated nested gamma activity with timing that is consistent between theta cycles. The reason for this variability is unclear, but because clock-like organisation may require well preserved networks, it may reflect damage to the local circuit inflicted during slicing. Nevertheless, these observations establish that in principle local theta drive to circuits in layer II of the MEC can generate gamma activity with clock-like properties in a substantial fraction of SCs.

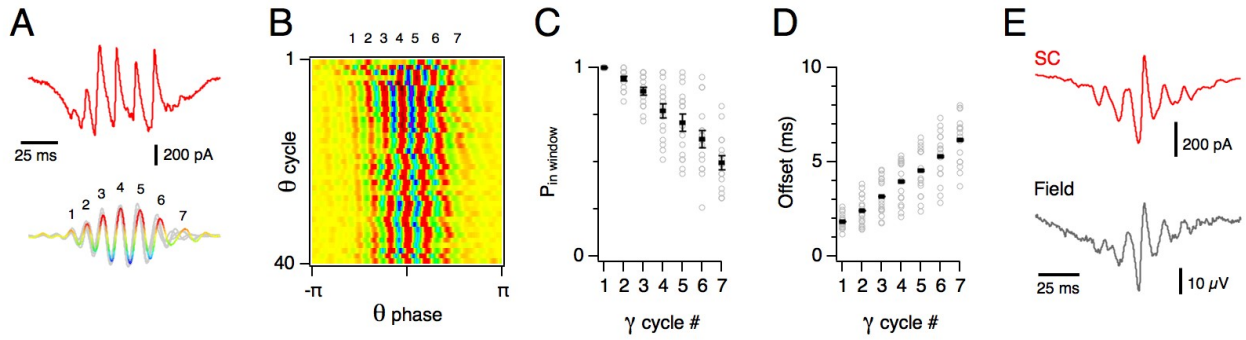

Figure 5.4: **Clock-like properties of nested gamma activity A** Example of a membrane current recorded from a SC during a theta cycle (upper) and corresponding bandpass filtered current (lower, coloured line). Also shown are filtered traces from 4 adjacent theta epochs (grey traces), illustrating the consistency of the nested gamma response between theta cycles. **B** Heat map of membrane currents during 40 consecutive cycles of theta stimulation from the cell in **(A)**. Colour scale and gamma cycles indices correspond to **(A)**. **C** Fraction of gamma cycles on which the peak current differs by less than $\pm$ 5 ms plotted as a function of the index of each nested gamma peak. **D** Average offset of individual gamma cycles compared to the mean gamma cycle plotted as a function of the index of each nested gamma peak. In **(C–D)**, open circles correspond to individual neurons and filled bars indicate the mean$\pm$ SEM (n = 12). **E** Examples of traces obtained by averaging responses triggered from the trough of each gamma cycle recorded simultaneously from a SC (upper) and the nearby field (lower). The side peaks are consistent with periodic gamma activity.

To further compare the timing of optically induced nested gamma with activity recorded *in vivo*, I averaged traces captured by triggering from the negative peak of each gamma oscillation. When nested gamma activity recorded from the MEC of behaving animals is analysed in this way, average traces contain side peaks adjacent to the central peak, indicating periodicity of the gamma activity (Chrobak and Buzsaki, 1998). Applying this analysis to optically induced nested gamma also reveals side peaks adjacent to the central peak (Figure 5.4 E). This analysis may in fact underestimate the theta-phase locking of gamma oscillation because gradual shift of the gamma frequency during each theta cycle will make the theta phase locking appear less reliable than it actually is. This comparison is consistent with the idea that theta-nested gamma oscillations in the entorhinal circuit provide a reference signal for hypothesised coding schemes that require precise temporal coordination of action potential firing (Lisman, 2005; Buzsaki and Wang, 2012).

5.3.5 *Properties of nested gamma oscillations depend on stimulation frequency*

In behaving animals the ongoing theta activity in the MEC has frequency of ~8 Hz (Mitchell and Ranck, 1980). However, it remains unknown whether an ~8 Hz activation frequency has advantages over activation frequencies outside of the the theta range. To test whether the properties of nested gamma oscillations are unique to theta frequency stimulation or whether they generalise to stimulation frequencies outside of the theta range, I additionally tested the response to stimulation below and above the theta range. To do this I changed the frequency of the sinusoidally modulated light stimulus between 2, 8 and 16 Hz (Figure 5.5 A–B) while retaining the same irradiance magnitude and total stimulus duration, so that the total number of stimulation cycles across the entire stimulation protocol was 10, 40 and 80 cycles for 2, 8 and 16 Hz stimulation frequencies respectively. These protocols permitted comparison of the circuit response to a range of stimulation frequencies.

I found that nested gamma activity was maintained during each of the 2, 8 and 16 Hz stimulation frequencies, with nested synaptic activity and LFP signals occurring at similar stimulation cycle phases for each of the different stimulation frequencies suggesting that nested synaptic activity and LFP signals reflect the same process across all the stimulation frequencies (Figure 5.5 A–C). The frequency with maximum power of the nested gamma activity did not vary across stimulation frequencies ($p = 0.12$, ANOVA) (Figure 5.5 D (upper)) and average spike rates were also comparable ($p = 0.99$ ANOVA) (Figure 5.5 D (lower)) indicating that a wide range of stimulation frequencies can elicit nested gamma activity with comparable frequencies and that circuits are equally activated during the different stimulation protocols.

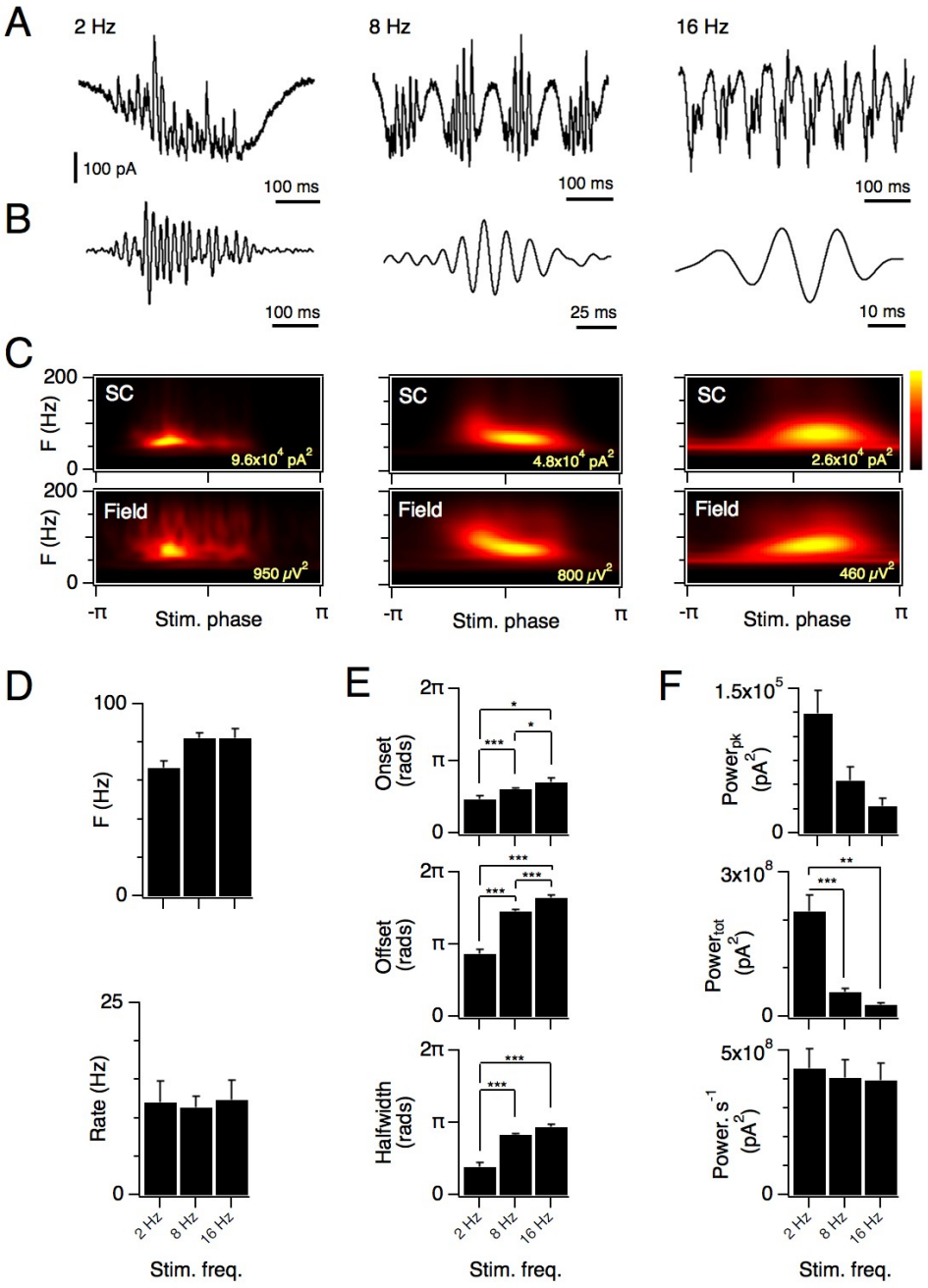

Figure 5.5: **Responses to optical stimulation at 2, 8 and 16 Hz. A** Examples of membrane currents recorded from SCs in response to optical stimulation at different frequencies. The number of gamma oscillations per stimulus cycle depended on the frequency of the optical input ($p < 10^{-9}$, ANOVA), and differed significantly between responses to 8 Hz and 2 Hz stimulation ($p < 10^{-9}$, t-test) and between responses to 8 and 16 Hz stimulation ($p < 10^{-9}$, t-test). The total number of gamma cycles per second of stimulation also depended on the frequency of the optical input ($p < 10^{-9}$, ANOVA), and differed significantly between responses to 8 Hz and 2 Hz stimulation ($p = 0.0003$, t-test) and between responses to 8 and 16 Hz stimulation ($p < 10^{-9}$, t-test). **B** A single stimulus cycle from each trace in **(A)**. The traces are bandpass filtered and the time base modified so that activity is shown relative to the scale of the driving stimulus. **C** Theta cycle averaged scalograms for membrane currents (upper) and field potentials (lower) for the example recordings in **(A–B)**. **D** Frequency of the maximum power (upper) ($n = 6, 45, 4$, $p = 0.12$, ANOVA) and action potential firing rate (lower) ($n = 8, 51, 8$, $p = 0.99$, ANOVA) in response to stimulation at 2, 8 and 16 Hz. **E** Phase of onset (upper) ($p = 4.6\times10^{-6}$) and offset (middle) ($p = 10^{-14}$) and half-width ($p = 1.9\times10^{-11}$), of gamma activity for each stimulation frequency ($n = 6, 45, 4$, ANOVA for all tests). **F** Peak power (upper) ($p = 0.1$), total power (middle) ($p = 9.3\times10^{-9}$) and power normalised to time ($p = 0.99$) (lower) for oscillatory responses to stimulation at each frequency ($n = 6, 45, 4$, ANOVA for all tests). Results of post-hoc t-tests are indicated on each panel, where * is $p < 0.05$, ** is $p < 0.01$, and *** is $p < 0.001$.

Do other properties of the nested gamma differ, despite similar activation of cells and gamma frequencies? To compare the phase and power of the nested gamma activity across different stimulation frequencies I obtained estimates of the stimulation cycle phase onset and offset of gamma (determined using the phases with half-maximum power) and total power in the gamma range (40–120 Hz) for the different stimulation frequencies by analysing scalograms averaged across all theta cycles for each cell. Notably, I found the phase of gamma activity differed between 2 Hz and 8 Hz stimulation (Figure 5.5 E). The phase of maximum gamma power occurred earlier in the 2 Hz stimulation cycle ($p = 0.0005$), and the gamma activity persevered through a narrower phase range of the stimulation cycle ($p = 1.1 \times 10^{-6}$) (Figure 5.5 E (lower)), indicating that gamma activity is maintained for a greater proportion of each cycle for 8 Hz activation. In contrast, while gamma phase of onset and offset differed between 8 Hz and 16 Hz stimulation frequencies ($p = 4.6 \times 10^{-6}$) and $p = 10^{-14}$ respectively) (Figure 5.5 E) the halfwidth of the gamma activity did not ($p > 0.1$). There was no significant difference in the maximum power of gamma elicited by the different stimulation frequencies ($p = 0.1$, ANOVA) (Figure 5.5 (upper)) and whereas the total gamma power per stimulation cycle was highest for the 2 Hz stimulation ($p = 9.3 \times 10^{-9}$, ANOVA) (Figure 5.5 (middle)), the total gamma power per second was indistinguishable across different stimulation frequencies ($p = 0.99$, ANOVA) (Figure 5.5 (lower)). These data and analyses show that while time averaged gamma power does not differ across different activation frequencies, gamma perseveres for larger proportions of the stimulus cycle during activation $\geqslant$8 Hz than for lower activation frequencies, which may have important consequences for temporal coding strategies.

To investigate the relationship between the stimulation cycle phase duration of gamma power and the number of gamma cycles available for coding I counted the average number of gamma cycles per stimulation cycle. To obtain the number of gamma cycles per stimulation cycle I bandpass filtered the data between 60 and 100 Hz and counted the number of peaks that exceeded 1.5 standard deviations of the baseline membrane current, which I defined as the quarter of the stimulation cycle that coincided with the light stimulation intensity trough (the LFP theta peak, or the parts of the trace with the least gamma power). With activation at 2, 8 and 16 Hz I observed 23 ± 0.3, 6.6 ± 0.1 and 2.7 ± 0.2 oscillations per stimulus cycle ($p < 10^{-9}$, ANOVA) (Figure 5.5 A–B) which translates to approximately 46, 53 and 43 gamma cycles per second for each stimulation frequency respectively, with activation at 8 Hz producing the highest number of gamma cycles per second ($p < 10^{-9}$, ANOVA).

Together, these data suggest that layer II of the MEC is configured to generate gamma oscillations for approximately half the duration of each activation cycle, but is less effective at sustaining gamma oscillations during stimulation at frequencies

outside the theta range. Furthermore, although lower frequency activation produces the highest number of gamma cycles per stimulation cycle, activation within the theta range produces the highest number of gamma cycles per second. An ~8 Hz activation frequency therefore appears to combine the highest overall number of gamma cycles available for coding with a high number of gamma cycles per activation cycle, features that play important roles in some temporal coding strategies (Lisman, 2005).

5.3.6 *Temporally coordinated feedback inhibition mediates nested gamma oscillations*

What circuit mechanisms mediate nested gamma oscillations? In principle, gamma frequency oscillatory activity can be generated exclusively by interneuron networks, or by networks that involve coordination of action potential firing by interneurons and excitatory neurons (Tiesinga and Sejnowski, 2009; Fries, 2009; Buzsaki and Wang, 2012). The respective roles of these mechanisms in generating theta-nested gamma oscillations in the MEC are not clear.

Both glutamatergic and GABAergic synaptic transmission are required for nested gamma oscillations

Although excitatory stellate cells clearly participate in the nested gamma rhythm, to assess whether synaptic input from excitatory cells is *required* for nested gamma oscillations I blocked excitatory synaptic transmission pharmacologically. Because variance in gamma power in control conditions was very large, to test for changes between pharmacological conditions I log transformed the gamma power measurements. However, I calculated power reduction factors from the original untransformed data. I found that perfusion of the ionotropic glutamate receptor (iGluR) antagonists NBQX and AP5 reduced total gamma power by a factor of 5.53 in SCs ($n = 23$, $p = 1.1 \times 10^{-8}$, paired t-test) and a factor of 28.9 in FS interneurons ($n = 5$, $p = 4.4 \times 10^{-4}$, paired t-test). As a result, spectral peaks at gamma frequencies were no longer observed (Figure 5.6), indicating that excitatory input from stellate cells is required for the generation of nested gamma activity.

To further investigate how circuit dynamics during nested gamma oscillations depend on excitatory synaptic transmission I compared the effects of blocking excitation on the firing rates and patterns of stellate cells and FS interneurons. Interestingly, antagonists of iGluRs had only very small effects on the mean firing rate (SCs: $p = 0.28$, $n = 24$, FS ints: $p = 0.04$, $n = 8$, paired t-tests) and did not change firing rate distributions (SCs: $p = 0.89$, $n = 24$, FS ints: $p = 0.6$, $n = 8$, Kolmogorov-Smirnov tests) (Figure 5.7 A–C, E–F). Action potential firing remained theta modulated in both conditions (SCs: 18/19 vs 19/19, FS ints: 8/8 vs 6/6, Kuiper tests for uniformity) and there was

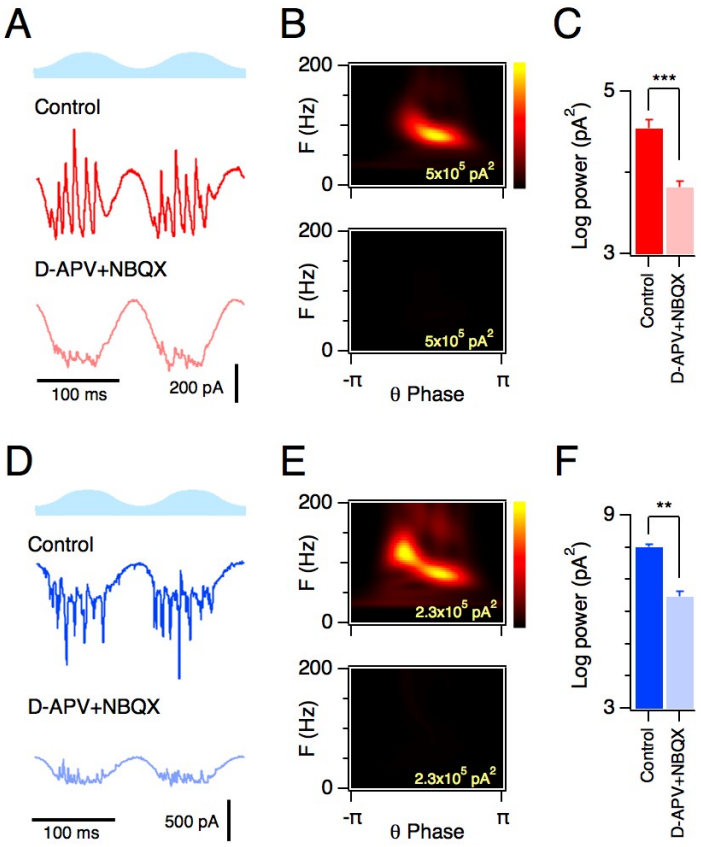

Figure 5.6: **Nested gamma oscillations require feedback inhibition A** Example of nested gamma frequency synaptic currents recorded from a SC before (control) and during block of iGluRs (NBQX + D-APV). **B** Scalograms for all theta epochs from experiment in **(A)** in control (upper) and after block of iGluRs with NBQX and D-APV (lower), demonstrating that iGluRs are required for nested gamma activity. **C** Mean data from all experiments indicating total power in control conditions and during block of iGluRs (n = 23, p = 1.1×10^{-8}, paired t-test). Data are log transformed to reduce the variance for statistical testing. **D–F** As for **(A–C)** except that data are for FS interneurons. For **(F)**, n = 5 and p = 4.4×10^{-4}.

no change of the distribution of spikes fired within theta cycles between the conditions (SCs: p = 0.1, n = 19, FS ints: p = 0.6, n = 6, Moore's test for paired angles) (Figure 5.7 D,H). Therefore the absence of gamma frequency activity during block of iGluRs is not explained by failure of interneurons to generate action potentials during optical theta stimulation. In addition, the lack of rhythmic synaptic activity in SCs during block of excitation indicates that intrinsic excitable mechanisms do not cause FS interneurons to fire rhythmically. Instead, these data indicate that excitatory synaptic transmission mediated by iGluRs is required to coordinate nested gamma frequency activity.

I next tested the role of inhibitory synaptic transmission. Consistent with a major role for GABAergic synaptic transmission in generating nested gamma oscillation, I found that perfusion of antagonists of $GABA_A$ and $GABA_B$ receptors, picrotoxin and CGP55845 respectively, substantially reduced theta-nested gamma activity in SCs (by an average factor of 13.5, p = 0.02, n = 8, paired t-test) (Figure 5.8 A–C). Consistent with an absence of recurrent excitation, block of synaptic inhibition slightly *increased* SC spike frequency (p = 0.046, n = 8, paired t-test) (Figure 5.8 D–F), but did not reduce theta modulation of action potentials fired by SCs (5/7 vs 7/7 significant, Kuiper test for uniformity). In addition, block of inhibitory synaptic transmission did not produce clear excitatory inward currents in recordings from SCs during theta stimulation, even though SCs fired at 13.4 ± 2.7 Hz, suggesting that even with the brighter light stimulus, significant excitation onto SCs is not recruited during generation of nested gamma activity. Together, these data are consistent with a circuit dominated by reciprocal interactions between stellate cells and FS interneurons and suggest that both inhibition onto stellate cells and excitation onto interneurons are necessary to produce nested gamma activity.

5.3.7 *ChR2 photocurrent dominates synaptic current*

In a circuit dominated by reciprocal interactions between excitatory and inhibitory cells the relatively small changes in firing rate occasioned by block of excitation is somewhat surprising. To investigate why the firing rates of stellate cells and FS interneurons only undergo small changes during block of iGluRs I measured the relative magnitude of the photocurrent and synaptically mediated current during light stimulation. Using the outward holding current as a baseline, I found the total net charge transferred before and during block of excitation (Figure 5.9 A,C shaded areas). As with other analyses, I excluded the first two theta cycles from the charge calculation to avoid light onset effects. From the total net charge I derived the average current and obtained the approximate synaptic current as the difference between

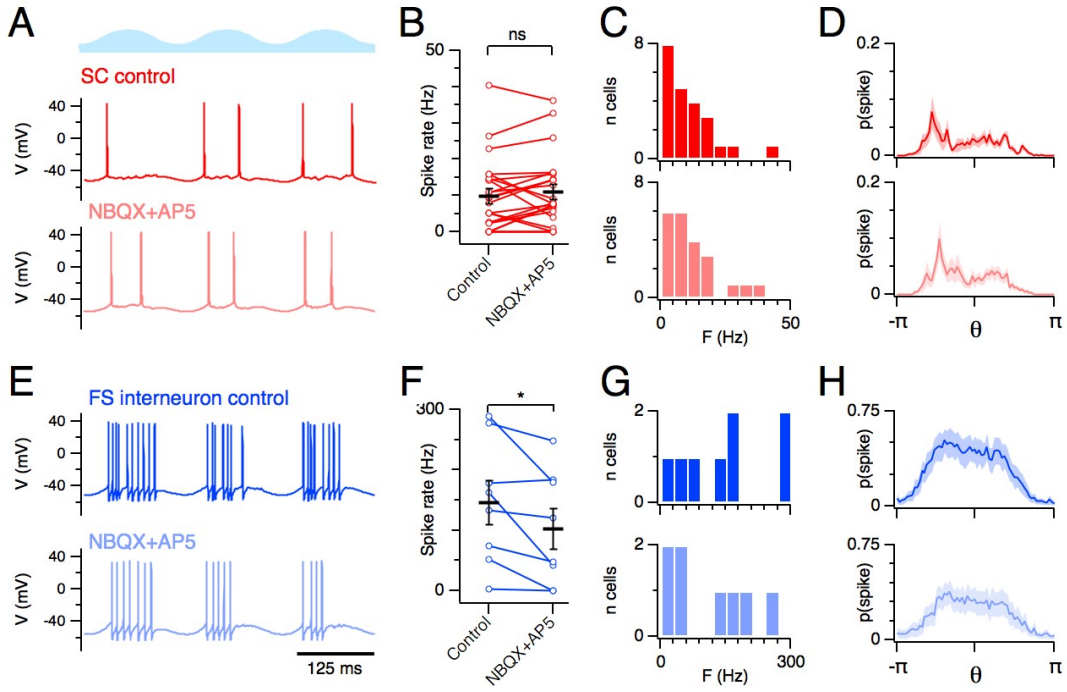

Figure 5.7: **Action potential firing by SCs and FS interneurons is maintained during block of iGluRs. A** Example of membrane potential responses of an SC to theta stimulation of layer II (upper trace) in control conditions (middle trace) and during block of iGluRs with NBQX (5 μM) and D-APV (50 μM) (lower trace). **B** Change in mean firing rate of SCs ($p = 0.28$, $n = 24$, paired t-test) between the pharmacological conditions. **C** Binned mean firing rate distribution for SCs in each condition ($p = 0.89$, $n=24$, Kolmogorov-Smirnov test). **D** Mean distribution of firing probability as a function of theta phase for all SCs. In both conditions firing probability differed as a function of theta phase (18/19 vs 19/19 significant, Kuiper test for uniformity). There was no significant difference between the firing phase of spikes in the two groups ($p = 0.1$, $n = 19$, Moore's test for paired angles). **E** Example of membrane potential responses of a FS interneuron to theta stimulation of layer II in control conditions (upper trace) and during block of iGluRs (lower trace). **F** Change in mean firing rate for interneurons in **(D-F)**, ($p = 0.04$, $n = 8$, paired t-test).**G–H** As for **(C–D)** except data are for FS interneurons (binned mean firing rate distributions: $n = 8$, $p = 0.6$, Kolmogorov-Smirnov test; theta phase distribution of firing: 8/8 vs 6/6 significant, Kuiper test, $n = 6$, $p = 0.6$; Moore's test for paired angles).

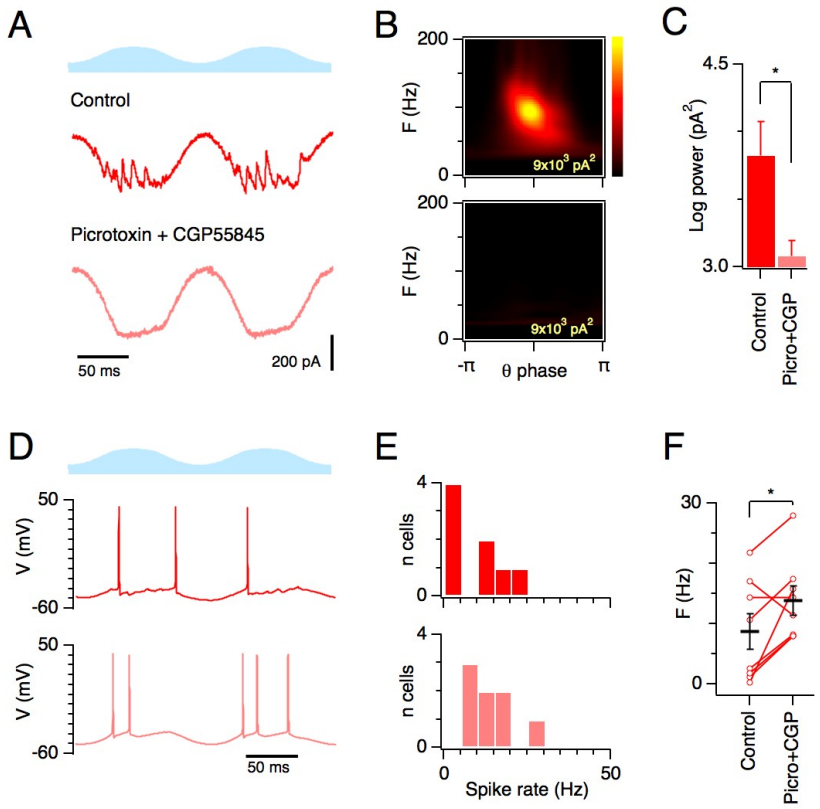

Figure 5.8: **Theta-nested gamma is mediated by feedback inhibition. A** Examples of membrane currents recorded from a SC during theta frequency network stimulation (upper) in control conditions (middle) and during block of GABA receptors with picrotoxin (50 μM) and CGP55845 (1 μM) (lower). Outward going synaptic currents are abolished when GABA receptors are blocked. **B** Average scalogram of synaptic activity recorded from the SC in **(A)** before (upper) and during block of GABA receptors (lower). **C** Total power of the largest peak in the scalogram is reduced by block of GABA receptors (n = 7, p = 0.02). **D** Examples of action potentials fired by an SC during theta frequency network stimulation (upper) in control conditions (middle) and during block of GABA receptors. **E** Binned mean spike frequency in control conditions (upper) and during block of GABA receptors (lower) (p = 0.26, n = 8, Kolmogorov-Smirnov test). **F** Change in mean spike frequency for individual SCs (p = 0.046, n = 8, paired t-test).

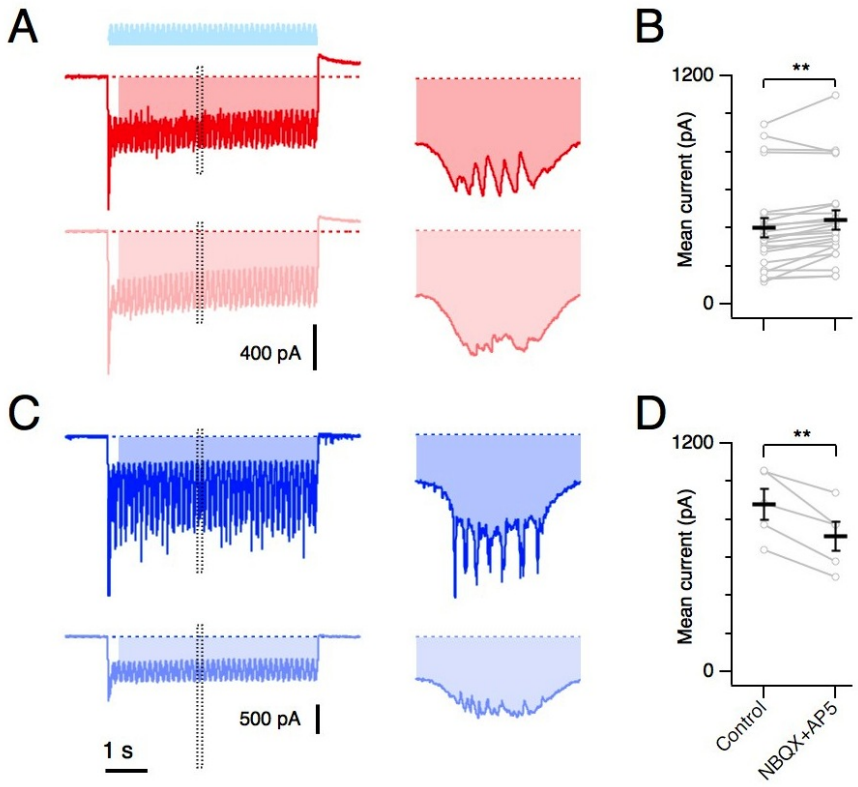

Figure 5.9: **Photocurrent dominates synaptic current during nested gamma oscillation. A** Example of membrane current responses of an SC to theta frequency activation of ChR2 in control conditions (upper) and during block of iGluRs (lower traces). The shaded areas indicate the area between the baseline holding current and the total current used to calculate average light stimulation induced membrane current. Left panels show trace from entire recording, right panels are expansions of the dotted areas in the left panels, showing the relatively small sizeof synaptic currents relative to photocurrents. **B** Change in mean membrane current of SCs ($p = 0.0014$, $n = 23$, paired t-test). **C** Example of membrane current responses of a FS interneuron in control conditions (upper) and during block of iGluRs (lower traces). **D** Change in mean membrane current of FS interneurons ($p = 0.007$, $n = 5$, paired t- test).

the average currents in the two pharmacological conditions. I found that synaptically mediated current was only a small proportion of the total net current in stellate cells (~10 %) and FS interneurons (~19 %) (Figure 5.9 B,D). Therefore, because the majority of the current driving action potential firing is mediated directly by activation of ChR2, which does not appear to change between the pharmacological conditions, spike rates will also not undergo large changes. The main effect of the gamma activity appears therefore to be to regulate the exact timing of spikes rather than to influence the overall firing rates in the circuit, which appear rely on sustained depolarisation of both SCs and FS interneurons and may be achieved *in vivo* by neuromodulatory influence.

5.3.8 *Theta-nested gamma is locally generated in layer II*

The strength of gamma activity has been shown to depend on the number of cells recruited into the network (Börgers et al., 2012) and in the MEC may therefore require interactions between cells in different layers. To determine if theta-nested gamma can be generated in layer II independently of synaptic connections from neurons in deeper layers of the MEC, I recorded from layer II neurons in slices in which the adjacent deeper layers of the MEC had been separated (Figure 5.10 A) (see Chapter 2 for method).

I found that optical theta-nested gamma activity could still be generated in slices in which layers II and III were separated (Figure 5.10 B (left panel), C). Because the characteristics of this gamma were indistinguishable from the optical gamma generated in intact slices, interactions between layer II cells and those in deeper layers of the MEC appear to be unnecessary to produce nested gamma activity. This indicates that the mechanisms required to generate to generate gamma with *in vivo* characteristics are local to layer II.

Some forms of pharmacological gamma in the MEC require recruitment of interneurons with somata in layer III (Middleton et al., 2008). Blocking NMDA receptors abolishes pharmacologically induced gamma activity generated by cells in layer II of the MEC and reveals lower frequency activity that requires interactions with cells in layer III (Middleton et al., 2008). If optically induced gamma were similarly reliant on NMDA receptors, I reasoned that if layer II is separated from the deeper layers and NMDA receptors blocked, gamma activity should disappear. In contrast, I found that gamma activity is maintained after block of NMDA receptors with D-APV in slices where layer II was separated from the deeper layers (Figure 5.10 B (middle panel), C) whereas further block of AMPA receptors with NBQX did abolish the optical gamma (Figure 5.10 B (right panel), C). Therefore, optical theta-nested gamma is generated locally in layer II of the MEC and, unlike gamma induced pharmacologically in layer II, it does not require activation of NMDA receptors.

5.3.9 *Generation of precise timing required for nested gamma*

How is the precise timing of the nested gamma oscillations generated? To analyse the timing of the gamma frequency synaptic currents I bandpass filtered traces between 60 and 100 Hz and cross correlated data from simultaneous SC and FS interneuron recordings. I found that the timing of gamma frequency synaptic currents was strongly correlated between SCs and FS interneurons (maximum correlation 0.56 $\pm$ 0.07), with excitatory input to interneurons preceding inhibitory input to SCs by 2.81

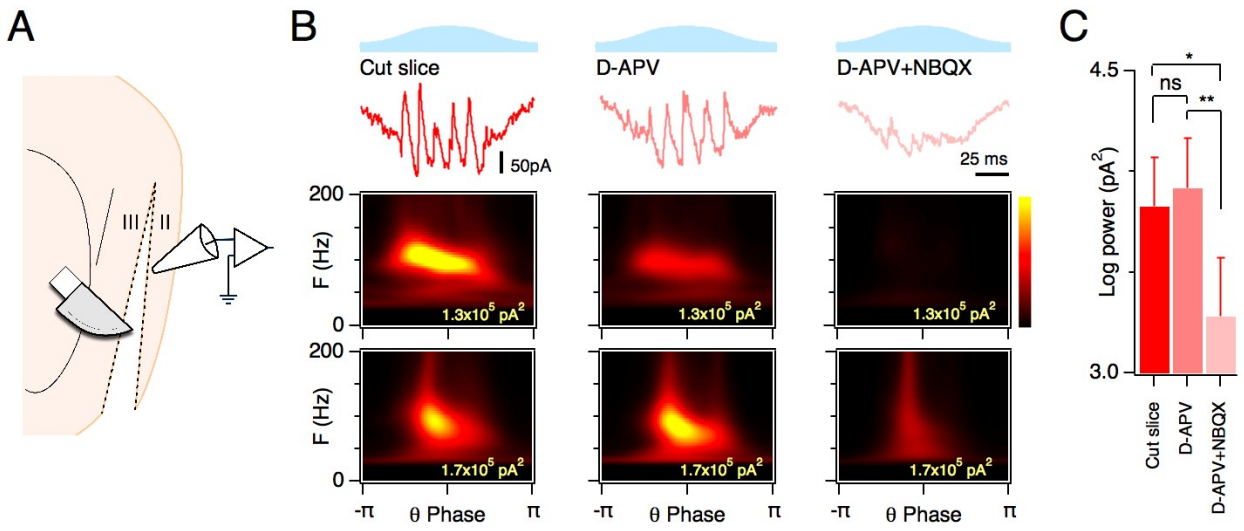

Figure 5.10: **Theta-nested gamma relies depends only on local layer II microcircuitry. A** Schematic indicating the slice cut to separate layers II and III. **B** Examples of synaptic currents (row 2), corresponding scalograms (row 3) and the mean scalograms for all experiments (row 4), each plotted as a function of the phase of theta modulated light stimulation (row 1), demonstrate that nested gamma is maintained when connections between layer II and III are cut (control) and after subsequent block of NMDA receptors with 50 µM D-APV, but is abolished by complete block of iGluRs. **C** Mean power is not significantly different following block of NMDA receptors ($p = 0.53$, $n = 6$, paired t-test), but is then reduced by complete block of iGluRs ($p = 0.0015$).

$\pm$ 0.59 ms ($n = 8$) (Figure 5.11 A–C). Synaptic currents were synchronised between pairs of nearby SCs (with lag < 1 ms), indicating that nearby SCs receive common synchronising drive from inhibitory neurons ($n = 17$) (Figure 5.12). These data suggest that gamma arises from coordinated excitatory input from stellate cells inducing FS interneurons to spike which, in turn, inhibit stellate cells. Then, after a fixed period, the inhibition decays, permitting the stellate cells to spike again and beginning a new gamma cycle.

Do SC and FS interneuron spike times relative to the gamma cycle corroborate this account of gamma generation? Spikes fired by SCs and interneurons were more likely on the rising phase shortly after the trough of the gamma cycle, but were not precisely locked to a particular gamma phase (Figure 5.11 D–F). The preferred firing phase of SCs was at $+0.32 \pm 0.02$ radians relative to the trough of the synaptic gamma oscillation, whereas firing of interneurons was later at $+0.85 \pm 0.02$ radians ($p = 0.002$, $n = 48$ SCs, $n = 11$ FS interneurons, NSOA). Therefore, excitatory SCs fire near the trough of each gamma cycle just as during exploratory behaviour (Chrobak and Buzsaki, 1998). This rapidly triggers spiking by FS interneurons, which then reduce the probability of SC firing until the trough of the next gamma cycle.

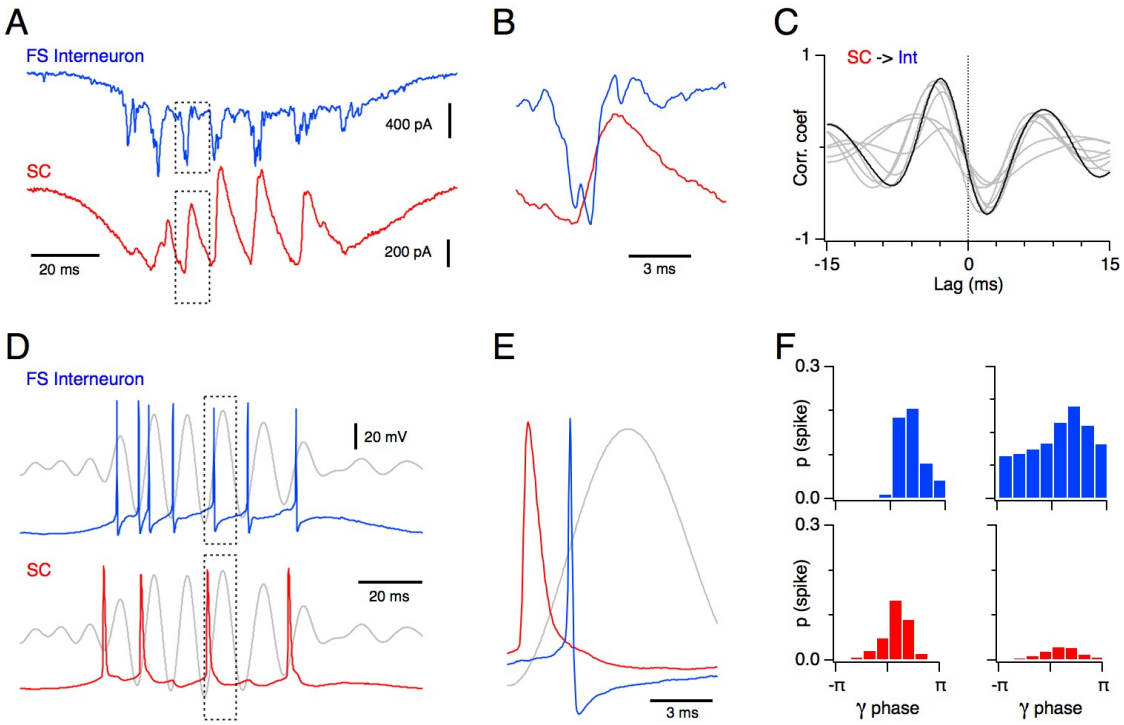

Figure 5.11: **Temporal organisation of synaptic events and action potential activity during nested gamma oscillations. A** Example of synaptic currents recorded simultaneously from a FS interneuron and a SC during a single cycle of theta frequency stimulation. **B** Detail of regions in **(A)** indicated by the box, demonstrates that excitatory input to interneurons arrives before inhibitory input to SCs. **C** Cross-correlation between SC and FS interneuron membrane currents during theta stimulation for the example in **(A-B)** and for 7 other experiments indicates that excitation to interneurons consistently leads inhibition to SCs (maximum correlation = 0.56 $\pm$ 0.07, lag = 2.81 $\pm$ 0.59 ms, n = 8). **D** Example of a simultaneously recorded FS interneuron, SC and extracellular field potential during a single epoch of theta stimulation. **E** Detail from **(D)** illustrating action potential initiation in the stellate cell earlier in the gamma cycle and preceding action potential initiation in the FS interneuron. **F** The probability of action potential initiation as a function of phase of the local field potential gamma signal for interneurons (upper) and SCs (lower) for the example recordings in **(D-E)** (left) and on average for all recordings (right).

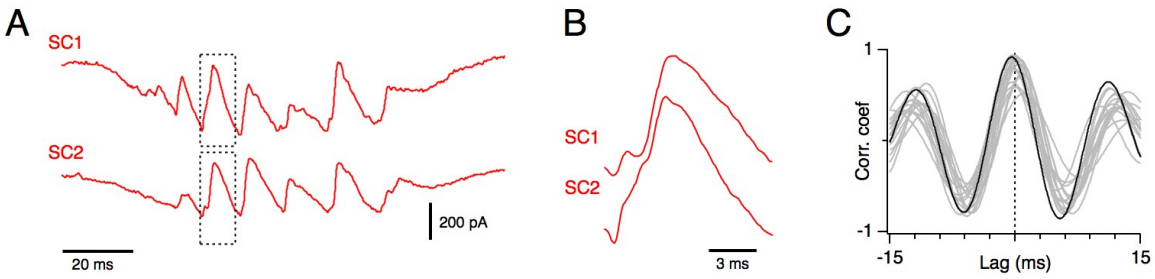

Figure 5.12: **Synchronisation of gamma frequency input to stellate cells by theta stimulation. A** Example of membrane currents recorded simultaneously from two stellate cells during a single epoch of theta stimulation. **B** Compound inhibitory synaptic currents indicated in **(A)** are shown on an expanded time scale. **C** Cross-correlation between membrane currents from simultaneously recorded pairs of stellate cells during theta frequency stimulation. The correlation for the example in **(A–B)** is indicated with a dark line and other cell pairs are indicated with grey lines. The average maximum correlation was 0.71 $\pm$ 0.04 and the lag was 0.077 $\pm$ 0.16 ms.

Together, these data suggest that coordinated timing of action potentials fired by SCs and FS interneurons mediates theta-nested gamma oscillations. This mechanism is distinct from pharmacological models of gamma activity in the MEC in which the frequency of excitatory drive to interneurons is less than the network gamma frequency (Cunningham et al., 2003) and in which NMDA receptor activation is required for oscillations generated within layer II (Middleton et al., 2008). Instead, in optical gamma subsets of SCs induced to fire before the trough of each gamma cycle generate EPSCs in FS interneurons. Action potential firing by FS interneurons then generates feedback inhibition onto SCs. Previous *in vivo* recordings are consistent with the mechanism suggested by these data (Chrobak and Buzsaki, 1998), but because such experiments were correlative they did not enable synaptic mechanisms to be tested directly. These experiments therefore establish a circuit mechanism underlying the generation of theta-nested gamma that is consistent with *in vivo* recordings and explains how theta frequency activation of the local circuitry is sufficient to produce nested gamma oscillations.

5.3.10 *Dorsal-ventral organisation of nested gamma activity*

Grid cell size and spacing follow a dorsal-ventral gradient (Hafting et al., 2005; Brun et al., 2008). Because nested gamma influences stellate cell output, a dorsal-ventral gradient in the properties of gamma activity may help explain the grid cell gradient. To investigate whether gamma properties followed a dorsal-ventral gradient I per-

formed linear regressions of gamma properties against the recorded location of cells along the dorsal-ventral axis.

When all cells with available location data were included there was a shallow but significant relationship between intracellularly recorded synaptic gamma frequency and dorsal-ventral location (R^2 = 0.14, p = 0.009, n = 43). Similarly, log peak synaptic gamma power also followed a shallow dorsal-ventral relationship (R^2 = 0.07, p = 0.04, n = 43) (Figure 5.13 B). Reasoning that optogenetic stimulation might activate dorsal circuits to a greater degree, I asked whether log gamma power predicts gamma frequency, but there was no significant relationship between log gamma power and gamma frequency (R^2 = 0.004, p = 0.28, n = 43) (Figure 5.13 C), suggesting that dorsal circuitry may intrinsically generate both higher frequency and more powerful gamma than ventral circuitry in layer II. However, when the analysis was restricted to fully activated circuits using the same 350 μV^2 criterion cutoff for the LFP power used in Section 5.3.2 no dorsal-ventral organisation of gamma frequency was evident (R^2 = -0.05, p = 0.78, n = 20) (Figure 5.13 D), indicating that fully activated circuits do not produce a gradient in properties of nested gamma. How can these data be reconciled? Figure 5.13 B shows that while many ventral cells have 'normal' gamma power, many also have relatively low gamma power. If ventral circuits are harder to activate, and when not fully activated produce lower gamma with lower frequency and power, this could lead to the apparent shallow dorsal-ventral gradients in gamma frequency and power when all data are included in the analysis.

To investigate whether ventral circuits were relatively poorly activated during illumination I asked whether SC and FS interneuron spike rates followed a dorsal-ventral gradient. I found that, similar to the results obtained during ramped light stimuli, during sinusoidally modulated light stimuli SC spike rates followed a significant dosal-ventral gradient (R^2 = 0.28, p = 5.9×10^{-5}, n = 48) (Figure 5.13 E), suggesting that ventral parts of the layer II network were indeed less activated during the light stimulus. Interneuron spike rates did not appear to follow a gradient I(R^2 = 0.06, p = 0.22, n = 12) (Figure 5.13 D) but because FS interneuron spike rates are extremely variable, the number of data points may not be sufficient to reveal an existing gradient. It remains unclear whether the stellate cell spiking gradient is due to greater ventral inhibition, lower expression of ChR2 or gradients in other intrinsic circuit properties. Therefore, any relationship between gamma properties and dorsal-ventral organisation of grid fields remains to be determined. Nevertheless, these data do show that, when sufficiently activated, circuitry across the dorsal-ventral extent of layer II of the MEC is capable of generating theta-nested gamma with structure resembling that observed *in vivo*.

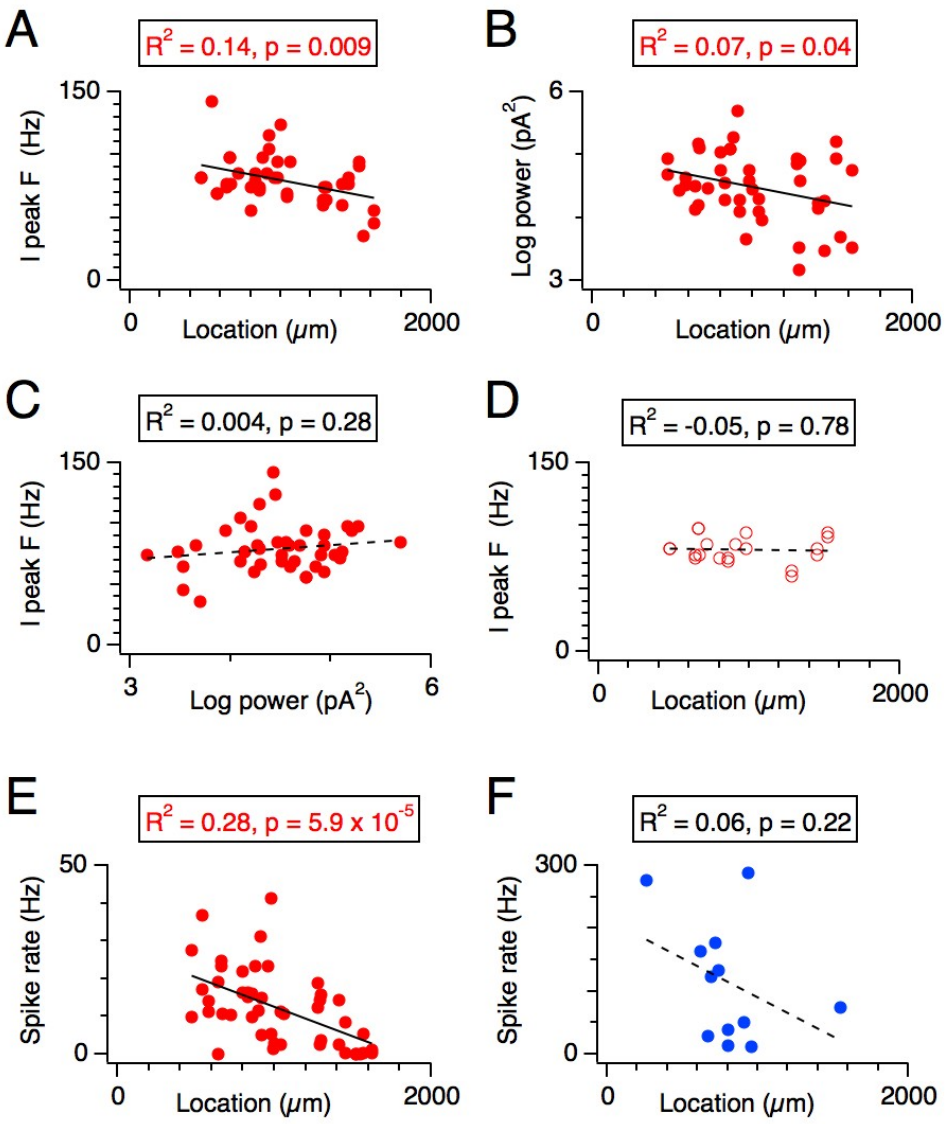

Figure 5.13: **Dorsal-ventral organisation of gamma and spiking frequencies. A** Intracellular synaptic gamma frequency plotted against location along the dorsal-ventral axis of the MEC showing a shallow but significant relationship (n = 43). **B** The log of peak gamma power plotted against location, again showing a shallow but significant relationship between log gamma power and location (n = 43). **C** There is no clear relationship between gamma power and frequency (n = 43). **D** Plot of gamma frequency against location for data from highly activated circuits showing a lack of relationship between gamma frequency and location (n = 20). **E** Plot of average SC spike rate against dorsal-ventral location (n = 48). Ventral cells are significantly less activated than dorsal cells. **F** Plot of average FS interneuron spike rate against dorsal-ventral location (n = 12). There is no significant gradient, possibly due to high variance in FS interneuron firing rates and low cell numbers.

5.4 DISCUSSION

The results discussed above show that an external theta frequency drive to layer II is sufficient for producing theta-nested gamma, indicating that nested gamma can develop and recede rapidly within individual theta cycles. Moreover, *in vitro* optical activation of layer II at theta frequency produces nested gamma activity that closely resembles theta-nested gamma activity observed *in vivo*. Both optical and *in vivo* forms of gamma have similar frequencies in the high gamma range (60-120 Hz) and exhibit very similar phase-amplitude coupling. In addition, during both forms of theta-nested gamma activity cells fire action potentials at similar overall rates (cf. Hafting et al., 2005; Sargolini et al., 2006; Hafting et al., 2008), FS interneuron and stellate cells spikes occur on the same phase of the theta cycle (Chrobak and Buzsaki, 1998; Hafting et al., 2008; Mizuseki et al., 2009) and spikes also occur at the troughs of gamma cycles (Chrobak and Buzsaki, 1998). Furthermore, the highly regular theta-nested gamma observed *in vivo* is consistent with the clock-like gamma produced during optogenetic stimulation. In comparison, previous pharmacological models of gamma in the MEC do not accurately reflect *in vivo* gamma. Instead, both optical and *in vivo* gamma differ from gamma induced by pharmacological methods. First, pharmacological gamma has much lower frequency (30–45 Hz) than optical and *in vivo* gamma and second, pharmacological gamma has no clear relationship to theta activity (van der Linden et al., 1999; Dickson et al., 2000a; Cunningham et al., 2003, 2004; Middleton et al., 2008) and so does not shed light on the mechanistic relationship between oscillations with different frequencies. Furthermore, pharmacological gamma and *in vivo* gamma have different layer-specific gamma phase profiles (Chrobak and Buzsaki, 1998; Cunningham et al., 2003) further suggesting they result from different mechanisms. Optical theta-nested gamma appears therefore to be a better model for *in vivo* theta nested gamma, suggesting that external theta-frequency drive to the MEC may be responsible for generation of nested gamma in behaving animals.

Because of the similarities between optical and *in vivo* gamma, insights into MEC function gained from pharmacological models of MEC gamma may need to be reevaluated. For example, during pharmacological gamma, the frequency of EPSPs onto interneurons during gamma activity can be lower than the gamma rhythm frequency (Cunningham et al., 2003), whereas during optical gamma they are the same, suggesting that instead of MEC gamma being generated by an I–I mechanism, it arises from an E–I mechanism. Optical and pharmacological gamma are further distinguished by contrasting dependence on NMDA receptors (Middleton et al., 2008), with NMDA receptors not being required for generation of optical theta-nested gamma in layer II, suggesting that these receptors are therefore not essential for *in vivo* gamma. These

differences suggest that future work on optically induced nested gamma may challenge other insights into oscillatory dynamics gained from pharmacological induction of circuit rhythms.

5.4.1 *Local feedback inhibition enables local optical theta-nested gamma*

Optically induced *in vitro* nested gamma provides an opportunity to dissect the circuitry underlying gamma generation. In optical theta-nested gamma, gamma oscillations rely on local reciprocal interactions between SCs and FS interneurons, with feedback inhibition onto SCs from FS interneurons reflecting the same process as the LFP nested gamma signal. FS interneurons in layer II do not spike rhythmically, ruling out intrinsic cellular mechanisms for the synaptic gamma recorded in stellate cells. Block of synaptic excitation abolishes gamma oscillations while maintaining interneuron spiking activity near control levels, thereby also ruling out recurrent inhibition between FS interneurons and therefore an I–I schema as a generator of gamma. In addition, optical gamma does not depend on interactions with neurons in the deeper layers of the MEC or other brain areas, as evidenced by the persistence of gamma activity after surgical separation of layer II from deeper layers – concomitant optogenetic activation of severed afferent GABAergic fibres would not lead to synchronised synaptic activity and the absence of synaptic input to stellate cells during block of inhibition indicates that afferent glutamatergic fibres originating from outside layer II remain unactivated. Together, these considerations argue for an E–I mechanism underlying nested gamma generation in response theta frequency activation of MEC layer II cells in behaving animals.

The relative timing of action potentials and rhythmic synaptic activity onto FS interneurons and stellate cells is also consistent with a purely feedback inhibition circuit mechanism. Stellate cell action potentials occur at an earlier phase of the gamma cycle than FS interneuron spikes and synaptic excitation onto interneurons precedes inhibition onto stellate cells by a similar interval. As the inhibition onto stellate cells subsides, they depolarise and spike, triggering a round of excitation onto interneurons and another activation cycle. Theta-nested gamma generated by this mechanism can be clock-like, with the timing of gamma cycles remarkably consistent between theta cycles. Although this phase-phase coupling of theta and gamma rhythms has not been previously described in entorhinal cortex, it is consistent with gamma activity recorded in behaving animals (Chrobak and Buzsaki, 1998). Together, these data indicate that layer II contains cellular machinery sufficient to generate theta-nested gamma with clock-like properties that support a range of temporal coding strategies.

5.4.2 *Local clock-like gamma enables temporal coding in MEC*

If external control of localised circuits at theta (or another) frequency is able to produce clock-like gamma, a wide range of coding and communication strategies become available for spatial computation in the MEC. First, nested gamma oscillations in layer II of the MEC may enable coincident firing of ensembles of SCs within time windows required for coincidence detection by downstream neurons in the dentate gyrus or other areas (Chrobak and Buzsaki, 1998; Buzsaki and Wang, 2012). Second, cross frequency phase-phase coupling provides a means to control the gain of information transfer between two connected regions (Canolty and Knight, 2010). Externally imposed clock-like theta-nested gamma provides a mechanism for implementing such gain control. If maximum information transfer is desired, two separate local circuits could be driven at a common frequency in the theta range with appropriately offset theta phases. Action potentials generated at the trough of LFP gamma cycles in the upstream area would arrive at the trough of gamma, when excitability of the downstream area is at its highest, thereby having a large effect on output in the downstream area. Conversely, if minimum gain is desired, simply shifting the phase of the imposed theta oscillation in one area could cause spikes to arrive at the downstream area at the peak of the gamma LFP, minimising their impact on downstream processing (Fries, 2009; Buzsaki and Wang, 2012). This would provide a means of synchronising the MEC output with its downstream targets, the dentate gyrus and CA1 (Colgin et al., 2009). Similarly, it could be employed to tune the effect of cortical inputs on MEC processing. Third, because different information could be encoded on separate gamma cycles (Lisman, 2005), clock-like theta-nested gamma could be used to encode and communicate temporally organised sequences of information. This may, for example, play a role in theta-phase precession of action potentials (Hafting et al., 2008) for which the role of gamma is currently unclear. Because the number of gamma cycles per theta cycle would be important for sequence coding, a theta frequency to drive circuits rather than another frequency outside the theta range, could provide an optimal compromise between the high number of gamma cycles per stimulation cycle associated with low frequency drives and the greater total number of gamma cycles available for coding associated with high frequency drives. Such communication and coding strategies are, however, likely not always active. Many cells in the rodent MEC are not theta modulated *in vivo* (Krupic et al., 2012) and MEC theta in bats is largely absent (Yartsev et al., 2011), suggesting that these mechanisms are not required for all MEC functionality and may only require the involvement of subsets of cells even in animals that do exhibit theta oscillations during behaviour.

5.4.3 *Conclusion*

Feedback inhibition in layer II of the entorhinal enables clock-like theta-nested gamma oscillations that may support a diverse range of temporal coding schemes. Because grid cells encode space using a rate code and rely on the same layer II circuitry it appears that a common microcircuit architecture may subserve both temporal and rate coding schemes. If these coding schemes process information in parallel it suggests that the cortical circuit architecture present in layer II of the MEC may be optimised to allow multiplexing of separate streams of information.

6

CONCLUSION

The medial entorhinal cortex is an important area for spatial learning and memory (Good and Honey, 1997; Steffenach et al., 2005; McNaughton et al., 2006; Jeffery, 2007). In behaving animals the output of cells in layer II of the MEC encodes space with rate coded grid firing fields (Hafting et al., 2005) and LFP activity provides a substrate for temporal coding of space by phase precession of action potentials relative to the theta frequency oscillations (Hafting et al., 2008), suggesting that separate and parallel coding schemes may underlie spatial computations performed in the MEC. The primary aim of the work presented in this thesis has been to elucidate MEC layer II circuit properties that could underpin and shape the grid firing fields and theta-nested gamma oscillations that are thought to mediate spatial computations in the MEC and the wider hippocampal formation (Lisman, 2005; McNaughton et al., 2006).

6.1 SUMMARY OF FINDINGS

To provide insights into how circuitry in layer II of the MEC generates its characteristic output I focussed on (i) characterising the intrinsic electrical properties of stellate cells in layer II, (ii) examining connections between different cell types that constrain the functional output of the area and (iii) recapitulating *in vivo* rhythms *in vitro* to enable functional circuit dissection during activated circuit states.

6.1.1 *The contribution of stellate cell intrinsic electrical properties to layer II circuit function*

Glutamatergic stellate cells are the most abundant cell type in layer II, form the majority of the output of layer II to the hippocampus and have long been thought to be grid cells (see e.g. Brun et al., 2008; Burgalossi et al., 2011), a proposition recently supported by *in vivo* whole-cell recordings from stellate cells in mice running on linear tracks (Domnisoru et al., 2013; Schmidt-Hieber and Häusser, 2013). Because of the central role that stellate cells are thought to play in the layer II network, their intrinsic electrical properties have received much attention, but exactly how their intrinsic electrical properties contribute to layer II circuit output remains unclear.

The task of evaluating how the intrinsic properties of stellate cells might contribute to the output of layer II has been hampered due to conflicting results being produced by different recording techniques. To address conflicting data produced by whole-cell and sharp electrode recording techniques and to obtain recordings with minimal disruption of intracellular processes, I examined intrinsic properties of stellate cells using the perforated patch-clamp recording method.

I found that the perforated patch recordings substantiated many intrinsic properties of stellate cells exhibited during recordings using the other techniques. For example, the input resistance, membrane time constant and resonant membrane frequency all follow dorsal-ventral gradients similar to those in studies using other recording techniques (Giocomo et al., 2007; Garden et al., 2008; Boehlen et al., 2010). In addition, analysis of peri-threshold membrane potential theta frequency fluctuations reveals that, similar to the results obtained during whole-cell recordings (Dodson et al., 2011), the fluctuations contain multiple frequency components that are unstable over time and therefore appear to be unsuitable for computations that require interactions between predictable and stable frequencies.

In contrast, however, the perforated patch experiments also showed that many intrinsic properties of stellate cells measured with this method differ from measurements by whole-cell and sharp electrode recording techniques. For example, perforated patch recordings indicate that stellate cells are more excitable than other recording methods suggest, and, when directly compared to whole-cell recordings, cells have narrower AHPs and spike clustering is much more robust. In addition, putative dorsal-ventral gradients in resonance magnitude (Boehlen et al., 2010) and spike clustering (Pastoll et al., 2012) that are present during whole-cell recordings do not follow a dorsal-ventral organisation in the perforated patch recordings.

Many models of grid cell function remain relatively unconstrained by known intrinsic properties of stellate cells (Giocomo et al., 2011b; Zilli, 2012). The results from perforated patch recordings provide accurate estimates of important intrinsic properties of stellate cells that could be used to constrain and improve future models of grid cell function. Such models may eventually prove crucial to understanding the link between intrinsic stellate cell properties and MEC circuit outputs.

6.1.2 *Functional dissection of the layer II microcircuit*

Despite the importance of the layer II circuitry for spatial computation, the organising principles of the circuitry remain largely unclear. Few of the synaptic inputs to and between electrophysiologically identified layer II cells have been definitively established, severely limiting our understanding of layer II function. To elucidate the

organising principles of the layer II circuitry I investigated connectivity between different cell types in layer II using both paired recordings and optogenetic techniques.

Consequences for the lack of recurrent excitation between stellate cells

One salient unresolved issue that previous studies have failed to definitively address has been the question of whether or not functional connections exist between excitatory stellate cells in layer II. On the one hand, paired intracellular recordings have not revealed functional connections (Dhillon and Jones, 2000) – on the other hand, indirect methods including glutamate uncaging (Kumar et al., 2007; Beed et al., 2010) and spiking probability analysis of *in vivo* extracellular recordings (Quilichini et al., 2010) have suggested that recurrent excitatory connections are in fact present in layer II. Because paired recordings may suffer from bias and undersampling, and indirect methods do not guarantee the identity of the source of excitatory inputs to recorded cells, these experiments have not been regarded as definitive. The experiments reported in Chapter 4 addressed this issue by adopting an optogenetic approach. Using a transgenic mouse line expressing ChR2 in stellate cells, but not pyramidal cells in layer II or adjacent layers, the postsynaptic effects of unbiased concurrent activation of large populations of stellate cells could be examined in recorded stellate cells. The absence of light-driven synaptic excitation onto stellate cells during recordings indicated that connections between stellate cells are in fact absent or extremely rare. This result was corroborated by additional paired recordings in the same slice preparation that also failed to detect connections between stellate cells. These findings are consistent with previous paired recording experiments (Dhillon and Jones, 2000) and have been further supported both by subsequent recordings from hundreds of pairs of stellate cells and by systematic optogenetic probing of connections between stellate cells (Couey et al., 2013).

The absence of recurrent excitation between stellate cells has important implications for layer II function beyond establishing an unusual connectivity principle. First, while these results do not rule out connections between pyramidal cells, they do suggest that the recurrent excitation required by some influential models of grid cell generation based on support attractor network dynamics (Fuhs and Touretzky, 2006; Guanella et al., 2007; Navratilova et al., 2012) is unlikely to be present layer II. Second, it limits the locus of plasticity that networks may depend on during grid field adaptation or expansion (e.g. Barry et al., 2007, 2012). Finally, the lack of recurrent excitation strongly suggests that layer II is unlikely to play a major role in the genesis of epileptiform activity in the hippocampal formation, as has previously been proposed (Kumar et al., 2007).

Stellate cells are embedded in dense inhibitory networks

Despite the importance of elucidating the nature of connections between stellate cells and interneurons in layer II for understanding computations in the MEC, the nature of interactions between these cell types has remained unknown. Optogenetic activation of the layer II circuit revealed a prominent excitation-driven component of inhibition onto stellate cells and paired recordings independently demonstrated abundant bi-directional connections between stellate and fast spiking interneurons. These findings (discussed in Chapter 4) show that stellate cells form functional connections with FS interneurons in layer II and that therefore, despite the lack of recurrent excitation, stellate cells can communicate with each other via indirect inhibitory connections. This circuit organisation is consistent with subsequently published research showing that in multiple simultaneous recordings spiking stellate cells produce inhibitory responses in other stellate cells that appear to be mediated by fast spiking interneurons, but do not involve interactions with low threshold spiking interneurons (Couey et al., 2013). The layer II circuitry therefore appears to be characterised by dense reciprocal inhibition between stellate cells and FS interneurons, raising the question how such a circuit organisation is able to support grid firing field generation.

Surround excitation in layer II of the MEC?

How might dense feedback inhibition in layer II support grid firing fields? Continuous attractor models of grid cell generation rely on circuit schemas where the likelihood and strength of connections between cells varies with the distance between cells in the network (Fuhs and Touretzky, 2006; Guanella et al., 2007; Burak and Fiete, 2009; Navratilova et al., 2012). The experiments discussed in Chapter 4 therefore aimed to address the question of whether the local spatial organisation of either inhibitory or excitatory connections resembles the centre surround configurations that have been proposed to be suitable for grid firing field generation (Fuhs and Touretzky, 2006; Guanella et al., 2007; Burak and Fiete, 2009).

Spatially restricted optogenetic activation of the layer II circuit along the dorsal-ventral axis at different distances away from recorded stellate cells produced distance-dependent profiles of the magnitude of direct inhibition and excitation-driven inhibition onto stellate cells. Critically, the observed profile of directly activated inhibition peaked at the position of recorded cells whereas the spatial profile of excitation-driven inhibition peaked at distances ~100 μm away from recorded cells. These spatial profiles are consistent with predictions made by circuits with surround excitation and local inhibition, but do not match the qualitative predictions of other circuit organisations. These results therefore suggest that grid firing fields may rely on surround

excitation in layer II. However, because these experiments do not activate pyramidal cells or other types of interneurons that do not express ChR2 (possibly including low threshold spiking interneurons), they cannot by themselves establish whether feedback inhibition with a surround excitation organisation is sufficient to produce grid firing fields or whether additional circuit elements may be required.

6.1.3 *Optical recapitulation of theta-nested gamma oscillations*

Theta-nested gamma LFP oscillations are a prominent feature of neural activity in behaving animals (Mitchell and Ranck, 1980; Chrobak and Buzsaki, 1998; Colgin et al., 2009) but the circuit mechanisms governing the relationship between different rhythms have not been well understood. The experiments discussed in Chapter 5 demonstrate that local theta frequency optogenetic activation of the layer II network produces nested gamma oscillations that closely resemble *in vivo* theta-nested gamma activity and which exhibit clock-like properties. The phase-amplitude and phase-phase coupling between the theta and gamma rhythms elicited in the MEC reveal that the circuitry is capable of generating rhythmic activity that could support a wide range of temporal coding strategies which may be important for spatial learning and memory (Buzsaki and Draguhn, 2004; Lisman, 2005; Fries, 2009; Fell and Axmacher, 2011; Buzsaki and Wang, 2012).

The sufficiency of theta frequency activation for nested gamma oscillations indicates that gamma activity can develop and synchronise within individual theta cycles in layer II of the MEC, but exactly how the gamma develops so rapidly or why the gamma activity is not clock-like in all cells remains unclear. While the mechanisms that generate theta frequency oscillations in the MEC remain unknown, these experiments suggest that theta modulated synaptic input (e.g. from the medial septum) targeted to spatially restricted parts of the layer II network may be able to independently control the generation of gamma oscillations at multiple locations in the layer II network. The sufficiency of theta activation for nested gamma oscillations may facilitate synchronisation of gamma activity between different areas driven by a common source. In particular, control of clock-like gamma in this manner could enable control over precise synchronisation of gamma cycles in two circuits by a third area that provides theta frequency input, thus facilitating transmission of information between the gamma synchronised areas (Buzsaki and Draguhn, 2004; Fell and Axmacher, 2011; Buzsaki and Wang, 2012).

Data presented in this thesis show that theta-nested gamma in layer II of the MEC is mediated by feedback inhibition. Whole-cell recordings during optical theta-nested gamma indicate that reciprocal synaptic interactions between fast spiking interneu-

rons and stellate cells underlie nested gamma generation. The relative timing of EPSCs onto fast spiking interneurons and IPSCs onto stellate cells, combined with the analysis of the gamma phase of spiking of each cell type indicates that temporally co-ordinated stellate cell spiking drives co-ordinated spiking of fast spiking interneurons, producing inhibition onto stellate cells. Only after the inhibition decays do stellate cells fire again, initiating a new gamma cycle. In the MEC this feedback inhibition mechanism generates nested gamma with frequencies in the high gamma range, and is distinct from pharmacological models of gamma which may depend on alternative mechanisms and exhibit gamma oscillations with frequency restricted to the low gamma range (see e.g. Cunningham et al., 2003; Middleton et al., 2008).

Changes to the layer II circuitry may underlie deficits in rhythm generation in the MEC and may help to explain behavioural deficits associated with mental disease. For example, pathophysiological oscillatory dynamics are common in Alzheimer's disease (Jeong, 2004), a condition associated with deficits in spatial memory and navigation (Pai and Jacobs, 2004). The superficial MEC is particularly prone to degeneration during Alzheimer's disease (Braak and Braak, 1985) suggesting that damage to the entorhinal networks may undermine normal rhythm generation. Knowledge of the circuit mechanisms underlying theta-nested gamma generation afforded by the optical model of *in vivo* theta-nested gamma could provide insights into which aspects of layer II circuitry in compromised neural tissue are relevant to rhythm generation.

6.1.4 *A common circuitry for rate and temporal coding in the MEC?*

Although feedback inhibition in layer of the MEC must play an important role in producing rate coded grid firing fields and supports theta-nested gamma oscillations with properties suitable to act as reference signals for temporal coding, it does not necessarily follow that circuits comprising only connections between excitatory and inhibitory cells can simultaneously generate both grid firing fields and signals suitable for temporal coding of space. Pastoll et al. (2013) addressed this question by investigating whether an attractor model of spiking integrate and fire neurons is able to simultaneously produce grid firing fields and theta-nested gamma oscillations.

In the model, consistent with the principle of of layer II circuit organisation established above, excitatory and inhibitory cells were reciprocally connected in a surround excitation configuration (Figure 6.1 A (cf Figure 4.9 E)) whereas connections between cells of the same type were not present (Pastoll et al., 2013). When provided with feedforward input that had magnitude modulated by movement direction and speed, the network produced grid firing fields in excitatory cells resembling those

observed *in vivo* (Figure 6.1 B), indicating that a surround excitation configuration of a purely feedback inhibition circuit is capable of generating grid firing fields. Interestingly, inhibitory cells in this model configuration produce inverted grid firing fields (Figure 6.1 C), a testable prediction that could distinguish between alternative circuit configurations. Importantly, when the magnitude of the feedforward input was modulated at theta frequency, not only were grid fields maintained, but the network also developed theta-nested gamma oscillations that manifested as inhibitory and excitatory nested gamma synaptic inputs to excitatory and inhibitory cells respectively (Figure 6.1 D) and had frequency comparable to both optically induced (see Chapter 5) and *in vivo* nested gamma in rodents (Chrobak and Buzsaki, 1998; Colgin et al., 2009). Together, these simulations show that circuitry comprising only reciprocally connected pools of inhibitory and excitatory cells in a surround excitation configuration is able to simultaneously produce rate coded grid firing fields and reference timing signals for temporal codes of space, suggesting that the MEC is able to multiplex rate and timing codes of space in behaving animals. If simple neural circuit schemes can support parallel rate and temporal coding of information, multiplexed coding schemes may be a common feature of cortical circuitry, suggesting that cortical circuits may have evolved to efficiently encode and transmit information by utilising parallel streams of information.

6.2 FUTURE WORK

Despite the increasing availability of detailed information about the circuitry of the MEC and continuously improving characterisations of the striking patterns of neural activity that it generates, the path from MEC circuitry to spatial behaviour remains largely unclear. Notably, the link between the observed physiological output of cells in the MEC and animals' navigational abilities remains to be directly tested in a manner that does not indiscriminately disrupt neural function in the MEC. While rate coded spatially modulated output (including grid firing fields (Hafting et al., 2005) and other types spatially modulated patterns of activity (Fyhn et al., 2004; Solstad et al., 2008; Krupic et al., 2012)) and theta phase precession of action potentials (Hafting et al., 2008) have been shown to *encode* space, the failure to establish a causal relationship between distinct features of these neural activity patterns and spatial behaviour prevents a complete understanding of the role of these patterns in spatial processing. Unfortunately, targeted and selective manipulation of activity patterns in the MEC of behaving animals remains extremely difficult, partly due to technological restrictions but also largely because our understanding of how different elements of the MEC circuitry interact to produce its characteristic output remains limited. To en-

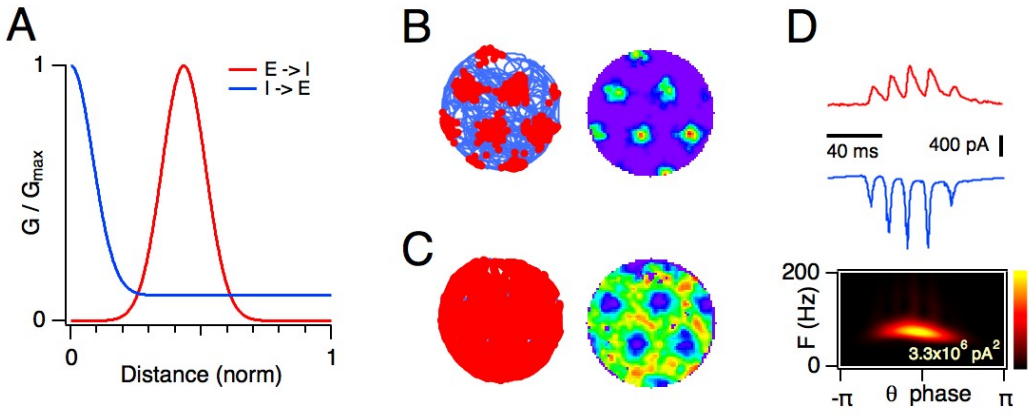

Figure 6.1: **Feedback inhibition enables multiplexing of grid firing fields and theta-nested gamma oscillations**. **A** Configuration of connectivity in the model. The distance dependent connectivity profiles of excitation onto inhibitory cells (red) and inhibition onto excitatory cells (blue) reflect a surround excitation organisation of the circuitry qualitatively similar to that shown in Figure 4.9 E. **B** Example grid firing field of an excitatory cell (left) showing the track of simulated mouse position (blue) and location of action potentials (red) and normalised rate map of action potential output (right). **C** Example inverted grid firing field of an inhibitory cell in the network (left) showing the locations of action potentials and associated normalised rate map (right). **D** Example nested gamma activity in a simulated excitatory cell (top, red) and inhibitory cell (blue, middle) during a single theta stimulation cycle and associated average scalogram for the nested synaptic gamma activity in the excitatory cell (bottom), revealing a nested gamma frequency of ~80 Hz. *All data and graphs in this figure were provided by Lukas Solanka.*

able more concrete predictions about how manipulation of specific circuit properties might alter patterns of neural activity *in vivo*, the relationship between the functional properties of the MEC circuitry and its output patterns during behaviour needs to be more fully understood.

6.2.1 *Identification and manipulation of intrinsic electrical properties relevant to MEC output*

The intrinsic electrical properties of cells in the MEC enable and constrain the circuit's functionality. However, it is often difficult to identify which of these properties are critical for observed patterns of neural activity, especially in the absence of a theoretical framework, as obvious links between intrinsic properties and output may be scarce. Identification of behaviourally relevant intrinsic properties has thus relied on heuristic approaches.

One such heuristic approach flags as important intrinsic properties that vary systematically along the dorsal-ventral axis of the MEC (e.g. Giocomo et al., 2007; Garden et al., 2008; Boehlen et al., 2010) because they reflect the dorsal-ventral organisation of grid field size and spacing (Hafting et al., 2005; Brun et al., 2008). However, significant doubt has been cast on the relevance to *in vivo* activity of some intrinsic properties with dorsal-ventral gradients, (e.g. peri-threshold membrane potential theta frequency fluctuations (Giocomo et al., 2007) do not persist in high conductance conditions *in vitro* (Fernandez and White, 2008) and are absent from cells at near threshold potentials in awake resting mice (Schmidt-Hieber and Häusser, 2013)), suggesting that this approach may not always successfully identify properties important for physiological circuit output. However, recent evidence indicates that while grid firing field properties do follow a dorsal-ventral gradient, the gradient is not continuous but is instead discretised, with properties clustering into discrete 'modules' (Stensola et al., 2012) and that therefore it may not be sufficient to flag intrinsic properties as important just because they follow a dorsal-ventral gradient. Ascertaining which intrinsic properties cluster in individual animals into discrete modules along the dorsal-ventral axis may therefore prove fruitful for identifying those intrinsic properties with particular importance for grid firing fields.

Another possible way to identify intrinsic properties important for behaviourally relevant *in vivo* neural activity is to manipulate ion channel expression in cells in the MEC. Changes in ion channel expression patterns, particularly if achieved using rapid and local induction techniques to minimise any compensation effects, will result in changes to the intrinsic electrical properties of cells which can then be compared to any changes in *in vivo* activity patterns. A recent example shows that HCN1

forebrain knockout mice, which exhibit altered integrative properties of stellate cells (Nolan et al., 2007), also exhibit changes to grid scaling (Giocomo et al., 2011a), suggesting that the affected integrative properties are important for controlling grid field spacing. However, in this case, the interpretation is complicated by the widespread and permanent nature of the knockout, meaning that the effects on grid field spacing could instead arise from changes in afferent activity or reflect compensation effects, highlighting the importance of achieving both temporal and spatial precision in genetic manipulations to probe the link between intrinsic properties and circuit output. Nevertheless, in principle such manipulations have the potential to greatly elucidate the relationship between intrinsic properties and neural activity patterns, particularly since animals with genetic alterations can be tested for changes to their navigational abilities, therefore enabling direct comparisons between changes to neural activity patterns and behavioural abilities.

Computational models constrained by known circuit properties will remain important for understanding the relationship between intrinsic electrical properties and circuit output. An experimental demonstration that some particular intrinsic property correlates with firing field properties is not sufficient to establish a causal relationship between the two, as ion channel expression that is regulated to tune a specific intrinsic property to produce desired properties of grid fields may also regulate other 'irrelevant' intrinsic properties in a similar fashion. Computational models that link intrinsic properties to circuit outputs will therefore likely prove to be essential tools for evaluating and predicting the effects of intrinsic properties on circuit output. Because of the complexity of the MEC circuitry, such models will not only require more detailed information about the intrinsic electrical properties of different cell types in the MEC, but also information about the connections between them in order to constrain the interactions between different cell types in the circuit.

6.2.2 *Fine grained dissection of MEC circuitry*

To understand neural circuits, knowledge of both the intrinsic electrical properties of cells and how they are organised into functionally connected circuitry is required (Silberberg et al., 2005). Further characterisation of the functional interactions between distinct cell types in all layers of the MEC will be critical for developing a mature understanding of how layer II produces its characteristic spatially modulated outputs.

Many aspects of the layer II circuit organisation remain unknown. The existence of surround excitation in layer II is an intriguing possibility that could be directly addressed by optogenetic activation of stellate cells at different distances away from recorded fast spiking interneurons. However, the apparent multitude of distinct in-

terneuron types revealed by anatomical differences (Canto et al., 2008; Gatome et al., 2010) shows that fast spiking interneurons may comprise heterogenous sub-populations, suggesting that only a subset of fast spiking interneurons may receive surround excitation. For this and other reasons it will be important to test whether fast spiking interneuron subtypes can be distinguished based on electrophysiological criteria and establish whether identified fast spiking interneuron subtypes align well with current anatomically derived categories. Synaptic connectivity between any interneuron subtypes and other cells within layer II will then have to be established. It has recently been shown that stellate cells connect to pyramidal cells in layer II (although possibly not vice versa) (Couey et al., 2013), but further characterisation of the these connections and the connections between pyramidal cells and different interneuron types will provide further essential insights into the functional circuitry that underlies computations in layer II.

Layers III–V of the MEC contain spatially modulated cells (Sargolini et al., 2006) that are thought to be important for the generation of spatially modulated activity patterns in layer II cells (see e.g. Navratilova et al., 2012). Although connections from deep to superficial MEC have been demonstrated (Köhler, 1986; Jones, 1994), substantial characterisation of functional connections between identified cell types will be important for establishing how the deep layers, which receive hippocampal inputs (van Strien et al., 2009), in turn influence the different cell types in layer II. This could be investigated by paired recording experiments, but if cell type specific expression of transgenic opsins can be achieved in deep layer cells, optogenetic techniques may prove more efficient in establishing connectivity principles.

6.2.3 *Neural rhythms and temporal coding in the MEC*

Theta-nested gamma oscillations may provide a substrate for temporal coding of space in the hippocampal formation. Proposed temporal coding schemes typically rely on coupling between rhythms in separate areas, but it is not always clear how this is achieved (Buzsaki and Wang, 2012). While local theta frequency activation appears to be sufficient to elicit theta-nested gamma in layer II, it is not known how gamma activity synchronises between different areas in the hippocampal formation (though reciprocal long distance inhibitory connections might play a role (Melzer et al., 2012)) or how either theta or gamma oscillations synchronise across layers in the MEC. Recordings from the deep layers of the MEC during optogenetic activation of layer II could provide insights into how rhythmic activity in one layer influences activity in other layers of the MEC. Theta frequency activation of other layers contain-

ing cells with appropriate expression of transgenic opsins could similarly provide insights into how rhythmic activity in these layers impacts activity in layer II.

Despite the mechanistic insights provided by the optogenetic experiments reported in this thesis, many properties of gamma oscillations in the MEC remain unexplained. One example is the variation in frequency of gamma oscillations in the MEC in behaving animals (Chrobak and Buzsaki, 1998; Yartsev et al., 2011). In the hippocampus, where gamma oscillations have been shown to phase lock with the MEC (Colgin et al., 2009), the gamma frequency depends on running speed (Ahmed and Mehta, 2012), suggesting that gamma frequency in the MEC could also be coupled to locomotion. It is unclear how changes in gamma frequency arise, but they may reflect the degree of activation of the local network. This link could be tested by systematically varying the magnitude of activation of layer II by providing different strengths of optogenetic stimulation and investigating how gamma frequency and magnitude vary with stimulation intensity.

An important long term challenge will be to elucidate the cellular mechanisms that enable phase precession of action potentials in the MEC relative to an ongoing theta rhythm. Experiments to reveal the cellular mechanisms of phase precession will provide important information about how systematically varying phase relationships between spiking and neural rhythms can occur, and therefore shed light on mechanisms underlying temporal coding in general.

BIBLIOGRAPHY

Adesnik, H. and Scanziani, M. (2010). Lateral competition for cortical space by layer-specific horizontal circuits. *Nature*, 464(7292):1155–1160. (Cited on page 123.)

Ahmed, O. J. and Mehta, M. R. (2012). Running Speed Alters the Frequency of Hippocampal Gamma Oscillations. *The Journal of Neuroscience*, 32(21):7373–7383. (Cited on page 162.)

Akaike, N. and Harata, N. (1994). Nystatin perforated patch recording and its applications to analyses of intracellular mechanisms. *The Japanese Journal of Physiology*, 44(5):433–473. (Cited on pages 48, 61, and 62.)

Akam, T., Oren, I., Mantoan, L., Ferenczi, E., and Kullmann, D. M. (2012). Oscillatory dynamics in the hippocampus support dentate gyrus–CA3 coupling. *Nature Neuroscience*, 15(5):763–768. (Cited on page 123.)

Alonso, A. A. and García-Austt, E. (1987). Neuronal sources of theta rhythm in the entorhinal cortex of the rat. II. Phase relations between unit discharges and theta field potentials. *Experimental Brain Research*, 67(3):502–509. (Cited on pages 7 and 23.)

Alonso, A. A., Khateb, A., Fort, P., Jones, B. E., and Mühlethaler, M. (1996). Differential oscillatory properties of cholinergic and noncholinergic nucleus basalis neurons in guinea pig brain slice. *The European Journal of Neuroscience*, 8(1):169–182. (Cited on page 12.)

Alonso, A. A. and Klink, R. (1993). Differential electroresponsiveness of stellate and pyramidal-like cells of medial entorhinal cortex layer II. *Journal of Neurophysiology*, 70(1):128. (Cited on pages 16, 23, 27, 28, 30, 31, 32, 59, 72, 81, 90, and 95.)

Alonso, A. A. and Köhler, C. (1984). A study of the reciprocal connections between the septum and the entorhinal area using anterograde and retrograde axonal transport methods in the rat brain. *The Journal of Comparative Neurology*, 225(3):327–343. (Cited on page 18.)

Alonso, A. A. and Llinás, R. R. (1989). Subthreshold Na+-dependent theta-like rhythmicity in stellate cells of entorhinal cortex layer II. *Nature*, 342(6246):175–177. (Cited on pages 11, 16, 24, 27, 28, 30, 31, 59, 68, 69, 71, 81, 82, 90, and 95.)

Amaral, D. G. and Witter, M. P. (1989). The three-dimensional organization of the hippocampal formation: a review of anatomical data. *Neuroscience*, 31(3):571–591. (Cited on pages 15 and 119.)

Andersen, P., Bliss, T. V., and Skrede, K. K. (1971). Lamellar organization of hippocampal excitatory pathways. *Experimental Brain Research*, 76(1):4A–5A. (Cited on page 119.)

Aravanis, A. M., Wang, L.-P., Zhang, F., Meltzer, L. A., Mogri, M. Z., Schneider, M. B., and Deisseroth, K. (2007). An optical neural interface: in vivo control of rodent motor cortex with integrated fiberoptic and optogenetic technology. *Journal of Neural Engineering*, 4(3):S143–56. (Cited on page 105.)

Arenkiel, B. R., Peca, J., Davison, I. G., Feliciano, C., Deisseroth, K., Augustine, G. J., Ehlers, M. D., and Feng, G. (2007). In vivo light-induced activation of neural circuitry in transgenic mice expressing channelrhodopsin-2. *Neuron*, 54(2):205–218. (Cited on pages 50, 92, and 93.)

Armstrong, C. M. and Gilly, W. F. (1992). Access resistance and space clamp problems associated with whole-cell patch clamping. *Methods in Enzymology*, 207:100–122. (Cited on page 49.)

Bamann, C., Kirsch, T., Nagel, G., and Bamberg, E. (2008). Spectral characteristics of the photocycle of channelrhodopsin-2 and its implication for channel function. *Journal of Molecular Biology*, 375(3):686–694. (Cited on page 50.)

Barry, C., Ginzberg, L. L., O'Keefe, J., and Burgess, N. (2012). Grid cell firing patterns signal environmental novelty by expansion. *Proceedings of the National Academy of Sciences*, 109(43):17687–17692. (Cited on pages 3, 120, and 153.)

Barry, C., Hayman, R., Burgess, N., and Jeffery, K. J. (2007). Experience-dependent rescaling of entorhinal grids. *Nature Neuroscience*, 10(6):682–684. (Cited on pages 3, 120, and 153.)

Beed, P., Bendels, M. H. K., Wiegand, H. F., Leibold, C., Johenning, F. W., and Schmitz, D. (2010). Analysis of Excitatory Microcircuitry in the Medial Entorhinal Cortex Reveals Cell-Type-Specific Differences. *Neuron*, 68(6):1059–1066. (Cited on pages 22, 39, 91, 116, and 153.)

Belluscio, M. A., Mizuseki, K., Schmidt, R., Kempter, R., and Buzsaki, G. (2012). Cross-Frequency Phase-Phase Coupling between Theta and Gamma Oscillations in the Hippocampus. *The Journal of Neuroscience*, 32(2):423–435. (Cited on page 8.)

Blair, H. T., Gupta, K., and Zhang, K. (2008). Conversion of a phase- to a rate-coded position signal by a three-stage model of theta cells, grid cells, and place cells. *Hippocampus*, 18(12):1239–1255. (Cited on pages 37 and 38.)

Boccara, C. N., Sargolini, F., Thoresen, V. H., Solstad, T., Witter, M. P., Moser, E. I., and Moser, M.-B. (2010). Grid cells in pre- and parasubiculum. *Nature Neuroscience*, 13(8):987–994. (Cited on page 2.)

Boehlen, A., Heinemann, U., and Erchova, I. (2010). The range of intrinsic frequencies represented by medial entorhinal cortex stellate cells extends with age. *The Journal of Neuroscience*, 30(13):4585–4589. (Cited on pages 27, 28, 29, 31, 33, 34, 35, 38, 59, 60, 66, 68, 69, 71, 75, 76, 80, 81, 82, 83, 152, and 159.)

Boehlen, A., Henneberger, C., Heinemann, U., and Erchova, I. (2013). Contribution of near-threshold currents to intrinsic oscillatory activity in rat medial entorhinal cortex layer II stellate cells. *Journal of Neurophysiology*, 109(2):445–463. (Cited on page 30.)

Bonnevie, T., Dunn, B., Fyhn, M., Hafting, T., Derdikman, D., Kubie, J. L., Roudi, Y., Moser, E. I., and Moser, M.-B. (2013). Grid cells require excitatory drive from the hippocampus. *Nature Neuroscience*, pages 1–11. (Cited on page 20.)

Börgers, C., Talei Franzesi, G., Lebeau, F. E. N., Boyden, E. S., and Kopell, N. J. (2012). Minimal Size of Cell Assemblies Coordinated by Gamma Oscillations. *PLoS Computational Biology*, 8(2):e1002362. (Cited on pages 13, 123, 124, and 141.)

Boyden, E. S., Zhang, F., Bamberg, E., Nagel, G., and Deisseroth, K. (2005). Millisecond-timescale, genetically targeted optical control of neural activity. *Nature Neuroscience*, 8(9):1263–1268. (Cited on page 50.)

Braak, H. and Braak, E. (1985). On areas of transition between entorhinal allocortex and temporal isocortex in the human brain. Normal morphology and lamina-specific pathology in Alzheimer's disease. *Acta Neuropathologica*, 68(4):325–332. (Cited on pages 15 and 156.)

Bragin, A., Jandó, G., Nádasdy, Z., Hetke, J., Wise, K., and Buzsaki, G. (1995). Gamma (40-100 Hz) oscillation in the hippocampus of the behaving rat. *The Journal of Neuroscience*, 15(1 Pt 1):47–60. (Cited on page 122.)

Brandon, M. P., Bogaard, A. R., Libby, C. P., Connerney, M. A., Gupta, K., and Hasselmo, M. E. (2011). Reduction of Theta Rhythm Dissociates Grid Cell Spatial Periodicity from Directional Tuning. *Science*, 332(6029):595–599. (Cited on pages 3, 7, and 12.)

Bruehl, C. and Wadman, W. J. (1999). Calcium currents in acutely isolated stellate and pyramidal neurons of rat entorhinal cortex. *Brain Research*, 816(2):554–562. (Cited on pages 25, 26, and 61.)

Brun, V. H., Solstad, T., Kjelstrup, K. B., Fyhn, M., Witter, M. P., Moser, E. I., and Moser, M.-B. (2008). Progressive increase in grid scale from dorsal to ventral medial entorhinal cortex. *Hippocampus*, 18(12):1200–1212. (Cited on pages 3, 4, 23, 33, 144, 151, and 159.)

Burak, Y. and Fiete, I. R. (2009). Accurate path integration in continuous attractor network models of grid cells. *PLoS Computational Biology*, 5(2):e1000291. (Cited on pages 37, 38, 39, 111, 119, and 154.)

Burgalossi, A., Herfst, L., von Heimendahl, M., Förste, H., Haskic, K., Schmidt, M., and Brecht, M. (2011). Microcircuits of functionally identified neurons in the rat medial entorhinal cortex. *Neuron*, 70(4):773–786. (Cited on pages 23, 46, 59, 118, and 151.)

Burgess, N. (2008). Grid cells and theta as oscillatory interference: theory and predictions. *Hippocampus*, 18(12):1157–1174. (Cited on pages 37, 38, and 119.)

Burgess, N., Barry, C., and O'Keefe, J. (2007). An oscillatory interference model of grid cell firing. *Hippocampus*, 17(9):801–812. (Cited on pages 30, 37, 38, 86, and 119.)

Burgess, N. and O'Keefe, J. (2011). Models of place and grid cell firing and theta rhythmicity. *Current Opinion in Neurobiology*, 21(5):734–744. (Cited on page 37.)

Burton, B. G., Economo, M. N., Lee, G. J., and White, J. A. (2008). Development of theta rhythmicity in entorhinal stellate cells of the juvenile rat. *Journal of Neurophysiology*, 100(6):3144–3157. (Cited on pages 16, 24, and 28.)

Burwell, R. D. (2000). The parahippocampal region: corticocortical connectivity. *Annals of the New York Academy of Sciences*, 911:25–42. (Cited on pages 15 and 18.)

Burwell, R. D. and Amaral, D. G. (1998a). Cortical afferents of the perirhinal, postrhinal, and entorhinal cortices of the rat. *The Journal of Comparative Neurology*, 398(2):179–205. (Cited on pages 15, 18, and 19.)

Burwell, R. D. and Amaral, D. G. (1998b). Perirhinal and postrhinal cortices of the rat: interconnectivity and connections with the entorhinal cortex. *The Journal of Comparative Neurology*, 391(3):293–321. (Cited on page 19.)

Buzsaki, G. (2002). Theta oscillations in the hippocampus. *Neuron*, 33(3):325–340. (Cited on pages 5, 6, 8, 11, and 12.)

Buzsaki, G., Anastassiou, C. A., and Koch, C. (2012). The origin of extracellular fields and currents–EEG, ECoG, LFP and spikes. *Nature Reviews Neuroscience*, 13(6):407–420. (Cited on page 11.)

Buzsaki, G. and Draguhn, A. (2004). Neuronal oscillations in cortical networks. *Science*, 304(5679):1926–1929. (Cited on pages 5, 6, 121, 122, and 155.)

Buzsaki, G. and Wang, X.-J. (2012). Mechanisms of Gamma Oscillations. *Annual Review of Neuroscience*, 35(1):203–225. (Cited on pages 6, 9, 12, 13, 121, 122, 132, 135, 149, 155, and 161.)

Cajal, R. y. (1995). *Histology of the Nervous System vol. II*. Oxford University Press, New York. (Cited on pages 16 and 59.)

Canolty, R. T., Edwards, E., Dalal, S. S., Soltani, M., Nagarajan, S. S., Kirsch, H. E., Berger, M. S., Barbaro, N. M., and Knight, R. T. (2006). High Gamma Power Is Phase-Locked to Theta Oscillations in Human Neocortex. *Science*, 313(5793):1626–1628. (Cited on page 122.)

Canolty, R. T. and Knight, R. T. (2010). The functional role of cross-frequency coupling. *Trends in Cognitive Sciences*, 14(11):506–515. (Cited on pages 6, 121, 122, and 149.)

Canto, C. B., Koganezawa, N., Beed, P., Moser, E. I., and Witter, M. P. (2012). All Layers of Medial Entorhinal Cortex Receive Presubicular and Parasubicular Inputs. *The Journal of Neuroscience*, 32(49):17620–17631. (Cited on pages 19 and 33.)

Canto, C. B. and Witter, M. P. (2011). Cellular properties of principal neurons in the rat entorhinal cortex. II. The medial entorhinal cortex. *Hippocampus*, pages 1277–1299. (Cited on pages 15, 16, and 17.)

Canto, C. B., Wouterlood, F. G., and Witter, M. P. (2008). What Does the Anatomical Organization of the Entorhinal Cortex Tell Us? *Neural Plasticity*, 2008:1–19. (Cited on pages 15, 16, 17, 89, and 161.)

Cardin, J. A., Carlén, M., Meletis, K., Knoblich, U., Zhang, F., Deisseroth, K., Tsai, L.-H., and Moore, C. I. (2009). Driving fast-spiking cells induces gamma rhythm and controls sensory responses. *Nature*, 459(7247):663–667. (Cited on page 123.)

Castelli, L. and Magistretti, J. (2006). High-voltage-activated Ca2+ currents show similar patterns of expression in stellate and pyramidal cells from rat entorhinal cortex layer II. *Brain Research*, 1090(1):76–88. (Cited on pages 25 and 26.)

Chapeton, J., Fares, T., Lasota, D., and Stepanyants, A. (2012). Efficient associative memory storage in cortical circuits of inhibitory and excitatory neurons. *Proceedings of the National Academy of Sciences*, 109(51):E3614–E3622. (Cited on page 91.)

Chapman, C. A. and Racine, R. J. (1997). Converging inputs to the entorhinal cortex from the piriform cortex and medial septum: facilitation and current source density analysis. *Journal of Neurophysiology*, 78(5):2602–2615. (Cited on pages 18 and 19.)

Chrobak, J. J. and Buzsaki, G. (1998). Gamma oscillations in the entorhinal cortex of the freely behaving rat. *The Journal of Neuroscience*, 18(1):388–398. (Cited on pages 7, 8, 9, 10, 13, 39, 120, 121, 122, 124, 125, 129, 132, 142, 144, 147, 148, 149, 155, 157, and 162.)

Colgin, L. L., Denninger, T., Fyhn, M., Hafting, T., Bonnevie, T., Jensen, O., Moser, M.-B., and Moser, E. I. (2009). Frequency of gamma oscillations routes flow of information in the hippocampus. *Nature*, 462(7271):353–357. (Cited on pages 6, 7, 8, 9, 13, 120, 121, 122, 125, 149, 155, 157, and 162.)

Couey, J. J., Witoelar, A., Zhang, S.-J., Zheng, K., Ye, J., Dunn, B., Czajkowski, R., Moser, M.-B., Moser, E. I., Roudi, Y., and Witter, M. P. (2013). Recurrent inhibitory circuitry as a mechanism for grid formation. *Nature Neuroscience*, pages 1–9. (Cited on pages 116, 119, 153, 154, and 161.)

Craig, S. and Commins, S. (2007). Plastic and metaplastic changes in the CA1 and subicular projections to the entorhinal cortex. *Brain Research*, 1147:124–139. (Cited on page 20.)

Crawley, M. J. (2005). *Statistics: An Introduction using R*. John Wiley & Sons, 1 edition. (Cited on page 62.)

Cunningham, M. O., Davies, C. H., Bühl, E. H., Kopell, N. J., and Whittington, M. A. (2003). Gamma oscillations induced by kainate receptor activation in the entorhinal cortex in vitro. *The Journal of Neuroscience*, 23(30):9761–9769. (Cited on pages 13, 14, 22, 90, 125, 144, 147, and 156.)

Cunningham, M. O., Halliday, D. M., Davies, C. H., Traub, R. D., Bühl, E. H., and Whittington, M. A. (2004). Coexistence of gamma and high-frequency oscillations in rat medial entorhinal cortex in vitro. *The Journal of Physiology*, 559(Pt 2):347–353. (Cited on pages 13 and 147.)

Cunningham, M. O., Hunt, J., Middleton, S., Lebeau, F. E. N., Gillies, M. J., Gillies, M. G., Davies, C. H., Maycox, P. R., Whittington, M. A., and Racca, C. (2006). Region-specific reduction in entorhinal gamma oscillations and parvalbumin-immunoreactive neurons in animal models of psychiatric illness. *The Journal of Neuroscience*, 26(10):2767–2776. (Cited on page 13.)

Deng, P.-Y., Poudel, S. K. S., Rojanathammanee, L., Porter, J. E., and Lei, S. (2007). Serotonin Inhibits Neuronal Excitability by Activating Two-Pore Domain K+ Channels in the Entorhinal Cortex. *Molecular Pharmacology*, 72(1):208–218. (Cited on pages 25 and 28.)

Deng, P.-Y., Xiao, Z., Yang, C., Rojanathammanee, L., Grisanti, L., Watt, J., Geiger, J. D., Liu, R., Porter, J. E., and Lei, S. (2009). GABAB Receptor Activation Inhibits Neuronal Excitability and Spatial Learning in the Entorhinal Cortex by Activating TREK-2 K+ Channels. *Neuron*, 63(2):230–243. (Cited on page 25.)

Destexhe, A., Rudolph, M., and Paré, D. (2003). The high-conductance state of neocortical neurons in vivo. *Nature Reviews Neuroscience*. (Cited on pages 86 and 87.)

Deuchars, J., West, D. C., and Thomson, A. M. (1994). Relationships between morphology and physiology of pyramid-pyramid single axon connections in rat neocortex in vitro. *The Journal of Physiology*, 478 Pt 3:423–435. (Cited on pages 22, 91, and 116.)

Dhillon, A. and Jones, R. S. (2000). Laminar differences in recurrent excitatory transmission in the rat entorhinal cortex in vitro. *Neuroscience*, 99(3):413–422. (Cited on pages 21, 22, 39, 91, 105, 116, 117, 119, and 153.)

Dickson, C. T. and Alonso, A. A. (1997). Muscarinic induction of synchronous population activity in the entorhinal cortex. *The Journal of Neuroscience*, 17(17):6729–6744. (Cited on page 12.)

Dickson, C. T., Biella, G., and de Curtis, M. (2000a). Evidence for spatial modules mediated by temporal synchronization of carbachol-induced gamma rhythm in medial entorhinal cortex. *The Journal of Neuroscience*, 20(20):7846–7854. (Cited on pages 12, 13, 14, 125, and 147.)

Dickson, C. T., Kirk, I. J., Oddie, S. D., and Bland, B. H. (1995). Classification of theta-related cells in the entorhinal cortex: cell discharges are controlled by the ascending brainstem synchronizing pathway in parallel with hippocampal theta-related cells. *Hippocampus*, 5(4):306–319. (Cited on page 23.)

Dickson, C. T., Magistretti, J., Shalinsky, M., Fransen, E., Hasselmo, M. E., and Alonso, A. A. (2000b). Properties and role of Ih in the pacing of subthreshold oscillations in entorhinal cortex layer II neurons. *Journal of Neurophysiology*, 83(5):2562. (Cited on pages 25, 28, 71, 81, and 82.)

Dickson, C. T., Magistretti, J., Shalinsky, M., Hamam, B. N., and Alonso, A. A. (2000c). Oscillatory activity in entorhinal neurons and circuits. Mechanisms and function. *Annals of the New York Academy of Sciences*, 911:127–150. (Cited on pages 30 and 38.)

Dickson, C. T., Mena, A. R., and Alonso, A. A. (1997). Electroresponsiveness of medial entorhinal cortex layer III neurons in vitro. *Neuroscience*, 81(4):937–950. (Cited on pages 11 and 17.)

Dodson, P. D., Pastoll, H., and Nolan, M. F. (2011). Dorsal-ventral organization of theta-like activity intrinsic to entorhinal stellate neurons is mediated by differences in stochastic current fluctuations. *The Journal of Physiology*, 589(12):2993–3008. (Cited on pages 11, 29, 30, 31, 34, 35, 38, 43, 67, 81, 82, 85, and 152.)

Doeller, C. F., Barry, C., and Burgess, N. (2010). Evidence for grid cells in a human memory network. *Nature*, 463(7281):657–661. (Cited on page 3.)

Dolorfo, C. L. and Amaral, D. G. (1998). Entorhinal cortex of the rat: organization of intrinsic connections. *The Journal of Comparative Neurology*, 398(1):49–82. (Cited on pages 15, 16, and 59.)

Domnisoru, C., Kinkhabwala, A. A., and Tank, D. W. (2013). Membrane potential dynamics of grid cells. *Nature*, 495(7440):199–204. (Cited on page 151.)

Dorval, A. D. and White, J. A. (2005). Channel noise is essential for perithreshold oscillations in entorhinal stellate neurons. *The Journal of Neuroscience*, 25(43):10025–10028. (Cited on pages 31 and 82.)

Dudman, J. T. and Nolan, M. F. (2009). Stochastically gating ion channels enable patterned spike firing through activity-dependent modulation of spike probability. *PLoS Computational Biology*, 5(2):e1000290. (Cited on pages 29, 31, 32, 33, 35, 72, and 84.)

Eder, C., Ficker, E., Gündel, J., and Heinemann, U. (1991). Outward Currents in Rat Entorhinal Cortex Stellate Cells Studied with Conventional and Perforated Patch Recordings. *The European Journal of Neuroscience*, 3(12):1271–1280. (Cited on page 24.)

Eder, C. and Heinemann, U. (1996). Potassium currents in acutely isolated neurons from superficial and deep layers of the juvenile rat entorhinal cortex. *Pflügers Archiv*, 432(4):637–643. (Cited on pages 24 and 26.)

Engel, T., Schimansky-Geier, L., Herz, A. V. M., Schreiber, S., and Erchova, I. (2008). Subthreshold membrane-potential resonances shape spike-train patterns in the entorhinal cortex. *Journal of Neurophysiology*, 100(3):1576. (Cited on pages 32, 33, and 72.)

Erchova, I., Kreck, G., and Heinemann, U. (2004). Dynamics of rat entorhinal cortex layer II and III cells: characteristics of membrane potential resonance at rest predict

oscillation properties near threshold. *The Journal of Physiology*, 560(1):89–110. (Cited on pages 16, 27, 28, 29, 30, 31, 59, 60, 65, 66, 81, and 82.)

Ernst, O., Murcia, P., Daldrop, P., Tsunoda, S., Kateriya, S., and Hegemann, P. (2008). Photoactivation of channelrhodopsin. *Journal of Biological Chemistry*, 283(3):1637. (Cited on page 50.)

Etienne, A. S. and Jeffery, K. J. (2004). Path integration in mammals. *Hippocampus*, 14(2):180–192. (Cited on page 1.)

Fell, J. and Axmacher, N. (2011). The role of phase synchronization in memory processes. *Nature Reviews Neuroscience*, 12(2):105–118. (Cited on pages 6, 9, 10, and 155.)

Fenno, L. E., Yizhar, O., and Deisseroth, K. (2011). The Development and Application of Optogenetics. *Annual Review of Neuroscience*, 34(1):389–412. (Cited on page 50.)

Fernandez, F. R. and White, J. A. (2008). Artificial synaptic conductances reduce subthreshold oscillations and periodic firing in stellate cells of the entorhinal cortex. *The Journal of Neuroscience*, 28(14):3790. (Cited on pages 32, 33, 37, 38, 73, 79, 80, 86, and 159.)

Fiete, I. R., Burak, Y., and Brookings, T. (2008). What grid cells convey about rat location. *The Journal of Neuroscience*, 28(27):6858–6871. (Cited on page 5.)

Finch, D. M., Tan, A. M., and Isokawa-Akesson, M. (1988). Feedforward inhibition of the rat entorhinal cortex and subicular complex. *The Journal of Neuroscience*, 8(7):2213–2226. (Cited on pages 106 and 117.)

Fino, E. and Yuste, R. (2011). Dense Inhibitory Connectivity in Neocortex. *Neuron*, 69(6):1188–1203. (Cited on page 117.)

Fransén, E., Alonso, A. A., Dickson, C. T., Magistretti, J., and Hasselmo, M. E. (2004). Ionic mechanisms in the generation of subthreshold oscillations and action potential clustering in entorhinal layer II stellate neurons. *Hippocampus*, 14(3):368–384. (Cited on pages 30, 32, 38, and 82.)

Fries, P. (2009). Neuronal gamma-band synchronization as a fundamental process in cortical computation. *Annual Review of Neuroscience*, 32:209–224. (Cited on pages 6, 9, 121, 135, 149, and 155.)

Fuhs, M. and Touretzky, D. S. (2006). A spin glass model of path integration in rat medial entorhinal cortex. *The Journal of Neuroscience*, 26(16):4266. (Cited on pages 14, 22, 37, 38, 39, 91, 111, 119, 153, and 154.)

Fyhn, M., Hafting, T., Treves, A., Moser, M.-B., and Moser, E. I. (2007). Hippocampal remapping and grid realignment in entorhinal cortex. *Nature*, 446(7132):190–194. (Cited on page 120.)

Fyhn, M., Hafting, T., Witter, M. P., Moser, E. I., and Moser, M.-B. (2008). Grid cells in mice. *Hippocampus*, 18(12):1230–1238. (Cited on page 3.)

Fyhn, M., Molden, S., Witter, M. P., Moser, E. I., and Moser, M.-B. (2004). Spatial Representation in the Entorhinal Cortex. *Science*, 305(5688):1258–1264. (Cited on pages 2, 7, 20, 122, and 157.)

Garden, D. L. F., Dodson, P. D., O'Donnell, C., White, M. D., and Nolan, M. F. (2008). Tuning of synaptic integration in the medial entorhinal cortex to the organization of grid cell firing fields. *Neuron*, 60(5):875–889. (Cited on pages 5, 16, 17, 20, 24, 25, 27, 28, 33, 34, 35, 36, 37, 38, 43, 46, 54, 60, 75, 76, 80, 81, 84, 85, 99, 100, 152, and 159.)

Gatome, C. W., Slomianka, L., Lipp, H. P., and Amrein, I. (2010). Number estimates of neuronal phenotypes in layer II of the medial entorhinal cortex of rat and mouse. *Neuroscience*, 170(1):156–165. (Cited on pages 16, 17, 59, 94, 105, 116, and 161.)

Giocomo, L. M. and Hasselmo, M. E. (2008). Time constants of h current in layer ii stellate cells differ along the dorsal to ventral axis of medial entorhinal cortex. *The Journal of Neuroscience*, 28(38):9414–9425. (Cited on pages 24, 34, and 82.)

Giocomo, L. M. and Hasselmo, M. E. (2009). Knock-out of HCN1 subunit flattens dorsal-ventral frequency gradient of medial entorhinal neurons in adult mice. *The Journal of Neuroscience*, 29(23):7625–7630. (Cited on pages 29, 31, 34, and 82.)

Giocomo, L. M., Hussaini, S. A., Zheng, F., Kandel, E. R., Moser, M.-B., and Moser, E. I. (2011a). Grid Cells Use HCN1 Channels for Spatial Scaling. *Cell*, 147(5):1159–1170. (Cited on pages 3, 36, 37, and 160.)

Giocomo, L. M., Moser, M.-B., and Moser, E. I. (2011b). Computational Models of Grid Cells. *Neuron*, 71(4):589–603. (Cited on pages 37 and 152.)

Giocomo, L. M., Zilli, E. A., Fransén, E., and Hasselmo, M. E. (2007). Temporal frequency of subthreshold oscillations scales with entorhinal grid cell field spacing. *Science*, 315(5819):1719–1722. (Cited on pages 11, 30, 31, 34, 37, 38, 60, 66, 68, 69, 71, 75, 76, 81, 82, 152, and 159.)

Gloveli, T., Schmitz, D., Empson, R. M., and Heinemann, U. (1997). Frequency-dependent information flow from the entorhinal cortex to the hippocampus. *Journal of Neurophysiology*, 78(6):3444–3449. (Cited on pages 20, 33, 90, 92, 105, and 117.)

Gnatkovsky, V. and de Curtis, M. (2006). Hippocampus-Mediated Activation of Superficial and Deep Layer Neurons in the Medial Entorhinal Cortex of the Isolated Guinea Pig Brain. *The Journal of Neuroscience*, 26(3):873–881. (Cited on page 20.)

Good, M. and Honey, R. C. (1997). Dissociable effects of selective lesions to hippocampal subsystems on exploratory behavior, contextual learning, and spatial learning. *Behavioral neuroscience*, 111(3):487–493. (Cited on pages 2, 59, and 151.)

Gradinaru, V., Thompson, K. R., Zhang, F., Mogri, M. Z., Kay, K., Schneider, M. B., and Deisseroth, K. (2007). Targeting and readout strategies for fast optical neural control in vitro and in vivo. *The Journal of Neuroscience*, 27(52):14231. (Cited on page 50.)

Guanella, A., Kiper, D., and Verschure, P. (2007). A model of grid cells based on a twisted torus topology. *International Journal of Neural Systems*, 17(4):231–240. (Cited on pages 14, 22, 37, 39, 91, 111, 119, 153, and 154.)

Haas, J. S. (2002). Frequency Selectivity of Layer II Stellate Cells in the Medial Entorhinal Cortex. *Journal of Neurophysiology*, 88(5):2422–2429. (Cited on pages 29, 59, and 81.)

Haas, J. S., Dorval, A. D., and White, J. A. (2007). Contributions of Ih to feature selectivity in layer II stellate cells of the entorhinal cortex. *Journal of Computational Neuroscience*, 22(2):161–171. (Cited on pages 28, 29, and 82.)

Hafting, T., Fyhn, M., Bonnevie, T., Moser, M.-B., and Moser, E. I. (2008). Hippocampus-independent phase precession in entorhinal grid cells. *Nature*, 453(7199):1248–1252. (Cited on pages 1, 4, 8, 23, 120, 121, 122, 129, 147, 149, 151, and 157.)

Hafting, T., Fyhn, M., Molden, S., Moser, M.-B., and Moser, E. I. (2005). Microstructure of a spatial map in the entorhinal cortex. *Nature*, 436(7052):801–806. (Cited on pages 1, 2, 3, 4, 5, 7, 8, 14, 23, 33, 122, 144, 147, 151, 157, and 159.)

Hajimiri, A. and Lee, T. H. (1998). IEEE Xplore - A general theory of phase noise in electrical oscillators. *IEEE Journal of Solid-State Circuits*. (Cited on page 30.)

Hamill, O., Marty, A., Neher, E., Sakmann, B., and Sigworth, F. (1981). Improved patch-clamp techniques for high-resolution current recording from cells and cell-free membrane patches. *Pflügers Archiv*, 391(2):85–100. (Cited on pages 47 and 60.)

Hasselmo, M. E. (2008). Grid cell mechanisms and function: contributions of entorhinal persistent spiking and phase resetting. *Hippocampus*, 18(12):1213–1229. (Cited on pages 37, 38, 86, and 119.)

Heinemann, U., Schmitz, D., Eder, C., and Gloveli, T. (2000). Properties of entorhinal cortex projection cells to the hippocampal formation. *Annals of the New York Academy of Sciences*, 911:112–126. (Cited on pages 16 and 92.)

Heys, J. G., Giocomo, L. M., and Hasselmo, M. E. (2010). Cholinergic modulation of the resonance properties of stellate cells in layer II of medial entorhinal cortex. *Journal of Neurophysiology*, 104(1):258–270. (Cited on pages 29, 30, 34, 60, 66, and 86.)

Horn, R. and Marty, A. (1988). Muscarinic activation of ionic currents measured by a new whole-cell recording method. *The Journal of General Physiology*, 92(2):145–159. (Cited on pages 47 and 61.)

Horne, J. and Baliunas, S. (1986). A prescription for period analysis of unevenly sampled time series. *The Astrophysical Journal*, 302:757–763. (Cited on page 68.)

Hu, H., Vervaeke, K., and Storm, J. F. (2002). Two forms of electrical resonance at theta frequencies, generated by M-current, h-current and persistent Na+ current in rat hippocampal pyramidal cells. *The Journal of Physiology*, 545:783–805. (Cited on page 29.)

Hussaini, S. A., Kempadoo, K. A., Thuault, S. J., Siegelbaum, S. A., and Kandel, E. R. (2011). Increased size and stability of CA1 and CA3 place fields in HCN1 knockout mice. *Neuron*, 72(4):643–653. (Cited on page 36.)

Hutcheon, B., Miura, R. M., and Puil, E. (1996). Subthreshold membrane resonance in neocortical neurons. *Journal of Neurophysiology*, 76(2):683–697. (Cited on page 29.)

Hutcheon, B. and Yarom, Y. (2000). Resonance, oscillation and the intrinsic frequency preferences of neurons. *Trends in Neurosciences*, 23(5):216–222. (Cited on pages 29 and 30.)

Insausti, R., Herrero, M. T., and Witter, M. P. (1997). Entorhinal cortex of the rat: cytoarchitectonic subdivisions and the origin and distribution of cortical efferents. *Hippocampus*, 7(2):146–183. (Cited on pages 16 and 59.)

Jeffery, K. J. (2007). Self-localization and the entorhinal-hippocampal system. *Current Opinion in Neurobiology*, 17(6):684–691. (Cited on pages 1, 2, 5, and 151.)

Jeffery, K. J., Donnett, J. G., and O'Keefe, J. (1995). Medial septal control of theta-correlated unit firing in the entorhinal cortex of awake rats. *Neuroreport*, 6(16):2166–2170. (Cited on page 12.)

Jeong, J. (2004). EEG dynamics in patients with Alzheimer's disease. *Clinical Neurophysiology*, 115(7):1490–1505. (Cited on page 156.)

Jones, R. S. (1994). Synaptic and intrinsic properties of neurons of origin of the perforant path in layer II of the rat entorhinal cortex in vitro. *Hippocampus*, 4(3):335–353. (Cited on pages 16, 20, 21, 27, 28, 31, 90, 92, 105, 117, and 161.)

Jones, R. S. and Bühl, E. H. (1993). Basket-like interneurones in layer II of the entorhinal cortex exhibit a powerful NMDA-mediated synaptic excitation. *Neuroscience Letters*, 149(1):35–39. (Cited on pages 17, 19, 20, 90, and 95.)

Jones, R. S. and Woodhall, G. L. (2005). Background synaptic activity in rat entorhinal cortical neurones: differential control of transmitter release by presynaptic receptors. *The Journal of Physiology*, 562(Pt 1):107–120. (Cited on pages 21, 99, 100, and 117.)

Kaada, B. R., Rasmussen, E. W., and Kviem (1961). Effects of hippocampal lesions on maze learning and retention in rats. *Experimental Neurology*, 3:333–355. (Cited on page 2.)

Kaczorowski, C. C., Disterhoft, J., and Spruston, N. (2007). Stability and plasticity of intrinsic membrane properties in hippocampal CA1 pyramidal neurons: effects of internal anions. *The Journal of Physiology*, 578(3):799–818. (Cited on pages 61, 84, and 85.)

Kerr, K. M., Agster, K. L., Furtak, S. C., and Burwell, R. D. (2007). Functional neuroanatomy of the parahippocampal region: the lateral and medial entorhinal areas. *Hippocampus*, 17(9):697–708. (Cited on pages 15 and 18.)

Khawaja, F. A., Alonso, A. A., and Bourque, C. W. (2007). Ca(2+)-dependent K(+) currents and spike-frequency adaptation in medial entorhinal cortex layer II stellate cells. *Hippocampus*, 17(12):1143–1148. (Cited on pages 25, 32, and 61.)

Killian, N. J., Jutras, M. J., and Buffalo, E. A. (2012). A map of visual space in the primate entorhinal cortex. *Nature*, 491(7426):761–764. (Cited on page 3.)

Klausberger, T. and Somogyi, P. (2008). Neuronal diversity and temporal dynamics: the unity of hippocampal circuit operations. *Science*, 321(5885):53–57. (Cited on page 6.)

Klink, R. and Alonso, A. A. (1993). Ionic mechanisms for the subthreshold oscillations and differential electroresponsiveness of medial entorhinal cortex layer II neurons. *Journal of Neurophysiology*, 70(1):144–157. (Cited on pages 16, 28, 31, 32, 71, and 72.)

Klink, R. and Alonso, A. A. (1997a). Morphological characteristics of layer II projection neurons in the rat medial entorhinal cortex. *Hippocampus*, 7(5):571–583. (Cited on pages 16, 28, and 46.)

Klink, R. and Alonso, A. A. (1997b). Muscarinic modulation of the oscillatory and repetitive firing properties of entorhinal cortex layer II neurons. *Journal of Neurophysiology*, 77(4):1813–1828. (Cited on page 11.)

Koenig, J., Linder, A. N., Leutgeb, J. K., and Leutgeb, S. (2011). The Spatial Periodicity of Grid Cells Is Not Sustained During Reduced Theta Oscillations. *Science*, 332(6029):592–595. (Cited on pages 3, 7, and 12.)

Köhler, C. (1986). Intrinsic connections of the retrohippocampal region in the rat brain. II. The medial entorhinal area. *The Journal of Comparative Neurology*, 246(2):149–169. (Cited on pages 16, 17, 20, 59, and 161.)

Krupic, J., Burgess, N., and O'Keefe, J. (2012). Neural Representations of Location Composed of Spatially Periodic Bands. *Science*, 337(6096):853–857. (Cited on pages 2, 3, 4, 8, 14, 120, 149, and 157.)

Kumar, S. S., Jin, X., Buckmaster, P. S., and Huguenard, J. R. (2007). Recurrent circuits in layer II of medial entorhinal cortex in a model of temporal lobe epilepsy. *The Journal of Neuroscience*, 27(6):1239–1246. (Cited on pages 14, 22, 39, 91, 116, and 153.)

Langston, R. F., Ainge, J. A., Couey, J. J., Canto, C. B., Bjerknes, T. L., Witter, M. P., Moser, E. I., and Moser, M.-B. (2010). Development of the spatial representation system in the rat. *Science*, 328(5985):1576–1580. (Cited on page 3.)

Li, W.-C., Soffe, S. R., and Roberts, A. (2004). A direct comparison of whole cell patch and sharp electrodes by simultaneous recording from single spinal neurons in frog tadpoles. *Journal of Neurophysiology*, 92(1):380–386. (Cited on page 60.)

Lindén, H., Tetzlaff, T., Potjans, T. C., Pettersen, K. H., Grün, S., Diesmann, M., and Einevoll, G. T. (2011). Modeling the Spatial Reach of the LFP. *Neuron*, 72(5):859–872. (Cited on page 11.)

Lisman, J. (2005). The theta/gamma discrete phase code occuring during the hippocampal phase precession may be a more general brain coding scheme. *Hippocampus*, 15(7):913–922. (Cited on pages 6, 9, 120, 121, 122, 129, 132, 135, 149, 151, and 155.)

Llinás, R. R. (1988). The intrinsic electrophysiological properties of mammalian neurons: insights into central nervous system function. *Science*, 242(4886):1654–1664. (Cited on page 24.)

Lomb, N. R. (1976). Least-squares frequency analysis of unequally spaced data. *Astrophysics and Space Science*, 39(2):447–462. (Cited on page 68.)

Luo, L., Callaway, E. M., and Svoboda, K. (2008). Genetic Dissection of Neural Circuits. *Neuron*, 57(5):634–660. (Cited on pages 50, 90, and 92.)

Magistretti, J. and Alonso, A. A. (1999). Biophysical properties and slow voltage-dependent inactivation of a sustained sodium current in entorhinal cortex layer-II principal neurons. *The Journal of General Physiology*, 114(4):491. (Cited on page 24.)

Magistretti, J., Ragsdale, D. S., and Alonso, A. A. (1999). Direct demonstration of persistent Na+ channel activity in dendritic processes of mammalian cortical neurones. *The Journal of Physiology*, 521 Pt 3:629–636. (Cited on pages 24 and 26.)

Manns, I. D., Mainville, L., and Jones, B. E. (2001). Evidence for glutamate, in addition to acetylcholine and GABA, neurotransmitter synthesis in basal forebrain neurons projecting to the entorhinal cortex. *Neuroscience*, 107(2):249–263. (Cited on pages 19 and 85.)

Mason, A., Nicoll, A., and Stratford, K. (1991). Synaptic transmission between individual pyramidal neurons of the rat visual cortex in vitro. *The Journal of Neuroscience*, 11(1):72–84. (Cited on pages 22, 91, and 116.)

McNaughton, B. L., Battaglia, F. P., Jensen, O., Moser, E. I., and Moser, M.-B. (2006). Path integration and the neural basis of the 'cognitive map'. *Nature Reviews Neuroscience*, 7(8):663–678. (Cited on pages 1, 3, 5, 37, 38, 111, and 151.)

McNeil, P. L. and Steinhardt, R. A. (2003). Plasma Membrane Disruption: Repair, Prevention, Adaptation. *Annual Review of Cell and Developmental Biology*, 19(1):697–731. (Cited on pages 60, 61, and 62.)

Melzer, S., Michael, M., Caputi, A., Eliava, M., Fuchs, E. C., Whittington, M. A., and Monyer, H. (2012). Long-Range-Projecting GABAergic Neurons Modulate Inhibition in Hippocampus and Entorhinal Cortex. *Science*, 335(6075):1506–1510. (Cited on pages 17, 20, and 161.)

Middleton, S., Jalics, J., Kispersky, T., Lebeau, F. E. N., Roopun, A., Kopell, N. J., Whittington, M. A., and Cunningham, M. O. (2008). NMDA receptor-dependent switching between different gamma rhythm-generating microcircuits in entorhinal cortex. *Proceedings of the National Academy of Sciences*, 105(47):18572. (Cited on pages 13, 14, 17, 22, 90, 92, 95, 125, 141, 144, 147, and 156.)

Miles, R. and Wong, R. K. (1986). Excitatory synaptic interactions between CA3 neurones in the guinea-pig hippocampus. *The Journal of Physiology*, 373:397–418. (Cited on pages 91 and 116.)

Mitchell, S. J. and Ranck, J. B. (1980). Generation of theta rhythm in medial entorhinal cortex of freely moving rats. *Brain Research*, 189(1):49–66. (Cited on pages 7, 121, 122, 132, and 155.)

Mitchell, S. J., Rawlins, J. N., Steward, O., and Olton, D. S. (1982). Medial septal area lesions disrupt theta rhythm and cholinergic staining in medial entorhinal cortex and produce impaired radial arm maze behavior in rats. *The Journal of Neuroscience*. (Cited on pages 12, 18, 19, and 85.)

Mittelstaedt, M. L. and Mittelstaedt, H. (1980). Homing by path integration in a mammal. *Naturwissenschaften*, 67(11):566–567. (Cited on page 1.)

Mizuseki, K., Sirota, A., Pastalkova, E., and Buzsaki, G. (2009). Theta Oscillations Provide Temporal Windows for Local Circuit Computation in the Entorhinal-Hippocampal Loop. *Neuron*, 64(2):267–280. (Cited on pages 7, 8, 23, 30, 122, 129, and 147.)

Monaco, J. D. and Abbott, L. F. (2011). Modular Realignment of Entorhinal Grid Cell Activity as a Basis for Hippocampal Remapping. *The Journal of Neuroscience*, 31(25):9414–9425. (Cited on page 120.)

Morris, R. (1985). Thy-1 in developing nervous tissue. *Developmental Neuroscience*, 7(3):133–160. (Cited on page 93.)

Moser, E., Moser, M. B., and Andersen, P. (1993). Spatial learning impairment parallels the magnitude of dorsal hippocampal lesions, but is hardly present following ventral lesions. *The Journal of Neuroscience*, 13(9):3916–3925. (Cited on page 2.)

Naber, P. A., Caballero-Bleda, M., Jorritsma-Byham, B., and Witter, M. P. (1997). Parallel input to the hippocampal memory system through peri- and postrhinal cortices. *Neuroreport*, 8(11):2617–2621. (Cited on page 19.)

Nagel, G., Szellas, T., Huhn, W., Kateriya, S., Adeishvili, N., Berthold, P., Ollig, D., Hegemann, P., and Bamberg, E. (2003). Channelrhodopsin-2, a directly light-gated cation-selective membrane channel. *Proceedings of the National Academy of Sciences*, 100(24):13940–13945. (Cited on pages 50 and 92.)

Navratilova, Z., Giocomo, L. M., Fellous, J.-M., Hasselmo, M. E., and McNaughton, B. L. (2012). Phase precession and variable spatial scaling in a periodic attractor map model of medial entorhinal grid cells with realistic after-spike dynamics. *Hippocampus*, 22(4):772–789. (Cited on pages 1, 14, 22, 32, 37, 38, 39, 91, 119, 153, 154, and 161.)

Neher, E. (1992). Correction for liquid junction potentials in patch clamp experiments. *Methods in Enzymology*, 207:123–131. (Cited on page 48.)

Neher, E. and Sakmann, B. (1976). Single-channel currents recorded from membrane of denervated frog muscle fibres. *Nature*, 260(5554):799–802. (Cited on page 47.)

Neher, E., Sakmann, B., and Steinbach, J. H. (1978). The extracellular patch clamp: A method for resolving currents through individual open channels in biological membranes. *Pflügers Archiv*, 375(2):219–228. (Cited on page 47.)

Nolan, M. F., Dudman, J. T., Dodson, P. D., and Santoro, B. (2007). HCN1 channels control resting and active integrative properties of stellate cells from layer II of the entorhinal cortex. *The Journal of Neuroscience*, 27(46):12440. (Cited on pages 25, 26, 27, 28, 29, 30, 31, 32, 34, 35, 36, 37, 38, 43, 59, 60, 64, 65, 66, 68, 69, 71, 72, 73, 78, 80, 81, 82, 83, 84, 86, and 160.)

Nolan, M. F., Malleret, G., Dudman, J. T., Buhl, D. L., Santoro, B., Gibbs, E., Vronskaya, S., Buzsaki, G., Siegelbaum, S. A., Kandel, E. R., and Morozov, A. (2004). A behavioral role for dendritic integration: HCN1 channels constrain spatial memory and plasticity at inputs to distal dendrites of CA1 pyramidal neurons. *Cell*, 119(5):719–732. (Cited on pages 36 and 65.)

O'Donnell, C. and Nolan, M. F. (2011). Tuning of synaptic responses: an organizing principle for optimization of neural circuits. *Trends in Neurosciences*, 34(2):51–60. (Cited on pages 5 and 118.)

O'Keefe, J. and Dostrovsky, J. (1971). The hippocampus as a spatial map. Preliminary evidence from unit activity in the freely-moving rat. *Brain Research*, 34(1):171–175. (Cited on pages 1 and 2.)

O'Keefe, J. and Recce, M. L. (1993). Phase relationship between hippocampal place units and the EEG theta rhythm. *Hippocampus*, 3(3):317–330. (Cited on pages 2, 4, and 8.)

Pai, M.-C. and Jacobs, W. J. (2004). Topographical disorientation in community-residing patients with Alzheimer's disease. *International Journal of Geriatric Psychiatry*, 19(3):250–255. (Cited on page 156.)

Panzeri, S., Brunel, N., Logothetis, N. K., and Kayser, C. (2010). Sensory neural codes using multiplexed temporal scales. *Trends in Neurosciences*, 33(3):111–120. (Cited on page 4.)

Pastoll, H., Ramsden, H. L., and Nolan, M. F. (2012). Intrinsic electrophysiological properties of entorhinal cortex stellate cells and their contribution to grid cell firing fields. *Frontiers in Neural Circuits*, 6:17. (Cited on page 152.)

Pastoll, H., Solanka, L., van Rossum, M. C. W., and Nolan, M. F. (2013). Feedback Inhibition Enables Theta-Nested Gamma Oscillations and Grid Firing Fields. *Neuron*, 77(1):141–154. (Cited on pages 119 and 156.)

Press, W. H., Teukolsky, S. A., Vetterling, W., and Flannery, B. P. (1992). Spectral Analysis of Unevenly Sampled Data. In *Numerical recipes in C*. Press Syndicate of the University of Cambridge, New York. (Cited on page 69.)

Quilichini, P., Sirota, A., and Buzsaki, G. (2010). Intrinsic circuit organization and theta-gamma oscillation dynamics in the entorhinal cortex of the rat. *The Journal of Neuroscience*, 30(33):11128–11142. (Cited on pages 7, 22, 27, 91, 116, 122, and 153.)

Reifenstein, E. T., Kempter, R., Schreiber, S., Stemmler, M. B., and Herz, A. V. M. (2012). Grid cells in rat entorhinal cortex encode physical space with independent firing fields and phase precession at the single-trial level. *Proceedings of the National Academy of Sciences*, 109(16):6301–6306. (Cited on pages 4, 8, 120, and 122.)

Remme, M. W. H., Lengyel, M., and Gutkin, B. S. (2010). Democracy-independence trade-off in oscillating dendrites and its implications for grid cells. *Neuron*, 66(3):429–437. (Cited on page 38.)

Robinson, D. W. and Cameron, W. E. (2000). Time-dependent changes in input resistance of rat hypoglossal motoneurons associated with whole-cell recording. *Journal of Neurophysiology*, 83(5):3160–3164. (Cited on pages 84 and 85.)

Robinson, R. B. and Siegelbaum, S. A. (2003). Hyperpolarization-activated cation currents: from molecules to physiological function. *Annual review of physiology*, 65:453–480. (Cited on page 25.)

Ruth, R. E., Collier, T. J., and Routtenberg, A. (1982). Topography between the entorhinal cortex and the dentate septotemporal axis in rats: I. Medial and intermediate entorhinal projecting cells. *The Journal of Comparative Neurology*, 209(1):69–78. (Cited on pages 16 and 59.)

Ruth, R. E., Collier, T. J., and Routtenberg, A. (1988). Topographical relationship between the entorhinal cortex and the septotemporal axis of the dentate gyrus in rats: II. Cells projecting from lateral entorhinal subdivisions. *The Journal of Comparative Neurology*, 270(4):506–516. (Cited on pages 16 and 59.)

Sargolini, F., Fyhn, M., Hafting, T., McNaughton, B. L., Witter, M. P., Moser, M.-B., and Moser, E. I. (2006). Conjunctive representation of position, direction, and velocity in entorhinal cortex. *Science*, 312(5774):758–762. (Cited on pages 3, 5, 14, 23, 31, 32, 147, and 161.)

Schmidt-Hieber, C. and Häusser, M. (2013). Cellular mechanisms of spatial navigation in the medial entorhinal cortex. *Nature Neuroscience*, pages 1–10. (Cited on pages 59, 86, 151, and 159.)

Schreiber, S., Erchova, I., Heinemann, U., and Herz, A. V. M. (2004). Subthreshold resonance explains the frequency-dependent integration of periodic as well as random stimuli in the entorhinal cortex. *Journal of Neurophysiology*, 92(1):408–415. (Cited on pages 29, 30, 59, 81, and 86.)

Schwartz, S. and Coleman, P. D. (1981). Neurons of origin of the perforant path. *Experimental Neurology*, 74(1):305–312. (Cited on pages 16 and 59.)

Segal, M. (1977). Afferents to the entorhinal cortex of the rat studied by the method of retrograde transport of horseradish peroxidase. *Experimental Neurology*, 57(3):750–765. (Cited on page 18.)

Serafin, M., Williams, S., Khateb, A., Fort, P., and Mühlethaler, M. (1996). Rhythmic firing of medial septum non-cholinergic neurons. *Neuroscience*, 75(3):671–675. (Cited on page 12.)

Sherman-Gold, R. and Maertz, W. H., editors (2008). *The Axon Guide*. MDS Analytical Technologies, 3rd edition. (Cited on page 49.)

Silberberg, G., Grillner, S., Lebeau, F. E. N., Maex, R., and Markram, H. (2005). Synaptic pathways in neural microcircuits. *Trends in Neurosciences*, 28(10):541–551. (Cited on pages 89, 116, and 160.)

Sohal, V. S., Zhang, F., Yizhar, O., and Deisseroth, K. (2009). Parvalbumin neurons and gamma rhythms enhance cortical circuit performance. *Nature*, 459(7247):698–702. (Cited on pages 6 and 123.)

Solstad, T., Boccara, C. N., Kropff, E., Moser, M.-B., and Moser, E. I. (2008). Representation of geometric borders in the entorhinal cortex. *Science*, 322(5909):1865–1868. (Cited on page 157.)

Song, S., Sjöström, P. J., Reigl, M., Nelson, S., and Chklovskii, D. B. (2005). Highly nonrandom features of synaptic connectivity in local cortical circuits. *PLoS biology*, 3(3):e68. (Cited on pages 22, 91, and 105.)

Spruston, N. and Johnston, D. (1992). Perforated patch-clamp analysis of the passive membrane properties of three classes of hippocampal neurons. *Journal of Neurophysiology*, 67(3):508–529. (Cited on pages 28, 60, and 61.)

Staley, K. J., Otis, T. S., and Mody, I. (1992). Membrane properties of dentate gyrus granule cells: comparison of sharp microelectrode and whole-cell recordings. *Journal of Neurophysiology*, 67(5):1346–1358. (Cited on page 60.)

Stanton, P. K., Jones, R. S., Mody, I., and Heinemann, U. (1987). Epileptiform activity induced by lowering extracellular [Mg2+] in combined hippocampal-entorhinal cortex slices: modulation by receptors for norepinephrine and N-methyl-D-aspartate. *Epilepsy Research*, 1(1):53–62. (Cited on page 91.)

Steffenach, H.-A., Witter, M. P., Moser, M.-B., and Moser, E. I. (2005). Spatial memory in the rat requires the dorsolateral band of the entorhinal cortex. *Neuron*, 45(2):301–313. (Cited on pages 2, 59, and 151.)

Stensola, H., Stensola, T., Solstad, T., Frøland, K., Moser, M.-B., and Moser, E. I. (2012). The entorhinal grid map is discretized. *Nature*, 492(7427):72–78. (Cited on pages 3, 4, 8, 33, and 159.)

Steward, O. and Scoville, S. A. (1976). Cells of origin of entorhinal cortical afferents to the hippocampus and fascia dentata of the rat. *The Journal of Comparative Neurology*, 169(3):347–370. (Cited on pages 16 and 59.)

Stewart, M., Quirk, G. J., Barry, M., and Fox, S. E. (1992). Firing relations of medial entorhinal neurons to the hippocampal theta rhythm in urethane anesthetized and walking rats. *Experimental Brain Research*, 90(1):21–28. (Cited on pages 30 and 36.)

Tamamaki, N. and Nojyo, Y. (1995). Preservation of topography in the connections between the subiculum, field CA1, and the entorhinal cortex in rats. *The Journal of Comparative Neurology*, 353(3):379–390. (Cited on page 20.)

Taube, J. S., Kesslak, J. P., and Cotman, C. W. (1992). Lesions of the rat postsubiculum impair performance on spatial tasks. *Behavioral and neural biology*, 57(2):131–143. (Cited on page 2.)

Taube, J. S., Muller, R. U., and Ranck, J. B. (1990). Head-direction cells recorded from the postsubiculum in freely moving rats. I. Description and quantitative analysis. *The Journal of Neuroscience*, 10(2):420–435. (Cited on page 2.)

Tiesinga, P. and Sejnowski, T. J. (2009). Cortical enlightenment: are attentional gamma oscillations driven by ING or PING? *Neuron*, 63(6):727–732. (Cited on page 135.)

Van Cauter, T., Camon, J., Alvernhe, A., Elduayen, C., Sargolini, F., and Save, E. (2012). Distinct Roles of Medial and Lateral Entorhinal Cortex in Spatial Cognition. *Cereb Cortex*. (Cited on page 15.)

van der Linden, S. and Lopes da Silva, F. H. (1998). Comparison of the electrophysiology and morphology of layers III and II neurons of the rat medial entorhinal cortex in vitro. *The European Journal of Neuroscience*, 10(4):1479–1489. (Cited on page 28.)

van der Linden, S., Panzica, F., and de Curtis, M. (1999). Carbachol induces fast oscillations in the medial but not in the lateral entorhinal cortex of the isolated guinea pig brain. *Journal of Neurophysiology*, 82(5):2441–2450. (Cited on pages 12, 13, 14, 125, and 147.)

van Groen, T. (2001). Entorhinal cortex of the mouse: cytoarchitectonical organization. *Hippocampus*, 11(4):397–407. (Cited on pages 46 and 54.)

van Groen, T. and Wyss, J. M. (1990a). Extrinsic projections from area CA1 of the rat hippocampus: olfactory, cortical, subcortical, and bilateral hippocampal formation projections. *The Journal of Comparative Neurology*, 302(3):515–528. (Cited on page 20.)

van Groen, T. and Wyss, J. M. (1990b). The connections of presubiculum and parasubiculum in the rat. *Brain Research*, 518(1-2):227–243. (Cited on page 19.)

Van Haeften, T., Wouterlood, F. G., Jorritsma-Byham, B., and Witter, M. P. (1997). GABAergic presubicular projections to the medial entorhinal cortex of the rat. *The Journal of Neuroscience*, 17(2):862–874. (Cited on page 19.)

van Strien, N. M., Cappaert, N. L. M., and Witter, M. P. (2009). The anatomy of memory: an interactive overview of the parahippocampal-hippocampal network. *Nature Reviews Neuroscience*, 10(4):272–282. (Cited on pages 19, 20, and 161.)

Vanderwolf, C. H. (1969). Hippocampal electrical activity and voluntary movement in the rat. *Electroencephalography and clinical neurophysiology*, 26(4):407–418. (Cited on page 5.)

Varga, C., Lee, S. Y., and Soltesz, I. (2010). Target-selective GABAergic control of entorhinal cortex output. *Nature Neuroscience*, 13(7):822–824. (Cited on pages 16, 17, and 22.)

Visan, V., Heinemann, U., Volynets, A., and Müller, W. (2002). Calcium currents in rat entorhinal cortex layer II stellate and layer III pyramidal neurons in acute brain slice. *Neuroscience Letters*, 327(3):153–156. (Cited on page 25.)

Wang, H., Peca, J., Matsuzaki, M., Matsuzaki, K., Noguchi, J., Qiu, L., Wang, D., Zhang, F., Boyden, E. S., Deisseroth, K., Kasai, H., Hall, W. C., Feng, G., and Augustine, G. J. (2007). High-speed mapping of synaptic connectivity using photostimulation in Channelrhodopsin-2 transgenic mice. *Proceedings of the National Academy of Sciences*, 104(19):8143–8148. (Cited on pages 92 and 93.)

Waters, J. (2006). Background Synaptic Activity Is Sparse in Neocortex. *The Journal of Neuroscience*, 26(32):8267–8277. (Cited on page 87.)

Welday, A. C., Shlifer, I. G., Bloom, M. L., Zhang, K., and Blair, H. T. (2011). Cosine directional tuning of theta cell burst frequencies: evidence for spatial coding by oscillatory interference. *The Journal of Neuroscience*, 31(45):16157–16176. (Cited on page 38.)

White, J. A., Alonso, A. A., and Kay, A. R. (1993). A heart-like Na+ current in the medial entorhinal cortex. *Neuron*, 11(6):1037–1047. (Cited on page 24.)

White, J. A., Klink, R., Alonso, A. A., and Kay, A. R. (1998). Noise from voltage-gated ion channels may influence neuronal dynamics in the entorhinal cortex. *Journal of Neurophysiology*, 80(1):262–269. (Cited on pages 23, 31, and 38.)

Whittington, M. A., Cunningham, M. O., Lebeau, F. E. N., Racca, C., and Traub, R. D. (2010). Multiple origins of the cortical gamma rhythm. *Developmental Neurobiology*, 71(1):92–106. (Cited on pages 12 and 13.)

Williams, S. R. and Mitchell, S. J. (2008). Direct measurement of somatic voltage clamp errors in central neurons. *Nature Neuroscience*, 11(7):790–798. (Cited on page 97.)

Witter, M. P., Groenewegen, H. J., Lopes da Silva, F. H., and Lohman, A. H. (1989). Functional organization of the extrinsic and intrinsic circuitry of the parahippocampal region. *Progress in Neurobiology*, 33(3):161–253. (Cited on pages 15 and 18.)

Witter, M. P. and Moser, E. I. (2006). Spatial representation and the architecture of the entorhinal cortex. *Trends in Neurosciences*, 29(12):671–678. (Cited on page 89.)

Wouterlood, F. G., Härtig, W., Brückner, G., and Witter, M. P. (1995). Parvalbumin-immunoreactive neurons in the entorhinal cortex of the rat: localization, morphology, connectivity and ultrastructure. *Journal of Neurocytology*, 24(2):135–153. (Cited on page 17.)

Wu, X., Liao, L., Liu, X., Luo, F., Yang, T., and Li, C. (2012). Is ZD7288 a selective block of hyperpolarization-activated cyclic nucleotide-gated channel currents? *Channels*, 6(6). (Cited on page 82.)

Yartsev, M. M., Witter, M. P., and Ulanovsky, N. (2011). Grid cells without theta oscillations in the entorhinal cortex of bats. *Nature*, 479(7371):103–107. (Cited on pages 3, 7, 8, 149, and 162.)

Yizhar, O., Fenno, L. E., Davidson, T. J., Mogri, M. Z., and Deisseroth, K. (2011). Optogenetics in Neural Systems. *Neuron*, 71(1):9–34. (Cited on page 50.)

Yoshida, M. and Alonso, A. A. (2007). Cell-type specific modulation of intrinsic firing properties and subthreshold membrane oscillations by the M(Kv7)-current in neurons of the entorhinal cortex. *Journal of Neurophysiology*, 98(5):2779–2794. (Cited on page 25.)

Yoshida, M., Giocomo, L. M., Boardman, I., and Hasselmo, M. E. (2011). Frequency of subthreshold oscillations at different membrane potential voltages in neurons at different anatomical positions on the dorsoventral axis in the rat medial entorhinal cortex. *The Journal of Neuroscience*, 31(35):12683–12694. (Cited on pages 11, 30, 34, 69, 81, and 82.)

Zar, J. H. (1998). *Biostatistical Analysis*. Pearson, 4 edition. (Cited on page 62.)

Zechmeister, M. and Kürster, M. (2009). The generalised Lomb-Scargle periodogram. *Astronomy and Astrophysics*, 496(2):577–584. (Cited on page 68.)

Zhang, F., Gradinaru, V., Adamantidis, A. R., Durand, R., Airan, R. D., de Lecea, L., and Deisseroth, K. (2010). Optogenetic interrogation of neural circuits: technology for probing mammalian brain structures. *Nature Protocols*, 5(3):439–456. (Cited on page 50.)

Zilli, E. A. (2012). Models of grid cell spatial firing published 2005-2011. *Frontiers in Neural Circuits*, 6:16. (Cited on pages 37 and 152.)

Zilli, E. A. and Hasselmo, M. E. (2010). Coupled noisy spiking neurons as velocity-controlled oscillators in a model of grid cell spatial firing. *The Journal of Neuroscience*, 30(41):13850–13860. (Cited on pages 119 and 120.)

Zilli, E. A., Yoshida, M., Tahvildari, B., Giocomo, L. M., and Hasselmo, M. E. (2009). Evaluation of the oscillatory interference model of grid cell firing through analysis and measured period variance of some biological oscillators. *PLoS Computational Biology*, 5(11):e1000573. (Cited on page 30.)

A

ESTIMATING CONNECTIVITY PROBABILITIES

This derivation was provided by Lukas Solanka and Dr. Mark van Rossum

Derivation of connectivity probability formula

Assuming that N potential connections were tested, with none showing a synaptic response.

We denote the *true* connection probability as p. We cannot claim that $p = 0$, as we haven't tested all of the potential connections. However we also cannot with certainty say that $p < 1/N$, because there is in fact non-zero probability that $p > 1/N$. Instead, we estimate the range of $p \in [0, p_{max}]$, given a confidence interval C, e.g. $C = 95\%$ or similar, in the following way:

We can estimate a posterior probability of p, given that optical stimulation does not evoke synaptic responses from N potential connections tested

$$P(p|N) = \frac{P(N|p)P(p)}{P(N)}, \tag{A.1}$$

As we don't have any prior knowledge about the connection probability $P(p)$ we assume it is uniform, while $P(N)$ is a constant. Therefore $P(p|N)$ is proportional to

$$P(p|N) \propto P(N|p),$$

which is the probability of randomly testing N potential connections and none of them showing a synaptic response, given that the actual probability of connection is p. That is a binomial distribution and therefore:

$$P(p|N) \propto P(N|p) = \binom{0}{N}(1-p)^N \tag{A.2}$$

which after normalization reads

$$P(p|N) = (N+1)(1-p)^N \tag{A.3}$$

This gives us a likelihood of the probability of connection p given N tested potential connections. We can now set a confidence value C and estimate p_{max} that satisfies that $P(p \leqslant p_{max}) = C$.

$$\begin{aligned} P(p \leqslant p_{max}) &= \int_0^{p_{max}} dp P(p|N) \\ &= 1 - (1 - p_{max})^{N+1} \end{aligned}$$

Therefore

$$p_{max} = 1 - \sqrt[N+1]{1 - C}$$

We can then say that with confidence C that the connection probability will be less than p_{max}. Therefore, with 2000 light-induced tested potential connections and 95% confidence,

$$p \leqslant 1.5 \times 10^{-3}$$